**SAINT-PETERSBURG STATE UNIVERSITY**

*Printed as a manuscript*

**Zherebchevsky Vladimir Iosifovich**

# «NUCLEAR REACTIONS AT LOW INTERACTION ENERGIES WITH THE FORMATION AND DECAY OF LIGHT AND MEDIUM MASS RANGE NUCLEONIC SYSTEMS »

1.3.15. «Physics of atomic nuclei and elementary particles, high energy physics»

THESIS

Submitted in conformity with the requirements

for the degree of doctor of physico-mathematical sciences

Translation from Russian

**Saint-Petersburg**

**2025**

# CONTENTS

# Introduction

## Relevance of the work

It is now more than ninety years since humans first achieved the transformation of elements. The dreams of medieval alchemists, who believed that gold could be obtained from other elements, had long been ridiculed. However, suddenly, there was a man who not only suggested the possibility of such transformations but also demonstrated it experimentally. This man was Ernest Rutherford, who sought to remove one of the constituent particles from the nucleus and thereby remake the nucleus of the atom. He showed that fast alpha particles, when passing through dry air or nitrogen, produce a number of long-range particles that can be detected by scintillations on a zinc sulfide screen. [1]. Thus, the first nuclear reaction was discovered, marking the beginning of an entire era of studying physical processes involving nuclei and particles interacting at low energies.

Currently, there is growing interest in the physics of nuclear reactions at low interaction energies, particularly in studying the mechanisms of formation and decay of nucleonic systems corresponding to light and medium mass nuclei. This is due to both interests of fundamental scientific inquiries and the significant role these reactions play in nuclear physics, nuclear astrophysics, and the industrial production of radionuclides. Nuclei, being complex systems, are characterized by a wide range of properties, shapes, and states. Over time, nuclear physics has accumulated extensive experience in studying such systems, developing a variety of analytical methods and approximate approaches. In this regard, nuclear physics serves as a laboratory for investigating the fundamental laws and symmetries of complex systems at the microscopic level. The obtained knowledge is important not only for nuclear physics but also for a wide range of natural sciences, including astrophysics, condensed matter physics [2], radiation ecology, biology, and medicine.

One of the fundamental challenges in modern physics is the quantitative description of the processes involved in the formation of elements in the Universe.

Addressing this challenge enhances our understanding of the mechanisms and processes occurring within stars. Furthermore, the analysis of various stellar evolution scenarios and the study of the peculiarities of primordial nucleosynthesis provide additional motivation for investigating processes on a cosmic scale. However, the difficulties associated with experimentally studying nuclear reactions under "terrestrial" (laboratory) conditions, particularly at energies typical for these processes (ranging from keV to several hundred keV) necessitate the development of new, indirect methods to clarify the behavior of nuclei at low energies.

One of the advantages of these methods is the use of well-established algorithms for analyzing nuclear reactions, such as the R-matrix formalism, the distorted-wave Born approximation (DWBA), and the coupled-channel method. Consequently, when analyzing nuclear reaction experimental data (relevant to astrophysical studies), it is often necessary to incorporate interaction potentials. These potentials enable the accurate consideration of effects related to particle transfer and interactions, as well as the behavior of nuclear systems involving multiple nucleons, the so-called nuclear clusters.

In this work, the study of nuclear reactions involved in the formation of elements in the Universe will provide essential information on interaction potentials relevant to stellar nucleosynthesis. The development of such potentials is linked to another significant and intriguing fundamental problem: the explanation (and prediction) of the astrophysical S-factor behavior in nuclear fusion processes at energies near the "Gamow window". To date, predictions within the energy range of 2–5 MeV are highly sensitive to the choice of potential, which in most cases is multiparametric and phenomenological. These predictions cover almost the entire range of excitation functions for a variety of nuclear fusion reactions, leading to the subsequent formation of radionuclides. This range includes behaviors from a sharp decline to nearly zero, as well as an exponential increase across the entire energy range under consideration.

Nuclear reactions in the low-energy region, particularly those involving ions and neutron-rich nuclear systems of the light mass group, are of significant interest for nuclear astrophysics, including processes such as the CNO cycle. A fundamental aspect

of studying the compound systems formed in such reactions involves investigating their level structures, identifying resonance states, and determining the quantum characteristics of these levels. Consequently, experimental and theoretical studies of low-energy nuclear reactions under laboratory conditions offer broad prospects for applying the results to the investigation of nuclear processes occurring in stars.

It is important to note that the necessity of incorporating the laws of the microscopic world into cosmological models was recognized quite some time ago. As is well known, nearly all the elements around us were formed through nuclear reactions in stars. Therefore, to test cosmological models, accurate information on reaction cross-sections leading to the formation of specific elements at energies near the "Gamow window" is essential. However, in many cases, determining these cross-sections with high precision remains challenging. Consequently, when addressing the most pressing nuclear physics problems to be solved in the near future, particular emphasis is placed on studying the formation of chemical elements in nucleosynthesis, as well as reactions related to the carbon and oxygen burning in stars [3].

One of the options to addressing the challenges associated with investigating the interaction processes of light mass group nuclei is the implementation of semi-microscopic potentials, which incorporate realistic nucleon-nucleon interactions. Therefore, the use of already well-established theoretical models alongside newly available experimental data, it becomes possible to study the mechanisms underlying these nuclear processes and predict the composition of elements and their isotopes in the Universe. This represents a highly relevant and pressing task in modern astrophysics [4].

The study of nuclear reactions is particularly significant in astrophysics, especially in the low-energy region, where two nuclei overcome repulsion (via tunneling) and come into close proximity, forming a single nuclear system. These processes are known as fusion reactions. Among these, the study of nuclear fusion reactions at energies below the Coulomb barrier is especially promising, as they play a key role in stellar evolution and determine the scenarios for supernova formation. However, studying such phenomena experimentally under terrestrial conditions is

highly challenging. Stars contain a huge amount of matter and exist for millions of years, allowing reactions to occur even with extremely low probabilities. On Earth we have to use a very small amount of matter and perform all the necessary measurements in a matter of days. [5]. In recent years, a rather extensive array of experimental data on nuclear fusion in the low-energy region has been accumulated, revealing a number of intriguing effects that require further investigation and explanation. Consequently, it has become increasingly relevant to compare experimental and theoretical results using simple nuclear physics models. In this dissertation, a model utilized by Nobel laureate William Alfred Fowler in the 1970s (the rectangular potential well model) was used [6]. Isotopes of the light mass group, ranging from carbon to silicon, were selected for this study. This choice is justified by the fact that heavy nuclei play a negligible role in the formation of new elements in stars, while very light elements have already been extensively studied. The calculations performed in this dissertation have enabled the description of the astrophysical S-factor energy dependence for all the reactions considered, bringing the results close to the energy ranges characteristic of stellar processes. These results are important not only for astrophysics. A good understanding of reactions using accelerated ions and neutron-excess nuclei of the light mass group is also required for solving fundamental problems, such as the synthesis of new superheavy elements, the study of nuclei near the stability limits under conditions of proton or neutron excess, and the investigation of exotic decays involving a large number of particles. Additionally, these reactions have practical applications in fields such as radiation material science, nuclear medicine, and the membrane filters production [5].

To address these challenges, it is essential to select an appropriate potential within a specific model framework and then perform a comparative analysis of the results obtained using this potential with existing theoretical estimates. These estimates incorporate nucleon density calculations based on the Dirac-Hartree-Fock model [7]. In this dissertation, it is necessary to demonstrate that such a potential accurately describes: (1) elastic scattering at low energies, (2) the cross-section of fusion reactions at low energies (astrophysical S-factor), and (3) the position of the resonance-like

structure in the nuclear reaction $^{12}C+^{16}O$. This is particularly significant for current studies of nuclear fusion reactions in the near-barrier region [8], where the folding potential (even when accounting for nucleon density), gives substantial errors [9]. In addition, this approach will have some benefit within the framework of studies of evaporation processes in the decay of these nuclear systems [10].

For the studied reaction, $^{12}C+^{16}O$, it is crucial to accurately describe both high-lying and low-lying rotational bands for resonance states, as accomplished in this dissertation. The significance and, more importantly, the challenges associated with incorporating such resonance states into nuclear physics models used today are discussed in detail in the review [11]. It is demonstrated that some states interpreted as resonances in this system may arise due to the presence of a Legendre polynomial (a procedure involving the approximation of the angular distribution of reaction products using Legendre polynomials) in the region of cross-section fluctuations. This results in an angular distribution pattern characteristic of resonances, which, however, does not correspond to a state with a well-defined partial wave.

This type of work, which involves a unified description of fusion, elastic scattering, and the formation of molecular states in reactions such as the carbon burning reaction (using the example of the $^{12}C+^{16}O$ reaction), is actively pursued by several scientific groups, as seen in [12]. The interest in studying such nuclear reactions lies both the investigation of specific nuclear effects [13] and their significance in describing nucleosynthesis in massive stars. It has been demonstrated that for each of these processes, there is uncertainty in the choice of potential. However, all three processes can be described simultaneously using a single potential, and this uncertainty can be resolved by setting the angular momentum of the low-energy states. All of the considered potentials predict the existence of resonances in the energy region below 3 MeV, corresponding to temperatures below $10^9$ K, which are achievable in hot stars. These resonances can significantly influence the intensity of element formation in fusion reactions involving light-mass ions during stellar nucleosynthesis. Their consideration provides important information for analyzing stellar evolution processes. In this dissertation, it was demonstrated the consistency of the potential approach with

the AMD method [14], which is widely used today, and propose the presence of resonances within the Gamow window as an extension of the work conducted by an international team [15]. The issue of the cross-section suppression effect at low energies, which has been actively studied over the past few years [11], was also considered.

If we now shift our focus to the mass range of heavier nuclear systems and ask what the study of neutron-rich nuclei in this region can reveal, the most significant findings emerge from the investigation of neutron and proton distributions in nuclei. A key result was obtained for the isotopes $^{40}$Ca and $^{48}$Ca, where it was demonstrated that while the neutron and proton radii ($r_n$ and $r_p$) coincide in $^{40}$Ca, they differ in $^{48}$Ca, with $r_n - r_p \approx 0.2$ fm. However, the results would be far richer if all possible isotopes from $^{31}$Ca to $^{70}$Ca were investigated. As we know, there are 10 stable and over 18 radioactive tin isotopes, with a potential total of 84 isotopes with neutron numbers from 42 to 126. At a fixed proton number Z = 50, three neutron shells (N = 50, 82, and 126) are filled. The existence of such tin isotopes could provide invaluable insights into the symmetry term of the mass formula, changes in nuclear shape, and the structure of the nuclear surface [2]. Of great interest in this context is the study of doubly magic neutron-rich nuclei, as clearly demonstrated by the nuclear system $^{132}$Sn, with conclusions about additional studies of the excited states scheme of this nucleus. Therefore, in dissertation work the studies of nuclear reactions on tin isotopes, addressing both applied and fundamental problems has been done.

Another urgent task in the study of interactions between light charged particles and medium-mass nuclei is the direct investigation of fusion reactions, such as (p,γ) and (α,γ). Even for stable nuclei, these reactions, which are crucial in modern astrophysics, remain insufficiently studied. Moreover, despite extensive experimental and theoretical research, a complete understanding of the dynamics governing the decay of excited states of compound light nuclei, into competing (α,n)-(α,γ) channels, has yet to be achieved [16]. The reason for this lies in the absence of a definitive theory of nuclear interactions that accounts for both the relatively well-studied collective freedom of degrees and the so-called cluster configurations. These configurations, along with the

nuclear processes associated with them, are studied quite intensively in the field of medium-mass nucleonic systems [17, 18]. Moreover, the transition to light-group nuclear systems offers an excellent opportunity to generalize the results obtained, enabling the explanation of clustering effects and peculiarities [19, 20] across a wide mass and energy range of interacting particles and nuclei. It is also worth noting that, even within the framework of existing models, calculations require highly complex and resource-intensive computations. This necessitates the use of modeling, employing all modern methods of computational mathematics and computing technologies, such as parallel and distributed computing, including Grid technologies and machine learning techniques. Information about the nuclear processes under study can be obtained through a comprehensive investigation of both the nuclear systems (formed in highly excited states), and their products which decay into various output channels, resulting in the formation of light charged particles and neutrons. In practice, this problem is addressed through multiparameter correlation experiments utilizing coincidence techniques. Such experiments rely on combinations of gas detectors with semiconductor and scintillation detector systems, which are used to register products of nuclear reactions in the medium-mass region [17, 18], as well as to study nuclear reactions involving light ions of astrophysical interest [19, 21, 22, 23]. The modern development of multilayer [24] and gas target technologies [25], structural nuclear-physical materials, and cooling systems [26, 27, 28, 29], which can be applied in target technologies, along with advancements in nuclear electronics [30, 31], enables high-precision identification of both charged particles and ions across a wide range of energies (from tens of keV to hundreds of MeV) and masses.

The need for such complex studies is due to the significant interest in understanding the properties, characteristics, and features of the decay products under investigation. The addition of several neutrons to the target nucleus introduces further intrigue in studying the structural features formed in nuclear reactions of nucleonic systems. This represents an important fundamental problem, which also has an applied component, as it involves the processes of medium-mass nuclear system formation in

reactions with low-energy protons (up to 20 MeV). In such reactions, the focus lies on studying channels involving the emission of one or more nucleons in the final stage.

In this context, the task becomes particularly relevant due to the production of radionuclides used in nuclear medicine. From a medical perspective, these radionuclides are designed for effective early diagnosis and treatment of various localized oncological neoplasms, utilizing modern nuclear-physical research methods. Among these methods are the latest techniques for non-surgical tumor treatment using radiotherapeutic approaches [32]. In modern nuclear medicine, a significant part of clinical information is obtained by observing the distribution of radiopharmaceuticals (radionuclides incorporated into drugs) within the patient's body. Radionuclide imaging, which involves radionuclides that emit single photons, provides both planar and three-dimensional images when single photon emission computed tomography (SPECT) techniques are utilized. On the other hand, radiopharmaceuticals labeled with positron-emitting radionuclides are used in positron emission tomography (PET). PET is the most precise diagnostic method available today and is widely applied in oncology, neurology, and cardiology [33]. Another important application of nuclear medicine methods is the targeted delivery of radiopharmaceuticals to cancer cells for subsequent non-surgical tumor treatment, known as radionuclide targeted therapy. The goal of this approach is to enhance the intracellular penetration of radiopharmaceuticals into tumor formations while minimizing harm to healthy cells. The combination of radionuclide imaging with radionuclide therapy in the theranostics method (therapy + diagnostics) can yield excellent results for the effective early detection and treatment of various localized malignant tumors, with minimal side effects [33, 34]. In this case, the key role is given to nuclear physics technologies, in which nuclear reactions for the production of radiopharmaceuticals come first. These radiopharmaceuticals should meet the following criteria: a) the half-life of the radionuclide included in the radiopharmaceutical should be comparable to (or slightly longer than) the duration of the medical procedure; b) the radionuclide should emit gamma quanta of predominantly low energies (up to 170 keV) as well as short-range charged particles; c) the radionuclide should be chemically active to allow incorporation into the drug molecule

without altering its biological behavior. Additionally, the radiopharmaceutical should accumulate only in the targeted area of the body, be relatively quickly excreted, be easy to manufacture, and have a low production cost [33–34].

SPECT and PET are widely used in medical practice. For diagnostic procedures related to SPECT, the radionuclide $^{99m}$Tc ($T_{1/2}$ = 6 hours, gamma-quantum energy 140.5 keV, intensity per 100 decay events: 89 quanta) is most commonly used. It is produced through nuclear reactions and also by generative means, such as the $^{99}$Mo ($T_{1/2}$ = 65.9 hours)/$^{99m}$Tc generator system. A generator is a device that contains a pair of long-lived parent and short-lived daughter radionuclides. Through appropriate radiochemical reactions, this daughter radionuclide is extracted for further use in nuclear medicine. Today, more than 80% of SPECT diagnostic procedures worldwide are performed using the isotope $^{99m}$Tc. Therefore, in this dissertation, nuclear reactions for the production of both $^{99m}$Tc and its generator $^{99}$Mo/$^{99m}$Tc, at low- and medium-energy charged particle accelerators, are discussed in detail. As for PET diagnostics, it becomes possible to track the distribution of biologically active compounds containing positron-emitting radionuclides within the body. This method has very high sensitivity, and the presence of organogenic elements, such as carbon, nitrogen, and oxygen, among positron-emitting radionuclides allows the use of biologically active substances labeled with these radionuclides, which are naturally present in the body [33]. An important task for PET scanners is to improve the quality of visualization and the spatial resolution of the entire tomographic system. Currently, the spatial resolution of such systems for radionuclide imaging of organs and tissues is approximately 1–3 mm. Therefore, it is necessary to actively apply modern nuclear-physical detector technologies to achieve of resolution in PET systems at submillimeter and micron levels. To address these challenges, new detector modules based on fast scintillators and silicon photomultipliers, including the “time-of-flight” technique, are being developed [33]. Additionally, the so-called “gamma-PET” method appears promising. In this approach, in addition to the two annihilation gamma quanta (standard PET method), a coincident gamma quantum (with energy in the range of 1100–1200 keV) is registered using a Compton-spectrometer. This enables 3D gamma imaging with high spatial resolution of

the investigated organs and tumors [35, 36]. The positron-emitting radionuclide $^{44}$Sc ($T_{1/2}$ = 4.04 hours) is suitable for the implementation of this method. In this radionuclide decay scheme, in addition to positrons and the corresponding annihilation gamma quanta of 511 keV (with an intensity of 188 quanta per 100 decay events), there are also gamma quanta with energy of 1157 keV (intensity of 100 quanta per 100 decay events). This radionuclide has also proven effective in preclinical and clinical studies for PET imaging and in theranostic applications [37]. The primary methods for producing this radionuclide are the $^{44}$Ca(p,n)$^{44}$Sc nuclear reaction, or the $^{44}$Ti/$^{44}$Sc generator method, in which the parent radionuclide $^{44}$Ti ($T_{1/2}$ = 59.1 years) is produced in nuclear reaction: $^{45}$Sc(p,2n)$^{44}$Ti. Therefore, the excitation functions of these two reactions are analyzed in detail in this dissertation.

Combining radionuclide imaging (SPECT or PET) and targeted radionuclide therapy into a single procedure (theranostics) can be achieved in several ways. The first method involves attaching two radionuclides to a biologically active carrier molecule: one for tumor imaging, such as $^{131}$I ($T_{1/2}$ = 8 days) for SPECT or $^{68}$Ga ($T_{1/2}$ = 1.8 hours) for PET and the other for therapy, such as $^{177}$Lu ($T_{1/2}$ = 6.64 days), which emits beta particles. Another approach is to incorporate one or more radioactive isotopes of the same element into a biological carrier molecule (see Figure 1) [33] for targeted delivery of the radionuclide to cancer cells [see 32 for more details].

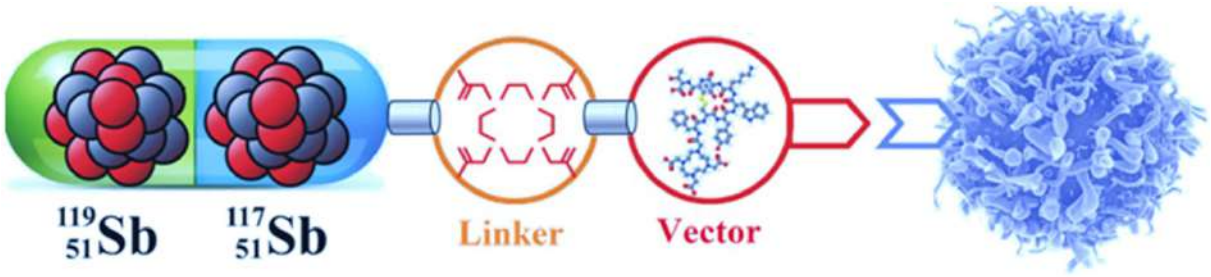


Figure 1 – Scheme of a radiopharmaceutical (containing antimony radionuclides: diagnostic – $^{117}$Sb and therapeutic – $^{119}$Sb) targeted delivery to a cancer cell [33].

It is preferable to use two or more radioactive isotopes (coordinated pairs of isotopes) of the same element, which have higher intensities of the corresponding radiations. Thus, a pair of radionuclides has found wide application in theranostics: $^{123}$I

($T_{1/2}$ = 13.2 hours) (for SPECT, gamma quantum energy – 159 keV, intensity 84 quanta per 100 decay events) and $^{131}$I (for beta therapy, average electron energy – 182 keV, intensity 100 per 100 decay events). Currently, even a matched quartet of radionuclides, in which terbium isotopes play the main role, has been developed for use in theranostic methods [38]: $^{152}$Tb ($T_{1/2}$ = 17.5 hours) for PET, $^{155}$Tb ($T_{1/2}$ = 5.32 days) for SPECT, $^{149}$Tb ($T_{1/2}$ = 4.12 hours) for alpha therapy and theranostics, and $^{161}$Tb ($T_{1/2}$ = 6.95 days) for beta therapy and SPECT diagnostics. Since the radionuclide $^{161}$Tb is a promising candidate for use in nuclear medicine techniques [39, 40], in this dissertation work separately the nuclear reaction: $^{160}$Gd(d,x)$^{161}$Tb has been analyzed, to produce this isotope using the deuteron reaction channel. However, it is undesirable to include alpha-emitting radionuclides in therapeutic methods due to the recoil nuclei produced by alpha decay, which can destroy biological carrier molecules. Beta-emitting radionuclides present a different challenge: because of the continuous beta spectrum, it is difficult to put the dose to the patient and to optimize treatment planning [33, 34, 41]. Therefore, radionuclides emitting Auger electrons are promising for the tumor targeted therapy [34, 42]. These electrons have a discrete spectrum with low energy (ranging from 3 to 30 keV) and a high linear energy transfer value, resulting in a range in tissues of the order 10 microns, as well as a high emission intensity (more than 100 per 100 decay events). In this case, radionuclides emitting Auger electrons can be effectively used to destroy small tumors and micrometastases with minimal impact on healthy tissues [33]. A matched pair of antimony radionuclides is well suited for theranostic methods: $^{117}$Sb ($T_{1/2}$ = 2.8 hours) for SPECT, with a gamma-ray energy of 158.5 keV and an intensity of 86 quanta per 100 decay events, and the radionuclide $^{119}$Sb ($T_{1/2}$ = 38.2 hours) for Auger therapy, as it emits L-series Auger electrons with an energy of 2.95 keV and K-series electrons with an energy of 21 keV, with emission intensities of 147 and 12 per 100 decay events, respectively [34]. By attaching these two antimony radionuclides to a biological vector carrier molecule using a specialized chemical agent (linker), a radiopharmaceutical is created that enters cancer cells by binding to their specific receptors located on the membrane (see Figure 1). Subsequently, by detecting gamma quanta from the radionuclide $^{117}$Sb using SPECT methods, tumor and metastases can be

visualized with high resolution, while the accompanying Auger electrons from the radionuclide $^{119}$Sb deliver the necessary therapeutic dose to destroy cancer cells within these tumors.

Therefore, this dissertation examines nuclear reactions with tin targets (both natural and highly enriched) to study the excitation functions of nuclear processes in which radionuclides: $^{119}$Sb and $^{117}$Sb, promising for use in nuclear medicine is produced. Regarding the general task of studying reactions in the medium-mass nuclei range, this work includes a comprehensive analysis based on a large dataset of both theoretical and experimental data [43].

Within the framework of this dissertation work, a series of experiments were done to obtain cross sections of nuclear reactions that produce radionuclides used in nuclear medicine, a whole class of monitor reactions was determined and analyzed to obtain excitation functions of these reactions. There was a stronger focus on the study of nuclear reactions with formation of antimony isotopes in the exit channel. At the first stage, experiments were performed for the excitation function in reactions on natural tin (natural content of tin isotopes) and a unknown output channel: $^{nat}$Sn(p,x), which is of interest to other scientific groups (see, for example, [44]). However, to study the mechanisms of light charged particle and neutron evaporation from compound nuclear systems formed in nuclear reactions induced by protons (e.g., reactions producing $^{117}$Sb and $^{119}$Sb isotopes in the exit channels), there is currently insufficient experimental data on the cross sections of such reactions. For the $^{117}$Sn(p,n)$^{119}$Sb reaction (particularly in the region of the excitation function maximum), the EXFOR experimental database [45] provides only a few experimental values [see also 46, 47], and for $^{117}$Sb, no experimental values are available in the energy region above 9 MeV. According to preliminary estimates, the excitation function maximum for such reactions is expected to occur at proton energies of 12–14 MeV, which are achievable at many compact medical cyclotrons. Therefore, the experiments conducted in this work, aimed at obtaining information on the cross sections of antimony radionuclide formation, are of interest not only from a fundamental but also from an applied perspective. Through model calculations performed in this study, it became possible to estimate the

probabilities of formation for all reaction products and to determine the yields (activity of radionuclides formed during target irradiation) of each of the studied radionuclides. Extending these studies to a wide range of tin isotopes used as targets it has opened significant prospects for analyzing the dynamics of (p,n) and (p,2n) reactions in the medium-mass range. Experimental investigations of the excitation function maxima of these reactions, using a novel target system, have provided critical information for the future industrial production of antimony radionuclides, which are promising for their application in advanced medical technologies for cancer therapy and diagnosis.

**The dissertation Objectives and Tasks**

The development of experimental and computational capabilities has made it possible to refine the procedure for studying nuclear reactions at low energies and to include reaction channels that play a significant role in nucleosynthesis processes. Advances in the study of nuclear reactions at low, "astrophysical" energies have enabled a transition from qualitative to quantitative descriptions of both stellar nucleosynthesis and processes related to the dynamical features of nuclear reactions involving light-mass ions. For nuclear reactions involving the formation of medium-mass radionuclides, many open questions remain, among which a detailed investigation of the excitation function of such reactions is of particular interest.

The primary goal of this dissertation was to provide a comprehensive study of nuclear reactions in the energy range from a 1 MeV to several tens of MeV, involving the formation and decay of light and medium-mass nucleonic systems.

To achieve this goal, the following tasks were undertaken:

1) Interpret the available experimental results in the field of low-energy nuclear reactions and propose a potential that accurately describes: a) elastic scattering at low energies; b) the cross section of fusion reactions at low energies (astrophysical S-factor); c) the position of the resonance-like structure in the reaction: $^{12}C + ^{16}O$.

2) Investigate the processes of fusion, elastic scattering, and the formation of molecular states in the reaction of carbon burning in stars, using the example of the

nuclear reaction: $^{12}C + ^{16}O$, and describe the positions of the high-lying and low-lying rotational bands for the resonance states in this reaction.

3) Studies of nuclear reactions leading to the formation of neutron-rich nucleonic systems in the light-mass group, such as $^{14}C$ and $^{22}Ne$.

4) Analyze nuclear reactions leading to the formation of nucleonic systems in the mass range $A < 30$ and investigate the excitation functions of nuclear reactions with neutron emission in the final state for the mass range $A > 40$.

5) Studies of nuclear reactions involving medium-mass nucleonic systems, leading to the formation of radionuclides in the exit channels, which are used in nuclear medicine.

6) To develop and implement experimental methodologies using highly enriched targets for studying the nuclear reaction excitation functions across a wide range of colliding particles and nuclei.

7) To carry out experiments involving the irradiation of highly enriched tin isotope targets ($^{117}Sn$ and $^{119}Sn$) to study the nuclear reaction excitation functions of $^{117}Sn(p,n)^{117}Sb$ and $^{119}Sn(p,n)^{119}Sb$, as well as to investigate the maxima of the excitation functions for these reactions.

8) Perform a detailed analysis of the nuclear reaction excitation functions for $^{117}Sn(p,n)^{117}S$ and $^{119}Sn(p,n)^{119}Sb$ using selected theoretical models.

9) Analyze the excitation functions of (p,n) reactions involving tin isotopes with mass numbers: 115, 116, 118, 120, and 122, leading to the formation of antimony radionuclides in the exit channels.

10) Determine the thick target yield functions for (p,n) reactions in which the radionuclides: $^{117}Sb$ and $^{119}Sb$ are produced in the exit channels.

**Scientific novelty of the work**

Answers to most of the problems addressed in this dissertation were obtained for the first time.

1) In this work, to investigate neutron-rich nuclear systems in the light-mass group ($^{14}$C), an experimental setup was developed using new charge-sensitive preamplifiers and a multi-sensor system for monitoring charged particle and heavy ion beams. This setup enabled high-resolution measurements of the energy spectrum of alpha-particle scattering on a highly enriched target of the neutron-rich $^{14}$C nucleus (containing 80% $^{14}$C and 20% $^{12}$C). It also allowed for the precise identification of the elastic scattering peak and the separation of nearby excited states in the nuclear systems $^{14}$C and $^{12}$C.

2) To detect the products of the studied reaction: $^{14}C(^{12}C,\alpha_1\alpha_2)\rightarrow^{26}Mg^*\rightarrow^{22}Ne^*\rightarrow^{18}O$, a multi-module experimental setup was developed. By using this setup the multiparameter correlation experiments were carried out with utilizing a specialized method for analyzing signals (pulse shape analysis) obtained from silicon detectors.

3) On a large background of registered alpha-particles in the reaction: $^{14}C(^{12}C,\alpha_1\alpha_2)\rightarrow^{26}Mg^*\rightarrow^{22}Ne^*\rightarrow^{18}O$ it was possible to identify the reaction channel associated with the formation of the neutron-rich nucleus $^{6}$He. Thus, events corresponding to the excited states of the $^{20}$Ne nuclei formed in the reaction: $^{14}C(^{12}C,^{6}He)^{20}Ne^*$ were identified. The detection of the exotic $^{6}$He nuclei was made possible through an original experimental technique, which included new silicon detectors and specialized charge-sensitive preamplifiers capable of analyzing signals via pulse shape technique, taking into account the different charge collection times in these detectors.

4) In the investigated reaction: $^{14}C(^{12}C,\alpha_1\alpha_2)\rightarrow^{26}Mg^*\rightarrow^{22}Ne^*\rightarrow^{18}O$ at a $^{12}$C beam energy of 44 MeV, five high-spin states in the $^{22}$Ne nucleus were observed within the excitation energy range of 16 to 30 MeV. Based on their characteristics, these states can be identified as rotational bands with distinct structures characteristic of nuclear molecules.

5) In analyzing the nuclear-physical features of the: $^{12}C + ^{16}O$ reaction, a specialized potential was applied to describe the reaction products angular distribution across a broad energy range, including states that can be attributed to rotational bands based on molecular configurations. For the nuclear system formed by the interaction of carbon

and oxygen ions, states with different global quantum numbers were identified. It was predicted that, over a sufficiently wide range of the compound nucleus excitation energies, a certain number of resonances should be expected, some of which occur near the “Gamow window” for stellar burning reactions.

6) The results of this work, utilizing selected interaction potentials to describe nuclear reactions in the light-mass range, have been applied to analyze nuclear fusion processes that play a significant role in astrophysical processes. In this context, the focus was on studying nuclear fusion reactions at energies near the Coulomb barrier. These processes are crucial for stellar evolution and determine the mechanisms of supernova formation.

7) A method for analyzing the astrophysical S-factor was developed, based on an approach involving a rectangular potential well with a small number of parameters. These parameters include the interaction radius, the real part of the potential (describing attraction or repulsion), and the imaginary part of the potential, which characterizes the intensity of nuclear fusion. This model formalism for determining the astrophysical S-factor of fusion reactions involving light spinless nuclei enabled a comparative analysis of the reaction intensity across different interacting systems. It became possible to determine the fusion cross sections at low energies, providing insights into the mechanisms of nuclear reactions for light nuclei of astrophysical interest.

8) For the mass range from A = 40 to A = 239, theoretical studies of the excitation functions of nuclear reactions involving neutron emission in the final state were done. The growing volume of experimental results for nuclear reactions in the low- and intermediate-energy range in recent years has enabled comprehensive data analysis using nuclear models with a limited number of parameters. Such analysis is essential, as the results of various experimental studies of specific nuclear reactions or systems often do not align with one another. Given the significant interest in these reactions for applied purposes, particularly in the production of isotopes (in particular (p,n) reactions) for nuclear medicine, it is crucial to develop theoretical estimates of the specific radionuclides yields. Therefore, to identify experimental data errors in global nuclear physics databases and isolate anomalous regions within large datasets for further

detailed study, a clear and straightforward analysis procedure with appropriate algorithms was developed in this dissertation. These algorithms incorporate nuclear-physical models and avoid fitting experimental results with polynomials of arbitrary orders. Due to the limited systematics available for (p,n) reactions, an analysis of existing experimental data was performed, yielding excitation functions for these reactions in the energy range from threshold energies up to 60 MeV, covering the mass region from A = 40 to A = 239.

9) Detailed studies of nuclear reactions leading to the formation of radionuclides used in medical technologies, such as $^{44}$Sc, $^{119}$Sb, $^{117}$Sb, $^{161}$Tb, and radionuclide generators like $^{44}$Ti/$^{44}$Sc and $^{99}$Mo/$^{99m}$Tc were done. These studies focused on analyzing the excitation functions of nuclear reactions to produce these isotopes.

10) The target complex was modernized to realize studies of nuclear reactions and measurements of reaction excitation function in a wide mass range of irradiated nuclei and protons, deuterons, alpha particles beams.

11) Using a modernized target complex, the excitation functions of the nuclear reactions: $^{117}$Sn(p,n)$^{117}$Sb and $^{119}$Sn(p,n)$^{119}$Sb were measured in the energy range of 7–15 MeV, with the aim of obtaining data in the excitation function maximum. Several experimental cross-section values for the excitation functions of these reactions were obtained for the first time.

12) Using selected and validated theoretical models, detailed studies of the excitation function maxima for the reactions: $^{117}$Sn(p,n)$^{117}$Sb and $^{119}$Sn(p,n)$^{119}$Sb were conducted. Based on the results obtained for the formation of the antimony radionuclides $^{119}$Sb and $^{117}$Sb in these reactions, there is possibility for combining advanced imaging techniques with radionuclide therapy using these isotopes.

13) Nuclear reactions were analyzed for a wide range of tin isotopes used as targets. This enables the studies of the dynamics of (p,n) and (p,2n) reactions in the medium-mass range, leading to the formation of antimony radionuclides. In the context of this task, new information on the excitation functions of the following reactions: $^{115}$Sn(p,n)$^{115}$Sb, $^{116}$Sn(p,n)$^{116}$Sb, $^{118}$Sn(p,n)$^{118}$Sb, $^{120}$Sn(p,n)$^{120}$Sb, $^{122}$Sn(p,n)$^{122}$Sb, $^{124}$Sn(p,n)$^{124}$Sb was obtained.

14) In this dissertation, new data were obtained on the thick targets yields of radionuclides which obtained in reactions leading to the formation of $^{99m}$Tc (as well as its generator form $^{99}$Mo/$^{99m}$Tc) and radionuclides promising for nuclear medicine applications: $^{117}$Sb and $^{119}$Sb. The evaluation of the accumulated activity allowed for conclusions regarding the feasibility of producing $^{99m}$Tc at proton accelerators in the energy range of 40–80 MeV, and antimony radionuclides at compact cyclotrons with energies up to 15 MeV, to cover the existing needs of medical institutions in appropriate radiopharmaceuticals.

**Practical significance**

The results obtained from studies of fusion processes, elastic scattering, and the formation of resonance states in nuclear systems formed by the interaction of particles and nuclei in the light-mass range, as well as the results of studies of nuclear reactions leading to the neutron-rich nucleonic systems formation, will provide insights into various scenarios of stellar evolution and the mechanisms of nucleosynthesis in the Universe through experiments carried out in terrestrial laboratories. This approach will help reduce the costs associated with expensive projects involving space stations and observatories in near-Earth and interplanetary space, as the answers to these questions can be sought through experiments performed on Earth.

In this dissertation, information on the excitation functions of nuclear reactions leading to the formation of radionuclides in the medium-mass range was also obtained. A key applied aspect of this work was the use of a modernized target complex. This target system was specifically designed to optimize irradiation conditions for various solid-state targets and can be used not only for fundamental studies of nuclear reactions in proton, deuteron, and alpha-particle beams but also for addressing applied challenges in the production of radionuclides for industrial and medical applications. During the experimental work, it was demonstrated that such a target complex can be utilized at many compact cyclotrons specializing in radionuclide production.

Returning to the challenges of studying the nuclear reactions excitation

functions, it can be stated that experimental data on the cross sections of several reactions for the production of radionuclides important for nuclear medicine are either insufficient (particularly in the incident proton energy range of 10–20 MeV) or entirely absent. Therefore, the new data obtained in this work can be effectively applied to the production of radionuclides used in advanced methods of radionuclide diagnostics and therapy for oncological diseases. By analyzing the results of experimental and theoretical studies of the (p, xn) reaction excitation functions in the energy range of 6–80 MeV for medium-mass nuclear systems, with radionuclides such as: scandium, technetium, antimony, and terbium, prerequisites were created for their industrial development with subsequent use in methods of precision visualization of malignant neoplasms, targeted radionuclide therapy and combined methods of cancer treatment – theranostics. Of significant practical importance are the calculations performed in this dissertation for the thick target yields of radionuclides formed in nuclear reactions on accelerators. These calculations include the reactor-produced radionuclide $^{99m}$Tc (as well as its generator form $^{99}$Mo/$^{99m}$Tc), which is widely used in global clinical practice, and promising radionuclides for theranostic applications, such as $^{117}$Sb and $^{119}$Sb. The obtained data enabled the estimation of accumulated activity and provided insights into the feasibility of producing $^{99m}$Tc using proton accelerators with energies of 40–80 MeV and antimony radionuclides using compact cyclotrons with energies of 7–15 MeV, thereby addressing the demand for radiopharmaceuticals based on these radionuclides in medical institutions.

**Methods**

To study the characteristics of the nuclear reaction: $\alpha + {}^{14}C$, where alpha particles accelerated to an energy of 27 MeV bombarded a radioactive target of the neutron-rich nucleus $^{14}$C (alpha-cluster structure of the $^{12}$C nucleus plus two additional neutrons), an experimental setup was developed. This setup included a scattering chamber, detector complexes based on four silicon surface-barrier sensors, and electronic modules for data acquisition and processing. Using an analog multiplexer and an analog-to-digital

converter (implemented with FPGA technology – field-programmable gate array), complete information from all four detectors was collected for subsequent off-line processing. The advantage of this setup lies in the use of minimal electronic equipment, as all four detectors are connected to a single multiplexer.

The on-line beam profile visualization significantly improved cyclotron beam extraction, increased the beam intensity on the target, and ensured acceptable beam focusing on the target through the use of a system of quadrupole lenses, correcting magnets, a bending magnet, and movable collimators. By employing a real-time monitoring system for beam shape and position (a multisensor system for monitoring charged particle and heavy ion beams), along with the adjustable ion-optical system of the cyclotron and the optimization of beam intensity and energy resolution, the energy spread of alpha particles in the beam was reduced to 0.5%. As a result, the elastic scattering peak in the studied reaction was identified with high accuracy and resolution, and closely spaced excited states in the $^{14}C$ and $^{12}C$ nuclear systems were successfully separated (see also Section 1.2.1; all subsequent references to the literature are provided in the corresponding chapters).

To study the nuclear reaction: $^{14}C(^{12}C,\alpha_1\alpha_2)\rightarrow^{26}Mg^*\rightarrow^{22}Ne^*\rightarrow^{18}O$, which involves the formation of high-spin states in light-mass nuclear systems, a beam of $^{12}C$ nuclei accelerated to 44 MeV was used to bombard a $^{14}C$ target. The detector system for the reaction products detecting, was placed in a vacuum scattering chamber with a diameter of 1.5 meters. The angular correlation method was employed to achieve particle-to-particle coincidence conditions. Due to the low coincidence frequency and the need for measurements at multiple angles to precisely identify spins, large-area position-sensitive detector telescopes were utilized in the experiment.

To identify events corresponding to the detection of alpha particles – reaction products in the process: $^{14}C(^{12}C,\alpha_1\alpha_2)\rightarrow^{26}Mg^*\rightarrow^{22}Ne^*\rightarrow^{18}O$ a specialized method of analyzing the corresponding signals using pulse shape technique was employed. This method is based on the principle that, in silicon detectors, particles of different masses and charges interacting with the detector material produce different charge collection times. The primary alpha particles ($\alpha_1$), which populate highly excited states in $^{22}Ne$

nuclei, were detected by two silicon PIN diode detectors (front detectors). To suppress the background from $^{12}C$ nuclei undergoing elastic scattering, the PIN detectors were covered with 15-micron-thick platinum foil. This setup enabled the detection of nuclei ranging from hydrogen to lithium, with an alpha particle detection threshold of approximately 10 MeV. The detection of secondary alpha particles ($\alpha_2$), resulting from the decay of excited states of neon nuclei, was performed using two large-area position-sensitive dE-E telescopes, covering angular ranges of 34° to 50° and 58° to 75° in the laboratory coordinate system. Each telescope consisted of a gas proportional detector with a single anode, serving as the dE detector, and 10 silicon PIN diodes used as stop detectors (E detectors). A multi-module system was specifically designed to collect signals from all detector complexes: two dE-E telescopes and two front silicon PIN detectors. As a result, this experimental setup enabled the identification of energy bands corresponding to protons, deuterons, tritons, alpha particles, and light nuclei, including $^{6,7}Li$, $^{9,10}Be$, $^{11}B$, and $^{12,14}C$. Additionally, the neutron-rich nucleus $^{6}He$ was detected in the reaction: $^{14}C(^{12}C, ^{6}He)^{20}Ne^*$, and several high-spin states in the $^{22}Ne$ nucleus were observed. The analysis of the characteristics of these states allowed them to be identified as rotational bands with distinct structures, which may correspond to nuclear molecules (see also Section 1.2.2).

Modern studies on the analysis of nuclear reactions using the double folding potential, which incorporates cluster degrees of freedom (DFC), have demonstrated the ability to describe elastic scattering cross sections across a wide range of energies and masses with a relatively small number of free parameters. Additionally, the potential of such models for describing the astrophysical S-factor has been highlighted, although challenges remain regarding the systematics of normalization factors. When studying reactions involving nuclei with mass numbers of 11–16 within the potential model, three approaches to defining the potential are possible. The first approach involves selecting a potential that accurately describes particle distributions in scattering experiments. However, this method faces challenges due to the strong energy dependence of the potential parameters (particularly for the imaginary part). Difficulties arise in analyzing angular distributions at low energies because of the significant

influence of the Coulomb field, and at high energies due to the need to account for inelastic processes. The second approach utilizes a semi-microscopic potential in the folding form. However, in this case, there is the restricted ability to parameterize the potential, with the depth normalization factor being the most natural parameter for adjustment. The third approach employs a mixed method, where the potential is treated in a semi-microscopic form but includes additional terms to allow for parameterization. This approach was applied in the dissertation to describe nuclear interactions while accounting for clustering effects.

Within the framework of the optical model, the angular distributions for the $^{12}C + ^{16}O$ reaction was analyzed using the selected potential at different energies and compared the results obtained in the angular range of 90°–180° with Legendre polynomials of various orders. The differential scattering cross section generally exhibits a complex angular dependence, but there are cases where a polynomial structure can be observed. This structure manifests as a series of maxima, which correspond to the maxima of the square of the function $P_l(\cos\theta)$ (where $P_l(x)$ is a Legendre polynomial of degree $l$) for a specific fixed value of $l$. However, even in such cases, the structure cannot be fully described by a single polynomial of degree $l$. In this dissertation, a procedure was developed to estimate the contributions of individual Legendre polynomials to a given model distribution. This procedure enabled the identification of the high-spin states. It was also observed that, in some cases, when a low-spin resonance occurs in a region with a polynomial structure at large angles, a false indication of a high-spin resonance may arise. Therefore, the technique described above, based on the analysis of Legendre polynomials, allows for the detection of so-called "false states," which can be identified as resonances belonging to the rotational band (see also Section 1.3).

It should be noted that when studying the characteristics of nuclear reactions and performing the corresponding model calculations, a number of parameters are required. This often leads to complex calculations and discrepancies between the results obtained from calculations and experiments. An elegant and, most importantly, simple method (for analyzing the astrophysical S-factor), based on an approach involving the use of a

rectangular potential well was proposed. The advantage of this model lies in its computational simplicity and the small number of parameters, which include the interaction radius, the real part of the potential (describing attraction or repulsion), and the imaginary part of the potential, which characterizes the intensity of nuclear fusion.

To study fusion reactions at energies below the Coulomb barrier, a method was developed using the formalism of a rectangular potential well. Calculations involving potentials based on folding and unified potentials reduce the number of parameters, but this approach is not always suitable for the imaginary part of the potential. Therefore, using a simplified version of the potential in the form of a rectangular well with a minimal number of parameters allows for the inclusion of both the real and imaginary parts of the potential, with the radii of the imaginary and real parts being equal. This approach addresses the challenge of describing sub-barrier nuclear fusion and provides insights into the systematics of the parameters of the rectangular potential model. Previously, this method was applied to individual nuclei, which did not allow for the determination of the dependence of the potential parameters on the charge and mass numbers of the reacting nuclei. Consequently, an analysis of fusion reactions between spin-zero nuclei, which play a key role in stellar nucleosynthesis processes, was done at energies below the Coulomb barrier. The range of nuclei considered was chosen from A = 12 to A = 28, and the wave function was selected to be proportional to the expression: exp(–iKr). The validity of this choice was confirmed by comparing the specified expression with the wave function obtained through the numerical solution of the Schrödinger equation using the potential described by splines. The formulas used for these calculations are presented in greater detail in Section 1.4, with corresponding references to the sources.

Nuclear processes involving combinations of different interacting nuclei: $^{12}$C, $^{16,18}$O, $^{20}$Ne, $^{24}$Mg, and $^{28,30}$Si were analyzed using experimental data. To determine the potential parameters (R, V, W), calculations were performed to minimize the $\chi^2$ value, and the discrepancy between theoretical calculations and experimental values of the astrophysical S-factor was analyzed, focusing on the energy region below the Coulomb barrier. For all these nuclear systems within the studied mass and energy range, a set of

parameters (R, V, and W) was determined, enabling an accurate description of the S-factor's dependence on energy. The observed minor deviations in the comparison results can be attributed to the fact that variations in these parameter can lead to differences in the S-factor at lower energies, particularly for light nuclei.

Thus, the described method, which employs the rectangular potential well model to determine the astrophysical S-factor of fusion reactions involving light spinless nuclei, enabled the comparison of process intensities across different interacting systems, even when cross sections vary by nearly 40 orders of magnitude. Using this approach, the normalized cross sections dispersion was reduced to within one order of magnitude. For various combinations of nuclei, the experimental S-factor values were normalized by the corresponding values obtained using the proposed approach, based on the energy of the studied nuclear systems divided by the height of the Coulomb barrier. Regions corresponding to the spreading of theoretical predictions and the energy ranges relevant to stellar reactions were identified. The analysis of these data revealed good agreement between theoretical calculations and experimental values. Consequently, this method not only allows for the prediction and determination of fusion cross sections at low energies but also analyzing of nuclear reaction mechanisms in the light-mass range, which are of significant interest in nuclear astrophysics (see also Section 1.4).

In the framework of theoretical studies of the nuclear reaction excitation functions with neutron emission in the final state for the mass range from $A > 40$ up to $A = 239$, it became necessary to establish a general systematics for all available experimental data. This is essential to identify reaction cross sections across a wide range of energies and masses involved in nuclear interactions. To address this problem, the excitation function in this dissertation was divided into three regions based on the energies of colliding protons: a region characterized by equilibrium processes typical of the formation and decay of compound nuclear systems, from the reaction threshold up to energies of 11 MeV and two regions corresponding to pre-equilibrium processes. The reaction cross section in the first region was calculated using the formation cross section and the decay width of the compound nucleus into the corresponding channel. Since in

this work the exit channels involving neutron and proton emission are considered, the proton and neutron widths were taking into account. These widths included: the excitation energy of the compound nucleus, the energy of the emitted particle, the binding energy of the proton and neutron, the Coulomb barrier penetrability coefficient, and the level density of the residual nucleus. The angular momentum-dependent penetrability coefficient was used to calculate the compound nucleus formation cross section, which was determined using a systematics based on the global optical potential. The excitation functions for the two pre-equilibrium regions were modeled as linear on logarithmic scales. All obtained dependencies were then normalized to the corresponding cross sections, and the integration of all considered regions into a continuous excitation function was performed (see Section 2.1 for more details). As a result, optimal parameters were obtained for all regions of the excitation function, enabling the identification of the studied nuclear processes mechanisms.

One of the widely used methods for determining nuclear reaction cross sections and obtaining their excitation functions is the stacked foil activation method. This method formed the basis of experimental studies of nuclear reactions with the formation and decay of nucleon systems of the medium mass range, carried out within the presented dissertation work. In such a method, the targets in which the nuclear reaction occurs are thin foils placed sequentially perpendicular to the beam. Additional thin foils, serving as beam monitors and energy absorbers, are positioned between these target foils. As a result, the entire set of foils is irradiated simultaneously. The foils selected as monitors are those in which nuclear reactions (a monitor reaction is a nuclear reaction with well-known cross sections in a given energy range) occur on specific isotopes within the foil, and their excitation functions are well studied. By measuring the activity of the radionuclide produced in a specific monitor foil, the cross section of the nuclear reaction is calculated using this activity. The beam energy corresponding to this cross section is then reconstructed using the known excitation function. This allows obtaining of the beam energy after passing through the foil. The beam current is determined in a similar manner. In the next step, the activity of the radionuclide produced in the target foil is measured, and, combined with the beam current information obtained from the

monitor foils, the cross section of the nuclear reaction producing the radionuclide is determined. By incorporating the beam energy data, it becomes possible to get the excitation function over a wide range of energies for the charged particles bombarding the target (for more details, see Section 2.2.2).

An important factor for all experimental studies in this dissertation work was the use of a modernized target system. This system was specifically designed to optimize irradiation conditions for various solid-state targets (for design features and operating principles, see Section 2.2.1).

In the study of the excitation functions of nuclear reactions leading to the formation of antimony radionuclides ($^{117}$Sb and $^{119}$Sb) in the exit channels, nuclear-physical models and theoretical approaches were employed. This enabled the investigation of the mechanisms of such reactions and gives the foundation for further research into nuclear systems in the medium-mass range. In this dissertation, the theoretical formalism implemented in the PRECO and TALYS programs was utilized (see Section 2.2). The PRECO program is based on a two-component exciton model, which accounts for the emission of light particles (up to alpha particles). It includes a separate subroutine for nucleon transfer processes, knockout and inelastic scattering involving particles, and collective excitation of states. Nucleon emission during the equilibrium phase of the reaction is permitted after the pre-equilibrium emission of a neutron or proton. The equilibrium cross sections are calculated using the Weisskopf-Ewing formula. The TALYS program offers broader capabilities for nuclear reactions modeling in the energy range from 1 keV to 200 MeV, with targets starting from mass number 12 and the ability to vary up to 340 parameters of the theoretical models. The nuclear reaction mechanisms included in TALYS are: elastic scattering, reactions through a compound nucleus, direct reactions, pre-equilibrium processes, and fission. The Hauser-Feshbach model, corrected for level widths fluctuations, is typically used as one of the nuclear-physical models in Talys to describe (p,n) nuclear reactions proceeding through a compound nucleus, with targets in the medium mass range. Additionally, the model accounts for the possibility of multiple particle emissions and incorporates pre-equilibrium processes. The pre-equilibrium component, both in

PRECO and Talys, was calculated using the Kalbach model. In this dissertation, the Back-shifted Fermi gas model was selected as the level density model in Talys. By adjusting the excitation energy shift and, in some cases, the level density parameter of the residual nucleus, the accordance with experimental data in the region of the cross-section decline after the peak can be improved (for further details, see Section 2.2 and the relevant literature references).

**Validity and approbation of the results**

The reliability of the results is ensured by the agreement between theoretical and model calculations and the experimental data available in the scientific literature, as well as by the reproducibility of the experimental results obtained in dissertation work. Furthermore, the results align with those reported in earlier studies by other research groups, thereby validating and building upon previous findings. This work also includes new experimental insights to further refine and advance these results. Additionally, the obtained results were confirmed in later scientific works on the relevant subject.

The results of this dissertation work have been presented at numerous scientific seminars, including those held at the Department of Nuclear Physics Research Methods of the Faculty of Physics at St. Petersburg State University (SPbU), as well as at working and scientific seminars hosted by the V.G. Khlopin Radium Institute (ROSATOM), the National Research Center (NRC) “Kurchatov Institute” PNPI, Ioffe Physical Technical Institute of Russian Academy of Science. Additionally, the findings were shared at scientific seminars at foreign universities and research institutions, such as Texas A&M University, the University of Jyväskylä, Nazarbayev University, the Eurasian National University named after L.N. Gumilev, and the Diagnostic Center of the University Medical Center in Astana. Also, the results were presented at various international and All-Russian conferences:

1. LX International Conference on Nuclear Physics “Nucleus 2010. Methods of Nuclear Physics for Femto- and Nanotechnologies”, Saint-Petersburg, Russia, 2010;

2. International Scientific Seminar “Accelerators for the Future of Russia”, Moscow State University, Moscow, 2013;

3. LXIV International Conference on Nuclear Physics “Nucleus 2014. Fundamental problems of nuclear physics, atomic power engineering and nuclear technologies”, Minsk, Belarus, 2014;

4. LXV International Conference on Nuclear Physics "Nucleus 2015. New Horizons in Nuclear Physics, Nuclear Engineering, Femto- and Nanotechnologies", Saint-Petersburg, Russia, 2015;

5. Scientific and Practical Conference “Nuclear Medicine and Radiation Therapy: Current State and Prospects”, Moscow, 2017;

6. X International Congress “Nevsky Radiologic Forum”, St. Petersburg, 2018;

7. LXVIII International Conference on Nuclear Physics “Nucleus 2018. Fundamental problems of nuclear physics, atomic power engineering and nuclear technologies”, Voronezh, Russia, 2018;

8. III NICA Days 2019 International Scientific and Engineering Conference, Warsaw, Poland, 2019;

9. LXX International Conference «Nucleus 2020. Nuclear physics and elementary particle physics. Nuclear physics technologies», Saint-Petersburg, Russia, 2020;

10. LXXI International Conference «Nucleus 2021. Nuclear physics and elementary particle physics. Nuclear physics technologies», Saint-Petersburg, Russia, 2021;

11. Conference “Nuclear Medicine and Cyclotron Technologies”, St. Petersburg, 2022;

12. V International Forum of Oncology and Radiotherapy, RATRO Congress, Moscow, 2022;

13. LXXII International Conference «Nucleus 2022. Fundamental problems and applications», Moscow, Russia, 2022;

14. LXXIII International Conference «Nucleus 2023. Fundamental problems and applications», Sarov, Russia, 2023;

15. LXXIV International Conference «Nucleus 2024. Fundamental problems and applications», Dubna, Russia, 2024;

## Publications

The main results of the dissertation work are presented in 20 published papers, all of which are indexed in Web of Science (WoS) and Scopus databases. Among these, five papers were published in journals ranked in the first quartile (Q1) according to the SCImago Journal Rank (SJR) and the Journal Citation Reports (JCR). Additionally, the author of the dissertation, in collaboration with Zemlin E.O. and Maltsev N.A., was granted a patent for invention (No. 2830097, dated 12 November 2024) titled "Multi-sensor system for monitoring charged particle and heavy ion beams."

## The author personal contribution

The research was done at St. Petersburg State University. The dissertation materials represent a synthesis of the author's work on the research topic and reflect his personal contribution to the development of this subject. A number of the studies were carried out in collaboration with S.Y. Torilov and N.A. Maltsev. While many of the research results presented in the dissertation have been published in works with shared authorship, all findings included in the dissertation were obtained either independently by the author or with his direct involvement.

## Support

The dissertation work was supported by grants from the Russian Foundation for Basic Research, the Russian Scientific Foundation, and research and development agreements with scientific centers of the Russian Federation. Additional funding was provided by grants from the Committee for Science and Higher Education of the Government of St. Petersburg, Federal Target Programs, and other government initiatives.

**The structure of the dissertation**

The dissertation consists of an introduction, _2_ main chapters, conclusion, _82_ figures, _3_ tables, a bibliography of _189_ titles, and a list of the author's publications consisting of __20__ titles. Each chapter discusses the main results obtained. The volume of the dissertation is _205__ pages.

**The main scientific results**

1. It has been demonstrated that the use of modern accelerator complexes, on-line beam diagnostics systems, and advanced electronic systems for processing signals from silicon detectors enables the effective study of nuclear reactions involving neutron-rich alpha-cluster unstable targets, as well as nuclear reactions with ions leading to the formation and decay of compound nuclear systems in the light and medium mass ranges [17–21] (with a personal contribution of at least 80%).
2. It has been demonstrated that the study of the nuclear reaction: $^{14}C(^{12}C,\alpha_1\alpha_2)\rightarrow^{26}Mg^*\rightarrow^{22}Ne^*\rightarrow^{18}O$ produces highly excited states. By utilizing a specialized method for processing detector signals, it was possible to identify energy bands corresponding to protons, deuterons, tritons, alpha particles, and light nuclei (such as $^{6,7}Li$, $^{9,10}Be$, $^{11}B$, and $^{12,14}C$) based on pulse shape analysis. Additionally, the exotic neutron-rich nucleus $^{6}He$ was detected in the reaction channel: $^{14}C(^{12}C,^{6}He)^{20}Ne^*$. Furthermore, a number of high-spin states in the $^{22}Ne$ nucleus were observed. The analysis of these states characteristics allowed for their identification as rotational bands with distinct structures, which may correspond to nuclear molecules [19, 21–23] (with a personal contribution of at least 80%).
3. In the investigated reaction $^{14}C(^{12}C,\alpha_1\alpha_2)\rightarrow^{26}Mg^*\rightarrow^{22}Ne^*\rightarrow^{18}O$ (with a $^{12}C$ beam energy of 44 MeV), five high-spin states in the $^{22}Ne$ nucleus were observed in the excitation energy range of 16 to 30 MeV. These states were assigned to rotational bands with distinct structures, which may correspond to nuclear molecules [19, 21–23] (with a personal contribution of at least 70%).

4. The use of a specialized potential enabled the description of the angular distribution of $^{12}C+^{16}O$ reaction products across a wide energy range, including states that can be associated with rotational bands (molecular configurations). Additionally, it was demonstrated that, for a significant range of excitation energies in the compound nucleus, a certain number of resonances is expected [107, 127] (with a personal contribution of at least 70%).

5. In dissertation work, the angular distributions of the $^{12}C+^{16}O$ reaction were analyzed and compared with Legendre polynomials of different orders. It was found that when a resonance with low angular momentum and a reduced width coincides with a region exhibiting polynomial structure at large angles, an erroneous pattern resembling the presence of a high-spin resonance can arise. Such states may be misidentified as resonances ("false resonances") belonging to a rotational band. Additionally, for the aforementioned reaction, the positions of possible resonances in the optical potential were determined [107] (with a personal contribution of at least 70%).

6. In the analysis of nuclear fusion processes, which play a significant role in astrophysical phenomena (particularly nuclear fusion reactions at energies near the Coulomb barrier), calculations of both the astrophysical S-factor and the reaction cross section were performed using potentials derived to describe nuclear reactions in the light mass range. The results of these calculations demonstrated that both potentials accurately describe the experimental data within the energy range up to 20 MeV. It is noted that this behavior persists even at the minimum cross-section values near the Gamow window [127] (with a personal contribution of at least 80%).

7. The method of analyzing the astrophysical S-factor, based on the formalism of the rectangular potential well, was employed. The advantages of this method include a small number of parameters: the interaction radius, the real part of the potential (which describes attraction or repulsion), and the imaginary part of the potential (which characterizes the intensity of nuclear fusion). Additionally, the method offers simplicity in calculations and minimizes computational resource requirements. Using this model, it became possible to study the phenomenon of S-factor reduction in stellar

nucleosynthesis reactions, specifically the suppression of cross sections at low energies and to compare these findings with calculations based on optical potentials. The proposed method enabled a comparative analysis of the intensity of processes in different interacting systems. A significant result is that the spread of the normalized cross section in the current calculations remained within one order of magnitude. Comparisons with experimental data demonstrated good agreement with the theoretical results obtained using this model. Consequently, this approach not only allows for the prediction and determination of fusion cross sections at low energies but also provides deeper insights into the reaction mechanisms of light nuclei of astrophysical interest [137] (with a personal contribution of at least 70%).

8. Theoretical studies of the excitation functions for (p,n)-type nuclear reactions in the medium and heavy mass range (from A = 40 to A = 239) have been carried out. A corresponding systematics was established, and optimal modeling parameters were selected for all considered regions of the excitation function. This approach enabled the confirmation of the mechanisms underlying these nuclear processes [145] (with a personal contribution of at least 80%).

9. A total of 120 experimental excitation functions for nuclear reactions were analyzed in the energy range from the reaction threshold to 60 MeV, covering the mass range from A = 40 to A = 60. A comparative analysis was performed with cross-section calculations based on the developed systematics. This analysis demonstrated good agreement between the calculated results and the experimental data. However, it was found that the huge deviations for the proposed systematics occur in the low-energy region. Additionally, discrepancies with the systematics were observed in some cases for energies below the Coulomb barrier. For several nuclear reactions near their threshold energies, a systematic energy shift was identified during the analysis of experimental data. These results in the appearance of non-zero cross-section values on the excitation function plot below the reaction threshold energy, indicating potential errors in the experimental data or in the procedure used to process the experimental results. On the other hand, the systematics demonstrates good agreement in regions associated with nuclear pre-equilibrium emission processes. The primary outcome of

these studies is that this approach can be applied to quantify the formation of specific radionuclides in exit channels for reactions with different targets, as the developed systematics accurately describes the dependence of the (p,n) reaction cross section on the energy of the incident proton. The observed discrepancies between theoretical calculations and experimental data for reactions involving tin nuclei, as well as $^{85}$Rb, $^{94}$Sr, $^{130}$Te, and $^{150}$Nd particularly in the region of the excitation function maximum provide a compelling argument for further experimental studies of nuclear reactions with such systems [145] (with a personal contribution of at least 80%).

10. The excitation functions of nuclear reactions were analyzed in detail to produce radionuclides, including: $^{44}$Sc, $^{119}$Sb, $^{117}$Sb $^{161}$Tb and generators: $^{44}$Ti/$^{44}$Sc, $^{99}$Mo/$^{99m}$Tc. The results of these calculations can be applied to the production of $^{99}$Mo/$^{99m}$Tc using medium-energy cyclotrons (ranging from 40 to 80 MeV), even under conditions where experimental data in this energy range are limited [33] (with a personal contribution of at least 80%).

11. The target complex was modernized to provide research on nuclear reactions and to address challenges related to radionuclide production. To accommodate multicomponent, multilayer, and thick targets, a gas and liquid cooling system was implemented. Additionally, a new system for monitoring target heating was developed, and optimal parameters for the target cooling system were established [24, 25, 26, 27, 28, 29, 41] (with a personal contribution of at least 80%).

12. Experiments with using targets composed of Ag, Cd, Cu, Fe, Ti, stainless steel, and $^{nat}$Sn were carried out. The experimental results were processed and comprehensively analyzed to determine the final technique for experiments involving multilayer and thick targets, with a particular focus on highly enriched tin targets [24, 25, 26, 27, 28, 29, 34, 41] (with a personal contribution of at least 80%).

13. Experiments with irradiation of highly enriched (more than 85%) tin targets: $^{117}$Sn and $^{119}$Sn have been performed to study the excitation functions of nuclear reactions: $^{117}$Sn(p,n)$^{117}$Sb and $^{119}$Sn(p,n)$^{119}$Sb [33, 34] (with a personal contribution of at least 80%).

14. Theoretical models for analyzing the excitation functions of nuclear reactions: $^{117}$Sn(p,n)$^{117}$Sb and $^{119}$Sn(p,n)$^{119}$Sb were selected [33, 34] (with a personal contribution of at least 80%).

15. Data from experiments investigating the excitation functions of the nuclear reactions: $^{117}$Sn(p,n)$^{117}$Sb and $^{119}$Sn(p,n)$^{119}$Sb have been processed [34] (with a personal contribution of at least 80%).

16. The reactions: $^{117}$Sn(p,n)$^{117}$Sb and $^{119}$Sn(p,n)$^{119}$Sb were analyzed using the proposed theoretical models [34] (with a personal contribution of at least 80%).

17. Experiments to study in detail the maxima of the excitation functions for the nuclear reactions: $^{117}$Sn(p,n)$^{117}$Sb and $^{119}$Sn(p,n)$^{119}$Sb were carried out. The obtained data were systematized [33, 34] (with a personal contribution of at least 80%).

18. An analysis of the (p,n) reactions excitation functions for the tin isotopes (mass numbers 115, 116, 118, 120, 122) leading to the formation of antimony radionuclides in the exit channels was done [34] (with a personal contribution of at least 80%).

19. Based on the obtained experimental data for the excitation functions of the reactions: $^{117}$Sn(p,n)$^{117}$Sb and $^{119}$Sn(p,n)$^{119}$Sb, estimates of the thick targets yields of antimony radionuclides were made for applied work aimed at their production using proton accelerators. It was demonstrated that irradiating a tin target for 6 hours with a proton beam of 10 μA current and 15 MeV energy can produce $^{119}$Sb and $^{117}$Sb radionuclides with activities of approximately 8 GBq and 120 GBq, respectively. These results provide an excellent opportunity to utilize the obtained yield functions when planning the production of $^{117}$Sb radionuclides in proton-induced reactions at energies greater than 15 MeV, particularly in energy regions where experimental data are currently unavailable [33] (with a personal contribution of at least 80%).

**Dissertation statements to be defended**

1. New results of studies on reactions involving the interaction of alpha particles with neutron-excess, alpha-cluster unstable targets, utilizing modern techniques for focusing and guiding the accelerator beam, along with real-time diagnostics.
2. Identification of high-spin, highly excited states in the $^{22}$Ne nucleus through studies of the nuclear reaction: $^{14}C(^{12}C,\alpha_1\alpha_2)\rightarrow^{26}Mg^*\rightarrow^{22}Ne^*\rightarrow^{18}O$. The characteristics of these states were analyzed and attributed to rotational bands of various structures, which may correspond to nuclear molecules. A specialized method for processing detector signals based on pulse shape analysis was applied. Using this method, energy bands corresponding to the reaction products were identified, including protons, deuterons, tritons, alpha particles, and light nuclei such as $^{6,7}$Li, $^{9,10}$Be, $^{11}$B, and $^{12,14}$C. Additionally, exotic neutron-rich $^{6}$He nuclei were detected, with the reaction channel identified as: $^{14}C(^{12}C,^{6}He)^{20}Ne^*$.
3. Analysis of the angular distributions for the $^{12}C+^{16}O$ reaction, including comparison with Legendre polynomials of different orders provides the identification of erroneously observed resonances ('false resonances') associated with the rotational band.
4. Calculations of the astrophysical S-factor and fusion reaction cross-sections using potentials obtained for describing nuclear reactions of the light mass range give the good agreement with experimental data in the energy range up to 20 MeV.
5. A method for analyzing of the astrophysical S-factor based on the formalism of a rectangular potential well is presented was proposed for applying this model to study phenomena dependent on fusion cross-sections in stellar nucleosynthesis reactions are developed. To determine the astrophysical S-factor for fusion reactions of light spinless nuclei, a comparison of process intensities in different interacting systems was performed using the rectangular potential well model. The results demonstrate that the spread of normalized cross-sections in the current calculations is within one order of magnitude. Comparison with experimental data confirms the feasibility of predicting and determining fusion cross-sections for low-energy nuclear reactions involving light nuclei which are of interest in nuclear astrophysics.

6. Theoretical studies of (p,n) nuclear reaction excitation functions were done across the mass range from A = 40 to A = 239. A systematics was developed, and optimal modeling parameters were selected for all considered regions of the excitation function, which made it possible to confirm the mechanisms of these nuclear processes.

7. Analysis of 120 experimental excitation functions for nuclear reactions was carried out in the energy range from the reaction threshold to 60 MeV and the mass range from A = 40 to A = 60. A comparative analysis with cross-section calculations based on the developed systematics was performed, demonstrating good agreement between the calculated results and experimental data. Conclusions were drawn regarding potential errors in a subset of the experimental data and in the error assessment procedure for scanning experimental results. It was shown that this approach can be used to obtain quantitative results in analyzing the formation processes of specific radionuclides in the output reaction channels with different targets. Additionally, the resulting systematics was found to provide a reliable description of the (p,n) reaction cross-section depended on proton energy. This systematics can be applied to guide further experimental studies of nuclear reaction excitation functions, particularly in the region of the cross-section maximum, within the intermediate mass range.

8. A detailed analysis of excitation functions for nuclear reactions leading to the formation of radionuclides: $^{44}$Sc, $^{119}$Sb, $^{117}$Sb $^{161}$Tb, as well as radionuclide generators: $^{44}$Ti/$^{44}$Sc, $^{99}$Mo/$^{99m}$Tc was done. The guidelines on the use of the obtained results in applied works on the production of $^{99}$Mo/$^{99m}$Tc at cyclotrons of medium energies: from 40 to 80 MeV have been developed.

9. In context of modernization of the target complex for nuclear reaction research and for solving problems related to radionuclide production a new system for monitoring target heating was developed, and optimal parameters for the target cooling system were obtained. The experiments with targets: Ag, Cd, Cu, Fe give an information for the selection of the final methodology for studies with highly enriched targets with tin isotopes.

10. The experiments with irradiation of highly enriched Sn targets to study the excitation functions of nuclear reactions: $^{117}$Sn(p,n)$^{117}$Sb and $^{119}$Sn(p,n)$^{119}$Sb allowing to choose the theoretical models for analysis of these nuclear reactions excitation functions. In experimental investigations on a detailed study of excitation functions maxima of the nuclear reactions: $^{117}$Sn(p,n)$^{117}$Sb and $^{119}$Sn(p,n)$^{119}$Sb the new results were obtained and the systematization of these data was done.

11. Analysis of (p,n) reaction excitation functions for tin isotopes with mass numbers: 115, 116, 118, 120, 122 allowed describe the behavior of such function for the antimony radionuclides in the exit channels formation processes.

12. Thick target yield functions of the reactions: $^{117}$Sn(p,n)$^{117}$Sb and $^{11}$9Sn(p, n)$^{119}$Sb in the context of applied work aimed at producing antimony radionuclides at proton accelerators. Estimates of the accumulated activity for specific irradiation parameters. Possibility of using the obtained yield functions when planning the production of $^{117}$Sb radionuclides in reactions with protons with energies greater than 15 MeV, where experimental data are not available to date.

## 1. Studies of nuclear reactions with the formation and decay of light mass range nucleonic systems

Modern developments in nuclear reaction physics, particularly in the field of light nuclear systems, are progressing along several key directions. First, significant attention is devoted to the study of neutron-deficient nuclei and their exotic structures, such as halo nuclei, nuclei with extreme N/Z ratios, magic neutron-deficient nuclei, strongly deformed nuclei, and clustering effects. Another equally important direction involves the investigation of alpha-cluster nuclei and the mechanisms of nucleon condensation into alpha clusters. A central focus in this area is the detection and study of new states of nuclear matter. The primary tool for experimentally exploring these directions is the use of reactions with accelerated ions. Let us schematically outline the processes taking place (see Figure 2), as we move toward a decrease in the transferred angular momentum $l$: target nuclei are bombarded by ions, and at high angular momenta, elastic scattering and Coulomb excitation of collective levels occur. If the ion approaches a sufficiently close distance, nearly grazing the target nuclei (grazing angular momentum - $l_{gr}$) entering the region where nuclear forces dominate, processes such as the excitation of giant resonances, transfer reactions, pickup reactions, and other nuclear reactions with a direct interaction mechanism become predominant. In such 'tangential' collisions of nuclei, interference between Coulomb and nuclear forces can be observed (region $\sigma_{El}$ + $\sigma_{CE}$ in Figure 2). The maximum in the elastic collision cross-section will occur at a smaller angular momentum compared to the case of pure Coulomb interaction (region $\sigma_D$ in Figure 2). As the transferred angular momentum $l$ decreases further, the contact time of the colliding nuclei increases, energy losses begin to rise, and the reaction transitions into the region of deeply inelastic processes (region $\sigma_{DIC}$ in Figure 2) [2].

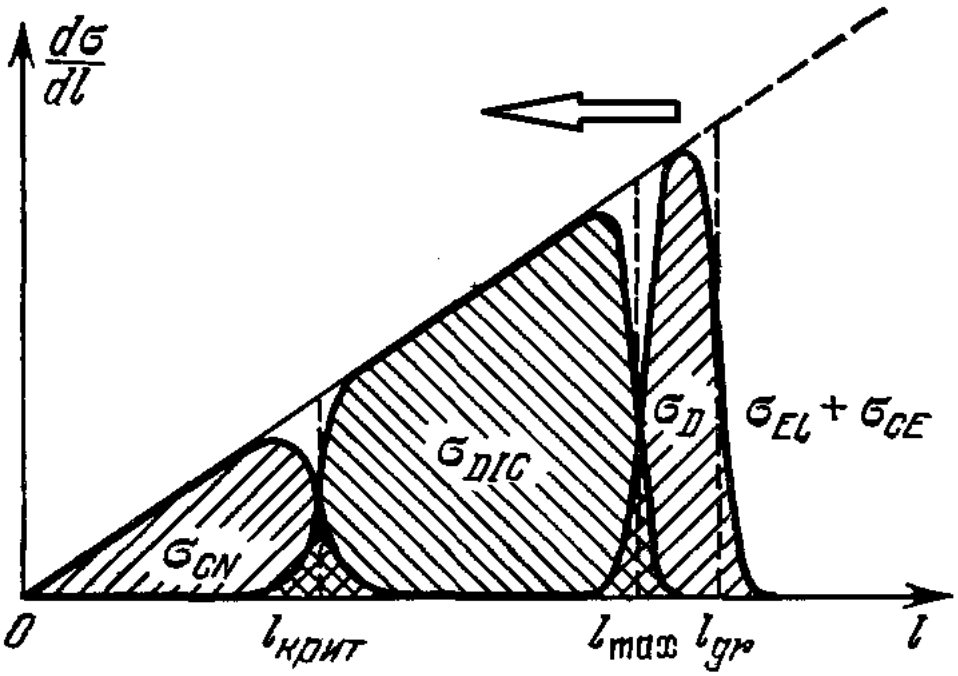


Figure 2 – Diagram of nuclear reactions with accelerated ions as a function of the transferred angular momentum (adapted from [2]).

Further, at $l < l_{cr}$, a fusion reaction occurs, leading to the formation of so-called compound states (region $\sigma_{CN}$ in Figure 2)."

In the studied reactions involving accelerated ions, unexpected effects and phenomena arise, occasionally leading to the formation of highly intriguing nuclear configurations and systems. In the 1960s, during investigations of one of the simplest carbon-ion reactions: $^{12}C+^{12}C$, so-called nuclear molecular (or quasi-molecular) states were discovered (see, for example, [48]). These states were identified through the observation of narrow resonances in the excitation function at energies up to 40 MeV. The description of such a phenomenon became possible after long theoretical and experimental studies of this reaction, when two $^{12}C$ nuclei do not immediately transition to the compound state during the interaction, but rotate relative to each other, remaining in the ground or first excited $2^+$ state (see Figure 3). As a result, rotational bands are formed above the primary rotational band of the $^{24}Mg$ nucleus.

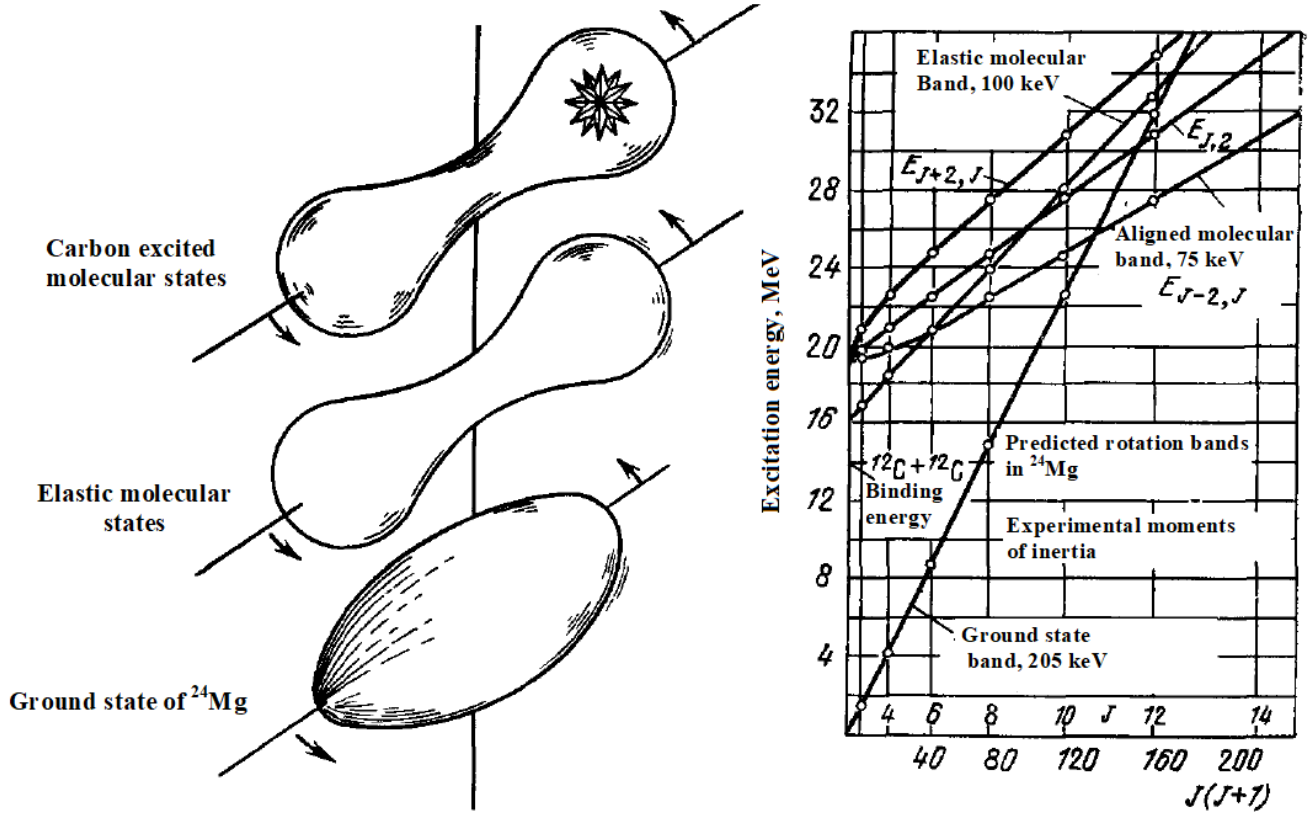


Figure 3 – Dynamic features of the $^{12}C$ + $^{12}C$ nuclear reaction, showing the formation of excited molecular states (left) and states corresponding to different rotational bands (right) (adapted from [2]).

The levels formed at such high excitation energies of the $^{24}Mg$ nucleus are relatively narrow, and the nucleus does not transform into other configurations. This is because, in the reaction under consideration, since in the reaction under consideration there is a small gap in which the density of these configurations is small. Rotational levels within this interval have limited opportunities to decay into other excited states [2]. Nuclear reactions leading to the formation of such molecular states are particularly interesting, as they provide a means to study the effective potential between two nuclei.

Therefore, in this dissertation, a nuclear reaction involving light mass ions: $^{12}C+^{14}C$ was investigated, with a focus on neutron-rich target nuclei $^{14}C$ in the context of studying high-spin, highly excited states of the resulting nuclei. Other reactions involving neutron-rich nuclear systems were also studied, utilizing extensive experimental data. As a result, answers were provided to several unresolved issues within current theoretical and model frameworks.

## 1.1. Using the cluster model in describing nuclear reactions

To describe the structural features of nuclei, it is essential to take into account for the nuclear boundary and the finite number of particles formed the nucleus. This approach is employed in the nuclear shell model, which utilize the concept of the mean nucleon field. In this framework, each nucleon moves within a specific single-particle potential, the parameters of which are adjusted to reproduce the correct energy spectrum of the nucleus under consideration. The mean field concept is also applied to describe scattering reactions of various particles on nuclei. However, in certain cases, the mean nucleon field fails to accurately interpret some nuclear features and reaction mechanisms. Cluster models, among which the alpha-cluster concepts are most often used, help to solve these problems.

To explain a number of nuclear structure features and the mechanisms of nuclear processes and reactions, this dissertation employs the concept of clustering [49, 17, 18, 20]. According to this concept, under certain conditions, nucleons in nuclei form relatively stable configurations known as clusters. These clusters are treated as elementary subunits of atomic nuclei, whose internal structure can be neglected. Indeed, the high stability of nuclei with N = Z and mass numbers that are multiples of 4, alpha decays of nuclei, and reactions involving the transfer or knockout of alpha particles such as (p,α), (α,2α), and ($^{16}$O,$^{12}$C) suggest that an approach in which alpha clusters move within a mean field can be applied. This model can be related to the mean nucleon field model. The main feature of this model is that, unlike nucleons, alpha clusters in nuclei are temporary associations that form and decay, but are long-lived so that their existence can be observed. This significantly simplifies calculations of nuclear system primary characteristics. Within this framework, it is possible to perform calculations of nuclear structure, followed by an analysis of the density of nuclear matter. As a result, the alpha-cluster model is successfully used to describe the structural features of nuclear systems with N = Z [50, 20], particularly through the well-established Brink-Bloch alpha-cluster model [51–52]. Additionally, this model is well-suited for describing the

binding energy dependencies in the ground states of nuclei, such as $^{12}C$ and $^{16}O$, when configurations from the shell model are added into the calculations [53].

When studying alpha clustering in nuclei, one considers infinite nuclear matter, initially consisting of nucleons between which there are no Coulomb forces. It is then important to understand how the formation of alpha clusters and the stability of nuclear matter depend on the density of nuclear matter. With high density and a significant energy of the first excited state (approximately 20 MeV), alpha particles can be considered as structureless components of nuclear matter, to which the concepts of cluster decomposition are applicable. In this case, the ground-state energy per particle is written as a sum:

$E = E_1 + E_2 + E_3 + \ldots + E_n$ , where $E_n$ is the energy contribution arising from the n-particle configuration. Theoretical calculations [54] predict the existence of a minimum in the region of the corresponding nucleon density in the nucleus. However, a detailed calculation based on this model requires the introduction of a two-particle potential. In this case, the presence of the so-called repulsive core (the interaction of two composite particles consisting of identical fermions, taking into account the Pauli principle, leads to a strong repulsion of particles at short distances; see, for example, [55]) creates significant difficulties in the calculations. Simpler calculations are carried out for an isotropic mixture of protons and neutrons in different spin configurations. Considering the nucleus from the Fermi gas model, it is possible to estimate the mean square distance between pairs of nucleons having opposite directions of both spin and isotopic spin (see Figure 4), with the coordinates of the nucleons chosen randomly. In this case, independent particle motion is considered, and the residual interaction proposed by Wheeler in [56] is not taken into account.

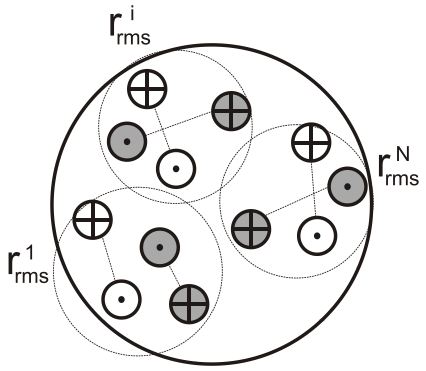


Figure 4 – Random distribution of nucleons in the nucleus and the mean square radii of their correlations.

Initially, there were two main prerequisites for considering nuclei as an alpha-particle system: the increased probability of alpha decay of heavy unstable nuclei and the proportionality of the binding energies of light self-conjugate nuclei to the number of bonds between their constituent alpha particles [57]. The first works that described the structure of light nuclei assumed a geometric model for the bound alpha particles. For example, the $^{8}$Be nucleus was described as a dumbbell-like shape with two alpha particles at the edges, the $^{12}$C nucleus as an equilateral triangle with alpha particles at the corners, the $^{16}$O nucleus as a tetrahedron, the $^{20}$Ne nucleus as a bipyramid, and so on. The shortest distances between neighboring alpha particles were called bonds, and the bond energies were calculated as the sum of the energies of their constituent alpha particles plus certain energy proportional to the number of such bonds. The proportionality coefficient was approximately 2.45 MeV, which remains valid up to the $^{32}$S nucleus. This confirms the previously made conclusion about the possibility of representing light self-conjugate nuclei as a set of interacting alpha particles. This model describes well the features of three nuclear systems: $^{8}$Be, $^{12}$C, and $^{16}$O. However, for the $^{8}$Be nucleus, the calculated binding energy differs significantly from the experimental value. For the remaining nuclei, it is necessary to introduce an approximation regarding the minimal contribution of the Coulomb field in excess of the energy accounted for by the number of bonds (materials from reviews [58–59] were also used).

Next, one can apply the cluster model to describe nuclear reactions. To do this, it is needed to obtain the quantum potential of the interaction between the cluster and the nucleus. Since the mechanism of alpha particle formation in the proposed model is assumed to be fluctuation, the alpha particles do not retain their individuality, as they constantly exchange nucleons.

For excited states of alpha-particle nuclei, in which one alpha particle is in the weak field of the remaining nucleons, a quantum mechanical model similar to the model using the folding potential can be applied. In this case, the potential obtained in [60] is well suited:

$$V_{nucl}(r) = -122.6225e^{-0.22 \cdot r^2} \qquad (1)$$

This potential well reproduces the phase shift of alpha-alpha scattering. It is assumed that all remaining alpha particles (core) have the same potential. Since the core does not have a spatially separated direction, the potential must be averaged over all directions for the resulting distribution of alpha particles. As a result, a potential well for the "valence" alpha particle could be obtained. Using the cluster model and the potential (1) to describe nuclear reactions, one can achieve good agreement with experimental data in the corresponding calculations for light nuclei [see, e.g., 61]. To obtain a general result, the following criteria for the potential used should be adopted:

1. Reproduction of rotational bands corresponding to cluster degrees of freedom.
2. Reproduction of the experimental value of splitting for bands of different parity.
3. The width of the levels should correspond to the experimental values.
4. The intensity values of gamma transitions should correspond to the experimental values.
5. With a certain imaginary part, the potential should provide a qualitative description of the angular distribution of alpha particles elastically scattered on the corresponding target.

## 1.2 Studies of neutron-rich nuclear systems of the light mass group: $^{14}$C, $^{22}$Ne

When studying excited states of atomic nuclei, it is often necessary to identify the process that led to the formation of the nuclear system under study. This task is of great importance when studying the features of nuclear reactions in the light mass range (from helium to carbon nuclei). Unlike the case of heavy nuclei, where, with increasing energy, processes occurring through the compound nucleus very quickly begin to dominate, for light nuclei, in almost any energy range, a simultaneous contribution of several types of reactions is observed. This seriously complicates the study of the mechanisms of excitation and the structure of excited states of a nuclear system. Also interest arises from the addition of several neutrons to the nucleus, forming a neutron-excess configuration with an alpha-cluster core.

Obtaining information on the properties of nuclei with excess neutrons is important for studying cluster structures, not only for light self-conjugate nuclei but also, to a greater extent, for nuclear systems with N≠Z and unstable nuclei [62]. On the other hand, such information is important for advancing the study of alpha condensation in nuclei [63–65]. It is still not entirely clear (from both theoretical and experimental perspectives) how a system of weakly bound alpha particles will behave in the presence of additional neutrons. In this context, suggestions have been made about possible additional stabilization of the condensate [66].

Of additional interest are studies of high-spin, highly excited states with large angular momentum in nuclear systems of the light mass group. In reactions with accelerated ions, nuclei can be "twisted" to an angular momentum of the order of several tens (in units of $\hbar$), with the rotational energy reaching fairly high values. The nucleus cannot take arbitrary values of angular momentum, and for light nuclei, the main limitation is that the centrifugal energy is less than or comparable to the depth of the potential well. If the nuclei are also highly excited, then, due to the emission of neutrons or gamma quanta, they will remove the excitation and reach the yrast band (a

set of levels in the nucleus with the lowest energy for a given spin) at a certain angular momentum. A simple example can show that, for a spherical neutron-excess nucleus with a core and additional (valence) neutrons, its angular momentum ($l$) is determined by the states of the valence nucleons. With increasing $l$, the core, polarized by external nucleons, begins to follow the motion of nucleons concentrated on the surface, and the nucleus transforms from spherical to a flattened, deformed shape. With a further increase in $l$, the deformation can take extreme forms (for example, hyper-deformed configurations of nuclear systems). Typically, such a phase transition begins to occur at $l > 10–20$, which has been well studied experimentally in nuclear systems of the middle mass group [17–18]. At the same time, studies of high-spin states with high angular momentum in light nuclear systems will help reveal a huge variety of nuclear transformations, transitions, and processes. The study of this area of nuclear structure has rich prospects.

### 1.2.1. Studies of the neutron-rich Nuclear System: $^{14}$C

In light neutron-rich nuclei, cluster structures with added neutrons have been the subject of numerous experimental and theoretical studies and a topic of heated debate over the past decades. This is especially true for neutron-rich carbon isotopes: $^{13}$C and $^{14}$C, where the nuclear core is the $^{12}$C nucleus with a cluster structure. As already noted, an important component of the cluster model is the choice of an adequate nuclear potential for describing nuclear reactions, for which the main requirement for the imaginary part is a qualitative description of the angular distribution of alpha particles elastically scattered on the target. In the context of this problem, the nuclear reaction studied in this dissertation is: $\alpha + {}^{14}C$, where alpha particles accelerated to energy of 27 MeV bombarded a radioactive target of the neutron-rich nucleus $^{14}$C (an alpha-cluster core of the $^{12}$C nucleus + two additional neutrons).

The experiment was carried out at St. Petersburg State University using an alpha-particle beam from the Cyclotron U-120 (Laboratory of Nuclear Reactions, SPbSU) [67] and a highly enriched (80% enrichment) carbon-14 isotope target [19, 21]. Let us

briefly describe the main details of this experiment. Over fifty years of operation, the Cyclotron U-120 has been constantly modernized, both in its accelerator component (the cyclotron itself) and in the beam channeling system, to meet the needs of experimental physicists. Figure 5 shows the beam channeling scheme of the Cyclotron U-120, including its main geometrical characteristics [68]. As can be seen from the presented scheme, the beam pipe is a composite structure. The connection between its parts is achieved using vacuum transition nozzles, which maintain the necessary vacuum throughout the entire beam pipe from the cyclotron to the targets. In this setup, it is possible to direct the beam into channels in several directions. The described experiment was carried out using the right channel (see Figure 5), in the so-called scattering chamber, and the schematic of the experimental setup is shown in Figure 6 [68]. The scattering chamber is separated from the cyclotron beam pipe by a gate valve and must first be evacuated by a forevacuum pump and then by a diffusion pump (before opening the gate valve) to a pressure of $10^{-6}$ mm Hg. The chamber is electrically isolated from the beam pipe. This allows for the measurement of the total charge accumulated during irradiation (in the Faraday cup, F.C.) and, consequently, the number of particles hitting the target using a current integrator. In our case, the target was a $^{14}C$ foil, 280 μg/cm$^2$ thick and enriched to 80% in the main isotope $^{14}C$ (the remaining 20% belonged to the isotope $^{12}C$) [19, 21], fixed to the target holder frame (T1–T2). The target holder is mechanically connected to a system of stepper motors, which ensures its movement in both horizontal and vertical planes, as well as clockwise and counterclockwise rotation. The stepper motors are controlled remotely using a PC. This design of the target unit provides the experimenter with significant flexibility, such as the replacement of the T1 target with the T2 target directly during the experiment without breaking the vacuum of the scattering chamber, enabling experiments (in various geometries) on the scattering of charged particles. The reaction products were detected by four silicon surface-barrier detectors (D1–D4) with a thickness of 380 μm and a thin input window. The signals from the detectors were then fed to preamplifiers located on the cover of the scattering chamber. The entire system of data collection and processing is shown in Figure 7 [67].

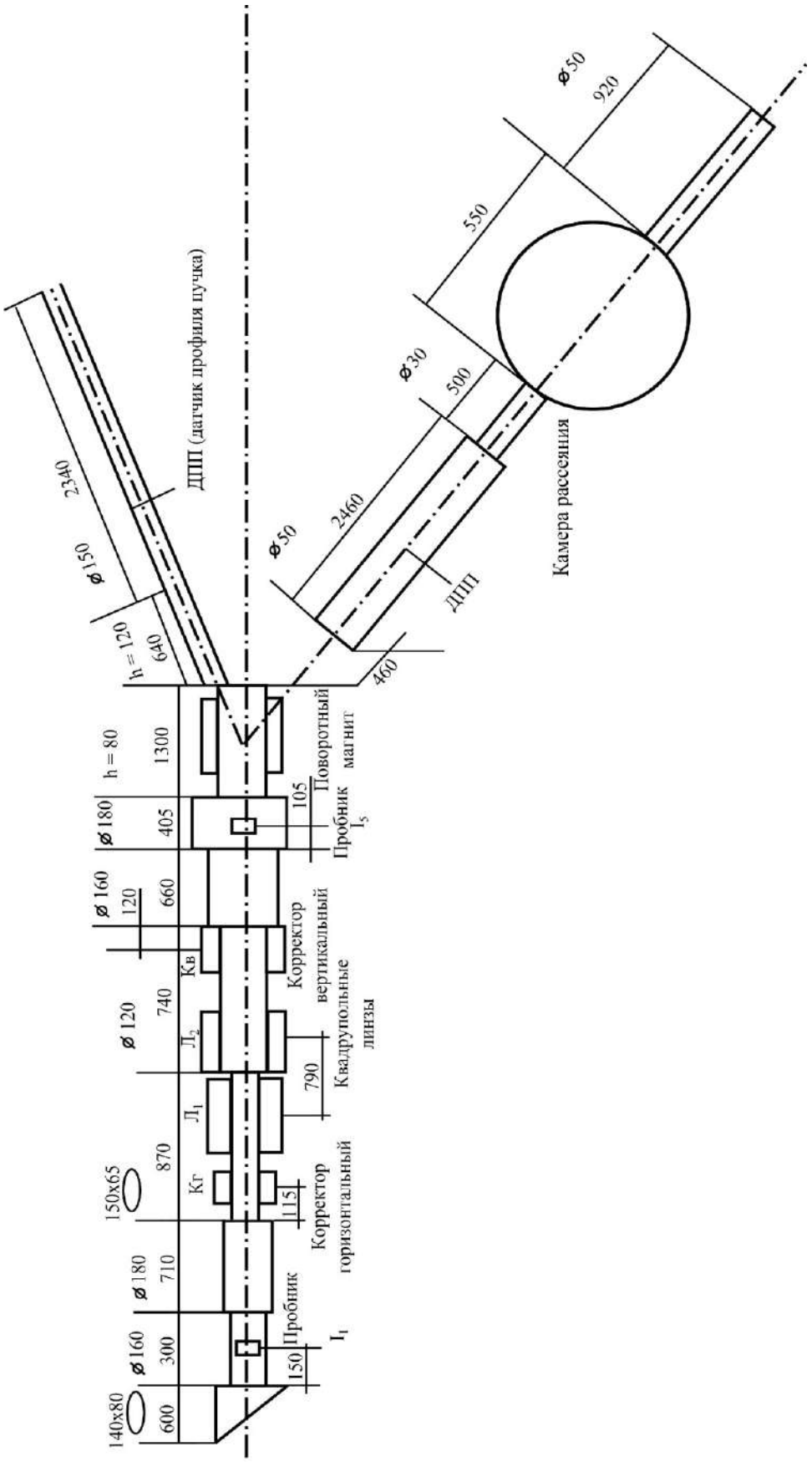


Figure 5 - The beam “routing” diagram at the U-120 cyclotron at St. Petersburg State University [68].

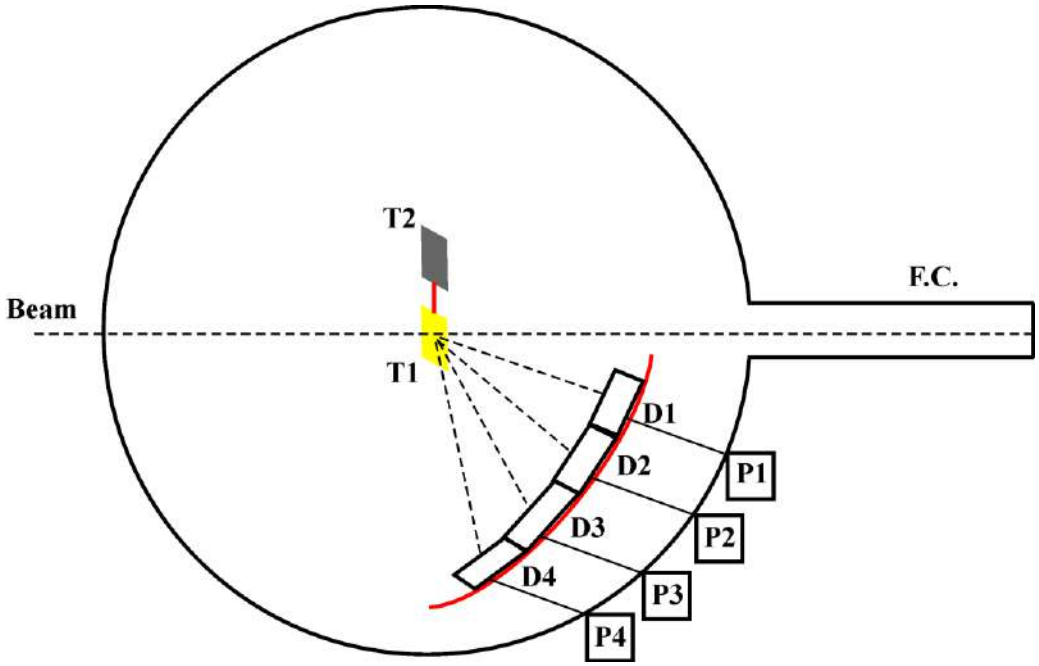


Figure 6 - Schematic diagram of the experimental setup for studying the nuclear reaction: alpha + $^{14}$C [68].

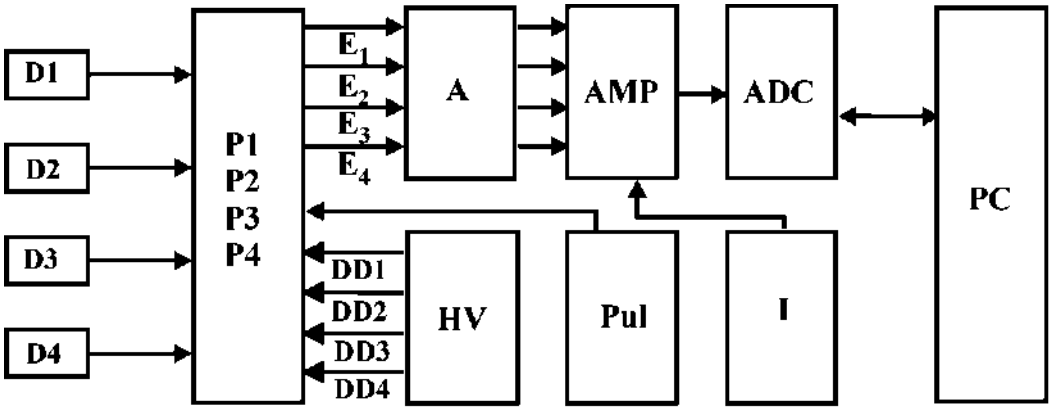


Figure 7 - Diagram of the system for collecting and processing information from detectors [67-68].

Since semiconductor silicon surface-barrier detectors (SSBD) were used in this work to register alpha particles, a significant factor determining the design principle of preamplifiers for such detectors is the dependence of the signal amplitude on the detector capacitance. Therefore, charge-sensitive preamplifiers are used when working with SSBD. In these preamplifiers, the current is integrated not on the detector capacitance but on a capacitor included in the amplifier circuit. This eliminates the dependence of the charge-to-pulse amplitude conversion coefficient on the detector

capacitance and significantly increases the conversion accuracy. To ensure that the signal at the amplifier output is independent of the bias voltage and, consequently, of changes in the detector capacitance, the preamplifier circuit incorporates negative charge feedback. This feedback is implemented by a capacitor connecting the amplifier output to its input. As a result, the signal amplitude at the preamplifier output is determined by the charge generated by the ionizing particle in the detector and the feedback capacitance, and it no longer depends on the SSBD junction capacitance or the applied bias voltage. Thus, the introduction of negative charge feedback stabilizes not only the amplifier but also the signal source itself, the semiconductor detector. The feedback capacitance must exhibit high stability, so a capacitor (on the order of tenths of a picofarad) with low temperature dependence was chosen [68]. To solve the experimental challenges of this dissertation work, a charge-sensitive preamplifier with low noise characteristics was developed at St. Petersburg State University. During the development of this device, the positive experience accumulated from operating similar preamplifiers with an array of position-sensitive silicon detectors in experiments studying the neutron-excess nuclear system $^{22}$Ne [19, 21] was taken into account. The preamplifier design is implemented as a small microcircuit mounted in a specialized housing. For this work, four preamplifiers were manufactured, each equipped with inputs for signals from the detectors (inputs D1–D4), inputs for supplying bias voltage to the detectors (inputs DD1–DD4), inputs for supplying a test signal from a pulse generator, and outputs (E1–E4) for signals amplified by the preamplifier (see Figure 7). Subsequently, the signals amplified by the preamplifier are fed to the spectrometric amplifier (A – spectrometric amplifier CAEN N568).

A comprehensive study of the developed charge-sensitive preamplifier was done to determine its main characteristics and verify its specified properties. In this context, the most important characteristic of any spectrometric setup is its energy resolution, which is determined not only by the characteristics of the detector used but also by the noise generated in the input circuits of the preamplifiers. The presence of noise leads to a broadening of the amplitude spectrum and a deterioration of the energy resolution of the entire detector system. In our case, the minimum possible noise level is ensured by

the appropriate design of the preamplifier. During the study, an equivalent noise charge (or energy equivalent of noise) of approximately 1 keV was achieved.

To test the noise characteristics of the developed preamplifier in detail, an experimental setup was created, the schematic of which is shown in Figure 8.

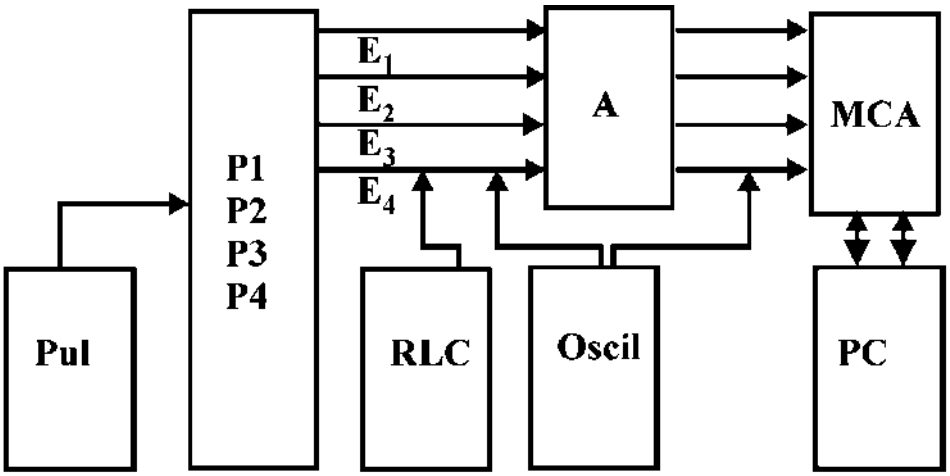


Figure 8 – Functional diagram of the experimental setup for testing the operation of the charge-sensitive preamplifier.

To provide the research, a G5-15 generator and an impedance meter – RLC meter were connected to the charge-sensitive preamplifier. The signals from the four channels of the preamplifier were then fed to a 16-channel amplifier (A – CAEN N568 spectrometric amplifier) and subsequently to a multichannel analyzer (MCA – Amptek MCA8000A). A personal computer connected to the analyzer enables automatic spectral processing. The charge-sensitive preamplifier converts the input charge into voltage and amplifies the resulting pulse. As previously noted, the preamplifier design includes an auxiliary input (“Gen.”), where pulses from the generator are fed to monitor the operation and calibration of the preamplifier. This input is connected to the main input of the preamplifier through a dosing capacitor $C_{dose}$ = 1 pF. Thus, when working with the generator, the charge entering the input circuit of the preamplifier is given by $Q_{in} = U_{gen} \cdot C_{dose}$, where $U_{gen}$ is the amplitude of the generator pulse.

The procedure for testing the developed preamplifier was as follows: pulses from the generator with amplitude of approximately $10^{-3}$ V were fed into the "Gen." input.

The amplitude of the generator pulses and the gain of the amplifier (A) were adjusted such that the generator peak in the spectrum appeared within the MCA channels ranging from the 30th to the 60th. Since the position of this peak in the spectrum is determined by the amplitude of the generator pulses ($U_{gen}$), and the width of the peak is influenced by the amplitude of the noise pulses, the mean square deviation of the noise can be readily determined by measuring the full width at half maximum (FWHM) of the peak. A smaller FWHM value indicates better performance of the preamplifier.

The developed preamplifier was compared with the 142A preamplifier manufactured by the American company ORTEC. Figure 9 presents the spectra of the generator signals fed to the respective preamplifiers: (a) the 142A ORTEC preamplifier and (b) the preamplifier developed at St. Petersburg State University. It is clearly seen that the FWHM of the developed preamplifier is better than the 142A ORTEC preamplifier, since its corresponding FWHM value is 1.68 channels, which is two times less than the similar model 142A ORTEC (3.75 channels). This improvement enabled high energy resolution in the detection of alpha particles during subsequent experimental studies (see the experimental results below).

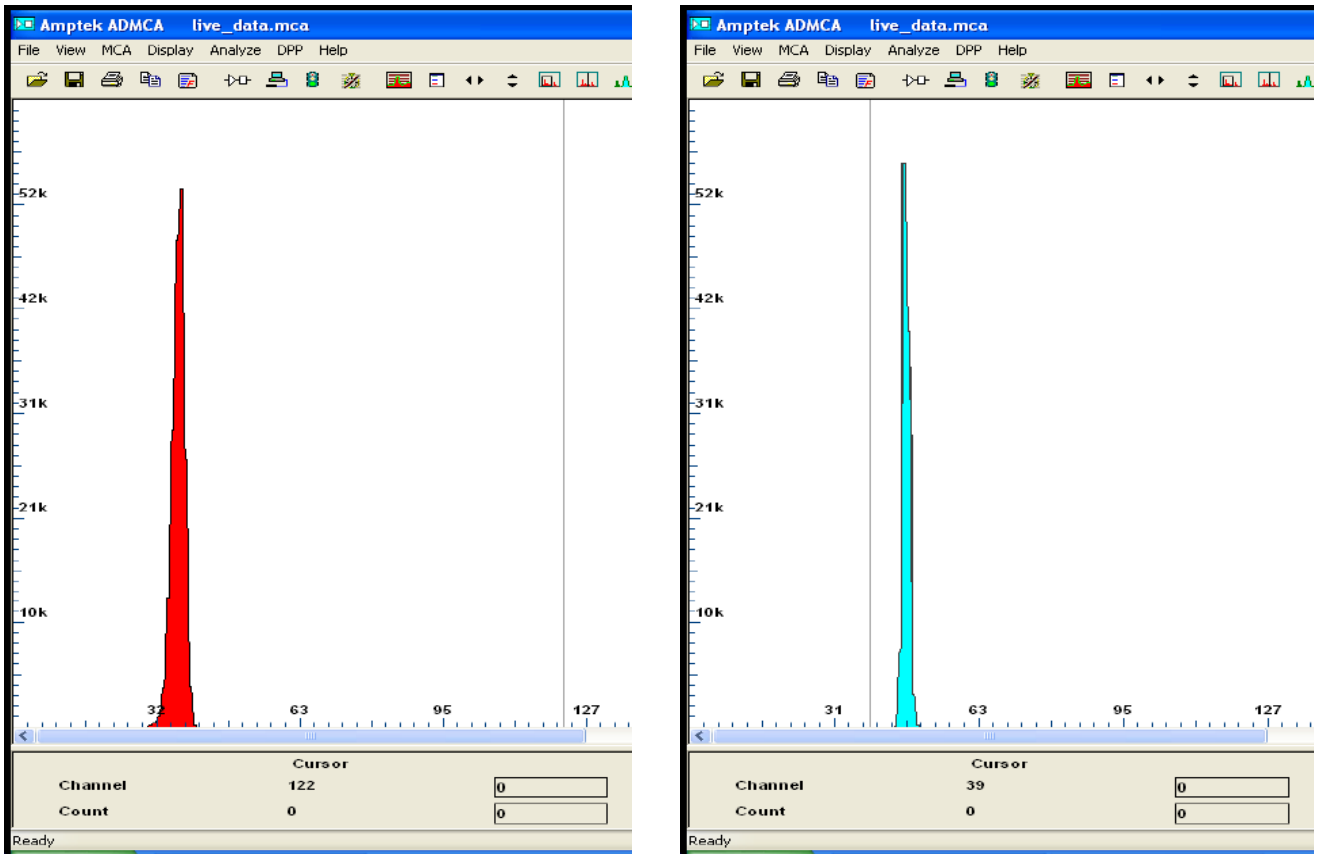


a b

Figure 9 – Spectra of the generator line obtained using: a) 142A ORTEC preamplifier; b) preamplifier developed at St. Petersburg State University.

After verifying and calibrating all spectrometric paths, we return to the description of the system for collecting and processing information from the detectors (see Figure 7). Signals from the spectrometric amplifier (A) are sent to the analog multiplexer (AMP). This device enables the sequential reading of information from each detection channel. The AMP's switching speed between channels is 50 ns. Additionally, the AMP receives a signal from the current integrator. Thus, the AMP directly outputs a signal from the detector, the number of the detector to which this signal belongs, and a signal from the current integrator. Then these signals are sent to the amplitude-to-digital converter (ADC), where they are encoded and transmitted to a personal computer. In this work, the ADC is a programmable device implemented using FPGA (field-programmable gate array) technology, based on the ALTERA programmable logic integrated circuit. A special feature of this device is that it can be

programmed for a specific experimental task. The electronic devices used namely, the AMR and ADC were also developed at St. Petersburg State University.

As previously mentioned, the signals from the four detectors, along with their corresponding detector identifiers and the signals from the current integrator [68], are encoded. This provides complete information from all four detectors for subsequent "off-line" processing. A key advantage of this scheme is the minimal use of electronic equipment, as all four detectors are connected to a single multiplexer.

During the experiment, energy spectra corresponding to various excited states of the $^{14}C$ nucleus were obtained (an example of an energy spectrum measured at an angle of 21.5° is shown in Figure 10). Additionally, the angular distribution for elastically scattered alpha particles was plotted (see Figure 11, black dots).

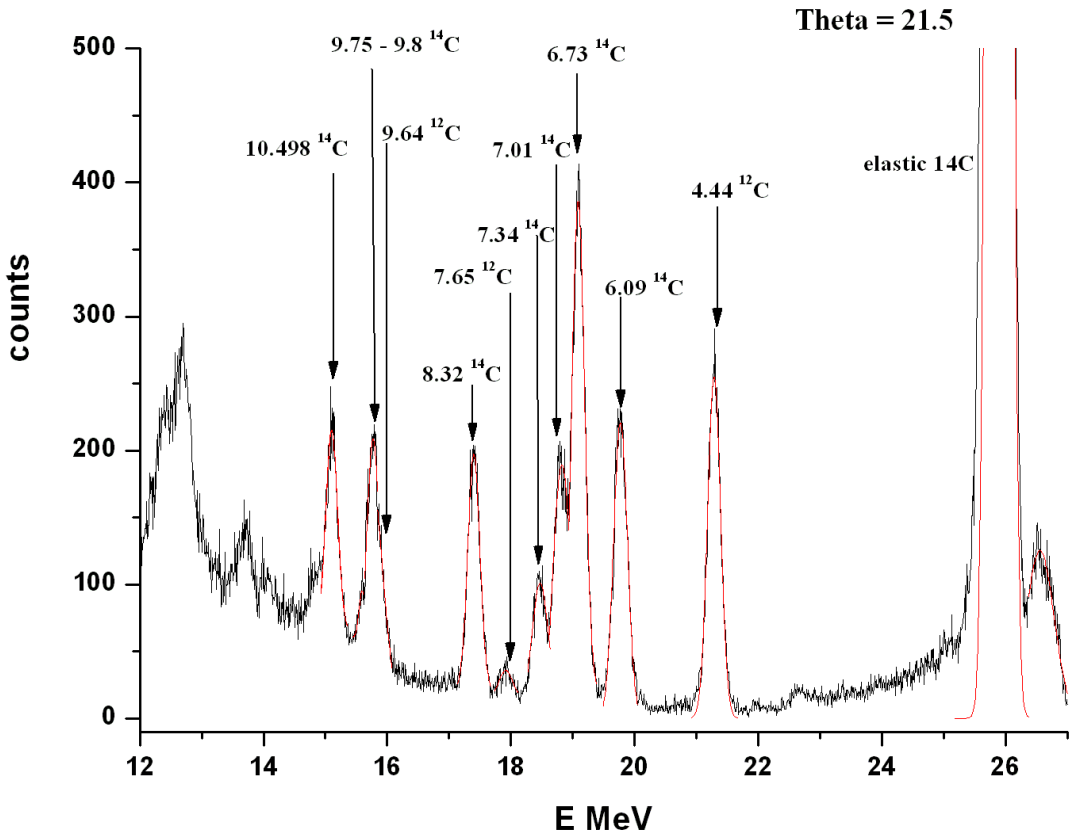


Figure 10 – Energy spectrum of alpha particles (energy 27 MeV) scattered by $^{14}C$ nuclei. The spectrum was obtained using a silicon surface barrier detector located at an angle of 21.5°.

The energy spectrum demonstrates that the excited states of the $^{14}C$ nucleus are well resolved: 6.09 MeV, 8.32 MeV, and 10.49 MeV, as well as a group of excited

states at 6.73–7.34 MeV (see Figure 10). Since the $^{14}C$ target contains a 20% impurity of $^{12}C$, the spectrum also includes excited states belonging to this nucleus. These states are similarly well resolved against the background of the investigated excited states in the $^{14}C$ nucleus. Such high resolution was achieved by reducing the energy spread in the alpha particle beam to 0.5% through energy monochromatization of the beam using a system of quadrupole lenses, correcting magnets, a bending magnet, in combination with a system of movable collimators. The system for guiding the charged particle beam from the cyclotron to the target (referred to as the channeling system) includes three deflecting elements and two focusing elements (see Figure 5). The first deflecting element, the horizontal corrector, is designed to shift the beam axis horizontally, aligning the cyclotron beam output system with the channeling system. The need for horizontal beam adjustment necessitates the use of an ion guide with an elliptical cross-section (in this case, 15 cm × 6 cm). To correct the vertical position of the beam axis, a vertical beam position corrector is located in the subsequent section of the beam pipe. These two devices ensure the alignment of the beam axis with the magnetic axis of the bending magnet situated in the seventh section. The total length of the beam pipe sections, from the cyclotron exit to the bending magnet entrance, exceeds 370 cm. Over such a distance, the initial beam spread naturally results in significant beam broadening and, consequently, a loss of intensity. However, the ion-optical system of the cyclotron includes two quadrupole lenses, which enable beam focusing in both the vertical and horizontal planes. By appropriately adjusting these lenses (it is known from beam physics that a doublet of quadrupole lenses can act as a focusing system in both planes under specific conditions), a ratio of the current on the first probe element ($I_1$) to the current on the second probe element ($I_5$) of 1.4 was achieved. This ensured that approximately 70% of the beam particles were successfully directed into the region of the bending magnet's influence.

Given the use of a small-area neutron-excess radioactive $^{14}C$ target in this experiment, particular attention was paid to beam guidance and focusing. A specially developed multi-sensor system for monitoring beams of charged particles and heavy ions was employed. This diagnostic system allows for on-line monitoring of the beam profile

during accelerator operation, enabling precise beam guidance to the target [69]. The main elements of the developed system were:

1. Multi-wire beam profile sensor (MWBPS, see Figure 5);
2. System for collecting and processing information from the beam profile sensor.

The operating principle of the multiwire beam profile sensor is based on the effect of secondary electron emission, which occurs when charged particles pass through a grid of thin scanning wires. The developed sensor consists of eight vertical and eight horizontal isolated tungsten wires (tungsten with gold sputtering), each with a diameter of 25 μm. The wires are spaced 2.5 mm apart, and the entire grid is fixed on a supporting frame mounted on a vacuum flange inserted directly into the beam pipe. As a result, the multiwire beam profile sensor functions as a position-sensitive secondary electron detector with a resolution of 2.5 mm. At a beam current of 400 nA (accelerated alpha particles with energy of 27 MeV), the secondary electron current measured on the wires is 800 pA. In each of the 16 channels corresponding to a single wire, the signal is amplified by low-noise current amplifiers integrated into a single electronic unit [see 69 for further details]. This unit is controlled by a trigger signal generated by the high-frequency RF system of the cyclotron. The trigger signal has a periodic structure: 1 ms pulse duration from the set generator, corresponding to Q = 1, 2, 3 squares, with a filling period of 100 ns (beam microstructure). The trigger signal is sent to a binary counter and then to an analog multiplexer, which is controlled by the binary counter. The amplified and integrated signal from each X- and Y-wire is fed into the analog multiplexer for further processing. Simultaneously, the analog multiplexer receives the signal from the binary counter. This setup enables sequential readout of all wires according to the trigger signal. Once the wire number is identified, the trigger signal generates a synchronization pulse corresponding to a specific X and Y coordinate. Subsequently, the output signal from the analog multiplexer and the synchronization pulse are sent to the analog-to-digital converter for further processing. The parameter values from the analog-to-digital converter are read by the data acquisition system, allowing the beam position (during the trigger time) to be identified in real-time (“on-line”) [69]. The use of a multi-sensor system for charged particles and heavy ions beam

monitoring, enabled real-time visualization of the beam profile. This significantly improved the extraction of the cyclotron beam, increased the beam intensity on the target (by ensuring optimal beam focusing), and reduced the time required for beam guidance. By employing this system for operational control of the beam shape and position, along with the adjustable ion-optical system of the cyclotron, and by selecting optimal beam parameters (intensity versus energy resolution), the energy spread of alpha particles in the beam was reduced to 0.5% [67]. As a result, the elastic scattering peak was identified with high accuracy and resolution, and closely spaced excited states in the nuclear systems of $^{14}$C and $^{12}$C were successfully resolved.

As a result, experimental data on the elastic scattering cross sections were obtained (see Figure 11, black dots), and the corresponding angular distribution of alpha particles interacting with $^{14}$C nuclei was plotted. The primary challenge in selecting an optical potential to describe elastic scattering lies in the need to account for the channels of various inelastic reactions (such as transfer and exchange) at large angles [67]. Several studies have attempted to combine multiple potentials [70–71], with the best results achieved using the folding potential [72]. However, the application and validation of such potentials for light neutron-rich nuclei have yielded inconsistent results. Therefore, in this dissertation work, we selected a potential of the SPP form [73], which is well established for describing scattering and fusion processes in reactions involving heavy ions. The real part of the model potential is related to the folding potential through the following expression:

$$V_N(R,E) = V_F(R) \cdot \exp\left(-\frac{4 \cdot v^2}{c^2}\right) \qquad (2),$$

where c – light velocity and v – velocity of the nuclei relative moving, corresponds to:

$$v^2(R,E) = \frac{2}{\mu} \cdot [E - V_C(R) - V_N(R,E)] \qquad (3)$$

$V_C$ and $V_F$ – Coulomb potential and the folding potential, which can be found as:

$$V_F(R) = \int\int \rho_1(\vec{r_1}) \cdot \rho_2(\vec{r_2}) \cdot V_0 \cdot \delta\left(\vec{R} - \vec{r_1} + \vec{r_2}\right) \cdot d\vec{r_1} \cdot d\vec{r_2} \qquad (4),$$

where $V_0$ = -456 MeV·fm$^3$ [69]. For the density distributions in this work, the parameterization for heavy ions [72] and the parameterization for alpha particles [74] were employed. Based on the analysis of experimental data on the scattering of nuclei with energies up to 200 MeV/nucleon [75], the imaginary part of the potential can be expressed in the following form: $N_I \times V_N(R,E)$, where R – distance between the nuclei, and $N_I$ – the normalization of the imaginary part of the potential, which is determined from the corresponding approximation based on experimental values..

For the angular distribution of alpha particles elastically scattered by $^{14}$C nuclei obtained in this experiment, a theoretical curve corresponding to potential (2) with the imaginary part parameter $N_I$=0.85 (defined for the SPP potential with this form of the imaginary part) was derived. It is evident that the theoretical curve shows good agreement with the experimental data across the considered range of angles (see Figure 11). This demonstrates the applicability of the SPP potential to light neutron-rich nuclei. However, significant deviations are observed for this potential when describing the experimental differential cross sections in the case of alpha particle scattering over an extended angular range. The potential discussed above enables the study of the dynamics of the nuclear reactions under investigation, as it also suggests the presence of a similar resonance within this energy range.

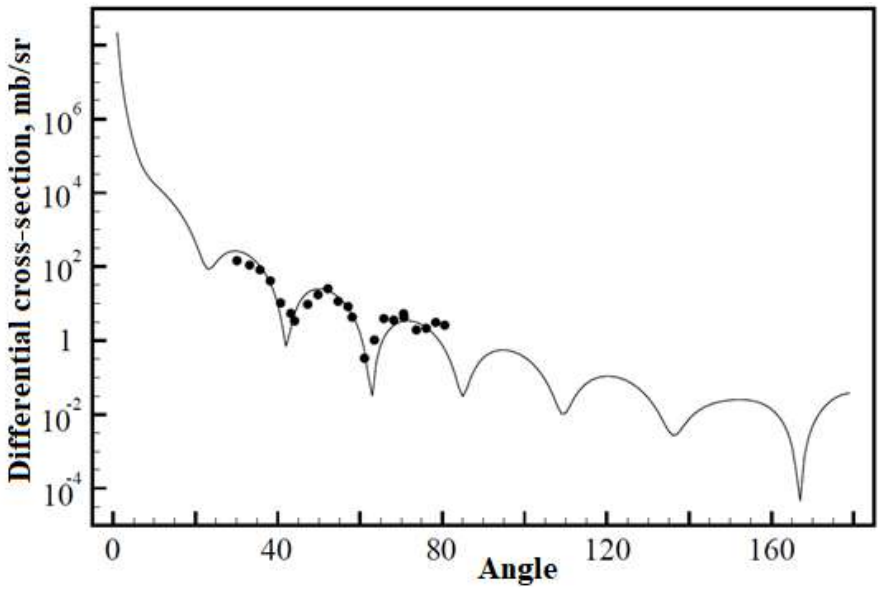


Figure 11 – Dependence of the differential cross section on the angle (angular distribution) for alpha particles elastically scattered by $^{14}$C nuclei. The dots represent experimental data, while the solid curve corresponds to the theoretical description obtained using the SPP potential [67].

The results obtained in this dissertation work further demonstrate the applicability of the SPP potential for describing reactions involving unstable neutron-rich nuclei. This enables the reduction of the range of optical potentials under consideration and subsequently choose the optimal one for a more detailed analysis of the dynamics and mechanisms of scattering reactions, including the case of exchange and elastic transfer. In the future, utilizing the experimental and theoretical insights from this study, a detailed analysis of excited states in neutron-rich nuclei will be done to investigate their configurational features, particularly in the context of cluster states.

### 1.2.2. Studies of the neutron-rich Nuclear System: $^{22}$Ne

Another well-studied alpha-cluster system is the $^{20}$Ne nucleus. By adding two neutrons to it, it becomes possible to investigate excited states in the $^{22}$Ne nucleus. The motivation here is similar to previous studies involving $^{14}$C nuclei, namely, to explain, verify, and predict a range of new properties of systems consisting of an alpha-cluster core supplemented by a few neutrons. In this context, a mechanism that is relatively complex, the multinucleon transfer reaction provides a valuable tool. This type of nuclear reaction (other names: deep inelastic scattering reactions, deep inelastic transfer reactions) was discovered over half a century ago at the Laboratory of Nuclear Reactions of the Joint Institute for Nuclear Research (JINR) by V.V. Volkov, A.G. Artyukh, J. Vilchinsky, G.F. Gridnev, and others [76–78]. Multinucleon transfer reactions occupy an intermediate position between direct nuclear reactions and reactions involving the formation of a compound nucleus. The mechanism of such reactions is based on the principle that interacting nuclei can exchange a significant number of nucleons, thereby forming new nuclei, including neutron-rich nuclei. Thus, multinucleon transfer reactions are characterized by the transfer of several nucleons between the target and projectile, which are typically ions ($Z > 2$). Initially, these reactions, which involve quasi-elastic and deep-inelastic collision mechanisms, were used to synthesize new radioactive elements and their isotopes. Furthermore, they demonstrated the potential for producing and studying neutron-deficient radionuclides

and nuclear systems [76, 79]. Today, with advancements in detector technology and precision methods of nuclear spectroscopy, multinucleon transfer reactions using stable and radioactive beams have become a key approach for investigating the structure of neutron-rich nuclei with small to medium neutron numbers, particularly those exceeding the filled nuclear core [80].

Although multinucleon transfer reactions are one of the primary tools for studying light nuclei near the stability limit, their complex dynamic features make them rarely used for investigating excited states. Even obtaining angular distributions over a wide range does not allow for the unambiguous determination of the structural characteristics of excited states. Furthermore, due to the large number of open channels and the necessity of obtaining exclusive spectra, studying the excitation functions of such reactions is challenging. However, it is important to emphasize that this reaction not only enables the production of nuclei near the breakup threshold but also, due to the transfer of significant angular momentum, it is possible to study of high-spin states and rotational bands. To achieve this, theoretical calculations should be performed to identify the processes involved in the formation and decay of nuclear systems. This will be demonstrated below using the example of the nuclear reaction $^{12}C + ^{14}C$, which results in the formation of the neutron-rich nucleus $^{22}Ne$. For the nuclear reactions considered in this dissertation work, the primary competing processes are:

1. Direct processes.
2. Fusion-decay processes.

Despite their distinct mechanisms and conditions, these processes are often challenging to separate, particularly in the case of multinucleon transfer reactions.

Let us analyze a typical reaction in which it is necessary to determine the mechanism of population-decay of states, a reaction in which ions of the light mass group act as a projectile, $^{12}C$ nuclei are the target, and alpha particles are emitted in the final state. In the case of a direct process, a multinucleon transfer reaction (two alpha particles) occurs with the formation of the nuclear system under study in the ground or excited state. In the case of a nuclear fusion process, an excited compound nucleus is

formed. These two processes are shown using the example of the multi-stage reaction studied in this dissertation: $^{14}C(^{12}C,\alpha_1\alpha_2)\rightarrow^{26}Mg^*\rightarrow^{22}Ne^*\rightarrow^{18}O$ (see Figure 12).

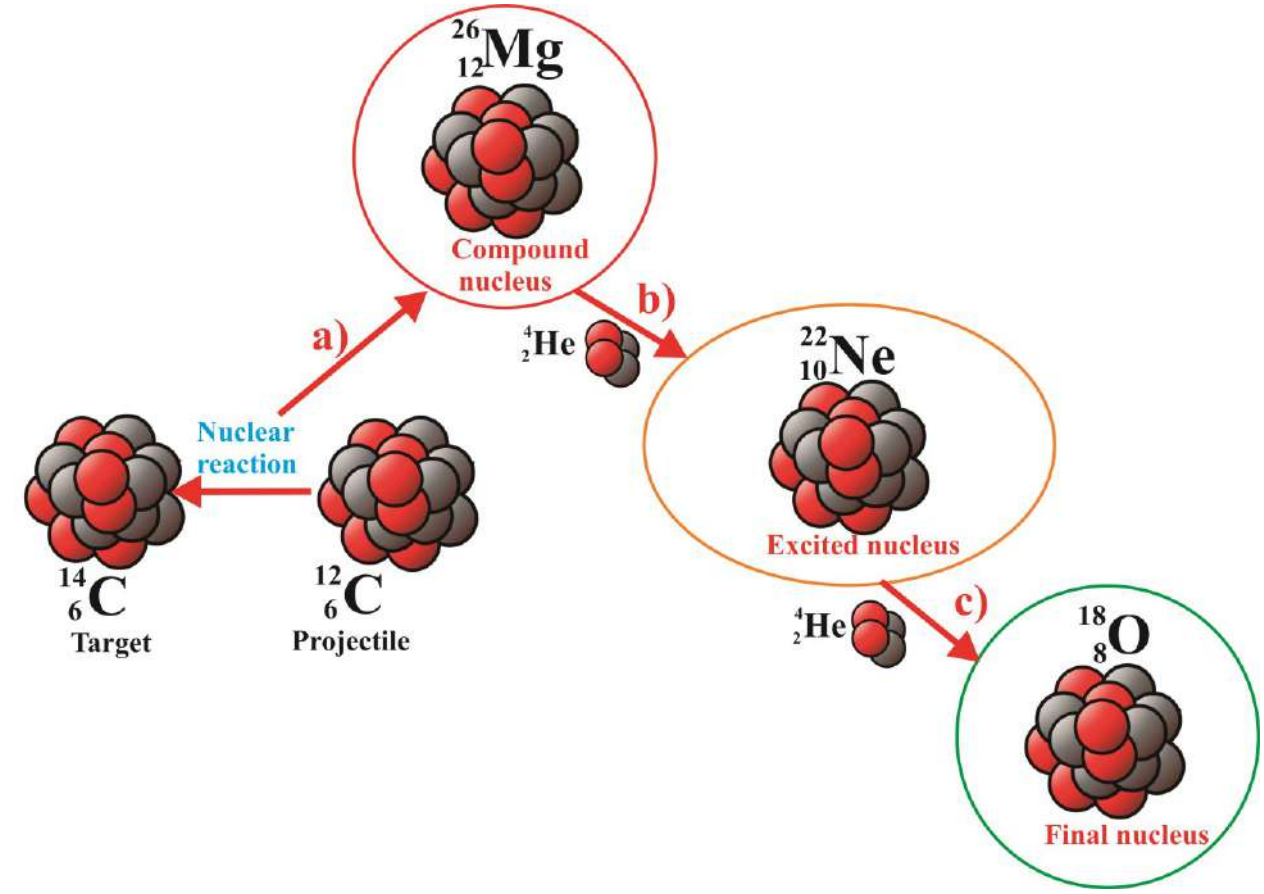


**1)**

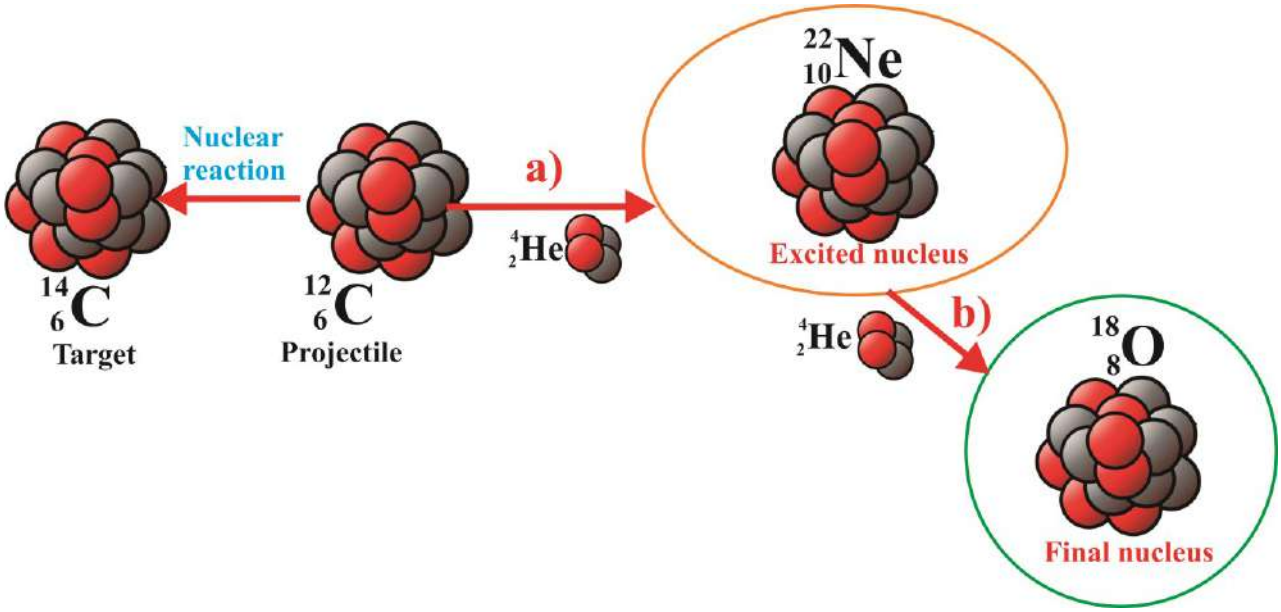


**2)**

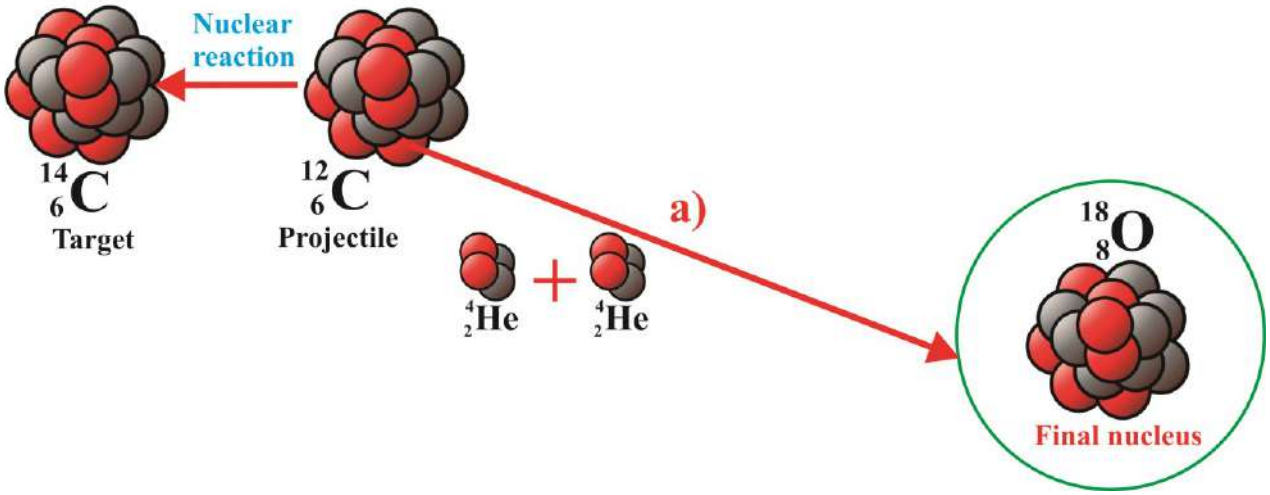


**3)**

Figure 12 - Possible mechanisms of the reaction: $^{14}C(^{12}C,\alpha_1\alpha_2)\rightarrow^{26}Mg^*\rightarrow^{22}Ne^*\rightarrow^{18}O$.

1) Reaction via a compound nucleus: a) formation of a compound nucleus $^{26}Mg$ in the reaction; b) decay of the compound nucleus $^{26}Mg$ with the formation of an intermediate excited nucleus $^{22}Ne$; c) decay of the intermediate excited nucleus $^{22}Ne$ into the ground state of the nucleus $^{18}O$.

2) Direct reaction: a) direct process with the formation of an excited nucleus $^{22}Ne$; b) decay of the excited nucleus $^{22}Ne$ into the ground state of the nucleus $^{18}O$.

3) Three-particle interaction channel: a) interaction of the projectile nucleus $^{12}C$ with the target nuclei $^{14}C$, with the transfer of two alpha particles, followed by population of the ground state of the nucleus $^{18}O$.

The system of two interacting heavy ions can form a compound nucleus (see part 1) in Figure 12). In the case of the presented reaction, a compound nucleus $^{26}Mg$ is formed. Subsequently, this nucleus decays via the evaporation of an alpha particle, resulting in the formation of the intermediate excited nucleus $^{22}Ne$ (see part 1) and channel b) in Figure 12). Following the emission of a second alpha particle, the nucleus passes to the ground state of $^{18}O$ (see part 1) and channel c) in Figure 12). In the studied nuclear reaction, a direct mechanism is also possible. In this scenario, an alpha particle is stripped from the projectile nucleus $^{12}C$ and picked up by the target nucleus $^{14}C$, leading to the formation of an excited nucleus $^{22}Ne$ (see part 2) and channel a) in Figure 12). This excited nucleus then decays into the ground state of $^{18}O$ by emitting an alpha particle (see part 2) and channel b) in Figure 12). Additionally, a three-particle decay

channel is possible in such nuclear reaction. In this case, two alpha particles leave the system, while the third alpha particle interacts with the projectile nucleus $^{14}C$, populating both the ground and excited states of the $^{18}O$ nucleus (see part 3) and channel a) in Figure 12).

As found in previous studies [81], for a simpler and similar reaction with self-conjugated nuclei $^{12}C+^{12}C$: $^{12}C(^{12}C,\alpha_1\alpha_2) \rightarrow ^{24}Mg^* \rightarrow ^{20}Ne^* \rightarrow ^{16}O$, in cases where resonance occurs in the system, the population of rotational bands in neon is observed. Therefore, to accurately investigate these processes, information about resonances in the beam-target system of two nuclei is essential. The study of resonances in light mass range ion systems remains a significant and relevant topic in low-energy nuclear reaction physics, as it can provide insights into the characteristics of so-called molecular states in nuclear systems (see Section 1.1). To date, numerous light nuclear systems have been investigated, and it has been demonstrated that high-spin resonances indeed occur in such systems. These resonances can be interpreted as quasi-bound states of two nuclei. The resonance parameters (spin and energy) are described by the following expression:

$$E_x = E_0 + \frac{\hbar^2}{2\cdot\theta}\cdot J\cdot(J+1) \qquad (5),$$

where: $\theta = 0.0104\cdot r_0^2\cdot\left(\frac{2}{5}\cdot\left(A_1^{\frac{5}{3}}+A_2^{\frac{5}{3}}\right)+\left(\frac{A_1\cdot A_2}{A_1+A_2}\right)\cdot\left(A_1^{\frac{5}{3}}+A_2^{\frac{5}{3}}\right)^2\right)$,

$E_0 = E_B + E_C$ ,

$$E_c = \frac{(1.21\cdot Z_1\cdot Z_2)}{\left(r_0\cdot\left(A_1^{\frac{1}{3}}+A_2^{\frac{1}{3}}\right)+0.5\right)}$$

here $A_{1,2}$ and $Z_{1,2}$ – masses and charges of the beam and target nuclei, the parameter $r_0$ is set to 1.3 fm. This dependence can help determine the positions of resonances. However, despite the relatively large width of such resonances, errors in estimating their positions can still occur. Therefore, obtaining experimental information on resonance states exhibiting properties of nuclear molecules is an important task.

Such information is typically derived from the analysis of nuclear reactions involving elastic or inelastic scattering. For example, in the context of the reaction studied in this dissertation, a separate investigation was done on the scattering of $^{12}C$ nuclei on $^{14}C$ (see D. Konnerth, W. Trombik et al., "Scattering and reactions of $^{14}C$+$^{14}C$ and $^{14}C$ + $^{12}C$," Nuclear Physics A, 436 (1985) 538–560). In this study, the $^{14}C$ nucleus in an excited state (6.73 MeV) was registered in the output channel. It was demonstrated that, in this case, a resonance with $l = 18$ is observed at an energy $E_{cm} = 23.5$ MeV, which is in good agreement with the formulas given above. To calculate the population of high-spin states in fusion reactions, the parabolic Hill-Wheeler model is particularly well-suited. This model accounts for the tunneling of a particle through a parabolic barrier [82], enabling a sufficiently general approach to accurately describe the probabilities of populating states with different angular momenta. In this model, the penetrability coefficient $T_l$ is expressed for the parabolic approximation as follows:

$$T_l = \frac{1}{\left(1+exp\left(\frac{2\cdot\pi\cdot(E_l-E)}{\hbar\cdot\omega}\right)\right)} \qquad (6),$$

where $E_l$ and $\hbar\omega$ – height and curvature of the barrier, which can be calculated as:

$$E_l = V(R_l) = V_N(R_l) + V_C(R_l) + \frac{\hbar^2\cdot l\cdot(l+1)}{2\cdot\mu\cdot R_l^2} \quad (7),$$

also:

$$\hbar\omega = \left|\frac{\hbar^2\cdot V''(R_l)}{\mu}\right|^{1/2}$$

The nuclear interaction potential was taken from the systematics [83], and the interaction cross-section in this case can be determined by the formula:

$$\sigma = \pi\cdot\lambda^2\sum_l(2\cdot l+1)\cdot T_l \qquad (8)$$

Using this formalism, the cross sections for the studied reaction $^{12}C$ + $^{14}C$ as a function of angular momentum were calculated. The results, illustrating the variation in

the cross section with increasing angular momentum, are presented in Figure 13. The reaction energy was set to 23.5 MeV, corresponding to a resonance with an angular momentum of 18. Analysis of the data in Figure 13 shows that the specified angular momentum is nearly equal to the critical value. This indicates that the experimental results are in excellent agreement with the model calculations.

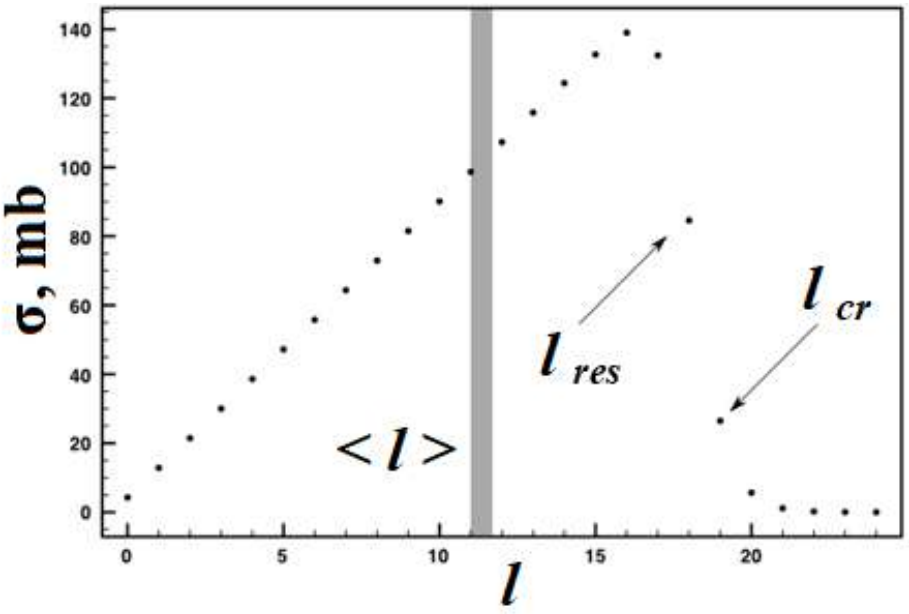


Figure 13 – Dependence of the cross section on the angular momentum for the formation of a compound nuclei. The cross section is shown at the critical angular momentum ($l_{cr}$=19), the experimental value of the observed resonance ($l_{res}$=18), and the average value of the formed compound system angular momentum.

For the case of the compound nuclear system formation, it is assumed that the angular momentum is approximately equal to $2/3l_{cr}$. In the reaction under consideration, this value is approximately 11.3 (indicated by the gray line in Figure 13). Returning to the reaction channels shown in Figure 12, it is worth noting that there is a possibility of direct three-particle decay of this nuclear system, but this case can be excluded taking into account the corresponding kinematic conditions. This problem becomes particularly interesting if, against the background of three-particle decay, events corresponding to the emission of the $^{8}$Be nucleus (correlated two alpha particles) are expected.

Further analysis of this reaction dynamics leads to the consideration of the studied nuclear system decay. For a comprehensive study of this process, an experiment aimed at studying the structure of excited states was prepared and carried out in the presented work. As the main task, it was formulated to determine the resonance states, with the corresponding spin and parity. A rather simple decay model was used, where the first alpha goes out at zero degrees to the beam. This gives to a characteristic dependence of secondary alpha particles distribution on the value of angular momentum in the case when the residual nucleus will be in the $0^+$ state:

$$W(\varphi) = \frac{2 \cdot l+1}{4 \cdot \pi} |P_l(cos\varphi)|^2 \quad (9),$$

here $\varphi$ – the angle for registration of second alpha-particle. In formula (9), the Legendre polynomial not only specifies the spin value of the level but also determines its parity [19, 21], which, for the given geometry, can only be natural. Let us formulate the experimental setup condition, which involves constructing the angular distribution of a specific level in a nuclear system with an excitation energy $E^*$ and spin value J. The calculating problem here reduces to determining the optimal angular range for detecting secondary alpha particles, aiming to increase statistical accuracy while ensuring unambiguous level identification. Typically, the energy region of nuclear excitation research is small and amounts to 5 – 10 MeV. However, it is important to note that regions with higher excitation energies remain relatively poorly studied. Additionally, it is necessary to use a laboratory coordinate system to simplify the experimental conditions. Figure 14 illustrates several Legendre polynomials corresponding to different angular momenta and different parities.

Under conditions of a strong angular range limitation, which arises due to the simultaneous use of a large number of detectors, it is necessary to select a region that eliminates the possibility of ambiguous determination of the angular momentum. It is known that the maximum sensitivity to a change in the phase of a sinusoidal signal occurs at the point where its derivative is maximized. In this case, the experimental data will be approximately halved, and considering the finite aperture of the detectors, it can be concluded that the optimal regions for analysis are the angular intervals marked in

Figure 14 as A and B. It is important to note that at small angles, the background increases significantly, while at large angles, the coincidence count rate drops sharply.

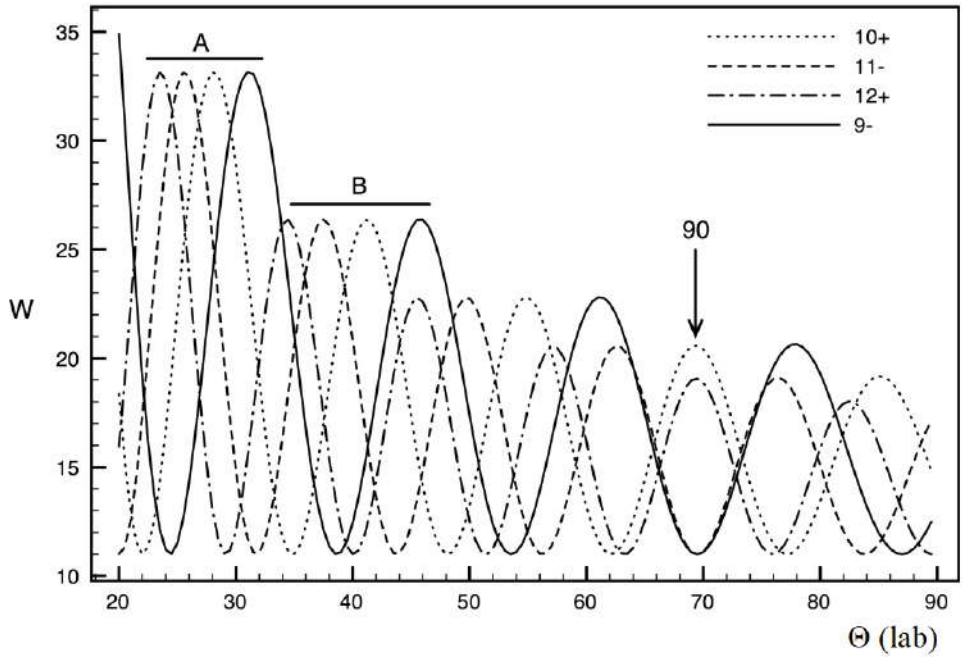


Figure 14 – Distributions of W(φ) for different angular momenta. The arrow shows the axis of symmetry corresponding to the angle of 90 degrees in the center of mass system.

The analysis of detector placement options in the scattering chamber has demonstrated that, from the perspective of experiment optimization, it is preferable to use two groups of detectors. The first group covers regions A or B, while the second group is positioned near the point corresponding to the axis of symmetry for polynomials in the center-of-mass system (see Figure 14). Thus, placing the second group of detectors in the region of 90-degree angles in the center-of-mass system allows for the unambiguous determination of parity: positive parity corresponds to a maximum, and negative parity corresponds to a minimum. In this case, only even (or odd) polynomials are permitted. This configuration enables operation with low statistics and a relatively small number of detectors, even if each detector could register events over a large solid angle.

The determination of angular momenta and the spectrum of excited states of reaction products enables the identification of the mechanisms underlying such nuclear reactions. As demonstrated above, the primary mechanisms of the studied reactions can

be realized through the following scenarios: direct processes and statistical decay. The basis for constructing a model that can distinguish between these two processes lies in the use of penetrability coefficients to determine the probability of populating states. By comparing these probabilities, we find that, in the case of resonance, higher states are preferentially populated. For example, in the reaction (studied in this dissertation): $^{14}C(^{12}C,\alpha_1\alpha_2)\rightarrow^{26}Mg^*\rightarrow^{22}Ne^*\rightarrow^{18}O$ the penetrability coefficients for the two $9^-$ states with energies of 20.1 MeV and 25.0 MeV differ by an order of magnitude. Therefore, a key motivation for this work was the study of high-lying, high-spin states of the $^{22}Ne$ nucleus, with subsequent identification in the context of their association with different rotational bands.

At present, a significant amount of information is available regarding the study of states in the $^{20}Ne$ nucleus. More than ten bands of varying structures have been identified in this nucleus [84]. However, data on another neon isotope: $^{22}Ne$, remain relatively scarce [85], with most studies focusing on low-lying levels and γ-ray spectroscopy [86]. Existing theoretical studies predict equally intriguing properties for this nucleus, particularly for high-spin states within rotational bands associated with nuclear molecular configurations.

It was demonstrated in [87] that, in the case of the elastic scattering reaction of $^{14}C$ nuclei on $^{12}C$ nuclei, high angular momentum resonances, similar to the molecular states observed in heavy-ion scattering [88] were detected. Additionally, a relatively high yield of alpha particles was registered in this reaction. Therefore, the beam energy corresponding to the $18^+$ resonance in the $^{14}C + ^{12}C$ system was selected to investigate the poorly studied excitation region of the $^{22}Ne$ nucleus in the experiment described below [19].

To study nuclear reactions with the formation of high-spin states in nuclear systems of the light mass group, the reaction: $^{14}C(^{12}C,\alpha_1\alpha_2)\rightarrow^{26}Mg^*\rightarrow^{22}Ne^*\rightarrow^{18}O$, was chosen [19, 21, 22, 23]. A 44 MeV beam of $^{12}C$ bombarded a $^{14}C$ target (target thickness 280 μg/cm$^2$, enrichment 80% in the main isotope $^{14}C$, the remaining 20% belonged to the isotope $^{12}C$).

The detector system for registering of the reaction products was positioned within a vacuum-controlled scattering chamber with a diameter of 1.5 meters. The angular correlation method was employed to satisfy the particle-to-particle coincidence conditions. Due to the low coincidence frequency and the need to cover a large number of angles for certain spin identification, it was essential to collect data at all these angles simultaneously. Consequently, large-area position-sensitive detector telescopes were used in the experiment. The experimental setup is shown in Figure 15.

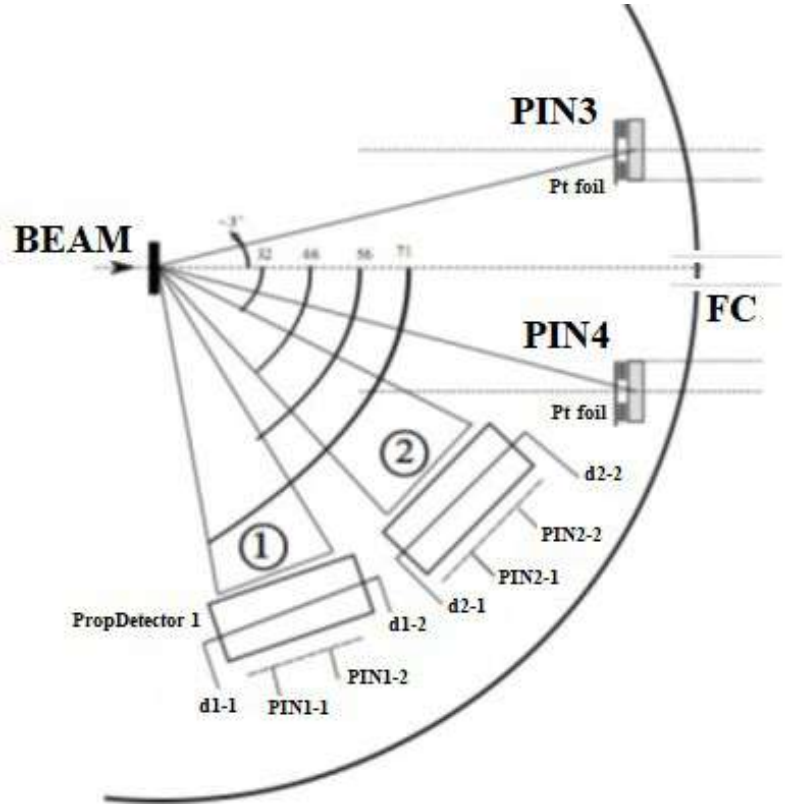


Figure 15 – Scheme of the experiment for studying the characteristics of the reaction: $^{14}C(^{12}C,\alpha1\alpha2)\rightarrow^{26}Mg^*\rightarrow^{22}Ne^*\rightarrow^{18}O$ with the formation of high-spin states in the nuclei of the light mass group.

The registration of primary alpha particles ($\alpha_1$) was carried out using two silicon detectors, known as PIN diodes: PIN3 and PIN4, each 300 microns thick. These detectors were positioned with their back sides at angles of $\pm3^o$ relative to the beam axis, in front of the Faraday cup (FC). To suppress the background from $^{12}C$ nuclei that have elastic scattered, the PIN detectors were covered with 15-micron-thick platinum foil [19, 21]. This configuration allowed for the detection of nuclei ranging from

hydrogen to lithium, with an alpha particle detection threshold of approximately 10 MeV. A specialized pulse-shape analysis method was employed to identify events corresponding to alpha particle registration. This method relies on the differences in charge collection times within silicon detectors when particles of varying mass and charge interact with the detector material [30–31]. Since a particle deposits a fixed amount of energy in the active volume of the detector, it is possible to determine its velocity and transit time, thereby obtaining information about its mass number – A. Additionally, the structure of the electrical signal (time dependence), formed by the processes in which the particle interact with the silicon detector material, allows for the determination of the charge collection time. This enables the generation of a "stop" signal to estimate the particle's transit time through the detector material, which in turn facilitates the identification of the particle's charge – Z. Further details on this original technique can be found in references [30–31].

A typical spectrum of the reaction products, obtained using this technique, is shown in Figure 16. Here, the X-axis represents the energy loss of the detected particles (in channels of the spectrometric system), while the Y-axis corresponds to the charge collection time (in channels of the Time-Amplitude Converter (TAC) system. For details one can see the block diagram of the electronics (see Figure 18) used for collecting and processing information from the detector modules.

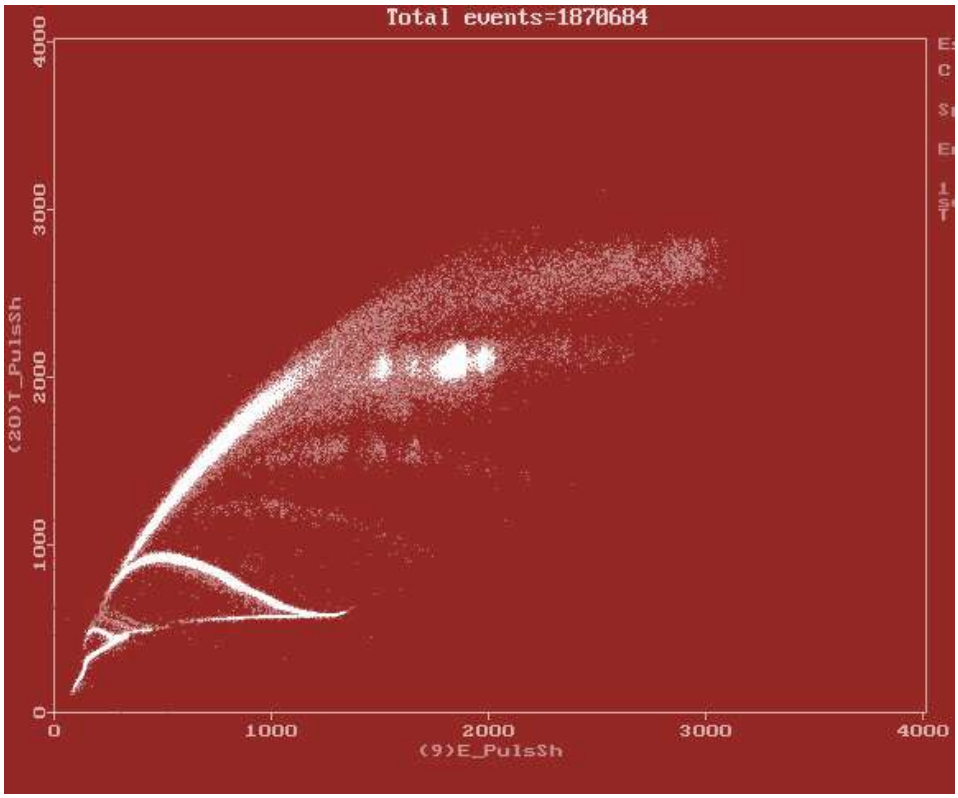


Figure 16 – Distribution of nuclear reaction: $^{12}C + ^{14}C$ products, registered on-line (without pre-processing), obtained with silicon PIN detectors by pulse shape analysis, using charge collection information.

The registration of secondary alpha particles ($\alpha_2$) from the decay of excited states of $^{22}Ne$ was performed using two large-area position-sensitive combined ΔE–E telescopes (Telescopes 1 and 2, see Figure 15). These telescopes covered angular ranges of 34° to 50° and 58° to 75° in the laboratory coordinate system and were protected by 15-micron-thick aluminum foil. Each telescope consisted of a gas proportional detector with a single anode, functioning as a ΔE-detector, and ten silicon PIN diodes [19, 21] serving as stop detectors (E-detectors). The thickness of the PIN diodes was 380 μm. In the gas proportional detector, signals generated at the anode were read from both ends: d1-1 and d1-2 for Telescope 1, and d2-1 and d2-2 for Telescope 2. These signals provided information on the energy loss and the X-coordinate in the corresponding ΔE-detector. The detector was filled with an Ar + 10% $CH_4$ gas mixture at a pressure of 250 Torr, with continuous gas renewal in its volume. As previously mentioned, each telescope used an assembly of 10 PIN diodes as the E-detector. To precisely determine

the angular range in which alpha particles were registered, each assembly was divided into pairs: PIN1_1 and PIN1_2 for Telescope 1, and PIN2_1 and PIN2_2 for Telescope 2. The accuracy of determining the particle registration angle was ±0.5°.

Typical two-dimensional spectra of signals from the ΔE-E telescopes are shown in Figure 17. Here, the X-axis represents information from the 10 silicon PIN diodes, while the Y-axis corresponds to information from the gas proportional detectors.

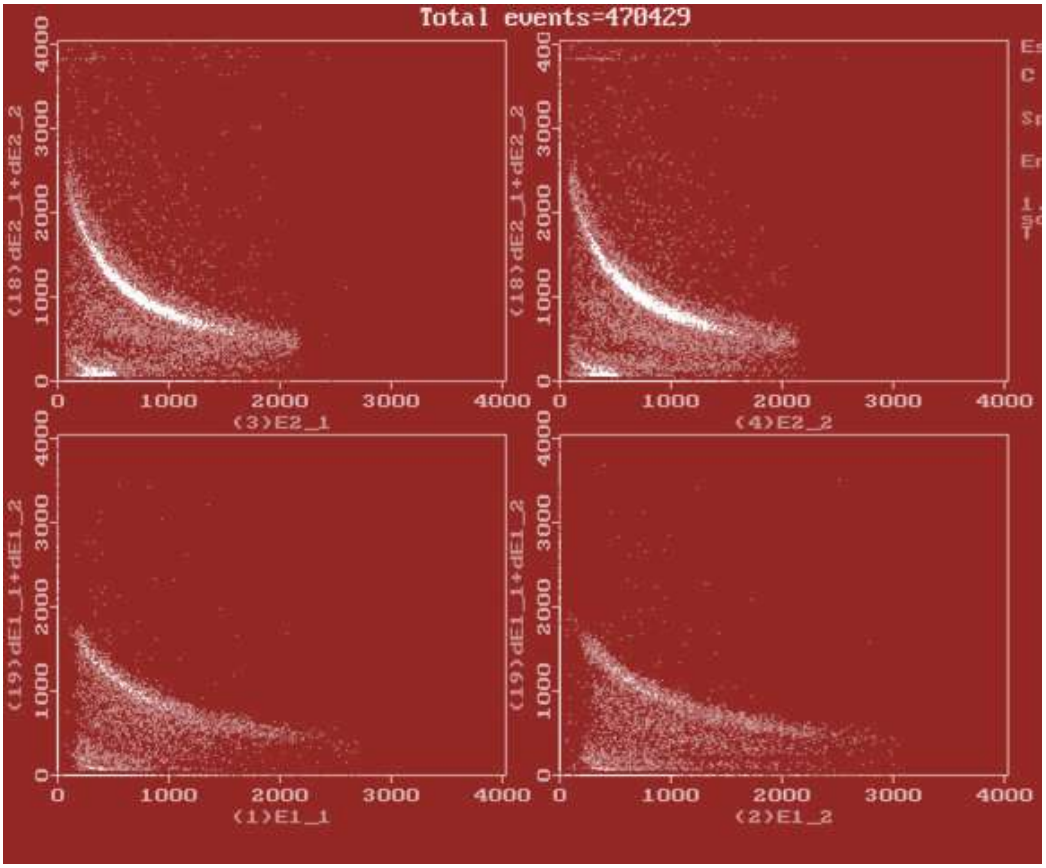


Figure 17 – Distributions of nuclear reaction $^{12}C+^{14}C$ products, registered on-line and obtained using gas proportional detectors (ΔE) and silicon PIN detectors (E) telescope system.

The block diagram of the data acquisition from all detector modules, including the two telescope sections and the two front silicon detectors (PIN3 and PIN4) is shown in Figure 18.

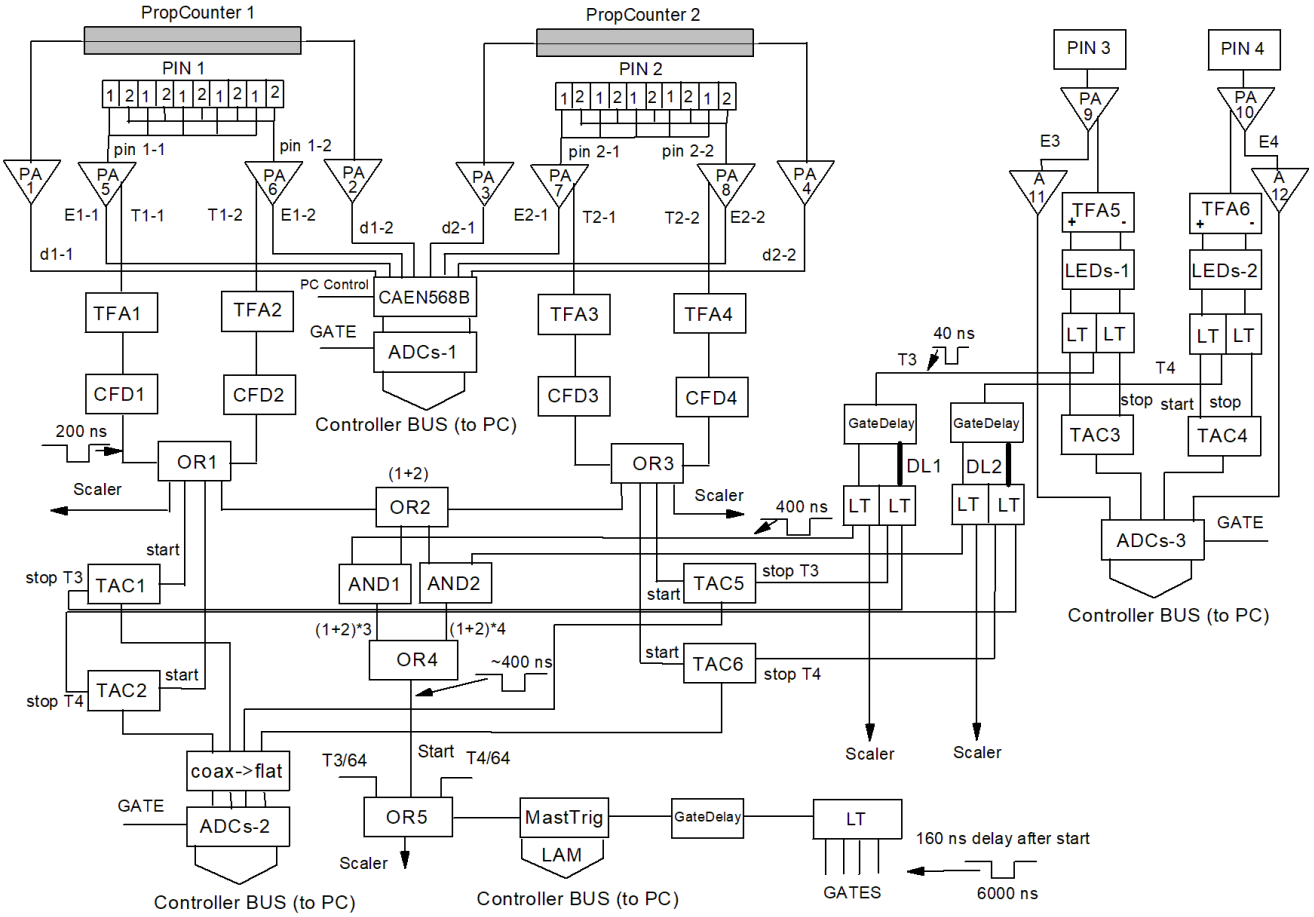


Figure 18 – Block diagram of the data acquisition from detector modules of two telescope sections (dE-part: gas proportional detectors; E-part: 10 silicon PIN detectors) and two front silicon detectors (PIN3 and PIN4).

The experimental data processing involved several stages. In the first stage, the reaction products (see Figure 16) registered by the detectors—PIN3 and PIN4 (see Figure 18, right side)—were identified using specialized charge-sensitive preamplifiers (Figure 18, PA9 and PA10). These preamplifiers enabled the implementation of the pulse-shape analysis technique, which accounts for the collection of corresponding charges in these detectors. The detectors were positioned at an angle of 18∘18∘ on both sides of the beam axis.

A detailed analysis of the obtained two-dimensional spectra (see Figure 16) of the reaction products allowed for the identification of the nuclei formed during the reaction. As a result, it was obtained a processed spectrum (see Figure 19) showing the dependence of the charge collection time (in channels of the Time-Amplitude Converter

(TAC) system on the energy loss of the registered particles. The spectrum clearly displays the identified reaction products.

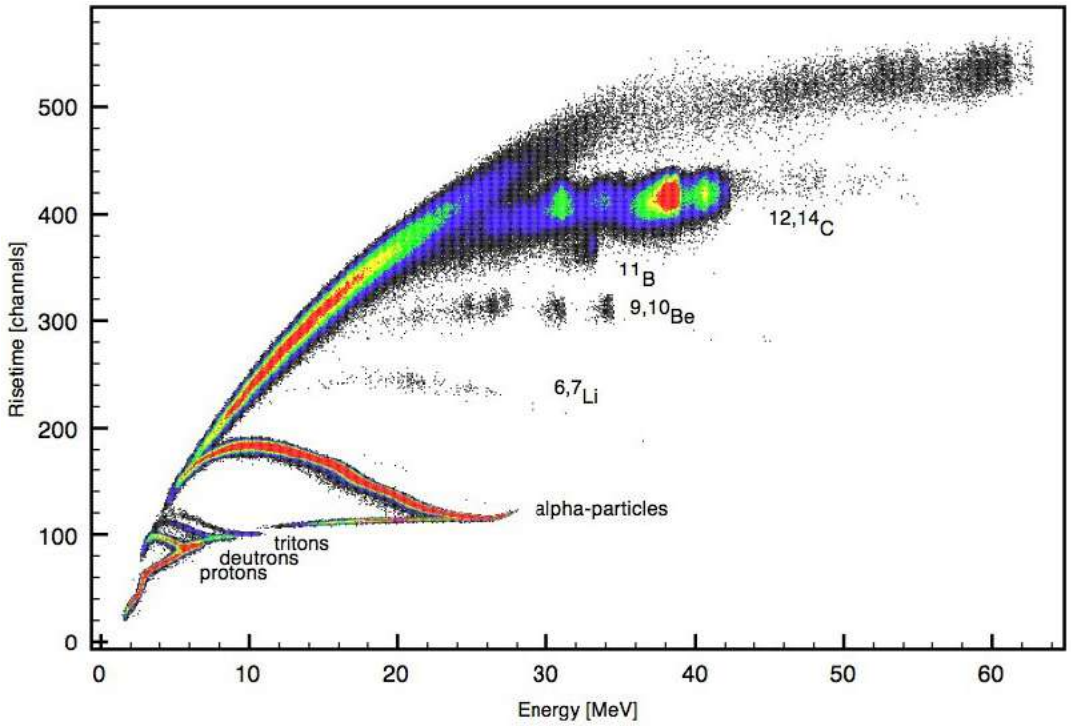


Figure 19 - Two-dimensional spectrum of the reaction $^{12}C+^{14}C$ products.

Thus, it was possible to identify the energy bands corresponding to protons, deuterons, tritons, alpha particles, and light nuclei in the studied nuclear reaction: $^{6,7}Li$, $^{9,10}Be$, $^{11}B$, $^{12,14}C$ (see Figure 19), as well as traces of heavier elements (upper line) resulting from the beam interaction with the structural materials of the detector diaphragms.

A closer examination of the bright band corresponding to alpha particles reveals a faint band composed of a small array of dots at the top. This band represents the neutron-rich nucleus $^{6}He$. At an angle of 18°, as in the presented case, only a few of these nuclei are registered. However, when the PIN3 and PIN4 detectors are positioned at angles of ±3° relative to the beam axis, a significantly higher number of helium-6 nuclei are observed. This is clearly shown in Figure 20, where, against the background of the main band of registered alpha particles, the identified events corresponding to the excited states of $^{20}Ne$ nuclei formed as a result of the reaction are displayed: $^{14}C(^{12}C,^{6}He)^{20}Ne^{*}$. The obtained result is significant because, in previous studies of this

reaction, the yield of such exotic neutron-rich nuclear formations had not been observed. The detection of these nuclei was made possible through an original experimental technique, which included new silicon detectors and specialized charge-sensitive preamplifiers. These components enabled the analysis of signals via pulse-shape analysis, taking into account the differences in charge collection times within the detectors [30–31]. As a result, it became possible to extract information on the dynamics of direct mechanisms that may occur in the studied nuclear reaction. Analysis of the two-dimensional distribution shown in Figure 20 allows for the identification of the first excited state ($2^+$ at 1.6 MeV) and the second excited state ($4^+$ at 4.2 MeV) in the $^{20}$Ne nucleus within the reaction channel: $^{14}$C($^{12}$C,$^{6}$He)$^{20}$Ne*. The selective population of these excited states is illustrated in detail in the one-dimensional energy spectrum of $^{6}$He nuclei, shown in Figure 21, where the X-axis represents the energy of the $^{6}$He nuclei registered in the reaction. Additionally, the highly excited states could not be identified due to their overlap with events corresponding to low-energy alpha particles. Within the framework of this reaction, it is possible to estimate the probability of conditions under which a two-alpha-particle transfer process occurs. If we analyze similar reactions, particularly the reaction $^{18}$O + $^{14}$C, it is noted that $^{6}$He nuclei were not experimentally detected, even at small angles [89]. Therefore, the results obtained in the studied reaction indicate a significant contribution of the $^{6}$He +$^{8}$Be nuclear system to the structural features of the neutron-rich $^{14}$C nucleus. This further allowed for the clear identification of the rotational band of the ground state ($K = 0^+$) in the $^{20}$Ne nucleus.

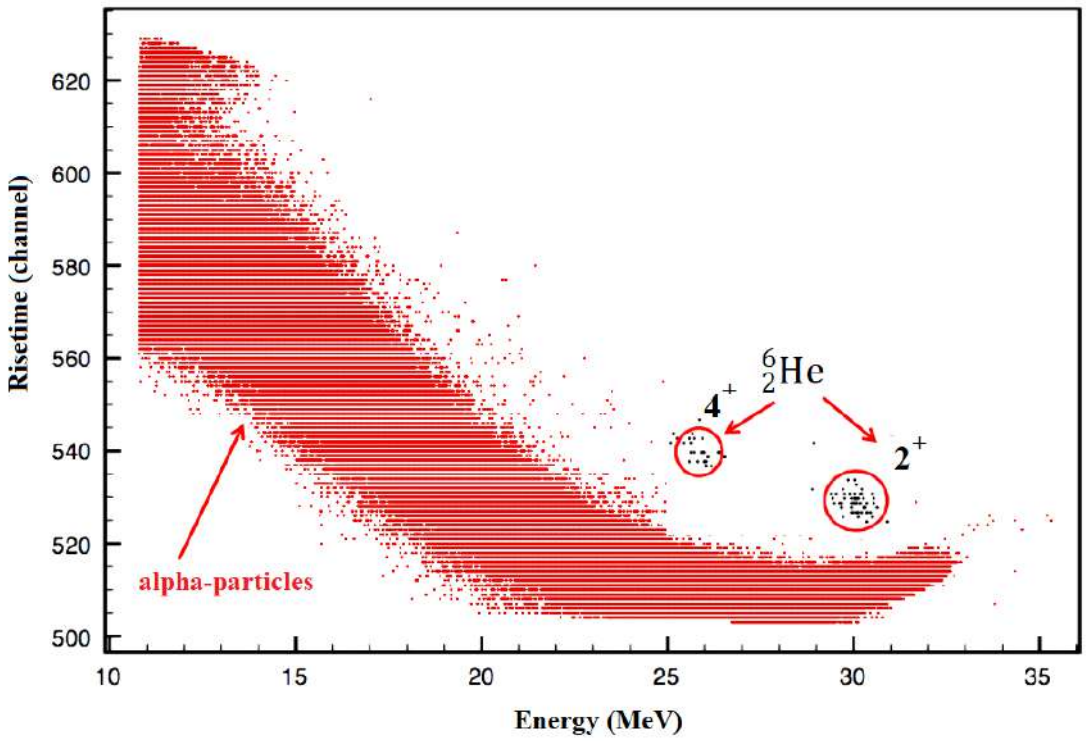


Figure 20 – Two-dimensional spectrum of alpha particles and $^{6}$He nuclei registered in the $^{12}$C + $^{14}$C reaction (areas in red circles). The detectors were positioned at an angle of 3° on both sides of the $^{12}$C beam.

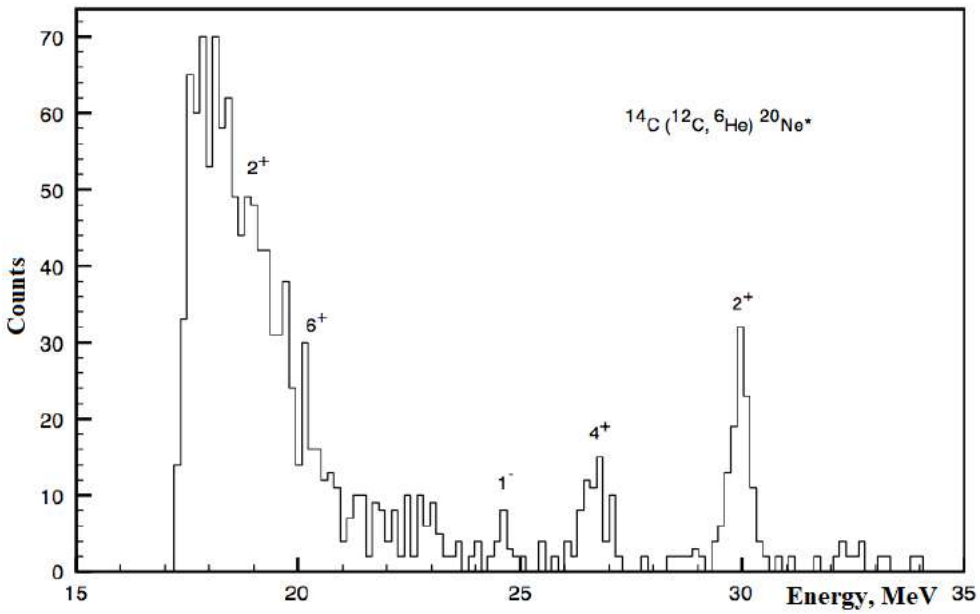


Figure 21 – One-dimensional energy spectrum of excited states of the $^{20}$Ne* nucleus arising in the reaction with the emission of $^{6}$He: $^{14}$C($^{12}$C,$^{6}$He)$^{20}$Ne*. The selective population of excited states $2^{+}$ (1.6 MeV) and $4^{+}$ (4.2 MeV) is well identified.

Let us now turn to the analysis of double alpha-alpha coincidence events registered in this experiment. The study of such events enabled to create the angular distributions of alpha particles. An example of this distribution is shown in Figure 22, which displays a two-dimensional spectrum of alpha particle detection using silicon PIN detectors (PIN3, PIN4) via the pulse-shape analysis method. The X-axis represents information derived from charge collection, while the Y-axis corresponds to data from the silicon PIN detectors (EE) of the second position-sensitive telescope (PIN2_1, PIN2_2) [19, 21]. Since a highly enriched $^{14}C$ target (80%) with an admixture of $^{12}C$ (20%) was used, the experiment allowed for the simultaneous study of features in two nuclear reactions: $^{14}C(^{12}C,\alpha1\alpha2)\rightarrow^{26}Mg^*\rightarrow^{22}Ne^*\rightarrow^{18}O$ and reaction: $^{12}C(^{12}C,\alpha1\alpha2)\rightarrow^{24}Mg^*\rightarrow^{20}Ne^*\rightarrow^{16}O$. To separate the decay channels resulting in the formation of $^{18}O$ or $^{16}O$ in the final state, a specific "gate" was applied to the corresponding bands during the processing of the experimental data, taking into account the reaction energy (Q-value).

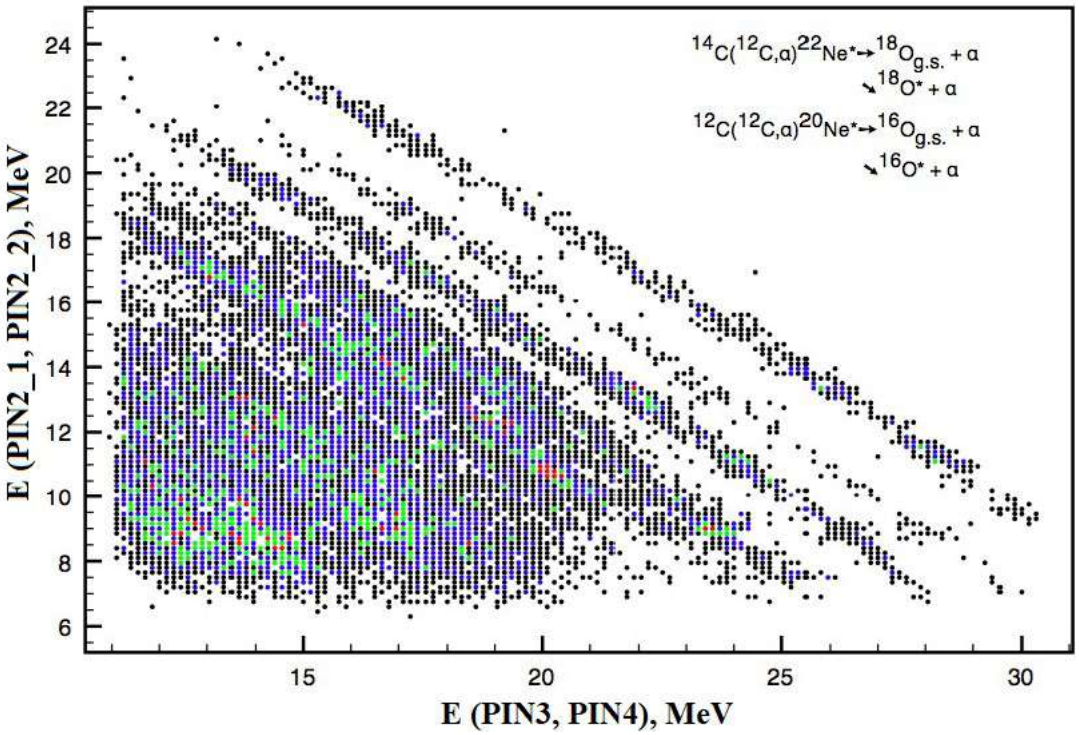


Figure 22 – Two-dimensional spectrum of alpha particle registration by silicon PIN detectors (PIN3, PIN4) and silicon PIN detectors of the second position-sensitive telescope (PIN2_1, PIN2_2).

Analysis of the spectrum shown in Figure 22 reveals bands corresponding to decays to both the ground state of $^{16}O$ and $^{18}O$ nuclei (from the reactions $^{12}C+^{12}C$ and $^{12}C+^{14}C$) and to the first excited state of $^{18}O$ (1.98 MeV, $2^+$), as well as a triplet of excited states of $^{18}O$ (3.55–3.92 MeV, $4^+$, $0^+$, $2^+$). Other bands represent a mixture of excited states of $^{16}O$ and $^{18}O$ nuclei. A distinct group of red dots with coordinates (20, 11) is clearly visible. This corresponds to the population of states in the $^{12}C+^{12}C$ reaction, involving the emission of an alpha particle and the formation of the $^{20}Ne$ nuclear system in an excited state (excitation energy 18.54 MeV, $8^+$ state in the $^{20}Ne$ nucleus). This nuclear system subsequently decays with a relatively high probability into excited states of the $^{16}O$ nucleus (doublets at approximately 6 MeV and 7 MeV, which cannot be resolved due to insufficient resolution), as demonstrated in [90]. The decay of this level (the $8^+$ state in the $^{20}Ne$ nucleus) was studied in beams with energies of 64 MeV and 80 MeV, where it was demonstrated that the probability of decay at 6 MeV is approximately 1.5 times greater than at 7 MeV [90]. In the case of our experiment (beam energy of 44 MeV), a significantly more marked decay of the state corresponding to the doublet at 7 MeV is observed, with a very low probability of decay for the doublet at 6 MeV. Within the studied energy range, as shown in [91], the excitation function of this level reaches a minimum value.

A detailed analysis of the energy spectra obtained in this dissertation work, during the detection of alpha particles as products of the corresponding nuclear reactions, leads to the identification of three key directions for data analysis:

1) the sum of the experimental data for two reactions:
$^{14}C(^{12}C,\alpha1\alpha2)\rightarrow^{26}Mg^*\rightarrow^{22}Ne^*\rightarrow^{18}O_{GS}$ and $^{12}C(^{12}C,\alpha1\alpha2)\rightarrow^{24}Mg^*\rightarrow^{20}Ne^*\rightarrow^{16}O_{GS}$;

2) the experimental data for reaction: $^{14}C+^{12}C$ with $^{18}O$ nucleus formation at excited state: $^{14}C(^{12}C,\alpha1\alpha2)\rightarrow^{26}Mg^*\rightarrow^{22}Ne^*\rightarrow^{18}O^*$ (1.98 MeV);

3) experimental data sum for the reaction: $^{14}C+^{12}C$ with formation of three excited states of $^{18}O$ nucleus: $^{14}C(^{12}C,\alpha1\alpha2)\rightarrow^{26}Mg^*\rightarrow^{22}Ne^*\rightarrow^{18}O^*$(3.55 MeV, 3.63 MeV, 3.92 MeV).

Figure 23 shows coincidence spectra for the case of decay into a sequential series of first excited states of the $^{18}O$ nucleus within the studied excitation energy range of 16

to 30 MeV [19, 21]. The intermediate nuclear system $^{22}$Ne, formed in the reaction within this excitation energy range, decays with a higher probability into the $4^+$ state (3.55 MeV) and with a lower probability into the $2^+$ state (1.98 MeV). The energies of these levels were determined with an uncertainty of ±100 keV.

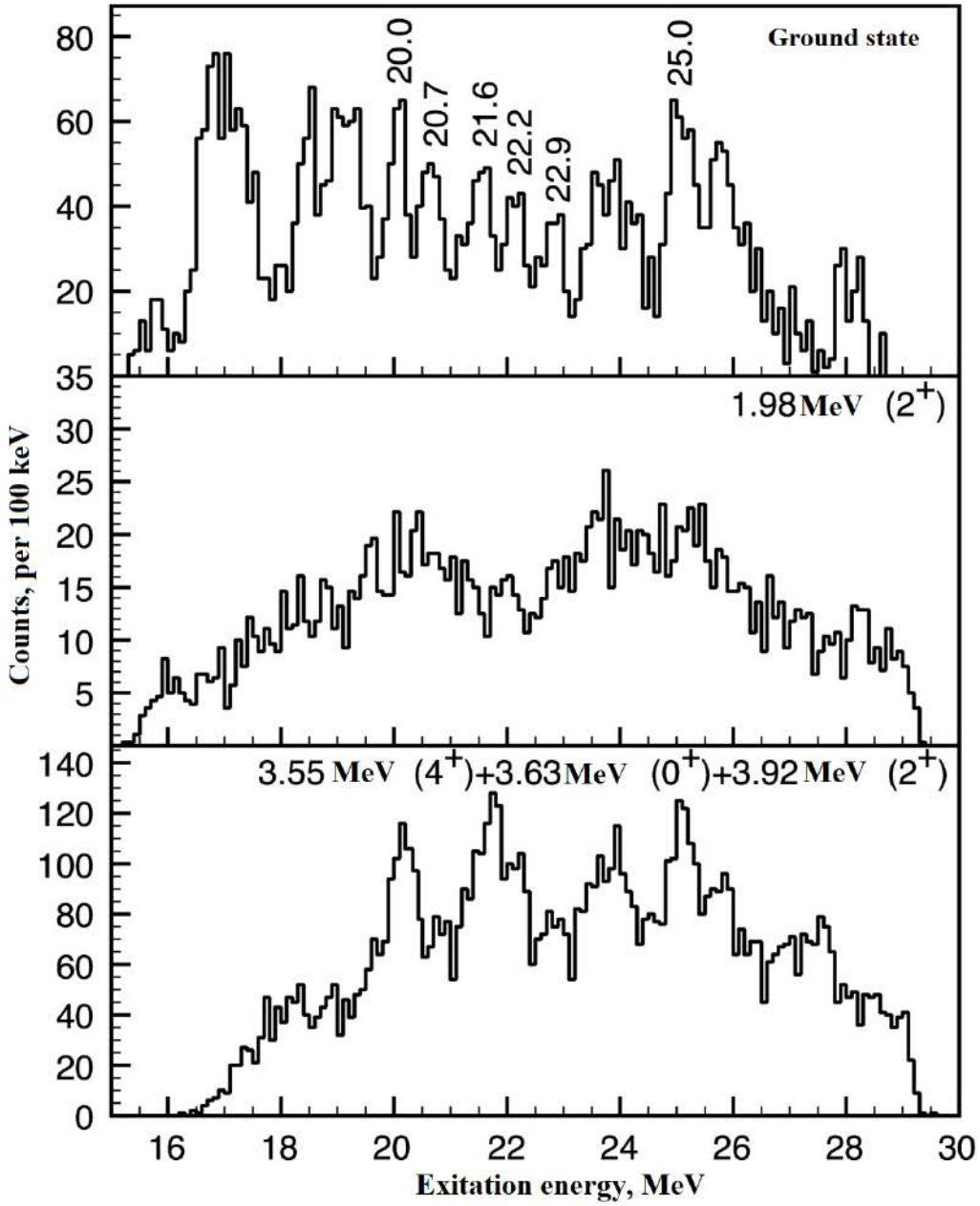


Figure 23 - Comparison of alpha-alpha coincidence spectra for the reaction: $^{14}C(^{12}C,\alpha1\alpha2)\rightarrow^{26}Mg^*\rightarrow^{22}Ne^*\rightarrow^{18}O$ for decay of $^{22}Ne^*$ to ground state and two excited states of $^{18}O$: $2^+$ (1.98 MeV) and $4^+$ (3.55 MeV). The energies of levels for which it is possible to determine the spin value using the angular correlation method are indicated [19, 21].

Next, an analysis of the angular distributions was carried out, enabling the determination of the spin values of the corresponding levels along with their associated angular momenta $l$ (see Formula 8). Figure 24 displays the angular correlations for five levels during the decay of the $^{22}$Ne nuclear system to the ground state. The experimental data points were fitted using the function $|P_l|^2$ + const, accounting for the moving to the laboratory coordinate system [19, 21]. This approach allows for the unambiguous determination of the angular momenta of these identified levels. The best fit was achieved for $l$ = 9 for levels at 20.0 MeV, 21.6 MeV, and 25.0 MeV, for $l$ = 11 for level 20.7 MeV, and at $l$ = 12 for level 22.2 MeV (see Figure 24). The observed background is relatively small and exhibits a non-resonant structure [19, 21].

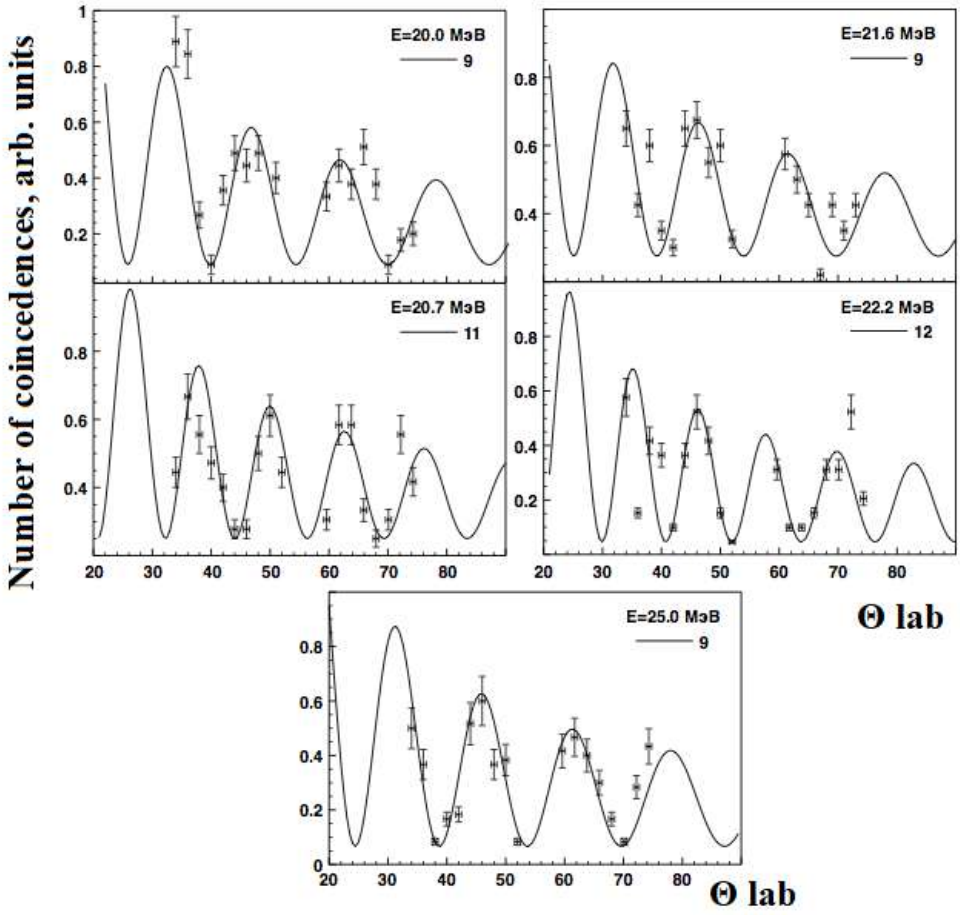


Figure 24 - Angular correlations for the levels 20.0 MeV, 21.6 MeV, 20.7 MeV, 22.2 MeV, 25.0 MeV during the decay of the $^{22}$Ne nuclear system to the ground state.

A comparison of the available theoretical and experimental data [85, 92, 93] on the structure of rotational bands in the $^{22}$Ne nucleus with the results obtained in this

dissertation work allows us to assign the identified levels to rotational bands of different structures. For example, for the identified level at 20.0 MeV ($9^-$), levels with similar energies of 19.9 MeV and 19.89 MeV were observed in a comparable nuclear reaction: $^{14}C(^{18}O, ^{18}O+\alpha)$. In the latter case, its spin was determined as $10^+$. Analyzing the spectra obtained in [87] during the population of the $4^+$ state (3.55 MeV) in $^{18}O$, several closely spaced levels with a strong dependence of the population probability on the beam energy were registered in this energy region. The most intensively populated level is below 20 MeV at beam energy of $E_{CM}$ = 20.75 MeV, while at higher energies, a peak at 20 MeV is observed.

Figure 25 shows the rotational bands found in the $^{22}Ne$ nucleus and the experimental results obtained in the presented dissertation. According to the systematics given in [85], one should expect the presence of two types of bands: alpha particle + $^{16}O$ with two covalent neutrons (low-lying band of negative parity) and alpha particle + $^{18}O$ (high-lying band of negative parity, marked with a dotted line). Thus, the $11^-$ state found in this dissertation may belong to one of these bands. In Figure 25, the dots are the levels that were taken from [85], and the dash-dotted line shows the possibility of combining the $11^-$ state with the known rotational bands: 1) based on the predictions of the potential model, 2) combining with low-lying states of negative parity.

The description of the quasi-molecular band using the Woods-Saxon potential shows a significant change in the moment of inertia for high-lying levels. In this case, one of the fragmented states is observed, which can lie even below the series of $9^-$ levels. Using theoretical models, it is possible to accurately describe the positions of the centers of the detected fragmented states, predicting the location of the group of $11^-$ states near 22 MeV (see Figure 25, dash-dotted line 1). On the other hand, the J(J+1) dependence, which approximates the behavior of the low-lying band with covalent neutrons, also predicts an excitation energy for the $11^-$ state within the same energy range (see Figure 25, dash-dotted line 2). Thus, the question of whether the $11^-$ state at 20.7 MeV belongs to the rotational bands remains unresolved. Additionally, Figure 25 shows the position of the yrast line (solid line) and marks the decay thresholds for the nuclear systems: α-cluster + $^{18}O$ (core) and 2α-cluster + $^{14}C$ (core) [19, 21].

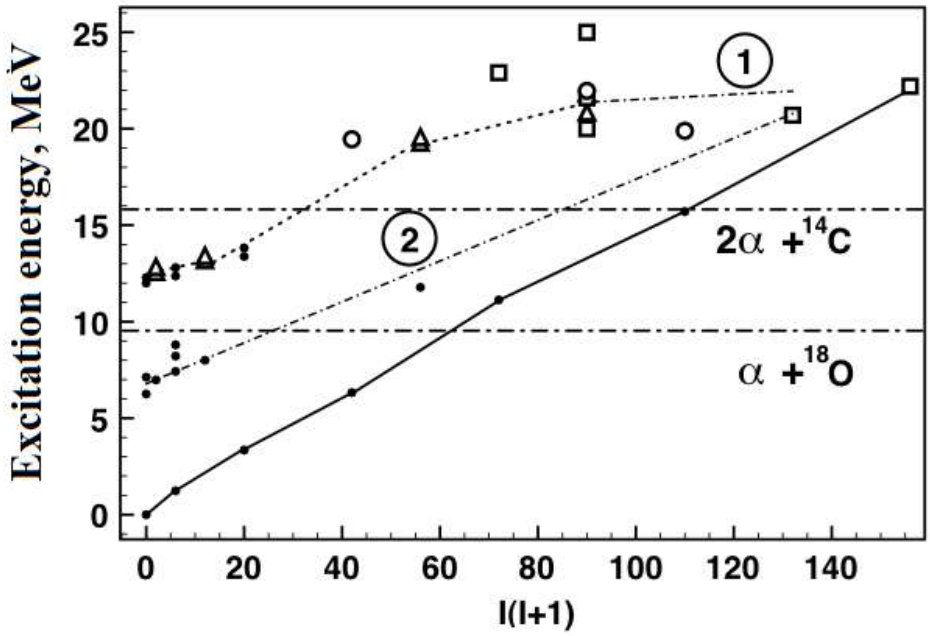


Figure 25 - Rotational bands in the $^{22}$Ne nucleus [19, 21]. The squares indicate the data of this dissertation, the circles indicate the data of [92], and the triangles indicate the data of [93]. The thresholds for the decay of the studied nuclear systems into their constituent clusters and cores are illustrated.

The analysis of the properties of the rotational bands in the $^{20}$Ne and $^{22}$Ne nuclei indicates their similar behavior. Considering the key principles of the shell model, it can be concluded that the bands of the K = $0^+$ ground states should terminate at the $8^+$ state for $^{20}$Ne and the $10^+$ state for $^{22}$Ne. This is confirmed experimentally, though challenges may arise in identifying the 10+ state for $^{22}$Ne. Meanwhile, for the high-lying bands in $^{20}$Ne, the $10^+$ state is theoretically predicted and has the potential to exist. Despite certain difficulties in experimentally observing these levels, states with such spin have now been detected [94]. This suggests that in the $^{22}$Ne nucleus, levels with even higher spin, such as the $12^+$ state, may also exist.

The analysis performed demonstrates the significant role played by the individual contributions of the alpha cluster and the core moment of inertia in the dynamics of rotational band formation. Given that the $^{8}$Be nucleus is poorly associated with the cluster concept (as it decays into two alpha particles), it can be inferred that these bands exhibit a symmetric structure of the 2α + core type, which aligns well with the absence of parity splitting. A structure of the $^{12}$C + 2n + α type has been proposed to describe the

bands with a high moment of inertia in the $^{18}O$ nucleus. Assuming the existence of bands with a similar structure in the $^{22}Ne$ nucleus, which exhibit parity splitting (as observed in the $^{18}O$ nucleus), it can be concluded that the experimentally discovered $11^-$ state (this dissertation) belongs to such bands. Despite the lack of reliable experimental data for all members of the high-spin states, calculations performed within the framework of Antisymmetrized Molecular Dynamics (AMD) for bands with different structures as in nuclear molecules [95] provide a means to describe a large number of closely located states with spin 9−, as registered in this dissertation work.

Summarizing the results of this experimental work, it can be stated that for the investigated reaction: $^{14}C(^{12}C,\alpha1\alpha2)\rightarrow^{26}Mg^*\rightarrow^{22}Ne^*\rightarrow^{18}O$ at a $^{12}C$ beam energy of 44 MeV, a number of high-spin states in the $^{22}Ne$ nucleus were observed in the excitation energy range from 16 to 30 MeV (see Table 1). Based on their characteristics, these states can be identified as rotational bands with different structures like a nuclear molecule. A new isoscalar (yrast) line state with spin $12^+$ at an energy of 22.2 MeV was also observed. Table 1 summarizes the data on the newly registered levels, and the analysis indicates that a high-spin resonance can be formed in the $^{12}C + {}^{14}C$ system, with an angular momentum on the order of 18.

Table 1 – List of levels identified in this dissertation work.

| Level, MeV | Spin, parity (where it was defined) | Level width, keV |
|---|---|---|
| 17.0 | - | Unresolved level group |
| 18.45 | - | ~330 |
| 19.13 | - | Unresolved level group |
| 20.0 | $9^-$ | ~270 |
| 20.7 | $11^-$ | 340 |
| 21.6 | $9^-$ | ~350 |
| 22.2 | $12^+$ | ~250 |
| 22.9 | - | ~290 |
| 24.0 | - | Unresolved level group |
| 25.0 | $9^-$ | ~350 |
| 25.9 | - | Unresolved level group |
| 27.0 | - | Unresolved level group |

## 1.3. Investigations of resonance states in nuclear reactions of the light mass range with A < 30. Determination of the interaction potential in elastic scattering nuclear reactions.

In studies of nuclear reactions, the use of semi-microscopic models and potentials based on them is limited by the nucleon-nuclear interaction. However, these models give good results for reactions involving light-mass ions. Consequently, nuclear reactions with such ions, leading to the formation of nuclear systems with mass numbers up to A < 30, are of particular interest for nuclear astrophysics. The strong influence of cluster configurations, as described in the Cluster Nucleosynthesis Diagram (CND) model [96, 97], adds further intrigue to this field of study. The CND model represents an extension of the cluster configurations formalism, based on the application of the Ikeda diagram [98]. Such diagrams allow for a natural extension to neutron-rich nuclei with covalent bonds [99], offering the possibility of incorporating cluster degrees of freedom in non-self-conjugate nuclei into problems of nuclear astrophysics [100]. The key experiments within this model involve reactions with alpha particles (elastic scattering, transfer, and (α, p) reactions), although this problem has not yet been fully resolved. A recently published study on the search for molecular states using the Antisymmetrized Molecular Dynamics (AMD) model [14] highlights the importance of studying cluster states and underscores the need to account for them when calculating interaction cross sections in stellar combustion reactions. Furthermore, the use of the clustering formalism within the potential model simplifies calculations by reducing the many-particle problem to a two-particle one. For this approach, several methods for describing the cluster-core interaction were considered, differing in how forbidden states are eliminated in the region of strong overlap between the cluster and the core. As a result, there is a need to determine the relationship between the optical potential and the two-particle interaction potential in the cluster model. Such studies were done in [101] and [102], with the latter employing a construction in the form of a sum of Woods–Saxon potentials (first power and cube) to accurately describe the position of the rotational doublet of the ground state for the nuclei $^{20}$Ne and $^{44}$Ti. Additionally, this

approach determined the intensities of the corresponding gamma transitions and angular distributions in the alpha particle energy range of 20–40 MeV. Remarkably, this was achieved using only one parameter, the depth of the imaginary potential (the Woods–Saxon surface potential for the $^{20}$Ne nucleus and the quadratic volume potential for $^{44}$Ti) and enabled the identification of several alpha particle resonances.

In this dissertation work, the focus was on the study of nuclear reactions involving light-mass ions: $^{12}$C + $^{16}$O. The relevance of this choice is supported by the results of studies [103], [10], which highlight the importance of considering cluster configurations when investigating interactions that play a significant role in the combustion processes during the final stages of the life cycles of heavy stars. It is also worth noting that the region on the Cluster Nucleosynthesis Diagram (CND) [96, 97] corresponding to this reaction is located near the center of the diagram. Additionally, the "asymmetry" between the cluster and the core should be taken into account, as it leads to the emergence of parity-split states. Despite the advantages of the $^{12}$C + $^{16}$O reaction, it remains relatively understudied compared to the $^{12}$C + $^{12}$C reaction.

The focus of this work was on the study of molecular states in the $^{12}$C + $^{16}$O system. For instance, in [104], the processes of radiative capture were discussed, which provide insights into the occurrence of resonances in reactions involving heavy ions. In another study [105], an optical potential derived from the analysis of $^{12}$C nuclei scattering on $^{16}$O nuclei at an energy of 75 MeV was used [106]. The study concluded that the resonances observed in this nuclear system can be described within the framework of quasi-bound states in such a potential. These resonances form rotational bands characterized by different global quantum numbers: $G = 2n + l$, where n is the number of nodes in the wave function of a given state, and $l$ is the angular momentum [74, 102].

In the study of the $^{12}$C + $^{16}$O reaction, this dissertation demonstrated the ambiguity in the choice of the global quantum number and highlighted the need to account for the contribution of partial waves to states with a pronounced resonance structure [107]. A two-particle complex potential was considered, which allows for the description of angular distributions across a wide energy range, including states that can

be attributed to rotational bands based on molecular configurations. In the system of interacting light-mass ions, states with different global quantum numbers were identified, and fragmentation of states was also observed. Consequently, for a broad region of excitation energies in the compound nucleus, the presence of a significant number of resonances is expected. Some of these resonances are formed in close proximity to the Gamow window for stellar burning reactions.

Currently, several methods exist for determining the angular momentum of specific resonances in reactions involving accelerated ions with masses up to $A < 30$. The most accurate approach for determining the spins of resonances that may correspond to molecular states involves comparing experimental angular distributions with Legendre polynomials. In this method, the region of the angular distribution at large angles where cross-section oscillations are clearly observed, is compared with functions of the form $A \cdot |P_l(\cos\theta)|^2$. The state is then assigned an angular momentum corresponding to the polynomial that provides the best match [107]. Within the optical model, it is possible to describe angular distributions for reactions involving light-mass ions using a selected potential at different energies. The results can then be compared in the angular range of 90°–180° with Legendre polynomials of various orders. Given that the differential scattering cross section exhibits a complex dependence on the angle, there are cases where the polynomial structure manifests as distinct maxima. These maxima can be compared with the maxima of the squared function $|P_l(\cos\theta)|^2$ (where $P_l(x)$ is the Legendre polynomial of degree $l$) for a fixed value of $l$ [107]. However, even in such cases, the structure cannot be fully described by a single polynomial of degree $l$. A special procedure was developed to estimate the contributions of individual Legendre polynomials. Using this procedure, the behavior of angular distributions and differential scattering cross sections for the studied reactions could be accurately described. The estimates were based on a comparison of the chi-square ($\chi^2$) values for polynomials of different orders with the model angular distribution derived from the optical potential [107]. A two-particle complex potential was taken, enabling the description of angular distributions across a wide energy range, including states that can be attributed to rotational bands based on so-called molecular configurations. When analyzing the data

obtained in [102] and [105] from nuclear reactions involving ions, processes of state fragmentation can be observed. Consequently, for nuclear systems in highly excited states, a large number of resonances may arise. Given that such studies allow for some flexibility in the choice of potential, it was proposed to use two potentials to analyze the angular distribution of elastic scattering in the $^{12}C + {}^{16}O$ system. The potentials from Okubo's work (WS1) [105], which were also used in [106] to describe the angular distribution of elastic scattering reactions, were considered. The parameters of the real part of the quadratic Woods–Saxon potentials (a special type of Woods–Saxon potential where the corresponding form factor is squared; see, for example, [101]) and the values of the volume integrals are presented in Table 2 [107]. However, that for the imaginary parts of these potentials, Woods–Saxon volume potentials were used. For the WS1 potential, the radius and diffuseness parameters were taken from [106], while for WS2, they were chosen as $R_w = 4.81$ fm and $a_w = 0.26$ fm. The depth of the imaginary part in both cases was determined based on the best agreement with experimental data [107]. Calculations within the optical model were performed using the FRESCO program [108]. The GAMOW program [109] was used to calculate the resonance positions.

Table 2 – Parameters of Woods–Saxon quadratic potentials (form factor in the form of the square of the Woods–Saxon potential) [107].

| Potential | Parameters | | | |
|---|---|---|---|---|
| | $V_0$, MeV | $R_v$, fm | $a_v$, fm | $J_v$, MeV · fm$^3$ |
| WS1 | 305 | 4 | 1,4 | 32 |
| WS2 | 320 | 4,184 | 1,3 | 378 |

A comparative analysis of the angular distributions obtained using the WS1 and WS2 potentials was carried out alongside the experimental data. The results are presented in Figure 26 (differential cross-section in mb/sr), which shows good agreement between the calculated angular distributions and the experimental data across the entire selected energy range for angles above 90°. It is noted that calculations within this potential model yield nearly identical dependencies of the energy levels on the

angular momentum. In this case, the value of the global quantum number for the WS2 potential increases by one, exceeding the values obtained from the phenomenological formula [110].

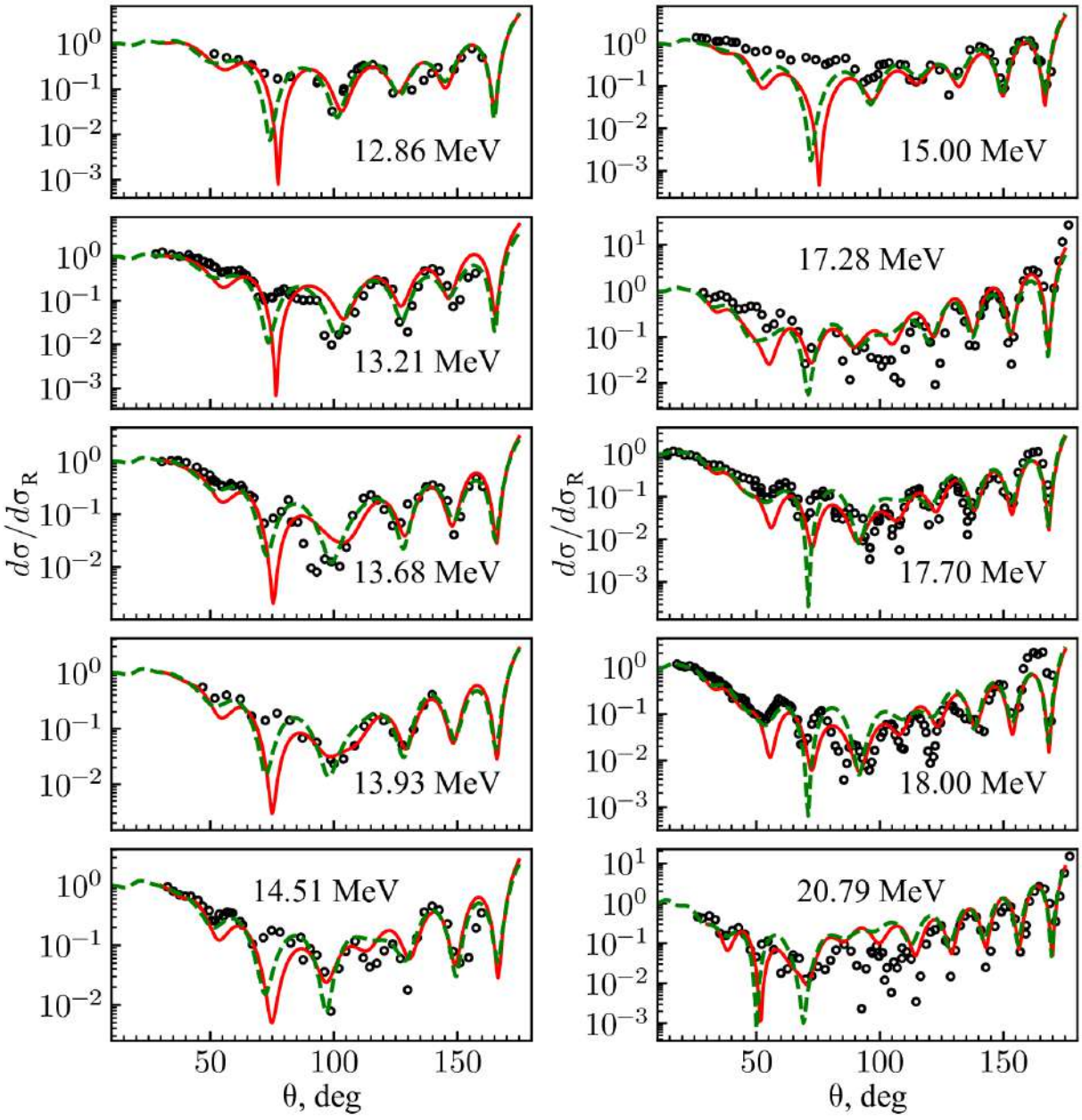


Figure 26 - Angular distributions (differential cross-section in mb/sr) of the elastic scattering reaction: $^{12}C + ^{16}O$. Black circles - experimental data (EXFOR nuclear reaction data base [45]); dashed green curve - calculation with the WS1 potential; solid red curve - calculation with the WS2 potential [107].

It can be observed that, across the entire considered energy range ($E_{cm}$ = 10–20 MeV), well-defined minima are present in the selected angular distributions. Figure 27 compares the positions of these minima with the resonance positions for even (odd) angular momenta, calculated using the potential model with G = 22 (23) for the WS1 potential and G = 24 (25) for the WS2 potential. For small values of angular momenta (l ≤ 10), the distributions are nearly identical. Additionally, Figure 27 illustrates the dependence for cluster rotational bands, based on the systematics reported in [88].

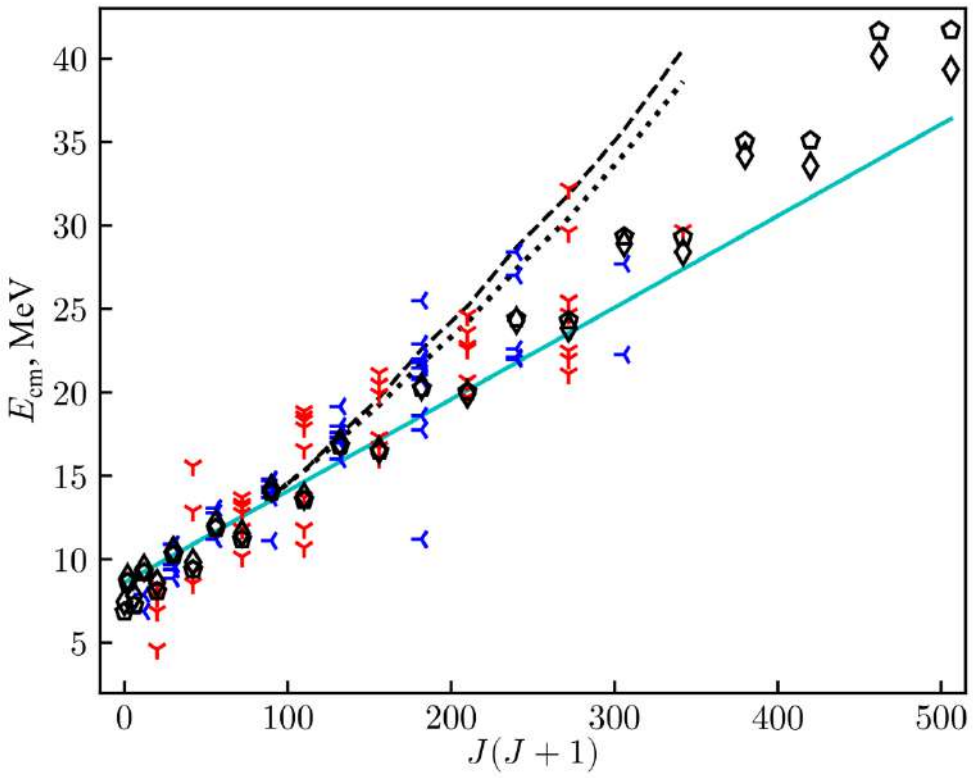


Figure 27 – Dependence of the energy of states in the reaction $^{12}C + ^{16}O$ in the center-of-mass system on the value of J(J+1). Experimental resonance values: red crosses – positive parity, blue crosses – negative parity. Solid line – systematics from Ref. [88]. Rhombuses and pentagons – resonances calculated within the potential model using the WS1 and WS2 potentials, respectively. Dashed lines and dots – positions of "false" minima for the WS1 and WS2 potentials [107].

The obtained results were analyzed from the perspective of unambiguously determining the angular momentum of the states by comparing the angular distributions with Legendre polynomials. The excitation function of the $^{12}C+^{16}O$ reaction was studied in detail in Refs. [111–113], where significant jumps in the cross sections were

observed at corresponding energies. Correlation studies indicate that only the state with an energy of approximately 19.7 MeV shows a deviation in the spectrum [114]. Based on a comparison with Legendre polynomials, the angular momentum $l$ = 14 was assigned to this state. Analysis of the corresponding angular distributions gave information that the excitation function contains a large number of resonances, which form rotational bands [115]. Therefore, using the comparison procedure with Legendre polynomials, the corresponding angular momenta were determined for a number of relatively narrow and less prominent states. Figure 27 presents the currently available data on resonances with known angular momenta in the $^{12}C + ^{16}O$ system. Most of these resonances (with the exception of a few low-lying ones) are clustered near a specific systematics, and several high-lying states can be identified. If these states are combined into a rotational band, they would exhibit a smaller moment of inertia than predicted by the potential model, even with an increase in the G number. The set of candidate levels for such states: $9^-$, 14,8, 14,4, 14,35 MeV [116, 117], $10^+$, 18,3, 18,55, 18,87 MeV [118, 119, 120], $11^-$, 17,29,17,98, 19,15 MeV [119, 120.], $12^+$, 19,9, 20,5, 21,4 MeV [112, 120, 121], $13^-$, 22,0, 22,9, 25,5 MeV [112, 122, 123], $14^+$, 22,79, 23,6, 24,6 MeV [111, 124], $15^-$, 25,5, 27,0, 28,4 MeV [111, 123, 124], $16^+$, 29,6, 32,2 MeV [113, 124] was proposed. All these states correspond to large cross sections observed in the excitation function of this reaction. The $11^-$, $14^+$, and higher angular momentum levels were investigated by analyzing angular distributions of elastic scattering at large angles. The $12^+$ level was analyzed using the angular distribution of the $^{12}C(^{16}O,^{8}Be)$ reaction, while the $9^-$ and $13^-$ levels were studied using reaction cross sections and elastic scattering data. The remaining levels were investigated through both elastic and inelastic scattering reactions, including the analysis of correlation polynomials from the decay of the compound nucleus. The main feature of these levels is that, compared to the predictions based on systematics and the potential model, they are located at higher energies.

In this dissertation, as part of the analysis of angular distributions (see Fig. 26), a comparison was made with Legendre polynomials of different orders. It was found that there is agreement both with the states discussed above and with lower-spin resonances.

When a fluctuation or resonance with a small angular momentum and reduced width coincides with a region exhibiting polynomial structure at large angles, an erroneous interpretation resembling the presence of a high-spin resonance may arise. Further detailed analysis using the procedure described in Ref. [107] revealed that, in the energy region corresponding to the minimum with $l$ = 14, an angular distribution (see Fig. 28) can be obtained for the scattering of $^{12}C$ + $^{16}O$ nuclei using the WS2 interaction potential, in comparison with the 14th-order Legendre polynomial. Figure 28 (differential cross-section in mb/sr) shows the results of optical model calculations for a full set of partial waves (black solid curve) and with the exclusion of the partial wave $l$ = 14 (green dashed curve), while the square of the 14th-order Legendre polynomial is represented by the red dotted curve. It is worth noting that although this model state coincides with the polynomial, it does not correspond to a resonance with an angular momentum of 14 and may not include a partial wave of this order (see Fig. 28). This highlights the need for a more careful approach in determining the positions and quantum characteristics of resonances in reactions involving light-mass interacting ions [107].

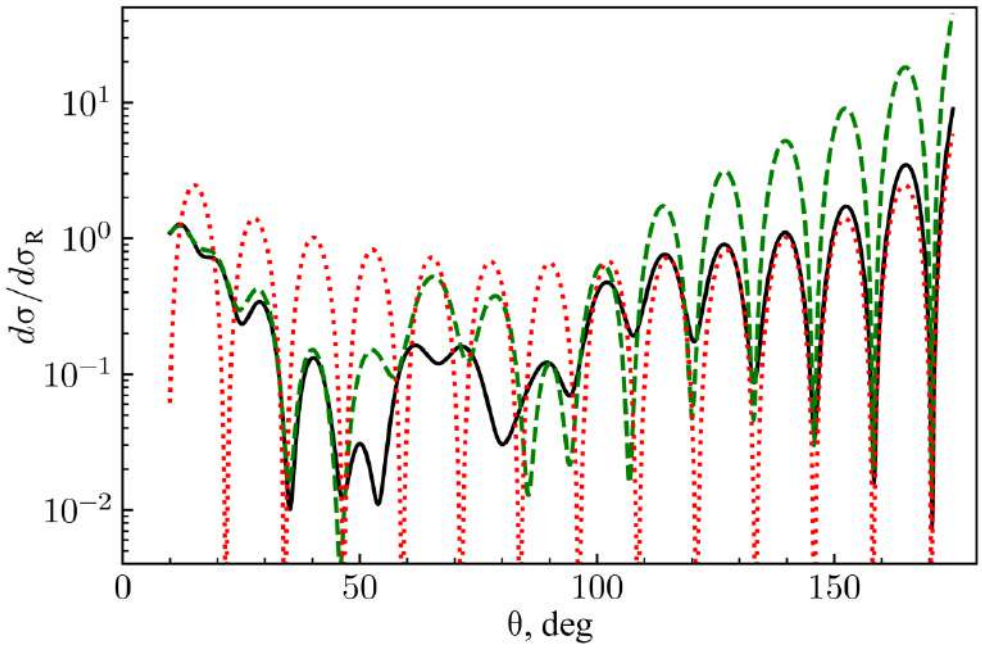


Figure 28 – Angular distribution (differential cross section in mb/sr) for the reaction: $^{12}C$ + $^{16}O$ compared to the 14th order Legendre polynomial: red dotted line – square of the 14th order Legendre polynomial; solid black line – calculations with the WS2 potential for the full set of partial waves; green dotted line – calculations with the partial wave $l$ = 14 excluded from consideration [107].

Thus, the analysis of the nuclear reaction $^{12}C + ^{16}O$ carried out in this dissertation showed that some states can be erroneously identified as resonances (“false resonances”) belonging to the rotational band.

## 1.4. Application of the found interaction potential to light nuclei fusion reactions and calculations of the astrophysical S-factor for the considered reactions.

The results of this dissertation, related to the analysis of various interaction potentials for describing nuclear reactions in the light mass range (see Section 1.3 above), can be successfully applied to the study of nuclear fusion processes. The investigation of nuclear fusion reactions at energies near the Coulomb barrier is particularly promising. These processes play a key role in stellar evolution and determine the scenarios for the formation of supernovae. Additionally, such reactions provide insights into the tunneling of multiparticle systems, a topic of significant importance in modern quantum mechanics [125]. Such studies require a more detailed analysis of experimental and theoretical data, and in some cases, they reveal new effects based on existing results. When investigating the evolutionary features of supernovae and the late stages of supermassive stars existence, it is essential to account for the processes of carbon and oxygen burning. This necessitates studying their fusion reactions at energies near the Gamow window. The success of experimental work on fusion reactions at low energies has enabled the determination of the astrophysical S-factor [4] (see the formula on page 97) for the nuclei $^{12}C$, $^{13}C$, and $^{16}O$. For instance, the $^{12}C + ^{16}O$ system is known for its numerous resonances, which are interpreted as members of rotational bands and are presumed to have a molecular nature. By applying the technique for eliminating "false resonances" (see Section 1.3) and the methodology from Ref. [107], it is possible to constrain the region of fragmented states. The processes leading to above- and below-threshold molecular resonances in the $^{28}Si$ nucleus at energies corresponding to the interaction of the $^{12}C + ^{16}O$ nuclear system near the Gamow window. This approach will allow for the study of the resonance-like

structure of the astrophysical S-factor. To address the issues highlighted in Ref. [126], which are associated with the application of the model that provides key insights into the features of the $^{12}C + ^{16}O$ nuclear reaction, the following conditions were selected for the corresponding interaction potential [127]:

1. The angular distribution is used for the elastic scattering of reaction products in the energy range corresponding to a low probability of alpha particle transfer through elastic processes.
2. Description within the potential model of the observed resonances belonging to the rotational band, which is located near the systematics from Ref. [88].
3. Agreement between the calculated fusion cross sections and the experimental values of the astrophysical S-factor at energies above 7.5 MeV.

In this case, the real part of the potential was chosen as the quadratic Woods–Saxon potential (with potential parameters taken from Ref. [106]), as described in Section 1.3. Based on the results obtained in Ref. [105], it is noted that this potential can describe a number of high-spin states within the formalism of the potential model. However, calculations using such a potential model require the introduction of a global quantum number, which cannot be determined for all potentials or all cluster-core combinations, particularly in cases where their masses are approximately equal. Therefore, in this dissertation, a potential with greater depth is employed (the parameters of the potentials used are provided in Table 2), and the depth of the imaginary potential was taken as a free parameter during the fitting of angular distributions. As a result, the potentials used (see Table 2) demonstrate good agreement with the experimental angular distributions in the energy range $E_{cm} = 10 - 30$ MeV, especially at large angles. Furthermore, when using the optical potential from Ref. [128], satisfactory agreement with the experimental data is also observed. This can be interpreted as evidence of the ambiguity in the choice of potential.

Let us now proceed to the practical results and turn to Figure 29 (a), which shows the energy dependence of the fusion reaction cross sections for $^{12}C + ^{16}O$ nuclei using the WS2 and WS1 potentials. This figure also includes experimental data for the corresponding reaction cross sections: $^{12}C + ^{16}O$ [129–132]. Theoretical calculations of

the cross sections were performed using the method proposed in Ref. [133], with the real potential taken from that work. The calculated data presented in Figure 29 (a) demonstrate that the application of the WS2 and WS1 potentials yields good agreement with the experimental results. This trend existed to the minimum values of the cross sections near the Gamow window. Note that similar results can be obtained for a wide class of potentials, including the deep double-folding potential [134] and the not so deep rectangular well potential [6]. However, in the low-energy region, the deep potential and the barrier penetration model [135] produce results that deviate from the experimentally obtained values of the astrophysical S-factor [136].

The obtained information can be applied to study the peculiarities of nuclear reactions in the context of astrophysical problems. Figure 29(b) shows the energy dependence of the astrophysical S-factor [4] for the studied reaction: $^{12}C + ^{16}O$.

$$S(E) = E \cdot \sigma(E) \cdot e^{2 \cdot \pi \cdot \eta} \quad (10)$$

where σ(E) – reaction cross section, η – Sommerfeld parameter, which is defined as: $\eta = \frac{Z_1 \cdot Z_2 \cdot e^2}{\hbar \cdot v}$, where $Z_1 \cdot Z_2 \cdot e^2$ – charge of the target ($Z_1$) and the beam ($Z_2$) and their relative speed. Thus, the exponential factor in Equation (10) characterizes the probability of particle penetration through the Coulomb barrier due to the tunneling effect.

The corresponding calculations of both the astrophysical S-factor and the reaction cross section were performed for the WS2 potential (solid red line in Figure 29) and the WS1 potential (dashed black line in Figure 29). These calculations demonstrate that both potentials provide a good description of the experimental results for the reaction cross section in this energy region, which is defined as:

$$\sigma(E) = \sigma_{res} + \sigma_{non} \quad (11)$$

where $\sigma_{res}$ – cross section of the resonance processes, $\sigma_{non}$ – cross section of the non-resonance interaction [133].

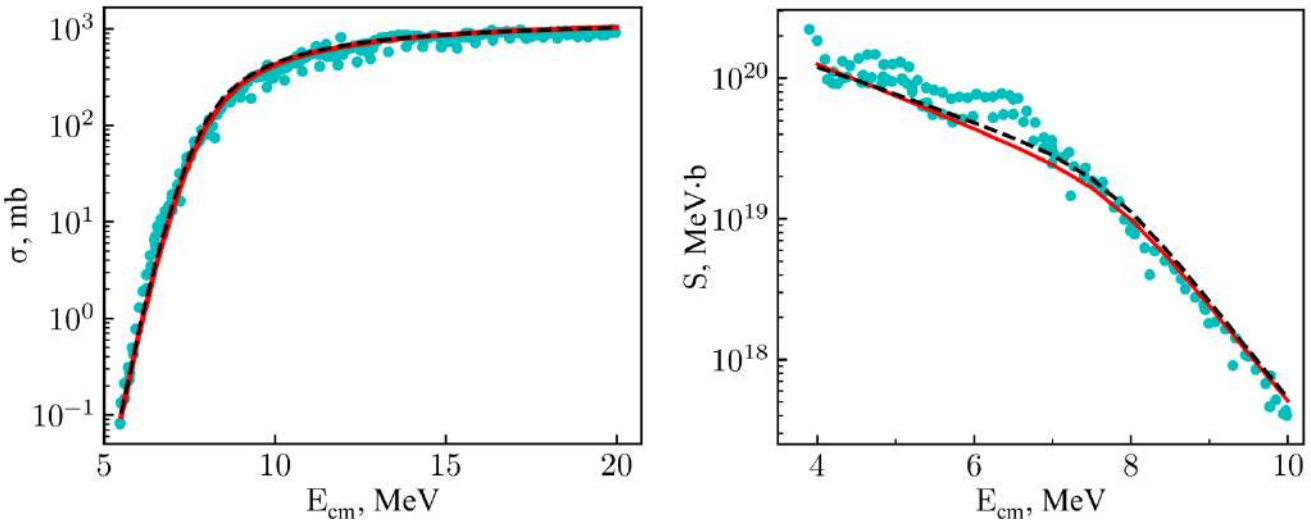


a) b)

Figure 29 – Modeling of the nuclear fusion reaction $^{12}C + ^{16}O$: (a) reaction excitation function. Dots represent experimental data. The red solid line corresponds to the calculated data for the WS2 potential, and the black dashed line corresponds to the calculated data for the WS1 potential; (b) dependence of the astrophysical S-factor on the reaction energy. The red solid line represents the calculated data for the WS2 potential, and the black dashed line represents the calculated data for the WS1 potential. The calculated and experimental data are taken from Ref. [127].

Note that when performing this type of modeling, a number of parameters should be taken into account, leading to complex calculations. The authors of Ref. [137] employed a method for analyzing the astrophysical S-factor based on an approach involving the use of a rectangular potential well. This model is commonly encountered in quantum mechanics problems; William Fowler utilized it in his pioneering works analyzing reactions in stars [6, 138]. The advantages of this model include a small number of parameters, simplicity of calculations, and minimized computational resource requirements [125]. The model has only three parameters: the interaction radius, the real part of the potential (which describes attraction or repulsion), and the imaginary part. Since Fowler's time and for several decades afterward, this simple model was forgotten due to a significant lack of experimental data. Scientists had access to very few analyzed nuclear reactions, and those available were at energies too high by stellar standards. However, this model was renewed several years ago, and its usefulness and convenience for nuclear astrophysics became evident. In Ref. [137], an analysis of

astrophysical important data known to date was done, and a systematics of parameters was established, enabling refined predictions for the astrophysical S-factor in the energy range relevant to stars. Finally, based on this parameter systematics, it was demonstrated that the primary contribution to the barrier at small distances comes from the Coulomb potential, while the contribution of the nuclear interaction is small and nearly constant across the entire considered range.

The fusion reactions at energies below the Coulomb barrier using the rectangular potential well formalism have been in more details analyzed. To describe the excitation functions in such reactions, either phenomenological models [139] or various versions of the potential model [136, 138] are typically used. The cross section for fusion reactions can be estimated by imposing a boundary condition on the wave function at a fixed radius where complete absorption occurs. Incorporating couple channels helps to extend the range of energies and masses for which these cross sections can be estimated [133]. A significant advantage of this approach is that the imaginary potential is eliminated, thereby reducing the number of model parameters [137]. Furthermore, the previously described uncertainties can be minimized by accounting for experimentally observed resonance states in the nuclear reactions under study [107]. Calculations involving potentials based on folding [140] and unified potentials [7] allow for a reduction in the number of parameters; however, this technique is not always suitable for the imaginary part of the potential. Therefore, using a simple version of the potential in the form of a rectangular well with a minimal number of parameters enables the inclusion of both the real and imaginary potentials, with the radii of the imaginary and real parts coinciding. As previously noted, the rectangular well model can be used to analyze fusion reactions that are of key importance in nuclear astrophysics [138]. The issues related to errors arising in the analysis of fusion reaction cross sections were considered separately, and conclusions were drawn regarding the suitability of using the rectangular well model [136]. Since this model assumes the presence of a nuclear core, the real part of the potential is chosen as positive [6]. However, it is noted that this behavior of the potential (a repulsive core) does not reflect its microscopic nature, such as accounting for the Pauli principle [136].

The presented dissertation work considers a problem that, within the framework of describing the subbarrier fusion of nuclei, provides information on the systematics of the parameters of the model with a rectangular potential. Previously, this approach was applied to individual nuclei, which did not allow for the determination of the dependence of the potential parameters on the charge and mass numbers of the nuclei participating in the reaction. Therefore, the fusion reactions between nuclei with zero spin, which play a key role in stellar nucleosynthesis processes at energies below the Coulomb barrier have been analyzed. The range of nuclei considered was chosen from A = 12 to A = 28 [137]. The theoretical formalism described in detail in Ref. [141] was used as the basis for the calculations, and a rectangular well of radius R with a complex potential V+iW (consisting of real and imaginary parts) was used. The penetrability coefficient for the partial wave $T_l$ is then expressed as:

$$T_l = \frac{4 \cdot P_l Im(f_l)}{[1 - S_l Re(f_l) + P_l Im(f_l)]^2 + [P_l Re(f_l) + S_l Im(f_l)]^2} \qquad (12),$$

where $f_l$ – complex logarithmic derivative of the wave function in the region of the potential well, and the functions: $P_l$ and $S_l$ are defined through regular and irregular Coulomb wave functions F and G:

$P_l = \frac{k \cdot R}{F_l^2 + G_l^2}$ and $S_l = k \cdot R \cdot \frac{F_l . F_l' + G_l . G_l'}{F_l^2 + G_l^2}$, where $k$ – wave vector modulus of the free particle: $k = \sqrt{\frac{2 \cdot \mu \cdot E}{\hbar^2}}$, and the modulus of the wave vector inside the well is defined as:

$$K = \sqrt{\frac{2 \cdot \mu \cdot (E - V + iW)}{\hbar^2}},$$

where μ – the reduced mass, E – the energy in the center-of-mass system, V – the real part of the potential, and W – the imaginary part of the potential. In Ref. [136], it was noted that the wave function is proportional to the expression: exp(−iKr). The validity

of this choice was confirmed by comparing this expression with the wave function obtained through numerical solution of the Schrödinger equation for the potential under consideration, which was described using splines [142]. Thus, the logarithmic derivative at the boundary of the potential can be expressed as: $f_l = \frac{i}{K \cdot R}$. To calculate the fusion reaction cross section one can use [136]:

$$\sigma_{fus}(E) = \frac{\pi}{k^2} \sum_l w_l \cdot (2 \cdot l + 1) \cdot T_l \qquad (13),$$

where factor $w_l = 1 + (-1)^l$ is used for the case of identical nuclei fusion [137]. Using Equations (10) and (15), the astrophysical S-factor was calculated. To compare theoretical results with experimental data, normalization was performed using $E/V_{coul}$, as energies below the Coulomb barrier are considered. In this case, the Coulomb barrier $V_{coul}$ was defined as:

$$V_{coul} = \frac{Z_t \cdot Z_b \cdot e^2}{1.36\left(A_t^{\frac{1}{3}} + A_b^{\frac{1}{3}}\right) + 0.5} \qquad (14)$$

where $A_t$, $A_b$, $Z_t$, $Z_b$ – mass and charge numbers of target and beam nuclei.

Next, the nuclear fusion processes was considered for various combinations of interacting nuclei: $^{12}C$, $^{16,18}O$, $^{20}Ne$, $^{24}Mg$, $^{28,30}Si$, with using of the experimental data [45]. To determine the potential parameters: R, V, W, calculations were carried out related to the minimization of the $\chi^2$ value (the discrepancy between the theoretically calculated values using Equation (10) and the experimental values of the astrophysical S-factor), with the energy range below the Coulomb barrier selected. The results are presented in Figure 30, which compares the theoretically calculated astrophysical S-factor with experimental data for a wide range of nuclear fusion reactions. Note that for all the specified nuclear systems within the studied range of masses and energies, a set of parameters: R, V, and W was determined, which allows for a good description of the dependence of the S-factor on energy. The observed minor deviations in the comparison results can be explained by the fact that, for such parameters, variations in their values

may lead to differences in the S-factor at lower energies, particularly for lighter nuclear systems.

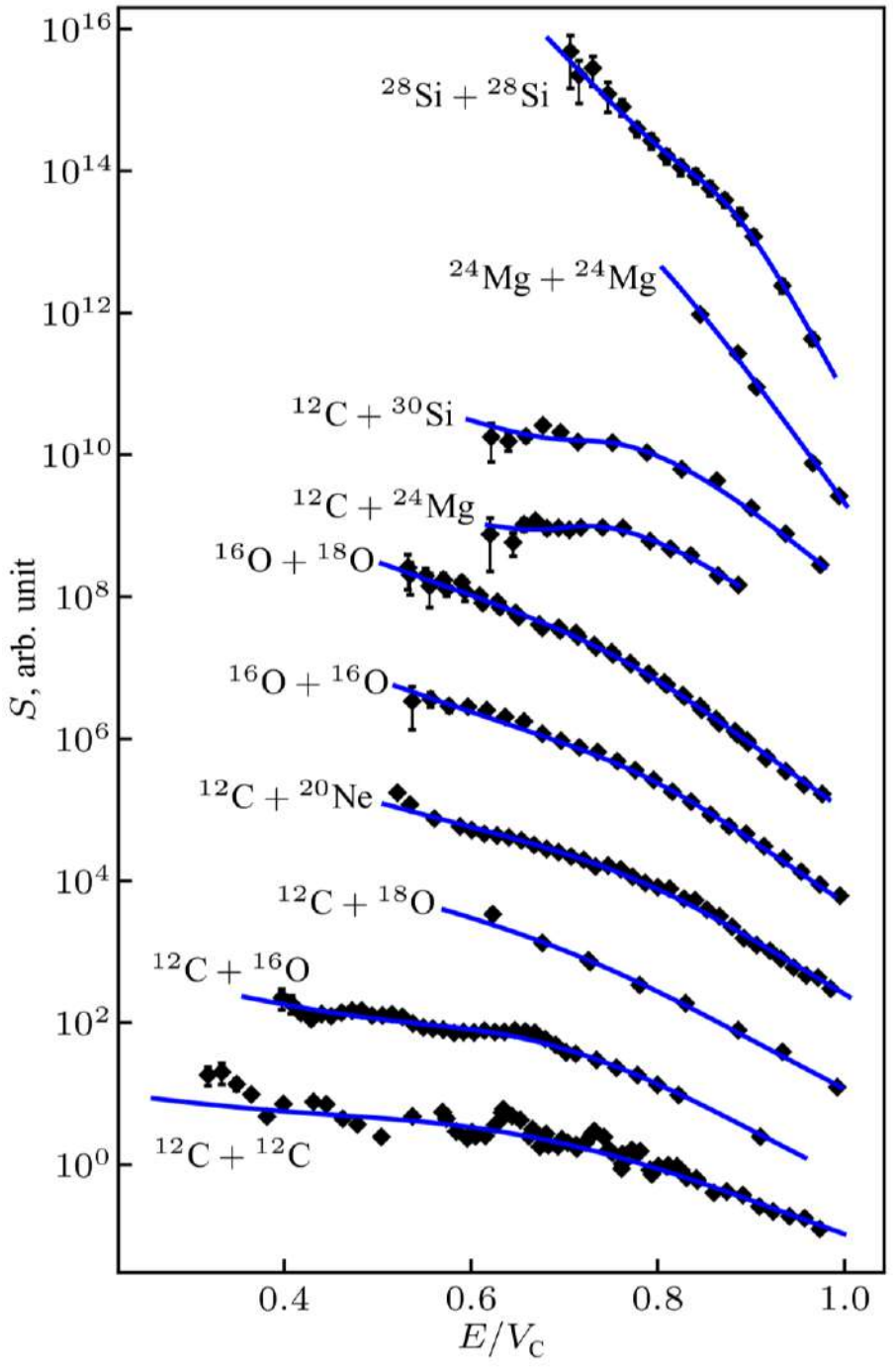


Figure 30 - Astrophysical S-factor as a function of energy normalized to the Coulomb barrier height. Shown are various combinations of interacting nuclei: $^{12}$C, $^{16,18}$O, $^{20}$Ne, $^{24}$Mg, $^{28,30}$Si, using experimental data (black diamonds) from Ref. [45]. Solid blue curves represent theoretical calculations from Ref. [137].

The formalism described above opens new ways for studying the phenomenon of fusion cross section suppression (fusion hindrance) in stellar nucleosynthesis reactions an effect observed at low energies compared to calculations based on optical potentials [11, 143, 144]. This suppression leads to a noticeable increase in the energy dependence of the astrophysical S-factor for some reactions involving light-mass ions, followed by a smooth decline in these values at low energies (see Figure 30).

For the modelling procedure using a rectangular potential well in the mass range of the considered nuclei, the aforementioned behavior of the S-factor cannot be accurately described. However, it is possible to describe the presence of a local maximum in the S-factor, provided that there is a local minimum in the low-energy region and a relatively smooth increase in the S-factor as the energy approaches zero. This feature (the presence of a local maximum) can be observed in the reactions $^{12}C$ + $^{30}Si$ and $^{12}C$ + $^{24}Mg$, as shown in Figure 30. The systematics of the obtained parameters was analyzed and presented in Figures 31, 32, and 33. For all the studied nuclear systems, an increase in the radius of the reaction interaction region is observed (Figure 31). In this case, this dependence on the value $A_M^{\frac{1}{3}} + A_\Pi^{\frac{1}{3}}$ (see formula 14) can be described by a linear function whose slope parameter is 1.35 ± 0.22 fm, and the offset parameter is equal to 0.92 ± 1.12 fm. This agrees well with the value of the Coulomb radius in such systems. The observed increase in the radius can also be explained by the presence of a potential jump [136], as identical radii for the real and imaginary parts of the potential can lead to enhanced absorption at large distances compared to the Woods-Saxon potential. Taking this interpretation into account, the variations in the values of the astrophysical S-factor for reactions involving light-mass nuclei within the studied range become clear.

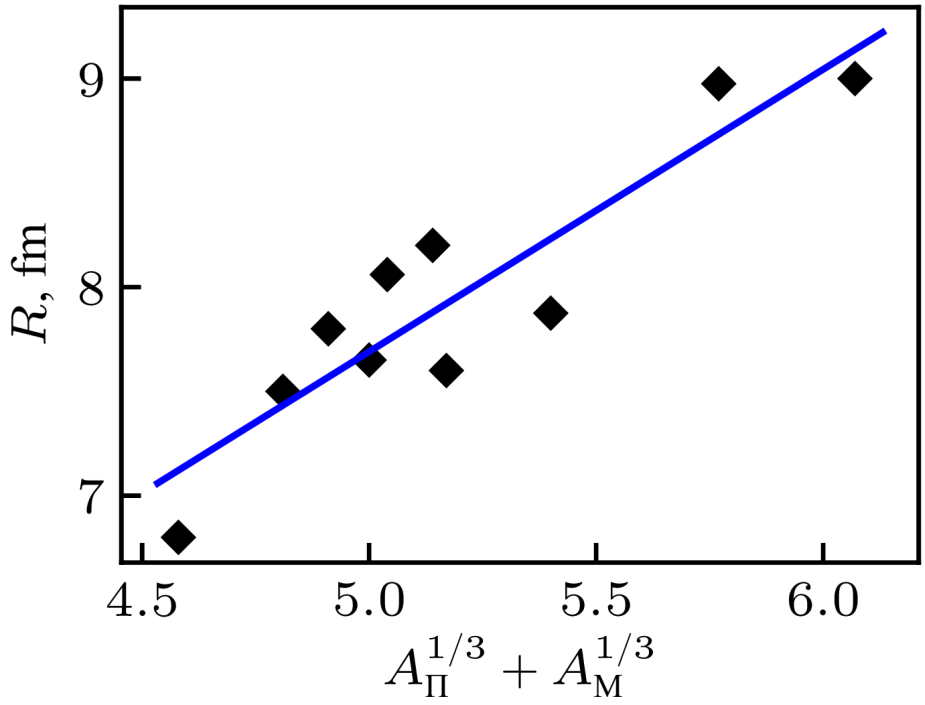


Figure 31 – Dependence of the radius R (entering the potential) on the values of the potential parameters: $A_M^{\frac{1}{3}} + A_{\Pi}^{\frac{1}{3}}$, dots – data from theoretical calculations [137], solid blue line – linear fit [137].

As for the potential real part, it is primarily determined by the Coulomb field and exhibits a linear dependence on the value: $\frac{Z_M \cdot Z_{\Pi}}{\left(A_M^{\frac{1}{3}} + A_{\Pi}^{\frac{1}{3}}\right)}$, as shown in Figure 32. This can lead to the existence of a repulsive core in the nuclear system. The parameters of the linear function that fit the dependence in Figure 32 are for the slope: 0.98 ± 0.02 MeV and for offset: –4.0 ± 0.3 MeV. The observed negative contribution is constant for all studied nuclear reactions from: $^{12}C+^{12}C$ to $^{28}Si+^{28}Si$ (see figure 30).

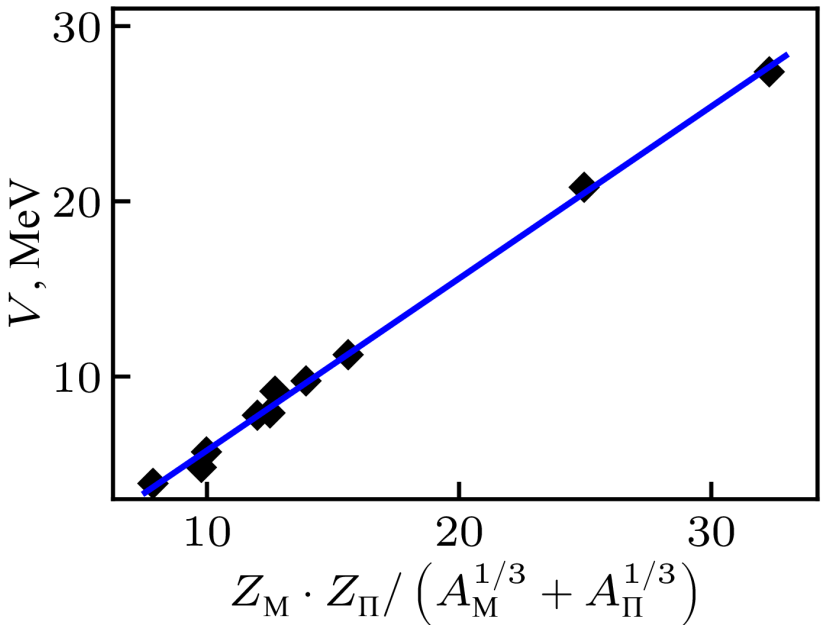


Figure 32 – Dependence of the real part of the potential V on the value of the potential parameter: $\frac{Z_{\text{М}} \cdot Z_{\text{П}}}{\left(A_{\text{М}}^{1/3} + A_{\text{П}}^{1/3}\right)}$, dots – data from theoretical calculations [137], solid blue line – linear fit [137].

The imaginary part of the potential, where its depth exhibits a wide range of values without any clear systematic dependence (see Figure 33) was also considered. Analysis of the data presented in Figure 33 reveals that for lighter nuclei, smaller values of the imaginary potential are observed, while for heavier nuclei, the potential increases proportionally to the mass of the compound nucleus: $A_{м}+A_{п}$. However, in several cases, good agreement with the S-factor values was achieved even with a reduced depth of the imaginary potential.

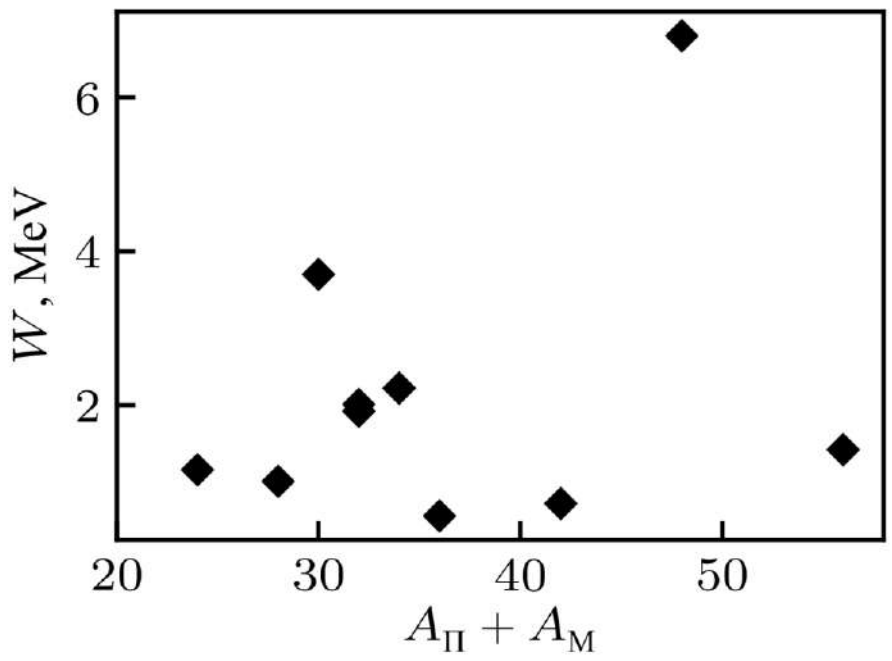


Figure 33 – Dependence of the imaginary part of the potential W on the mass of the compound nucleus: $A_п$+$A_м$ [137].

In summary, it can be noted that the described method, which uses the rectangular potential well model to determine the astrophysical S-factor for fusion reactions of light spinless nuclei (important for studying stellar processes), provides an excellent opportunity to compare the intensity of processes occurring in different interacting systems. The results of analytical studies shows that, for the available experimental data based on the S-factor, there is a spread of values spanning almost 40 orders of magnitude! By using a simple approach within the considered model, the spread of the normalized cross section is reduced to within one order of magnitude. These results are presented in Figure 34, where experimental values of the S-factors for various combinations of nuclei are shown, normalized to the values obtained using the proposed approach. The dependence is plotted against the energy of the nuclear systems under study, divided by the height of the Coulomb barrier. The region corresponding to the spread of theoretical predictions and the energy range relevant to reactions in stars are marked. Based on the analysis of the data presented in Figure 34, it is evident that there is good agreement between theoretical calculations and experimentally obtained values, corresponding to the quantities discussed in Ref. [125]. Thus, this approach not only

enables the prediction and determination of fusion cross sections at low energies but also provides a deeper understanding of the mechanisms underlying nuclear reactions involving light nuclei of astrophysical interest.

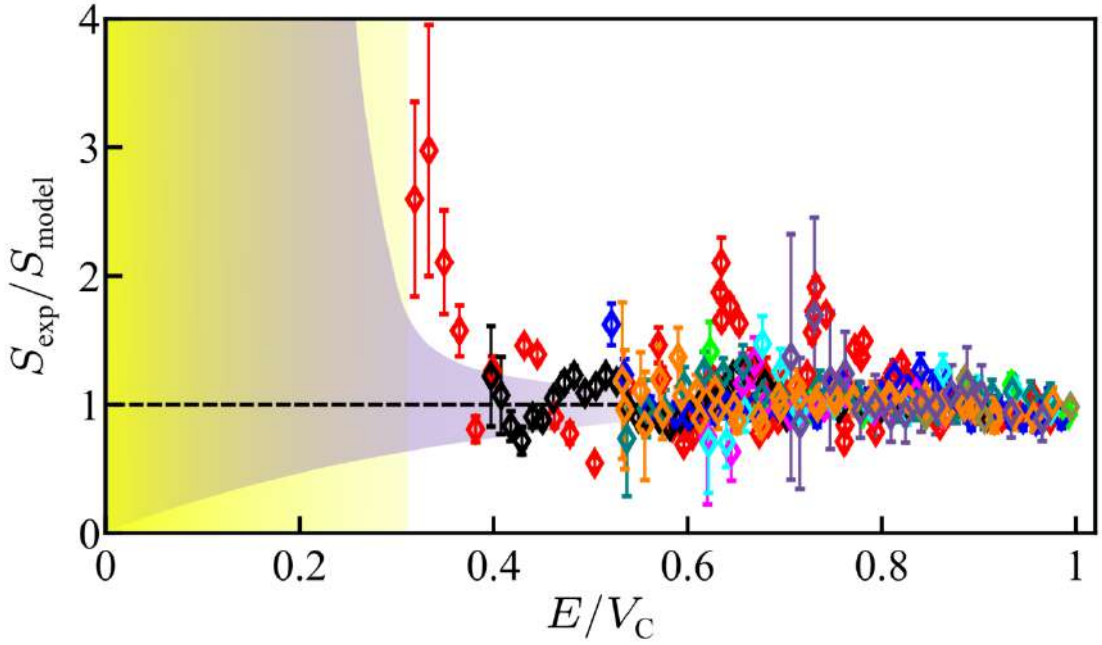


Figure 34 – Ratio of the S-factor obtained from experimental data to the S-factor calculated using the rectangular potential well model, plotted as a function of the energy of the nuclear systems under study divided by the height of the Coulomb barrier (colors correspond to different combinations of nuclei). The purple region represents the spread of theoretical predictions, while the yellow region corresponds to the conditions for reactions in stars [125].

## 2. Studies of nuclear reactions with formation and decay of medium mass range nucleonic systems

### 2.1 Theoretical studies of nuclear reaction excitation functions with the neutron emission in the final state, for the mass range from A = 40 to A = 239

In recent years, the amount of experimental data on nuclear reactions in the low- and intermediate-energy regions has grown significantly. This trend is evident from working with the EXFOR database, a widely used resource for experimental data on nuclear reactions in nuclear physics research centers [45]. The availability of such extensive data enables comprehensive and complex analyses using multivariate models. These analyses are essential because results from different studies on the same nuclear reaction or nuclear system often show poor agreement. A critical task in this context is identifying potential errors in the obtained data. However, it is sometimes impossible to conclusively determine the unreliability of these results based solely on the analyzed experimental studies. On the other hand, despite the large amount of experimental information available today, spanning a wide range of energies and masses of interacting nuclei, gaps remain in the nuclear data, particularly concerning the excitation functions of specific reactions. This situation is especially prevalent in reactions involving projectile particles with energies greater than 20 MeV in the entrance channel and the production of one or more neutrons in the exit channel [145]. Given the significant interest in such reactions, particularly in (p,n)-type reactions for the production of isotopes used in nuclear medicine [33, 41, 146], it is essential to estimate the yield of the corresponding radionuclides accurately. At the same time, to exclude erroneously obtained data or to identify anomalous regions within a large dataset for subsequent detailed study, it is necessary to develop a clear and straightforward analysis procedure with appropriate algorithms. These algorithms should incorporate nuclear-physical models and avoid relying on fitting experimental results to polynomials of specific orders. Currently, there are numerous systematics for (n,p) reactions, covering

both specific energies and functional dependencies. However, for (p,n) reactions, such systematics are scarce, despite the importance of these processes for solving various applied problems [146]. Therefore, it is crucial to carried on a phenomenological analysis of the data to obtain excitation functions for (p,n) reactions in the energy range from threshold energies up to 60 MeV, for the mass region $40 < A < 239$, involving the nuclei under consideration.

In the work [147], cross sections for the (p,n) reaction were obtained using a simple semi-empirical systematics for incident proton energies of 7.5 MeV, 12.4 MeV, and 24.8 MeV. For the first two energies: 7.5 MeV and 12.4 MeV a function was selected to which the equilibrium neutron emission formula was applicable. For the energy of 12.4 MeV, it was also assumed that the (p,2n) reaction channel would be open [147]. For the highest energy, 24.8 MeV, the cross section of the (p,n) reaction was determined using a formula based on pre-equilibrium emission processes [147]. As a result, it was concluded that in such (p,n) reactions, equilibrium processes predominantly prevail in the energy range up to 12 MeV. On the other hand, the energy of 12.4 MeV, in most cases, corresponds to the maximum of the excitation function for (p,n) reactions within the considered energy range. The use of this systematics demonstrated good agreement with the experimental results.

If the excitation functions (plotted on a logarithmic scale for both axes) for (p,n) reactions on target nuclei with mass numbers ranging from $A = 11$ to $A = 239$ and proton collision energies from 11 to 60 MeV are analised, using the method proposed in [148], two distinct linear regions can be identified. The first region of the excitation function, as described in [148], extends from 11 to 25 MeV and is denoted as PE1, while the second region, extending from 25 to 60 MeV, is denoted as PE2. Additionally, in [148], conclusions were drawn regarding the dominance of pre-equilibrium processes (processes that occur during the evolution of a composite system toward equilibrium) in these regions. Since pre-equilibrium processes are primarily described by the exciton model (which accounts for the entire relaxation process, including the formation and decay of the compound nucleus) [149], the observed behavior of the excitation function aligns with theoretical calculations based on this model [150]. A significant advantage

of this approach is its simple parameterization, which can be used to describe the data in the region of the excitation function slope. However, a disadvantage is that this technique alone cannot provide absolute values of the cross sections for the reactions under consideration. Therefore, it is necessary to establish a general systematics for the available experimental data to determine reaction cross sections across a wide range of energies and masses of interacting nuclei. To address this problem, the present dissertation divides the excitation function into three regions: 1) the region extending from the reaction threshold to incident proton energies of 11 MeV. This region is characterized by equilibrium processes typical of the formation and decay of compound nuclear systems. 2) The region corresponding to PE1 from [148]. 3) The region corresponding to PE2 from [148]. As noted earlier, the latter two regions are dominated by pre-equilibrium processes. The reaction cross section in the first region was calculated using the formula:

$$\sigma_{\text{рв}} = K \cdot \sigma \cdot \frac{\Gamma_n}{\sum_i \Gamma_i} \qquad (15),$$

where K – normalizing factor, σ – cross section of compound nucleus formation, $\Gamma_i$ – the decay width into the corresponding channel is considered; for example, when i = n, the decay into the exit channel with the emission of a neutron is taken into account [145]. Since the dissertation focuses on the study of channels involving the emission of a neutron and a proton, the proton width ($\Gamma_p$) and neutron width ($\Gamma_n$) are given by the following expressions:

$$\Gamma_p = \int_0^{\mathrm{E_c}-\mathrm{B}_p} \varepsilon \cdot P(\varepsilon) \cdot \rho(E) d\varepsilon \qquad (16),$$

$$\Gamma_n = \int_0^{\mathrm{E_c}-\mathrm{B}_n} \varepsilon \cdot \rho(E) d\varepsilon \qquad (17),$$

where $E_c$ – excitation energy of a compound nucleus, ε – energy of the emitted particle, $B_p$ and $B_n$ – binding energy of a proton and a neutron, respectively, P(ε) – Coulomb barrier penetrability coefficient, ρ(E) – residual nucleus level density. The penetrability coefficient is given by the expression proposed in [151]:

$$P(\varepsilon) = \begin{cases} 1 \; at \; \varepsilon \geq V_{coul} \\ \frac{\varepsilon}{V_{coul}} \; at \; \varepsilon < V_{coul} \end{cases} \quad (18),$$

where $V_{coul}$ – the height of the Coulomb barrier, which is determined by the expression:

$$V_{coul} = 1.03 \cdot \frac{Z-1}{A^{1/3}+1} \cdot \left(1 - \frac{1.13}{A^{1/3}}\right) \quad (19),$$

where A – mass number of target nuclei, Z – charge of target nuclei.

For the level density the following expression can be written:

$$\rho(E) = \frac{e^{E/T}}{T} \quad (20),$$

where T – nuclear temperature, which is determined using the expression: $E = a \cdot T^2 - T$, in which a – the level density parameter was chosen based on the Bardeen approximation [152] and was equal to: a = A/22. To calculate the cross section of the compound nucleus formation, the formula (13) was used, in which $T_l$ – the penetrability coefficient was selected using a systematics based on the use of the global optical potential [153]. The coefficient K in formula (20) was determined by fitting the experimental data and for energies above 7.5 MeV its value was determined as:

$$\begin{cases} K = K_1 + K_2 \cdot \varepsilon, \\ K_1 = 1.0 - K_2 \cdot 7.5, \\ K_2 = \frac{F-1}{3.5}, \\ F = \frac{1}{(0.0595 - 0.2218 \cdot \frac{A-2 \cdot Z}{A}) \cdot (1 + A^{1/3})^2}. \end{cases} \quad (26)$$

For energies below 7.5 MeV, the coefficient K in formula (20) was determined as:

$$\begin{cases} K = (K_1 + K_2 \cdot \varepsilon)^{1/3}, \\ K_1 = -K_2 \cdot Q_1, \\ K_2 = \frac{1}{7.5 - Q_1}, \\ Q_1 = Q \cdot (1 + \frac{1}{A}). \end{cases}$$

where Q was defined as the reaction energy [145].

The excitation functions for the PE1 and PE2 regions were chosen to be linear on logarithmic scales, similar to work [148]. Then, the obtained dependencies were normalized to the corresponding sections taken in work [147]. After this, all the regions under consideration were stitched together into a continuous excitation function. The result is shown in Figure 35, for the case of the excitation function of the reaction: $^{75}$As(p,n)$^{75}$Se, where the Y axis represents the corresponding reaction cross section, and the X axis represents the energy of the incident proton that triggers the reaction. These and the following examples of nuclear reactions were selected based on the potential use of the radionuclides produced in such reactions for diagnostic and therapeutic applications in nuclear medicine. In Figure 35, the equilibrium region is represented by a solid line, while the aforementioned regions of the excitation function PE1and PE2 from [148], are indicated by blue and green dotted lines, respectively.

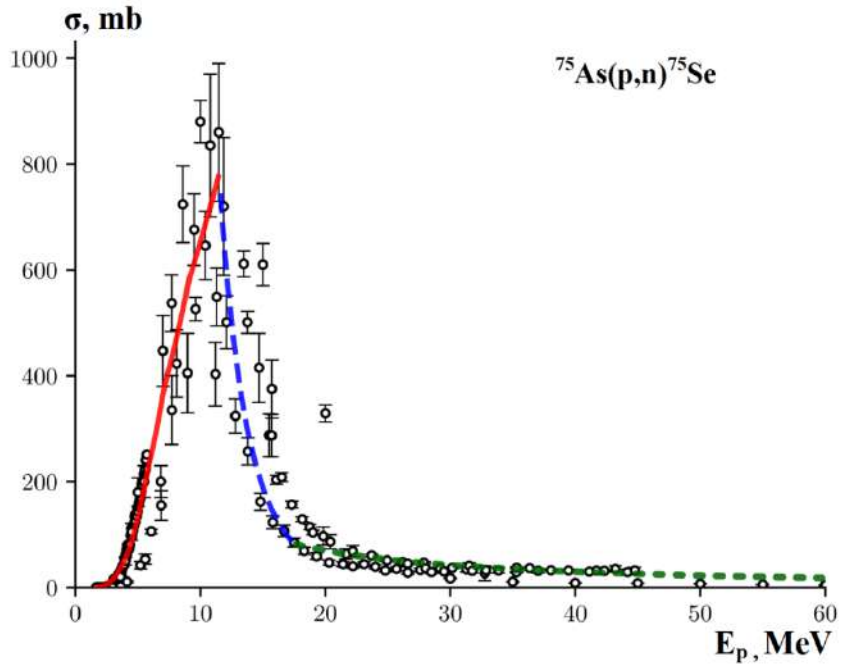


Figure 35 – Excitation function of the reaction $^{75}$As(p,n)$^{75}$Se [145], where the experimental results (EXFOR nuclear database [45]) are shown as circles. The solid red line is the equilibrium contribution, the blue dotted line is the first region PE1, and the green dotted line is the second region PE2. Regions PE1 and PE2 correspond to the selected ranges of the excitation function from [148].

An analysis of the results presented in Figure 35 demonstrates that optimal fitting parameters were selected for all sections of the excitation function under consideration (achieving optimal agreement with the experimental data for the lines corresponding to the calculated dependencies). This enabled us to draw specific conclusions regarding the mechanisms and nuclear processes involved in such reactions.

As a result, 120 excitation functions for nuclear reactions were analyzed within the specified energy and mass ranges. Figures 36–39 present examples of experimental excitation functions for nuclear reactions, compared with cross-section calculations performed using the developed systematics. The following nuclear reactions were considered: $^{51}V(p,n)^{51}Cr$ (see figure 36), $^{65}Cu(p,n)^{65}Zn$ (see figure 37), $^{117}Sn(p,n)^{117}Sb$ (see figure 38) and $^{197}Au(p,n)^{197}Hg$ (see figure 39). The analysis of these distributions demonstrates good agreement between the calculated results and the experimental data. A general conclusion can be drawn regarding the energy ranges in which the nuclear reactions under consideration occur. Specifically, for lighter nuclear systems in the medium mass group, equilibrium processes are realized within a specific (often narrow) energy range of incident protons that initiate a given reaction, followed by a sharp transition to reaction mechanisms dominated by pre-equilibrium processes. For heavier nuclei in the medium mass group, equilibrium processes span a broader energy range, and a smooth transition to pre-equilibrium processes is observed.

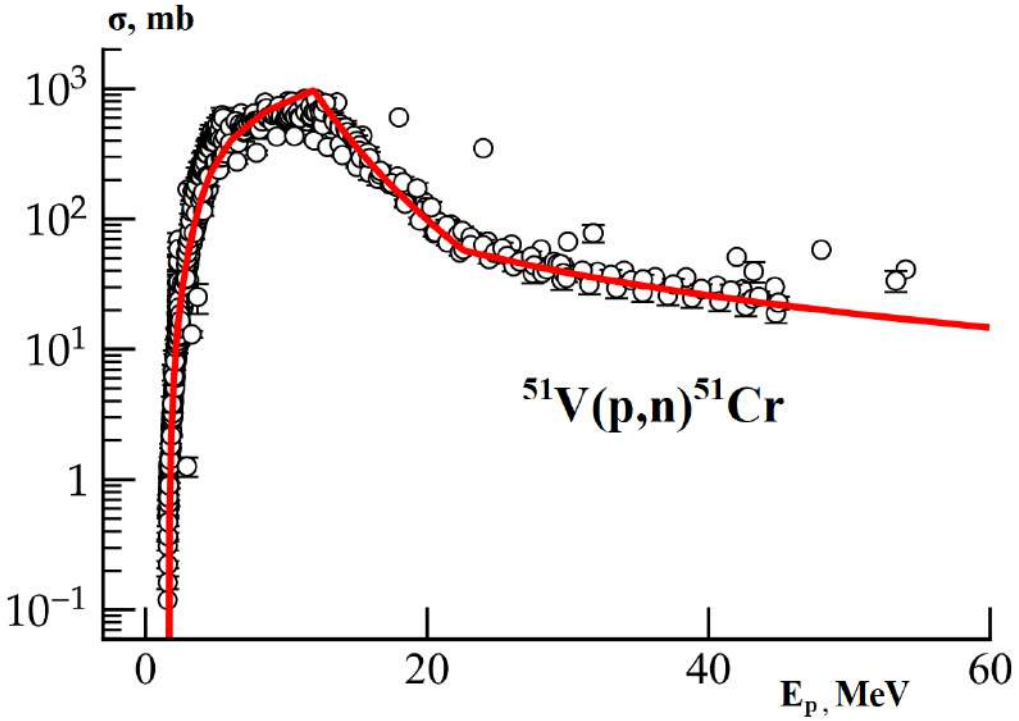


Figure 36 – Excitation function of the reaction $^{51}V(p,n)^{51}Cr$, where the experimental results (EXFOR database [45]) are shown by circles, and the solid red line shows the results obtained within the framework of the developed systematics [145].

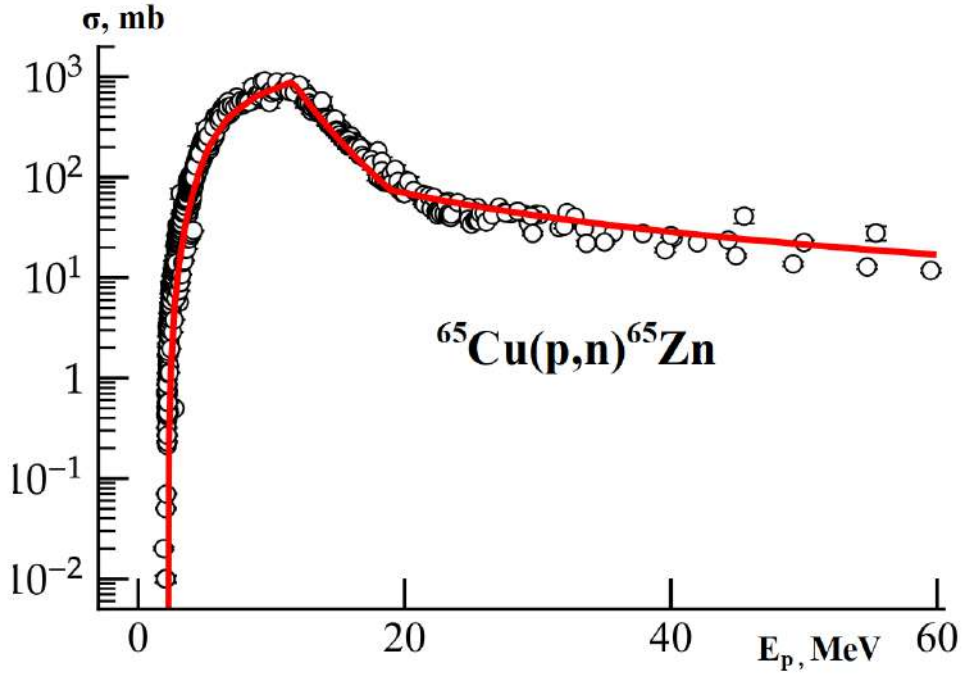


Figure 37 – Excitation function of the reaction $^{65}Cu(p,n)^{65}Zn$, where the experimental results (EXFOR database [45]) are shown by circles, and the solid red line shows the results obtained within the framework of the developed systematics [145].

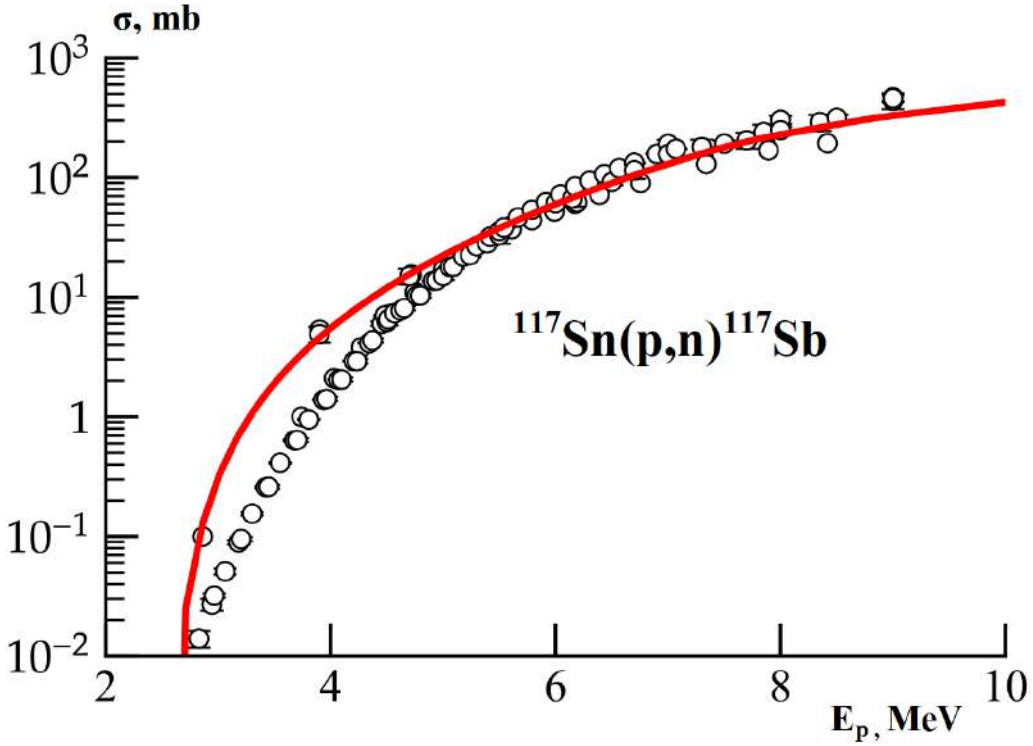


Figure 38 – Excitation function of the reaction $^{117}$Sn(p,n)$^{117}$Sb, where the experimental results (EXFOR database [45]) are shown by circles, and the solid red line shows the results obtained within the framework of the developed systematics [145].

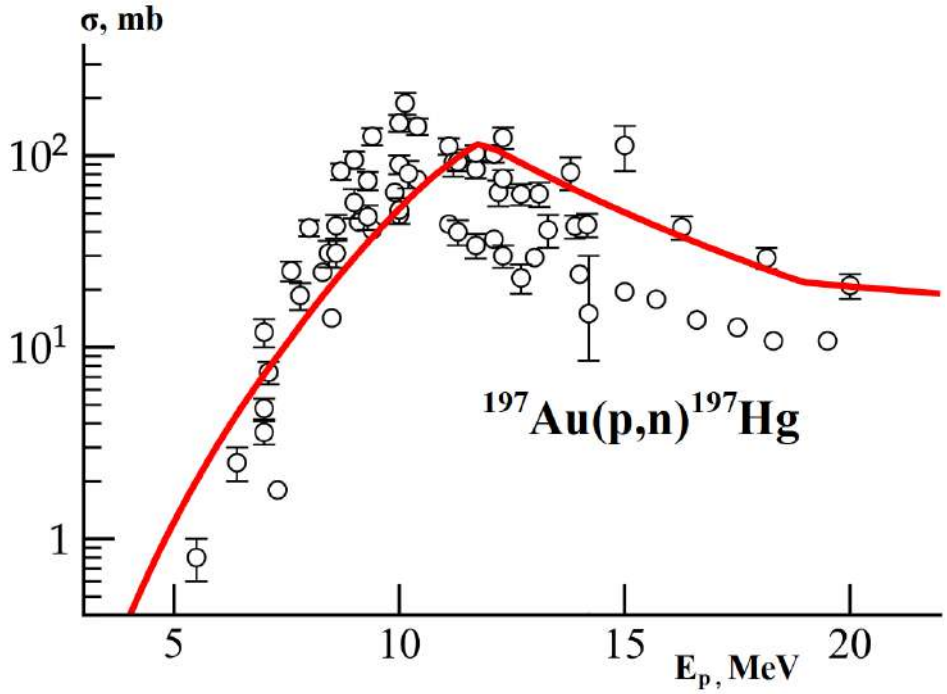


Figure 39 – Excitation function of the reaction $^{197}$Au(p,n)$^{197}$Hg, where the experimental results (EXFOR database [45]) are shown by circles, and the solid red line shows the results obtained within the framework of the developed systematics [145].

Next, for the energy range under consideration, we averaged the corresponding cross-sections obtained using the developed systematics and plotted a dependence of the ratio of these cross-sections ($\sigma_{syst}$) to the corresponding experimental values ($\sigma_{exp}$). Figure 40 illustrates this dependence for the equilibrium region, while Figures 41 – 42 present similar dependences for the PE1 and PE2 regions, respectively.

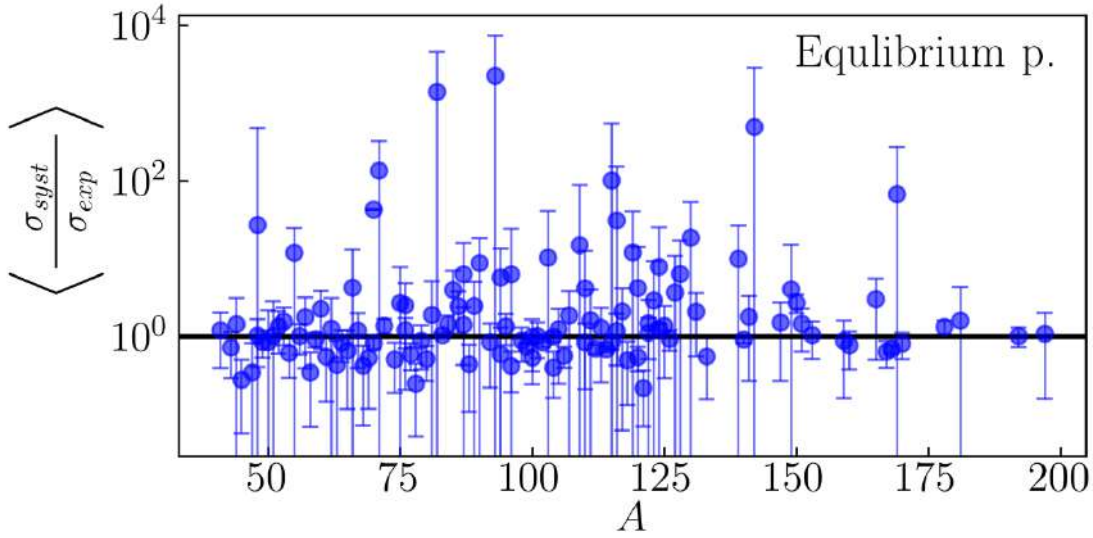


Figure 40 – Ratio of the averaged cross-sections obtained using the developed systematics to the experimental cross-sections for the equilibrium region [145].

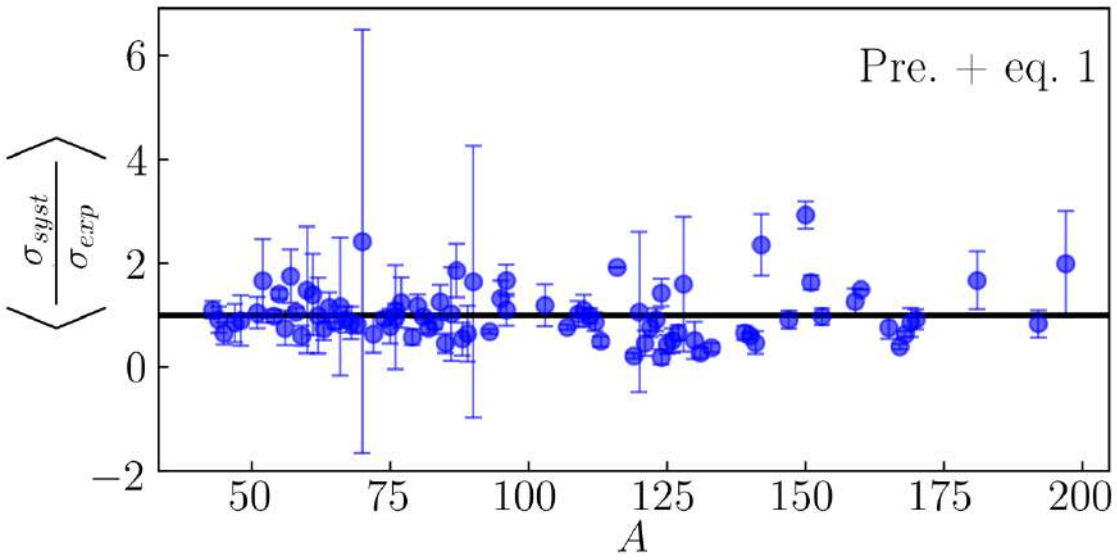


Figure 41 – Ratio of averaged cross-sections obtained within the framework of the developed systematics to experimental cross-sections for the PE1 region [145].

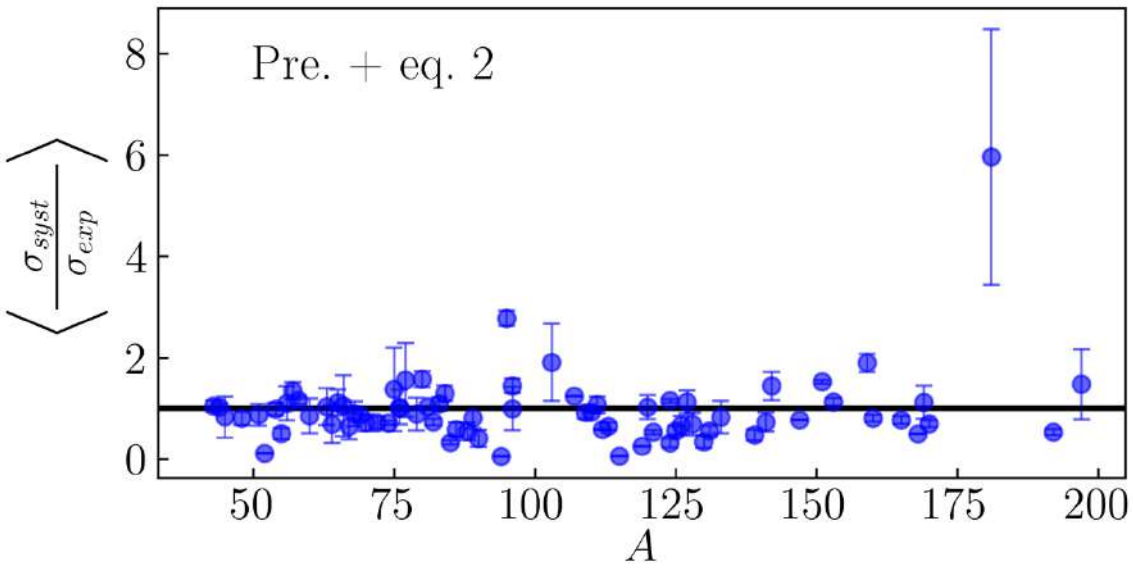


Figure 41 – Ratio of averaged cross-sections obtained within the framework of the developed systematics to experimental cross-sections for the PE2 region [145].

One can conclude that by analyzing the distributions presented in Figures 40 – 42, it is evident that the greatest deviations for the proposed systematics occur in the low-energy region (see Figure 40). This suggests the presence of potential errors and inaccuracies in the experimental data (including systematic errors within the experimental data uncertainties), as the cross-sections in this energy region have relatively small values. In several cases, discrepancies with the systematics are observed for the energy region below the Coulomb barrier. This is clearly illustrated by the example of the nuclear reaction: $^{117}$Sn(p,n)$^{117}$Sb (see figure 38). For some nuclear reactions, a systematic energy shift in the experimental data was observed in regions close to their threshold. This shift results in non-zero cross-section values appearing on the excitation function graph below the reaction threshold energy. Such anomalies indicate potential errors in the experimental studies, as well as inaccuracies in the procedure for processing the experimental results. On the other hand, the systematics demonstrates good agreement in regions associated with nuclear processes involving pre-equilibrium emission.

Further analysis of the obtained results enabled us to draw detailed conclusions. The first conclusion is that when using this systematics, errors may arise for the

normalization point at 12.4 MeV (as noted earlier, at 12.4 MeV, the (p,2n) reaction channel may open, and for several reactions, this energy corresponds to the maximum of the excitation function [147]). This is because the 12.4 MeV value may lie either to the right or to the left of the region where the excitation function reaches its maximum (see, for example, Figure 37 or Figure 39). For nuclear reactions with a high energy threshold leading to the formation of two neutrons in the exit channels, this can result in a loss of accuracy when describing the excitation function of such (p,2n) reactions. Therefore, when using the systematics, it is preferable to take cross-section values with energies ≥ 15 MeV.

The second conclusion is that the energy range for the PE1 region decreases when compared with the similar range from [148]. The presented analysis shows that this range corresponds to the energy range from 13 MeV to 20 MeV.

The third conclusion is that there are a number of nuclear reactions that show large deviations in cross-sections within the framework of this systematics. These deviations can be divided into two groups:

1) The deviation arises because the maximum of the excitation function lies at energies > 12 MeV, resulting in a smaller cross-section value in the PE1 region. This energy value was chosen based on the requirement to establish a boundary for the transition from one dependence to another (see [147]) and, consequently, for the normalization procedure. The transition boundary was carefully selected to ensure compatibility with the largest possible number of experimental datasets. Examples of such deviations include nuclear reactions involving the following target nuclei: $^{70,73}$Ge, $^{76}$Se, $^{86}$Sr.

2) The deviations arise when describing the equilibrium spectrum (typical for the region near the maximum of the excitation function). Such results can be explained by specific features in the behavior of the level density function. Examples of these deviations include nuclear reactions where the targets are the following nuclei: $^{87}$Sr, $^{87}$Rb, $^{119}$Sb. In this case, in the pre-equilibrium region for the PE1 region, deviations occur only for nuclei: $^{117,119,124}$Sn, $^{131}$Xe, $^{133}$Cs, $^{150}$Nd, $^{167}$Er. For the PE2 region, a

similar situation is observed for nuclei: $^{52}$Cr, $^{85}$Rb, $^{94}$Zr, $^{95}$Mo, $^{115}$In, $^{181}$Ta, and also for tin isotopes: $^{117,119,124}$Sn [145].

This approach can be used to estimate the yields of radionuclides produced in reactions with different targets, as the systematics developed in this dissertation provides a reliable description of the (p,n) reaction cross-section dependence on the incident proton energy. At the same time, the observed discrepancies between the systematics and experimental data for certain nuclear reactions involving specific target isotopes highlight the need for additional experimental studies of such reactions.

Given the importance of the nuclear processes involved in the production of radionuclides used in modern nuclear medicine (e.g., antimony isotopes $^{117}$Sb and $^{119}$Sb), and the fact that cross-sections for these nuclear reactions in worldwide databases are often inconsistent, it is clear that there is an urgent need for further experimental studies of the excitation functions of such reactions. This has been done in the present dissertation through detailed investigations of reactions with tin isotopes as targets (see Sections 2.3–2.5), including a thorough analysis of the maximum region of the corresponding excitation functions.

## 2.2 Studies of nuclear reactions with medium mass group nucleonic systems for production of radionuclides used in nuclear medicine

Currently, several radionuclides used in nuclear medicine are produced using nuclear reactors. A prominent example is the reactor-based production of the $^{99}$Mo/$^{99m}$Tc generator system. The parent radionuclide, $^{99}$Mo, can be produced through fission reactions using either highly enriched uranium targets or low-enriched uranium targets (which are easy to manufacture and cost-effective). Alternatively, $^{99}$Mo can also be produced via neutron capture reactions using molybdenum targets, such as highly enriched $^{98}$Mo or natural molybdenum [154]. The reactor method offers the advantage of high radionuclide yields (i.e., the activity of radionuclides formed during target irradiation) and low production costs. This is due to both the mass of the irradiated targets (as it is possible to load relatively large targets containing a significant amount of the irradiated material into the reactor) and the availability of reactors with high neutron flux densities. However, the disadvantages include the limited number of possible nuclear reactions that lead to the formation of neutron-excess radioactive nuclei. Additionally, with the production of purpose-oriented radionuclides, other nuclear reactions occur in the irradiated target, resulting in the formation of radioactive impurities with relatively long half-lives. This drawback can be mitigated by using isotopically enriched targets, but challenges in target fabrication arise, increasing the cost of producing the target radionuclide [33]. The disadvantages of the reactor method include complex radiochemical processing and the generation of significant amounts of radioactive waste [154]. As an alternative, particle accelerators are widely used in global practice for radionuclide production. Note that nearly all short-lived and ultra-short-lived radionuclides used in cancer diagnostics are produced in cyclotrons, primarily through (p,n) reactions, within the proton energy range of 10 to 30 MeV. Nuclear reactions involving deuterons (e.g., (d,n + X)) and alpha particles (e.g., (α,n + X)) are used for this purpose far less frequently. The primary advantages of the accelerator method for producing radionuclides include the ability to initiate a wide range of reactions, resulting in radioactive elements with various types of radiation

suitable for diagnostic studies and radionuclide therapy. Additionally, particle accelerators can produce carrier-free radioactive elements, meaning they are free from stable isotopes of the same element. To produce radioactive isotopes, the optimal nuclear reaction and accelerator beam energy are selected based on the criterion of minimizing the formation of long-lived radioactive impurities. As a result, the target radionuclide extraction process and purifying it from impurities becomes less labor-intensive, and the challenges associated with radioactive waste disposal are significantly reduced. However, the accelerator method also has disadvantages, including lower radioactive elements yield from the target, compared to the reactor method, and difficulties in producing highly enriched targets.

When selecting radionuclides for use in nuclear medicine, the following factors are considered: demand for a specific radiopharmaceutical by the medical community or significant potential interest in it; high yield of the target radionuclide and the ability to produce it in large quantities with minimal long-lived radioactive impurities, at a relatively low cost. This criterion necessitates a detailed study of the excitation functions of the corresponding nuclear reactions, as well as the selection of optimal beam parameters and irradiation schemes for various targets. Special requirements are imposed on the targets: a) the target material and its container must remain intact under the conditions of nuclear reactions; b) flammable substances must not be used; c) no chemical reactions should occur within the target; d) the target must be isotopically pure or contain only minimal impurities; e) the target material must allow for the efficient extraction of the produced radionuclides using radiochemical methods; f) the material should be commercially available and relatively inexpensive [33, 34]. In the production of targets, materials in the form of foils or films are often used. These are arranged on a suitable substrate and placed in specially cooled containers. The primary methods for reducing the production of impurity radionuclides in targets include optimizing irradiation parameters and employing effective radiochemical treatment and purification techniques. Analysis of the processes and nuclear reactions occurring in the target has identified several limitations to their effective implementation: a) significant heating of the target; b) degradation of the target substrate when thin foils are used; c) loss of the

target's starting material and deterioration of its quality during the subsequent extraction of produced isotopes; d) big labor input in target-related operations [34]. To address these challenges, a specialized target complex was used. This system provided conditions not only for the production of certain radionuclides, but also represented an experimental setup for studying nuclear reactions in a wide range of charged particle beam energies and a large set of solid targets.

### 2.2.1 Experimental setup for investigations of the nuclear reactions

To provide fundamental studies of nuclear reactions and address challenges related to radionuclide production, an experimental facility was employed. This facility included a modernized target complex and a semiconductor gamma spectrometer for measuring the activity of the produced radionuclides. The target complex was developed through close collaboration among the Prometey Central Scientific Research Institute Of Structural Materials (with V.V. Darmograi as the lead designer), the Institute of Analytical Instrumentation of the Russian Academy of Sciences, and St. Petersburg State University. This target complex is capable of operating with high-intensity beams of protons, deuterons, and alpha particles in the energy range from a few MeV to several hundred MeV, enabling the irradiation of a wide variety of solid-state targets. The modernization of the target complex, carried out as part of this thesis, incorporated the positive experience gained from experiments with multicomponent, multilayer, and thick targets (including gas targets), as well as advancements in gas and liquid cooling systems and the use of advanced carbon composite structures [24, 25, 26, 27, 28, 29]. Experiments to study nuclear reactions with nucleon systems of the medium mass group for the production of radionuclides used in nuclear medicine which will be described in detail later in this dissertation, were carried out using proton beams from the MGC-20 cyclotron at Radium Institute named after V.G. Khlopin (ROSATOM) and the MGC-20 cyclotron at the Scientific and Technical Centre "Nuclear Physics" of SPbPU.

The target complex consists of eight main components and a number of auxiliary devices. Figure 43 illustrates the key elements of this complex, whose primary advantage is the efficient removal of significant thermal power density generated during the target's interaction with high-intensity charged particle beams. This capability is critical for studying nuclear reactions in charged particle accelerators.

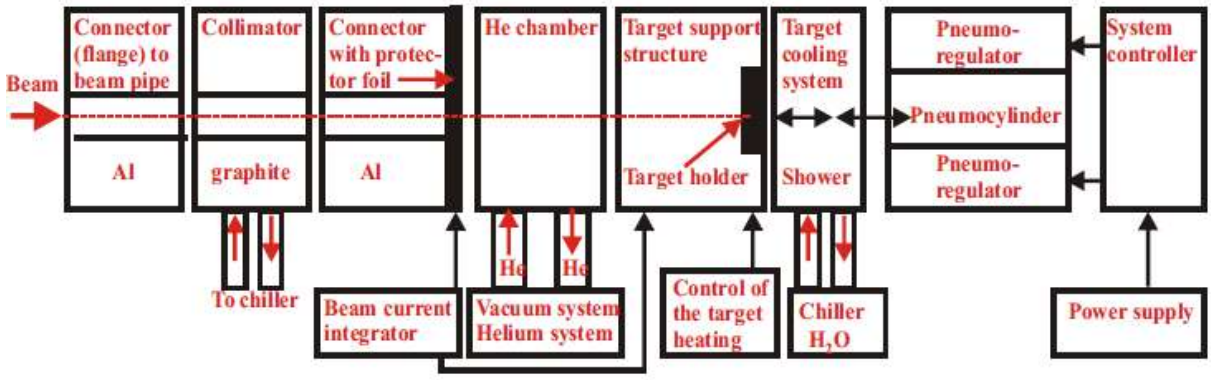


Figure 43 – Diagram of the target complex.

The complex consists of the following components: a docking module for attaching the target device to the accelerator beam pipe; a graphite collimator with an internal channel diameter of 12 mm, water-cooled along the external circuit; a module equipped with a protective metal foil, electrically isolated from the ion guide (see Figure 43). This foil serves as a barrier between the high-vacuum volume of the beam pipe and the target complex, within which helium circulates to cool the front part of the targets (see description below). Experience with thick gas targets at varying pressures has demonstrated that, depending on experimental conditions, foils of different thicknesses and materials can be used, such as titanium foils or foils made of Kapton or Khavar alloy [25]. In this dissertation, aluminum foil with a thickness of 30 μm was used for precision measurements of cross-sections in the region of the nuclear reactions excitation function maximum, minimizing the energy losses of the proton beam. Corresponding calculations were performed, showing that the energy loss of protons for the maximum energy of the MGC-20 cyclotron (Radium Institute named after V.G. Khlopin), 14 MeV, is only 200 keV [34]. The module with the protective foil is

connected to the helium chamber (see Figure 43). The helium chamber, a short cylinder with external size of 50 mm in diameter and 14.8 mm in height, is designed to be filled with helium for cooling the front part of the target. Before introducing helium, in the chamber vacuum is created. Jet cooling (a semi-restricted wall jet) of the front part of the target was implemented in the helium chamber. Helium is supplied to the target surface through a channel with a cross-section shaped like a flat nozzle. The nozzle is inclined at an angle of 27° relative to the target plane, and the angle of incidence of the jet increases to 31° after exiting the nozzle. Flowing along the target surface, helium is removed through a symmetrically positioned channel. The calculations of the cooling conditions for thin aluminum, copper, and steel foils under proton beam irradiation (up to 14 MeV and 20 μA current), with helium pressure in the chamber ranging from 1 to 1.5 atm and cooling of the rear part of the target holder module, showed that the temperature on the target surface does not exceed 60 °C. After passing through the chamber, the helium is heated from 19 °C to 27 °C. To re-cool the helium, a heat exchanger can be used. In this system, the gas flows inside a stainless steel tube (10 mm in diameter) and is cooled either by a counter-current stream of water (at a flow rate of 0.4 m/s and a temperature of +10 °C), by an air flow (at a speed of > 5 m/s), or by exposure to cold nitrogen vapor at a minimal flow rate.

A cooling system was also implemented for the graphite collimator, which is constructed from carbon composite materials. These materials have been successfully used in high-energy physics experiments as support and cooling structures for novel silicon systems [26, 27]. The use of a carbon composite frame for the graphite collimator, integrated with a cooling system, enabled a uniform temperature distribution across the collimator and increased heat removal from cooled surfaces by nearly 4.2 times. Another advantage of this cooling system is its ability to provide additional heat removal from the thin aluminum foil of the corresponding module. The design's key benefit lies in the use of carbon composite materials, which ensure both the necessary rigidity and thermomechanical stability of the entire cooled system, as well as efficient heat removal [28, 29].

The target holder module is connected to a current integrator to measure the beam current directly on the target. The ORTEC 439 Digital Current Integrator is used for this purpose, with its data transmitted to a CAEN Four-Fold Programmable Logic Unit module, which serves as a scaling device connected to a personal computer. This setup allows for remote, on-line monitoring and detecting of the proton beam current. The target holder module functions as a movable base into which the target holder is inserted. Prior to irradiation, the module with the target holder is hermetically sealed to the helium chamber using pneumatic cylinders. The target holder consists of a tantalum substrate shaped as a disk with a diameter of 22 mm. Tantalum has proven effective as a substrate in numerous similar experiments and is also successfully utilized with multilayer targets (see, for example, [24]). At the center of the tantalum substrate disk, there is a 1.6 mm deep recess with a diameter of 12 mm and a bottom thickness of 400 μm. Various solid targets, as well as foils for monitoring beam parameters, are encapsulated within this recess. The design of the target holder is illustrated in Figure 44, which depicts a tantalum substrate with inserted targets, secured along the diameter by a thin aluminum clamping ring. The substrate is elevated above the corresponding module of the target holder within the target complex. The entire complex is mounted on the beam pipe of the MGC-20 cyclotron at the Scientific and Technical Centre "Nuclear Physics" of SPbPU.

Figure 44 – The target holder is shown together with the target complex.

Target Cooling System consists of two modules. The first module is designed to cool the rear surface of the tantalum substrate of the target holder. It includes seven small-diameter holes, implementing a "shower" cooling scheme. Engineering analysis of various target cooling schemes demonstrated significant advantages of this approach compared to single-jet cooling systems. Preliminary calculations indicate that the thermal power removed from the target surface can reach up to 600 W/cm². The second module of the cooling system is responsible for supplying and distributing the coolant. Since the primary function of the cooling system is to remove heat generated by intense beams of charged particles in the target, an analysis of various cooling options was performed to determine the optimal system parameters. As a result, a coolant consisting of an alcohol-containing liquid (64% alcohol + distilled water) was selected instead of water. This allowed for testing at reduced coolant temperatures (down to +4 °C). Additionally, the use of a specialized recirculation system significantly increased the flow rate of the liquid through the nozzles.

Pneumatic cylinders with a system of pneumatic regulators are used to connect the first module of the cooling system to the target holder module. A target heating

control system was developed and implemented. This system includes thermocouple sensors (copper-constantan) with a reduced junction diameter and a circuit for compensating noise and electrical interference. One sensor was mounted in the end section of the tantalum substrate of the target holder, with additional thermal contact achieved using thermal paste. Other sensors were mounted on the pipes of the first module of the cooling system to monitor the coolant temperature. The sensors are connected to a corresponding data acquisition system (for further details, see [26]). Thus, during irradiation, the target heating temperature was on-line monitored. The system controller was used to distribute and control the power supply to the pneumatic regulators and monitor a number of electrical parameters of individual modules [41].

The entire target complex is capable of removing thermal power from a target of up to 600 W/cm$^2$, while existing world analogues [155] can operate at thermal power of up to 500 W/cm$^2$. Special studies were done to evaluate the performance of the target complex using an experimental setup developed at St. Petersburg State University (see Figure 45). These studies yielded all the key operational parameters of the target complex, including coolant flow rate, flow velocity, liquid pressure, helium pressure in the helium chamber, and various temperature and operational modes under steady, subcritical, and critical conditions.

The developed target heating control system was tested using proton beams from the MGC-20 cyclotron at V.G. Khlopin Radium Institute (ROSATOM) and the MGC-20 cyclotron at the Scientific and Technical Complex "Nuclear Physics" of St. Petersburg Polytechnic University (see Figure 46). The results of target heating and cooling are presented in Section 2.2.3.

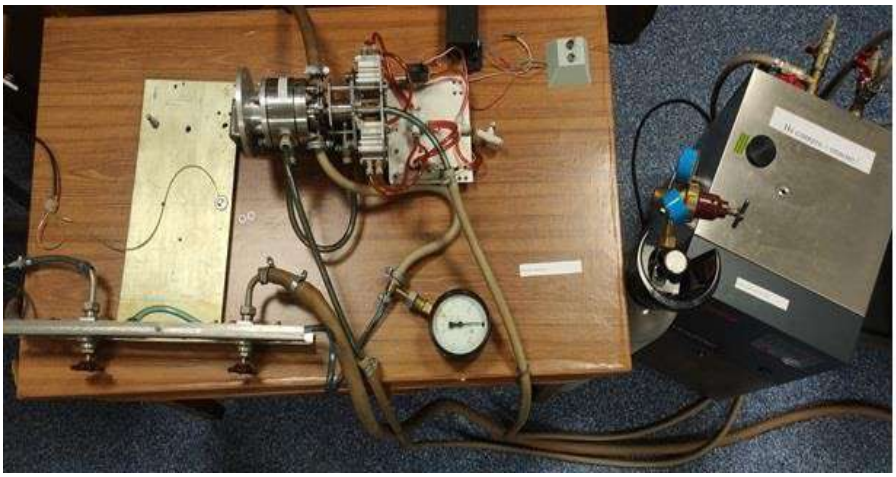

Figure 45 – Experimental setup for studying the characteristics and parameters of the target complex: external view of the assembled experimental stand.

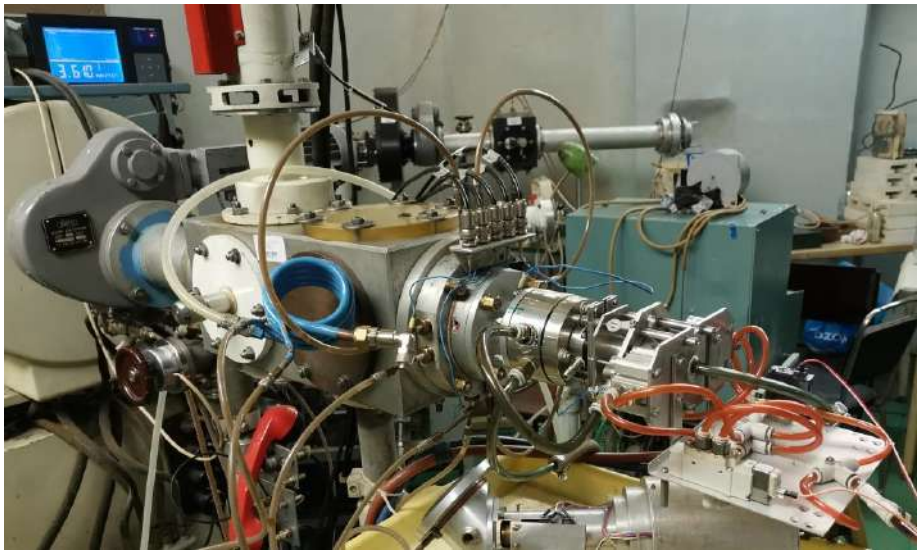

Figure 46 – Target complex mounted on the beam pipe of the cyclotron MGC-20 of the Scientific and Technical Centre “Nuclear Physics” of SPbPU.

The second part of the experimental setup was a complex of semiconductor gamma spectrometers. It consists of: an ultra-pure germanium detector – HPGe detector GX1018 with an energy resolution for the 88 keV photopeak of no worse than 620 eV, for the 1332 keV photopeak of no worse than 1.6 keV, a digital analyzer – LYNX (Canberra Industries Inc., U.S.A.), and a low-energy germanium detector – Ultra-LEGe, GUL0035 with an energy resolution for the 5.9 keV photopeak of no worse than 130 eV [34].

### 2.2.2 Experimental technique for nuclear reaction studies

One of the well-established methods for determining nuclear reaction cross-sections and studying their excitation functions is the "stacked foil method." In this approach, the primary targets, thin foils in which the nuclear reaction under study occurs, are arranged sequentially and perpendicular to the direction of the irradiating beam. Between these foils, additional thin foils are placed to serve as beam monitors and energy absorbers [43]. The entire stack of foils is irradiated simultaneously [34]. The energy losses of the beam particles are typically determined through calculations and modeling. In this dissertation, the SRIM [156] and GEANT 4 [157] programs were used for planning all experimental studies, providing initial estimates of energy losses. However, this method has several limitations, particularly when the targets contain impurities. To address this, experimental studies incorporate a technique based on the use of monitor foils to determine the energy and intensity of the beam, in addition to calculations and modeling. Monitor foils are selected based on their isotopic composition, which participates in a nuclear reaction (a monitor reaction is a nuclear reaction with well-known cross-sections within a specific energy range) and has a well-studied excitation function [34]. By measuring the activity of a specific radionuclide produced in a monitor foil, the cross-section of the corresponding nuclear reaction is calculated using the measured activity. The known excitation function is then used to determine the energy of the charged particle beam corresponding to this cross-section. In this way, the beam energy is determined after passing through the foil, and the beam current is measured similarly. Next, the activity of the radionuclide produced in the main target during the nuclear reaction under study is measured. Using the beam current information obtained from the monitor foils, the cross-section of the nuclear reaction producing this radionuclide is calculated. By combining this with the beam energy data (derived from the monitor foils and energy loss calculations), it becomes possible to determine the excitation function of the nuclear reaction under study across a wide range of energies of the charged particles bombarding the target.

The common errors that may arise in experimental studies of nuclear reaction excitation functions were considered. Significant systematic errors include: a) incorrect estimation of the beam current; b) uncertainties in estimating energy losses during the particle beam going through all targets in a foil stack. A straightforward method for determining the beam current is to measure the charge accumulated in a Faraday cup when the beam is completely stopped within the cup's material. However, the emission of secondary electrons or ions can introduce significant errors in measuring the induced charge and, consequently, the beam current. Therefore, the use of monitor foils and monitor reactions, combined with precise measurements of the accumulated activity, provides beam current information with much smaller errors. A major advantage of this approach is that if the monitor foil contains multiple isotopes of different elements, selecting a specific channel corresponding to a monitor reaction on a chosen isotope allows for immediate determination of the beam energy and current at that foil. The following requirements are imposed on monitor reactions: 1) the cross-sections of monitor reactions should be well-measured (with extensive experimental data consistent within error limits) across a wide range of incident particle energies; 2) the excitation function of such reactions should vary smoothly with increasing particle energy. Reactions with narrow resonances in the excitation function should be avoided; 3) nuclear reactions in monitor foils involving secondary particles (produced during the interaction of primary particles with the foils) should either be absent or have minimal cross-sections; 4) the half-lives of the reaction products should not be too short or too long compared to the irradiation time, and significant errors should not arise when measuring their activity; 5) the physical properties of the target should remain stable during irradiation. Materials with low melting points should be avoided; 6) the reaction products should remain within the target material during and after irradiation [34]. In this dissertation, using the stacked foil method, a series of experiments were carried out with targets such as: Ag, Cd, Cu, and Fe. These experiments aimed to study target heating processes and refine the methodology for subsequent precision measurements of reaction cross-sections across a wide range of energies and nuclear masses.

## 2.2.3 Experiments with targets: Ag, Cd, Cu, Fe, Ti, stainless steel, $^{nat}$Sn. Selection of the methodology for experiments with highly enriched tin targets

In this dissertation, using the proposed stacked foil method, a series of experiments were done with the following targets: Ag, Cd, Cu, Fe, Ti, stainless steel, and tin with natural isotopic composition ($^{nat}$Sn). These experiments aimed to refine the methodology for doing studies with highly enriched tin targets. In all experiments described in this chapter, protons accelerated to an energy of 14 MeV were used. The primary objectives of the experiments were: a) to evaluate the suitability of copper, iron, and stainless steel foils as monitor foils; b) to study the heating of the tantalum substrate and the cooling of the targets and monitor foils inserted into it.

### 2.2.3.1 Experimental studies with targets: Ag, Cd, Cu, Fe, Ti, stainless steel, $^{nat}$Sn and development of the experiments methodology with using the modernized target complex

In the first stage of the experimental work, studies were carried out using copper foils as candidates for nuclear reaction monitors. The experimental setup included two copper foils ($^{nat}$Cu – natural isotopic composition of copper isotopes $^{63}$Cu and $^{65}$Cu), each 20 μm thick: the first positioned along the beam path and the last positioned along the beam path. Between these foils, a silver plate (Ag foil, 140 μm thick) was placed. The silver foil provides excellent thermal conductivity (see Figure 47) and ensures additional thermal contact between the monitor foils. Helium cooling (in the helium chamber) was not applied to the front part of the targets. Beam current measurements were performed directly on the cyclotron probe and, using a current integrator, directly on the target holder (see Section 2.2.1). Analysis of these measurements yielded a beam current on the target of approximately 1 μA. When protons interacted with $^{nat}$Cu, the following reactions occurred: a)$^{63}$Cu(p,n)$^{63}$Zn; b) $^{63}$Cu(p,2n)$^{62}$Zn; c) $^{65}$Cu(p,n)$^{65}$Zn.

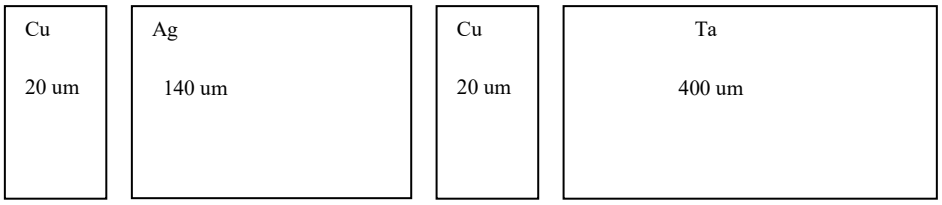


Figure 47 – Scheme of proton going through monitor foils. The monitors $^{nat}$Cu foils were used.

As a result of the experiment (the irradiation time was 90 minutes) in the copper foils the radionuclides: $^{65}$Zn, $^{63}$Zn, $^{62}$Zn were produced, and all three radionuclides were accumulated only in the first copper target. On the second copper target, the radionuclide $^{62}$Zn was not detected, as the reaction threshold for the formation of $^{62}$Zn is 13.48 MeV, and the beam energy on the second copper target after passing through the input aluminum window, the first copper foil, and the silver foil was only 10.2 MeV. The activities of these radionuclides were determined by detecting the corresponding gamma rays using an HPGe GX1018 detector (see Section 2.2.1) and were measured on the first target: $^{63}$Zn – 202,2 MBq, $^{65}$Zn – 20,4 kBq, $^{62}$Zn – 0,58 kBq; on the second target: $^{63}$Zn – 250,8 MBq, $^{65}$Zn – 32,6 kBq. A comparative analysis using the obtained activities, the corresponding reaction cross-sections, and the experimental cross-sections of the monitor reactions on $^{nat}$Cu from [158] was carried out. This analysis revealed that most of the produced Zn radionuclides did not remain in the copper targets. Due to the absence of helium cooling on the front part of the target and insufficient contact between the targets and the cooled substrate of the target holder, the targets were practically uncooled. As a result, the heating of the copper targets by the proton beam caused partial evaporation of the zinc radionuclides from the hot copper foils. After completing these experiments, helium was supplied to the helium chamber at a temperature of +17 °C and a pressure of 1.5 atm. This enabled effective cooling of the front part of the targets and ensured that the target foils were pressed firmly against each other and the substrate of the target holder.

After analyzing the activities of the produced Zn isotopes, the beam current on the targets was determined to be 0.87 μA, which is 13% lower than the results

obtained from probe measurements. This discrepancy can be attributed to insufficient data on the cross-sections of the excitation functions for reactions producing $^{62}$Zn and $^{65}$Zn radionuclides in the energy range up to 14 MeV. Consequently, it was decided to discontinue the use of copper monitors and take stainless steel foils with varying isotopic compositions of iron. These targets were later replaced with foils made of natural tin to develop a methodology for experimental studies of the excitation functions of nuclear reactions producing antimony radionuclides (primarily $^{122}$Sb and $^{124}$Sb) in the exit channels. During these experiments, the processes of target heating and cooling were also investigated. On-line monitoring of the target heating temperature demonstrated the effectiveness of the target complex, as the temperature of the tin targets increased by only 4 °C during the irradiation period (over 1.5 hours; see Figure 48). Calculations of the initial heating temperature of the target under the operating beam parameters yielded a value of approximately +36.5 °C (indicated by a dotted line in Figure 48). It is evident that, in this case, the initial cooling of the target was lower than the calculated value. The slight temperature increase observed during the experiment was due to the use of water (from cyclotron cooling sistem) as the cooling liquid in the second module of the target cooling system (see Figure 43 and Section 2.2.1). This water also cools the components and systems of the MGC-20 cyclotron, and its temperature rise contributed to the increase in target temperature. Subsequently, the target cooling system module was upgraded, and an autonomous cooler (Huber Minichiller 300) with an alcohol-based coolant was used in later experiments (see Section 2.2.1). Based on the results of this work, it was concluded that this target complex is suitable for use in many compact cyclotrons specializing in radionuclide production [41].

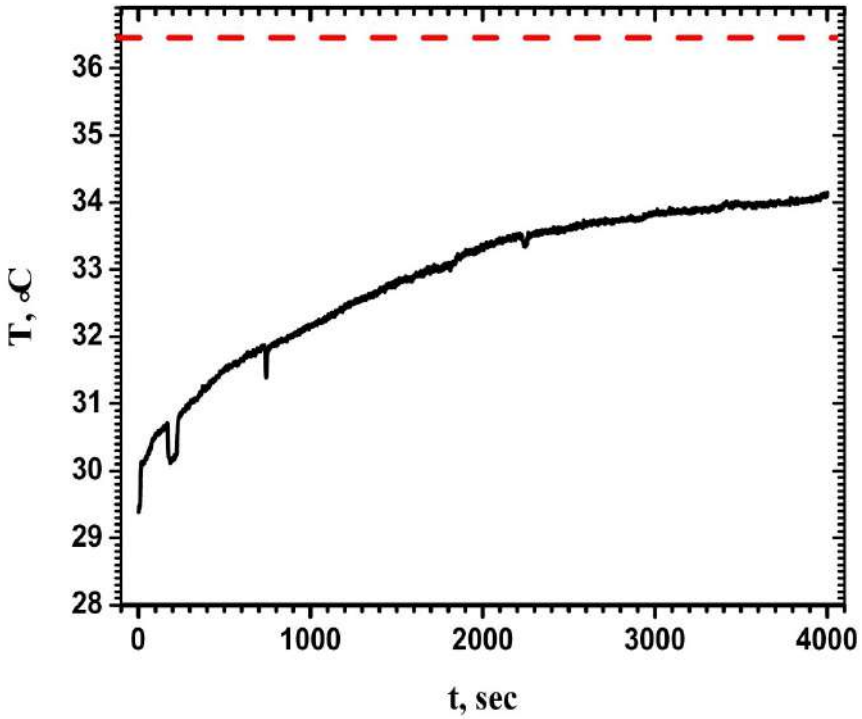


Figure 48 – Heating of $^{nat}$Sn targets when irradiated with 14 MeV protons and a current of 2 μA. The dotted line shows the calculated temperature during the initial heating of the target.

In the second phase of the research, experiments were performed using Fe foils and Cd targets. The goal of these experiments was to determine the optimal parameters for target cooling. The experimental setup is illustrated in Figure 49, which, in addition to the targets under study, includes a helium chamber (helium pressure: 1.5 atm), an input aluminum window 50 μm thick, and a cooled tantalum substrate of the target holder (see Section 2.2.1). All the foils under investigation were inserted into this substrate. The cadmium targets had a diameter of 11 mm and a thickness of 190 μm, while the iron monitors were 25 μm thick. The nuclear reaction contributing predominantly to these monitors was: $^{56}$Fe(p,n)$^{56}$Co. As a result of irradiating the foil containing $^{56}$Fe, the accumulated activity of the $^{56}$Co radionuclide averaged 76 kBq, corresponding to a current of 4.9 μA. The current measured by the probes was 5 μA. This indicates stable accumulation of the $^{56}$Co radionuclide, the absence of its evaporation, and, consequently, effective cooling of all targets.

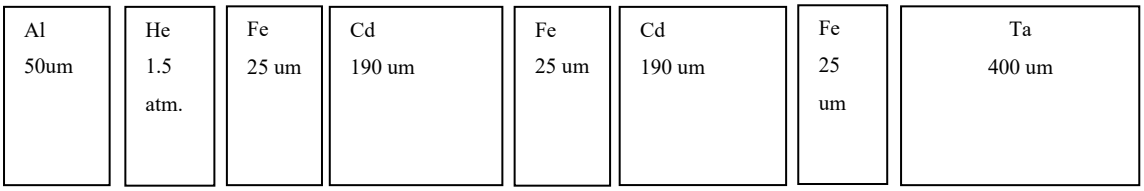


Figure 49 – Schematic diagram of the proton beam going through Fe and Cd targets.

Additionally, measurements of the heating of cadmium targets were done with on-line monitoring of the heating of the tantalum substrate. Prior to the measurements, the heating conditions of the tantalum substrate were simulated, and the upper heating limit of this substrate was estimated. For a substrate thickness of 400 μm (664 mg/cm²) and a beam diameter of 9 mm, the heating (considering only heat-conducting losses) was calculated as T = 95.4 °C for a beam current of 5 μA and T = 110 °C for a beam current of 6 μA [34]. The results of measuring the heating of the tantalum substrate and, consequently, the Cd targets fixed within it are shown in Figure 50 for beam currents of 5 μA and 6 μA. The sharp dips in the temperature distribution, corresponding to decreases in the thermocouple sensor readings (see Figure 50), are attributed to short-term beam dumps on the cyclotron probes and the absence of the beam on the targets and substrate. From the obtained data, it is evident that for a beam current of 5 μA, the average heating of the tantalum substrate was +30.5 °C, while for a beam current of 6 μA, it was +39.2 °C.

After removing the Cd targets from the substrate, the activity of the Indium radionuclides produced in them was measured, and the cross-sections of the corresponding reactions were calculated. Good agreement was found between the obtained results and the experimental data available in the EXFOR nuclear reaction database [45]. This suggests optimal fixation of the targets in the holder, stable contact with the tantalum substrate, and effective cooling. As a result, real-time target heating control was successfully implemented, and a target cooling technique was developed [34].

During these experiments, with an increase in beam current and a decrease in beam diameter, a thermal power of 657 W/cm² was achieved without overheating any of the targets. This demonstrates that the use of this target complex can ensure the production of the target radionuclide in the studied nuclear reactions at nearly the maximum achievable level.

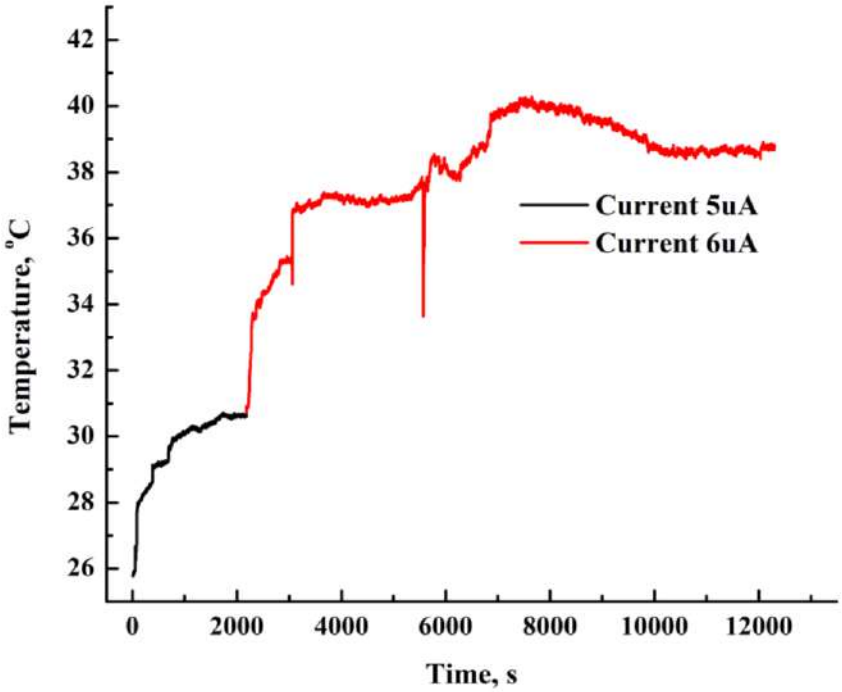


Figure 50 – Heating of targets when irradiated with proton beams with energy of 14 MeV and a current of 5 μA and 6 μA [34].

As noted earlier, to study nuclear reactions producing radionuclides: $^{122}$Sb and $^{124}$Sb, a natural tin target was irradiated with a 14 MeV proton beam. The stacked foil method was employed, and monitor reactions were additionally investigated. Stainless steel foils with high iron content and low nickel content were used as monitors: Fe – 70%; Cr – 25%; Ni – 5%, with a thickness of 25 μm, along with titanium foils 60 μm thick. In this case, the excitation functions of the following reactions were studied: $^{52}$Cr(p,n)$^{52}$Mn, $^{56}$Fe(p,n)$^{56}$Co, and $^{nat}$Ti(p,X)$^{48}$V. Additionally, experimental studies were carried out using austenitic stainless steel foils with a reduced thickness of 10 μm (resulting in lower energy losses and less heating). These foils had the following composition: Fe – 60%, Cr – 20%, Ni – 20%, with the nickel content increased by a

factor of four. In this case, an additional monitor channel associated with the reaction $^{58}Ni(p,\alpha)^{55}Co$ was utilized. After analyzing the activities of the produced isotopes: $^{56}Co$, $^{52}Mn$, and $^{55}Co$, the beam current on the targets was determined with high accuracy: 6.90 ± 0.30 μA. This value aligns, within the margin of error, with the results obtained from cyclotron probe measurements (beam current: 7.0 μA). Furthermore, using the excitation functions of these monitor reactions [158], the beam energy on these foils was determined. The discrepancies between these energies and those obtained from calculations and modeling using the SRIM and GEANT 4 programs [156, 157] were 120 keV. Based on these results, these foils were selected as monitors for the main experiment involving the irradiation of highly enriched tin targets (enrichment > 85%) [34].

#### 2.2.3.2 Results of experimental studies with targets: Ag, Cd, Cu, Fe, Ti, stainless steel, $^{nat}Sn$ and selection of methodology for experiments with highly enriched tin targets

The results of cross-section measurements for the (p,n) and (p,X) monitor reactions producing the radionuclides $^{52}Mn$, $^{56}Co$, and $^{48}V$ were analyzed. These data are presented in Figures 51, 52, and 53, respectively. For comparison, experimental results from the EXFOR nuclear reaction database [45] and the monitor reaction database [158] were used.

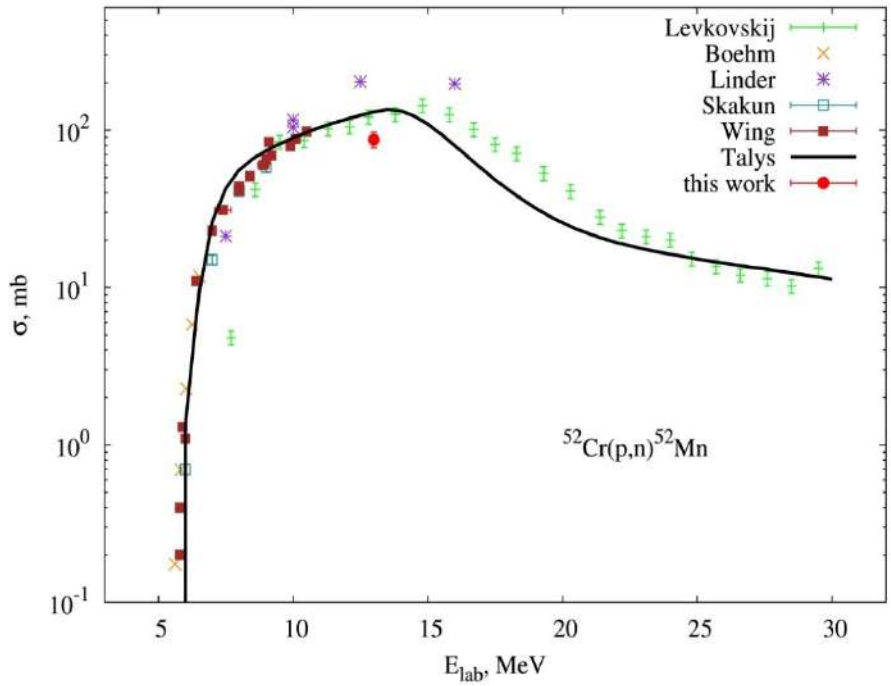


Figure 51 – Excitation function of the reaction $^{52}$Cr(p,n)$^{52}$Mn. The experimental data are taken from EXFOR [45] and the database on monitor reactions [158], the red dot is the experimental result obtained in this dissertation. The solid line is the model using the Talys program [159].

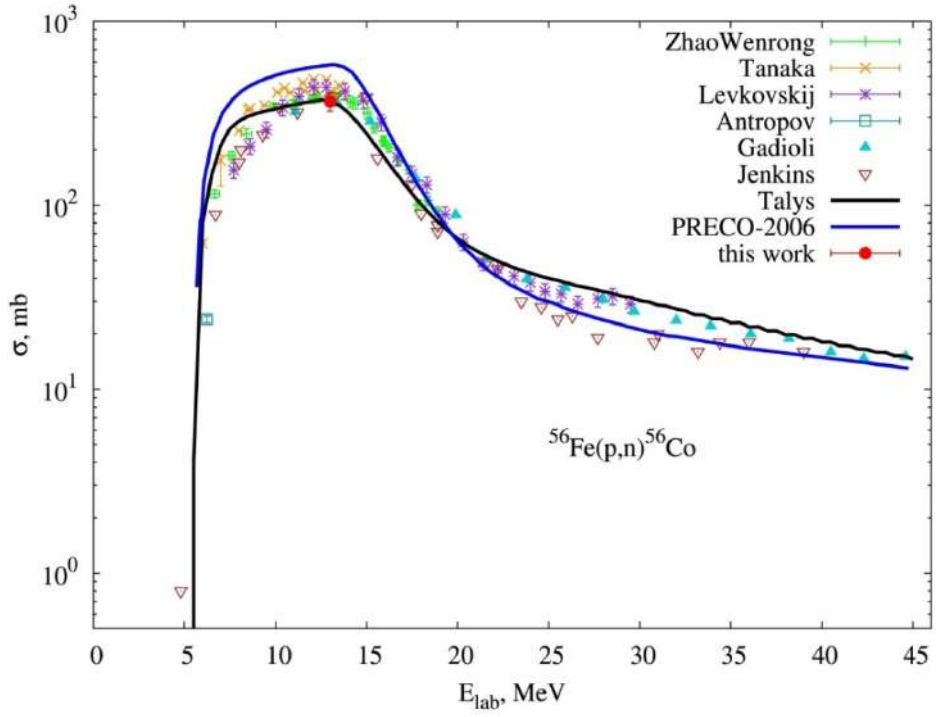


Figure 52 – Excitation function of the reaction $^{56}$Fe(p,n)$^{56}$Co. The presented experimental data are taken from EXFOR [45] and the database on monitor reactions [158], the red dot is the experimental result obtained in this dissertation. The solid black line is theoretical calculations using the Talys program; the solid blue line is theoretical calculations using the PRECO-2006 program [160].

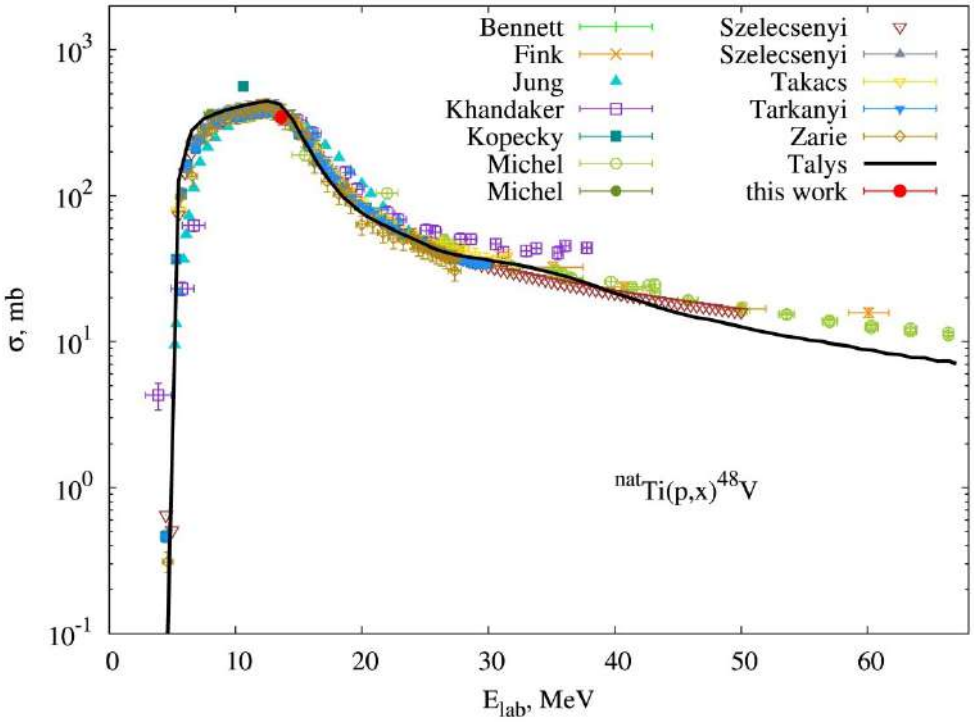


Figure 53 – Excitation function of the reaction $^{nat}$Ti(p,X)$^{48}$V. The experimental data are taken from EXFOR [45] and the database on monitor reactions [158], the red dot is the experimental result obtained in this dissertation. The solid line is theoretical calculations using the Talys program [159].

As noted earlier, experimental studies were done for the monitor reactions to determine the cross-section (σ) of each reaction. The obtained cross-section values are: σ = (87 ± 10) mb for the reaction $^{52}$Cr(p,n)$^{52}$Mn, σ = (366 ± 42) mb for the reaction $^{56}$Fe(p,n)$^{56}$Co, and σ = (344 ± 38) mb for the reaction $^{nat}$Ti(p,X)$^{48}$V. These results are in good agreement with theoretical calculations performed using nuclear physics models, specifically the Hauser-Feshbach model and the two-component exciton model, implemented in the TALYS [159] and PRECO [160] programs. Using the obtained cross-section values of these monitor reactions, as well as the proton beam current and energy values derived from these data (see the methodology in Sections 2.2.2 and 2.2.3.1), the cross-sections of the following reactions were determined: $^{nat}$Sn(p,X)$^{122}$Sb: σ = (8.21 ± 0.94) mb, and $^{nat}$Sn(p,X)$^{124}$Sb: σ = (7.55 ± 0.85) mb. The excitation functions of these reactions are presented in Figures 54 and

55. As shown, all cross-sections are in good agreement with the theoretical calculations.

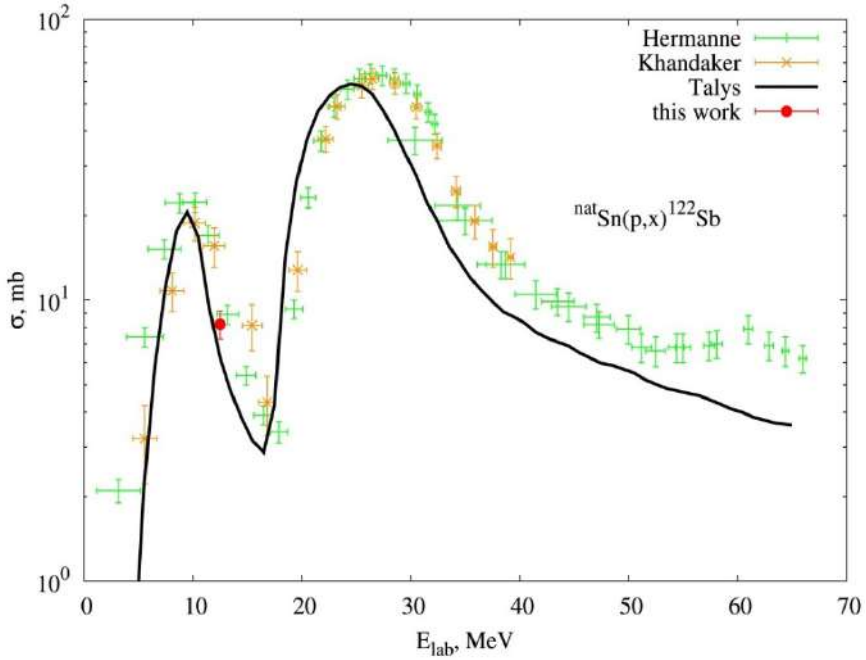


Figure 54 – Excitation function of the reaction $^{nat}Sn(p,X)^{122}Sb$. The experimental data are taken from the EXFOR nuclear reaction database [45], the red dot is the experimental result obtained in this dissertation. The solid line is theoretical calculations using the Talys program [159].

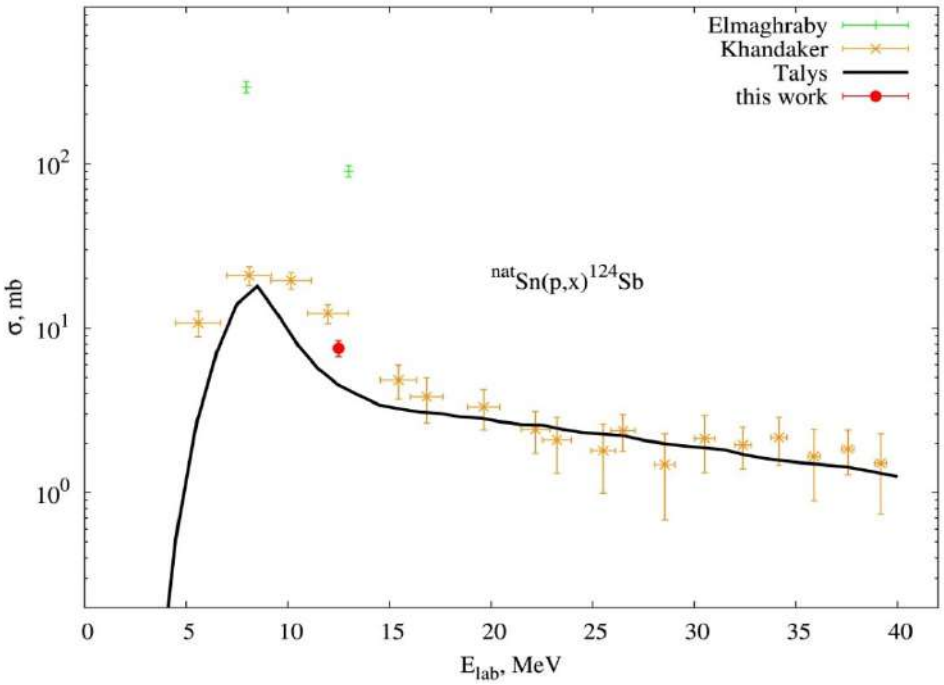


Figure 55 – Excitation function of the reaction $^{nat}Sn(p,X)^{124}Sb$. The experimental data are taken from the EXFOR nuclear reaction database [45], the red dot is the experimental result obtained in this dissertation. The solid line is the theoretical calculations using the Talys program [159].

Since the use of highly enriched tin isotopes: $^{117}$Sn and $^{119}$Sn is proposed, theoretical studies of the nuclear reactions: $^{119}$Sn(p,n)$^{119}$Sb and $^{117}$Sn(p,n)$^{117}$Sb leading to formation of antimony isotopes were done at this stage of the work. For calculating the excitation functions, the modified PRECO-2006 program [160] was used. This program is based on a two-component exciton model that accounts for the possibility of secondary nucleon emission. To analyze the experimental data, a systematics for nuclei within the corresponding mass range was used [161]. The use of optical proton and neutron potentials from other studies did not yield better agreement with the experimental results [41].

The distributions shown in Figure 52 and Figures 54–55 demonstrate that the applied methodology yields good results in describing the experimental data for the excitation functions of the reaction $^{56}$Fe(p,n)$^{56}$Co and the reactions $^{nat}$Sn(p,X)$^{122}$Sb and $^{nat}$Sn(p,X)$^{124}$Sb in the energy range above 15 MeV. However, significantly less agreement is observed in the lower-energy region of the excitation functions. On the other hand, for the reaction $^{52}$Cr(p,n)$^{52}$Mn, the agreement between theoretical calculations and experimental data is poorer. This discrepancy can be attributed to the influence of the magic neutron shell and the need to account for collective degrees of freedom, including gamma-ray emission. Detailed calculations were performed using nuclear physics models implemented in the TALYS program [159]. This program enables comprehensive modeling of nuclear reactions in the energy range from 1 keV to 200 MeV by combining various nuclear models relevant to this energy region. TALYS allows for flexible adjustments to model parameters and supports the use of parameter values derived from systematics (parameters are selected from established nuclear databases and systematics obtained from the analysis of characteristics of numerous nuclei). The particles included in the modeling (both incident and emitted during reactions) are neutrons, photons, protons, and nuclei such as $^{2}$D, $^{3}$He, and alpha particles. Nuclides with mass numbers $A \geq 12$ and heavier can be used as targets [41].

In the presented part of the dissertation, two mechanisms of nuclear reactions within the selected range of incident particle energies were investigated: in the low-

energy region (up to 9 MeV), where particle emission from a compound nucleus is dominant, the Hauser-Feshbach model was applied, incorporating a correction for the fluctuation of the Moldauer widths. In the high-energy region (above 9 MeV), pre-equilibrium processes were considered, as described by the exciton model (theoretical formalism detailed in [159] and [160]). At energies exceeding 20 MeV, a multiple pre-equilibrium mechanism was included in the calculations, accounting for the simultaneous emission of several particles during the pre-equilibrium process. Additionally, an important reaction channel involving gamma-ray emission was also incorporated into the calculations. The differences in the calculations performed using the PRECO and Talys programs for the reaction $^{56}$Fe(p,n)$^{56}$Co in the energy range below 20 MeV (see Figure 52). These differences may arise from the specific characteristics of the models employed, particularly in their accounting of gamma-ray emission processes. Specifically, if a gamma quantum is not emitted during the de-excitation of the compound system formed in the reaction, the remaining energy is going into the neutron emission process. This leads to an increase in the cross section of the reaction under consideration (see Figure 52). Additionally, the observed differences in the decay region of the excitation function at higher energies can be attributed to the inclusion of pre-equilibrium processes [41]. In calculations involving targets with isotopes present in natural concentrations, the (p,n) reaction mechanism dominates. For the reaction $^{nat}$Ti(p,X)$^{4}$8V, this dominance is primarily due to the significant contribution of the $^{48}$Ti isotope, which constitutes approximately 74% of the natural isotopic mixture (see Figure 53). For the $^{49}$Ti and $^{50}$Ti isotopes (each present at about 5% in the natural titanium mixture), the (p,2n) and (p,3n) reactions become significant. These reactions begin to influence the growth of the cross section at an incident proton energy of 35 MeV, as they involve the emission of two or three neutrons, respectively. The good agreement between the calculations and the experimental data supports this interpretation (see Figure 53). Similarly, calculations for reactions involving a target composed of the natural mixture of tin isotopes, $^{nat}$Sn, also demonstrate good agreement with experimental data. For the reaction $^{nat}$Sn(p,x)$^{122}$Sb (see Figure 54), the following reaction channels

are predominant: $^{122}$Sn(p, n)$^{122}$Sb and $^{124}$Sn(p, 3n)$^{122}$Sb, since the isotopes $^{122}$Sn and $^{124}$Sn constitute 4.63% and 5.79%, respectively, of the natural isotopic mixture of tin, their presence significantly influences the behavior of the excitation function. This explains the appearance of two distinct peaks in the cross section of the reaction $^{nat}$Sn(p,X)$^{122}$Sb within specific energy ranges (see Figure 54). Thus, the application of nuclear-physical models has enabled the identification of several features in the reaction mechanisms involving nuclei across a wide mass range, from 48 to 124 [41]. The good agreement with experimental data (up to 30 MeV) further validates the use of these models for analyzing the excitation functions of reactions: $^{117}$Sn(p,n)$^{117}$Sb and $^{119}$Sn(p,n)$^{119}$Sb. For the first reaction, there are no experimental data available beyond 11 MeV. For the second reaction, the region around the maximum of the excitation function has very little data, making it difficult to draw unambiguous conclusions (the available data predate the experiments described in this dissertation). Figures 56–57 present the excitation functions of the nuclear reactions: $^{117}$Sn(p,n)$^{117}$Sb and $^{119}$Sn(p,n)$^{119}$Sb, which clearly show the situation being described.

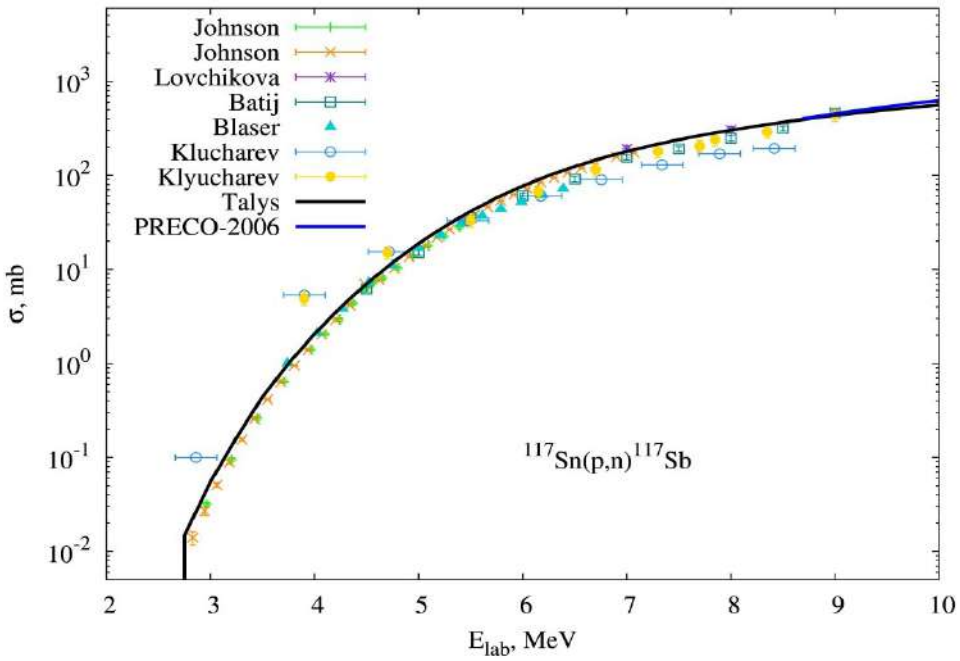


Figure 56 – Excitation function of the reaction: $^{117}$Sn(p,n)$^{117}$Sb. The experimental data are taken from (EXFOR database [45]). The solid black line is theoretical model calculations using the Talys program [159]; the solid blue line is theoretical calculations using the PRECO-2006 program [160].

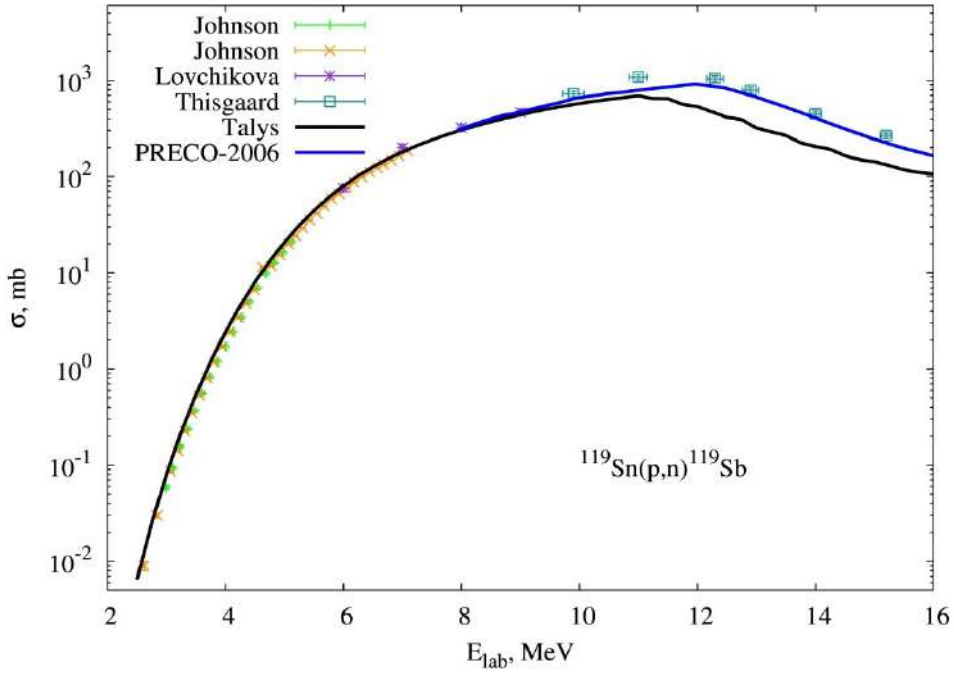


Figure 57 – Excitation function of the reaction $^{119}$Sn(p,n)$^{119}$Sb. The experimental data are taken from (EXFOR database [45]). The solid black line is theoretical model calculations using the Talys program [159]; the solid blue line is theoretical calculations using the PRECO-2006 program [160].

During the calculations, the regions of maxima in the excitation functions of the reactions $^{117}$Sn(p,n)$^{117}$Sb and $^{119}$Sn(p,n)$^{119}$Sb were identified, for proton energies of 12.5 MeV and 12 MeV, respectively. Using the target complex equipped with a on-line operational control system for heating and cooling the irradiated targets, several monitor reactions were selected as optimal for determining proton beam parameters. This information is crucial for experimental studies involving highly enriched tin isotopes to produce radionuclides, such as $^{119}$Sb and $^{117}$Sb, on compact cyclotrons for applications in medical technologies. These experimental studies were cdone as part of this dissertation and are detailed in Sections 2.2.4 and 2.2.5.

### 2.2.4 Studies of nuclear reactions in which the radionuclides used in medical technologies are formed in exit channels

The analysis of information on diagnostic and therapeutic radionuclides used in nuclear medicine, as well as the evaluation of current experimental and production

capabilities of modern accelerator and target complexes, enabled the formulation of a specific set of problems and tasks. These problems were addressed in this dissertation through a detailed study of the nuclear reaction excitation functions for production of isotopes: $^{44}$Sc, $^{119}$Sb, $^{117}$Sb $^{161}$Tb, and radionuclide generators: $^{44}$Ti/$^{44}$Sc, $^{99}$Mo/$^{99m}$Tc.

#### 2.2.4.1 Nuclear reactions with formation of $^{44}$Sc radionuclide

Let us begin with the radionuclide $^{44}$Sc (and the corresponding $^{44}$Ti/$^{44}$Sc generator), which is well-established in preclinical and clinical studies for PET imaging and theranostics [162, 163, 164] (see also Introduction). This radionuclide can be produced through a nuclear reaction: $^{44}$Ca(p, n)$^{44}$Sc with low-energy proton beams (up to 18 MeV) irradiation, both on targets with natural calcium content and on highly enriched targets of $^{44}$Ca carbonate or oxide [165, 166]. It is also possible to use proton beams, but with energies greater than 25 MeV and scandium targets in the reaction: $^{45}$Sc(p, 2n)$^{44}$Ti to get the generator: $^{44}$Ti/$^{44}$Sc [167]. In a number of studies (see, for example, [31]), experimental values of the excitation function for the reaction $^{45}$Sc(p, 2n)$^{44}$Ti were obtained in the energy range of 4 to 18 MeV. Good agreement between these values and model calculations is observed, both in the region of the maximum and in the region of the decay of the excitation function. However, the theoretical description of this function in the low-energy region (5 to 8 MeV) often deviates from experimental results. Therefore, in this dissertation, studies of the excitation function for these reactions: $^{44}$Ca(p, n)$^{44}$Sc and $^{45}$Sc(p, 2n)$^{44}$Ti were carried out. The use of various models included in the Talys program [159] demonstrates good agreement between the calculated cross sections and experimental data [168] in the low-energy region (up to 20 MeV), particularly at the rise of the excitation function. However, the modeling results for the region of the excitation function maximum cannot always unambiguously describe the experimental cross sections for nuclei of medium and heavier mass groups formed in reactions [168, 169, 170], even with an appropriate choice of model parameters. Therefore, in this work, the region of the excitation function maximum was analyzed using the channels and mechanisms of nuclear reactions with a specific set of

such parameters [33]. The results are presented in Figure 58, which shows the excitation function of the $^{44}$Ca(p, n)$^{44}$Sc reaction. It is evident that in the energy region starting from 8 MeV and above, there is good agreement between the experimental data and the model calculations. The reaction in PRECO-2006 was described using the Koning-Delaroche potential [171] and parameters corresponding to the systematics for pre-equilibrium reactions [172]. Calculations performed in the Talys program yield similar results (see Figure 58), with the default parameters based on the potential also used in PRECO-2006. Note that when the single-particle level density parameter is chosen in PRECO-2006 below the systematic one, a better agreement with the experimental data is observed for the energy range above 15 MeV and the result obtained is in good agreement with the permissible deviations in the systematics [33].

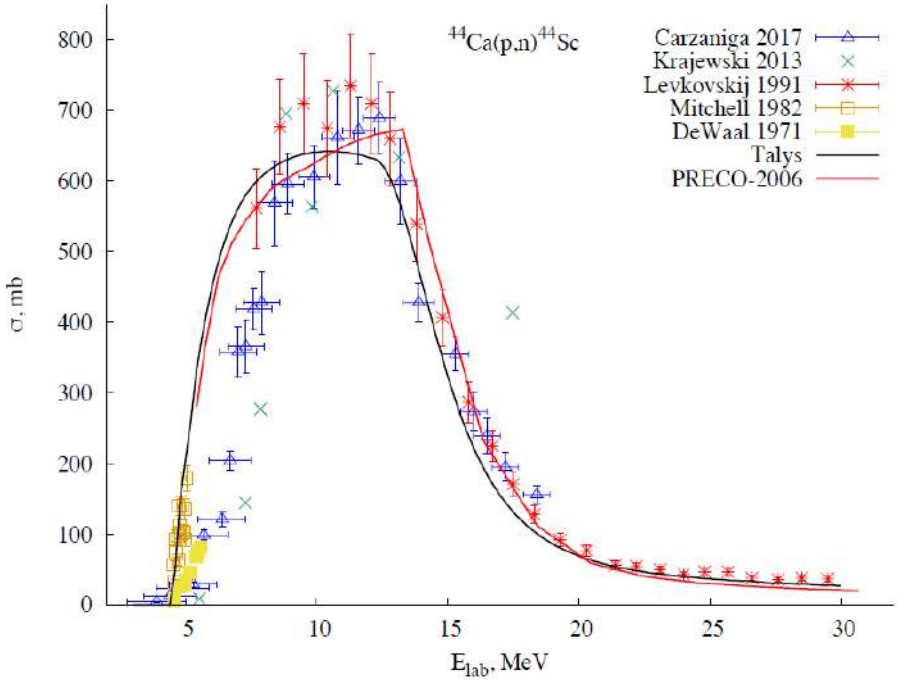


Figure 58 – Excitation function of the reaction $^{44}$Ca(p,n)$^{44}$Sc. The experimental data are taken from [173]. The solid black line is theoretical calculations using the Talys program; the solid red line is theoretical calculations using the PRECO-2006 program.

Now one can go to the energy region below 8 MeV, where an overestimation of the cross sections derived from systematics is observed compared to the experimental data [174, 175, 176], although the data near the reaction threshold are well reproduced. Since the shape of the excitation function in this energy region is primarily determined

by the energy dependence of the cross section for the formation of a compound nucleus, which depends on the interaction potential in the input channel, it is advisable to perform calculations using other potentials available in the Talys program. Satisfactory results in describing the experimental data are achieved when using the Jeukenne–Lejeune–Mahaux (JLM) potential model [177] in the energy region above 13 MeV; however, the systematic overestimation of the cross section at low energies persists. A similar result was obtained in [178] using the optical potential derived from the analysis of elastic scattering. This indicates that the permeability coefficients for nucleons are correctly accounted for. Such behavior of the excitation function in the low-energy region may suggest either errors in the experimental data or a strong suppression of the reaction in the energy region below 8 MeV, where a more detailed analysis is currently unavailable. To advance technologies for producing $^{44}$Sc in cyclotrons with low-energy proton beams, it is essential to provide additional studies of this reaction excitation function at energies near the threshold [33].

Next, the nuclear reaction: $^{45}$Sc(p, 2n)$^{44}$Ti, in which produces $^{44}$Ti, with further decays into $^{44}$Sc (radionuclide generator: $^{44}$Ti/$^{44}$Sc). Figure 59 shows the excitation function of this reaction, where the black solid curve represents calculations in Talys with default parameters. It is evident that the results obtained for the cross sections of this reaction largely disagree with the experimental data. The results can be improved by applying a specific adjustment of the JLM optical potential parameters ($R_w$, $a_w$, $W_v$, $W_s$) for the proton-nucleus interaction and setting a specific parameter K = 13 MeV (default K = 15 MeV), which determines the single-particle level density (see Figure 59, blue dashed-dotted curve). In this case, the interaction potential influences the behavior of the excitation function in the energy region up to 17 MeV (where the cross section increases). Through finer adjustment of the parameter K (within acceptable limits), it is also possible to describe the behavior of the excitation function in the decline region.

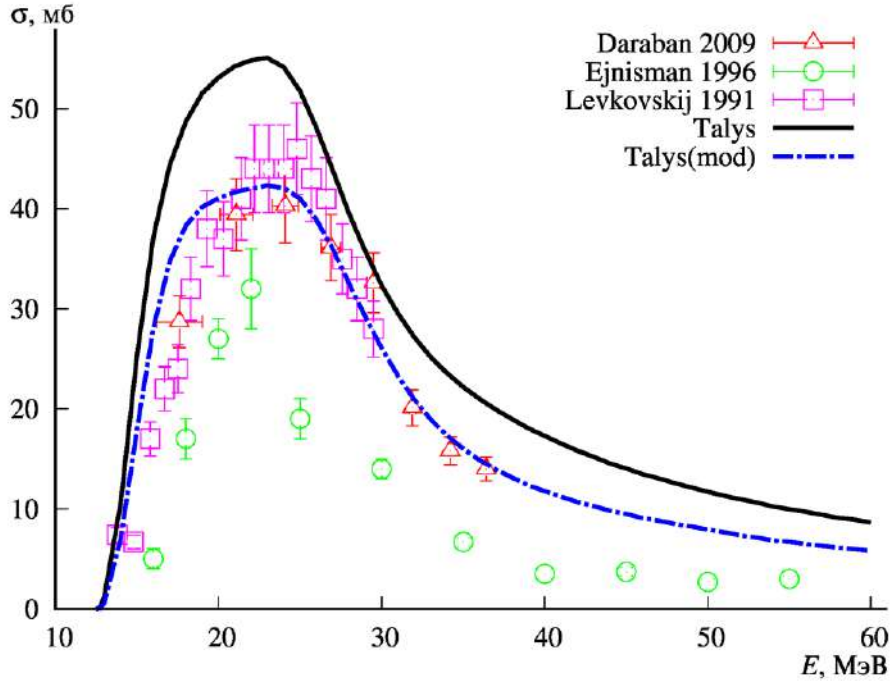


Figure 59 – Excitation function of the reaction: $^{45}Sc(p,2n)^{44}Ti$. The experimental data are taken from [173]. The solid black line is theoretical calculations using the Talys program with default parameters; the blue dash-dotted curve is theoretical calculations using the Talys program with modified parameters [33].

### 2.2.4.2 Nuclear reactions with formation of $^{99m}$Tc radionuclide

The heavier nuclei and nuclear reactions for production of the radionuclide $^{99m}$Tc, which is in high demand in nuclear medicine were also investigated in present dissertation work. To begin, the nuclear reaction: $^{100}Mo(p, x)^{99}Mo$ (in which the generator nuclide $^{99}$Mo – generator $^{99}Mo/^{99m}Tc$ produces) was analysed. Figure 60 shows the excitation function of this reaction. As in the previous case, the black solid curve (Talys default) represents the results of model calculations in the Talys program with default parameters. The blue curve corresponds to calculations in the PRECO-2006 program for the (p,n) channel of this reaction, where cross sections of direct processes involving deuteron formation were also taken into account (see the description of the influence of this channel below and Figure 62). Due to the limitations of the program, calculations for incident particle energies above 30 MeV were not performed. The purpose of these calculations was to explain the "shift" of the excitation function at low

energies, attributed to the implementation of direct reaction channels. The red curve in Figure 60 (Talys mod.) was obtained through modeling in the Talys program by adjusting the parameters $r_v$, $a_v$, and $W_d$ of the Koning–Delaroche optical potential (within the limits allowed by the systematics used) and selecting the parameter K = 13 MeV. Note that both the Talys calculations with default parameters and the modified calculations with adjusted parameters show underestimated cross sections in the region up to 20 MeV. In the high-energy region, where experimental data are scarce (with significant variability in the experimentally obtained cross sections), it is not possible to unambiguously determine the parameters of the model used.

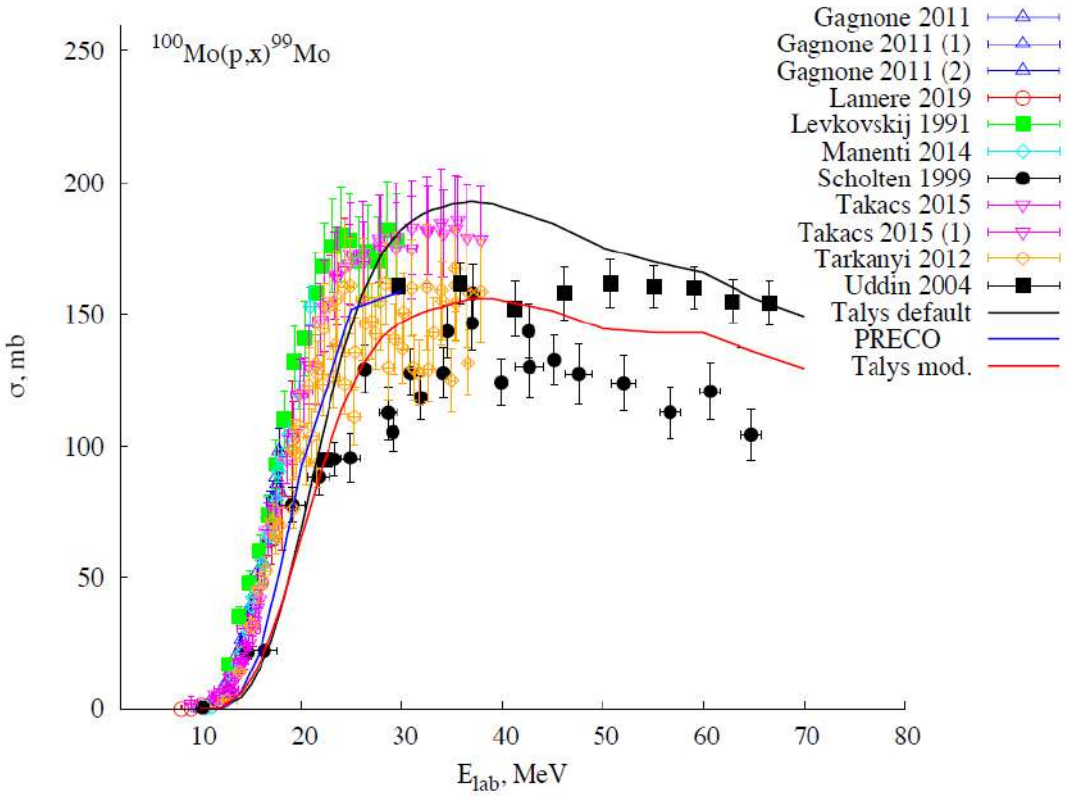


Figure 60 – Excitation function of the reaction $^{100}$Mo(p, x)$^{99}$Mo. The experimental data are taken from [173]. The solid black line is theoretical calculations using the Talys program with default parameters; the red curve is theoretical calculations using the Talys program with modified parameters; the blue curve is theoretical calculations in the PRECO-2006 program taking into account direct processes.

In this case, a valuable practical result was obtained for the thick-target yield function (such functions are used for applied purposes to calculate the accumulated

activity during the production of radionuclides in accelerators) of the reaction: $^{100}$Mo(p, x)$^{99}$Mo (see Figure 61). For this reaction, a comparative analysis was carried out between the yield function obtained from the calculations and the corresponding function derived from the approximation of selected experimental data [179] (see Figure 61). It was noted that in the low-energy region, the dependence of the yield function on the energy of the incident protons reflects the aforementioned result, which is manifested in a decrease in the values of the corresponding cross sections. Starting at an energy of approximately 30 MeV, the approximated cross-section data practically coincide with those calculated in Talys (with modified parameters). At the same time, the cross-section values obtained with the default parameters are overestimated. In this energy range and extending to higher energies, the cross section decreases, though not as sharply as observed in the excitation functions of other nuclear reactions. This observation supports the use of proton beams with energies starting from 80 MeV up to and including the maximum region (see Figure 60) for the efficient production of the $^{99}$Mo isotope. Based on the modeling performed, estimates of the yield of the $^{99}$Mo isotope in the reaction: $^{100}$Mo(p, x)$^{99}$Mo were made for both the low-energy range and the energy range above 40 MeV (red dashed curve in Figure 61). Note that for the quantitative determination of the yield of this isotope during irradiation of highly enriched $^{100}$Mo targets with protons of energies above 40 MeV, values should be taken from the region bounded by the black solid and blue dash-dotted curves in Figure 61.

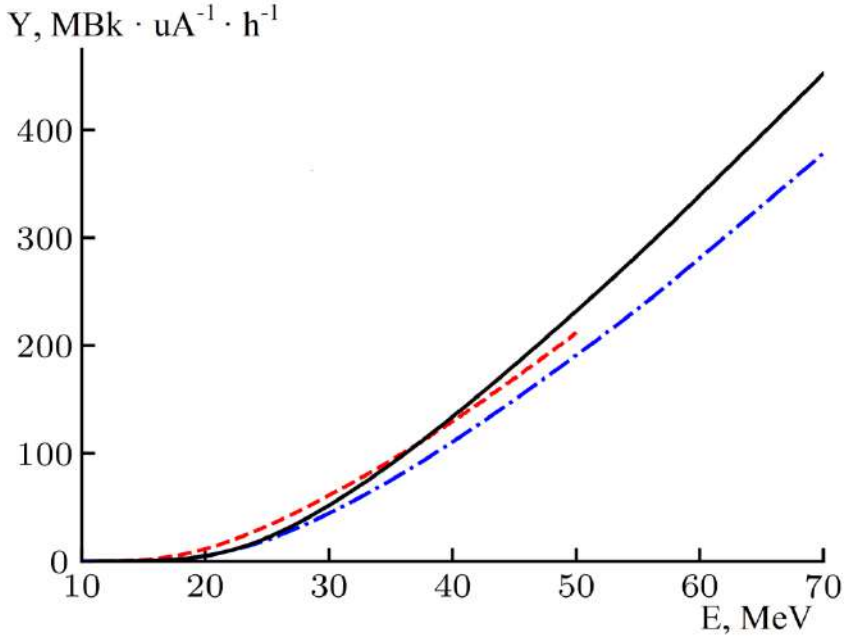


Figure 61 - Thick target yield function of the reaction: $^{100}$Mo(p, x)$^{99}$Mo. Red dashed curve - calculations based on an approximation of the experimental excitation function [179]; solid black curve - calculations using the excitation function obtained in Talys with default parameters; blue dashed curve - calculations using the excitation function obtained in Talys with modified parameters [33].

Thus, the results of these calculations (see Figure 61) can be applied in practical work on the production of $^{99}$Mo/$^{99m}$Tc using medium-energy cyclotrons with energies ranging from 40 to 80 MeV (for example, the C-80 cyclotron currently being commissioned at the Kurchatov Institute, PNPI), even under conditions of limited experimental data in the specified energy range [33]. For instance, irradiating a molybdenum target for 10 hours with a proton beam of 50 MeV energy and 100 μA current can produce an activity of $^{99}$Mo of approximately 150 GBq. Accounting for 20% losses during subsequent target processing and the isolation of pure $^{99}$Mo isotope, about 100 doses of the radiopharmaceutical preparation can be obtained per day. Furthermore, to produce this radionuclide, the cyclotron would only need to operate 1–2 times per week, making it possible to meet the regional demand for this isotope product.

We will continue the analysis of the excitation function for the reaction: $^{100}$Mo(p,x)$^{99}$Mo, focusing on its low-energy region. Figure 62 shows, for energies below 30 MeV, a comparison of the theoretically calculated excitation functions for the

reaction channels: $^{100}$Mo(p, pn)$^{99}$Mo (blue dashed curve) and $^{100}$Mo(p,d)$^{99}$Mo (green dashed-dotted curve) with the available experimental data. When studying the reaction channel involving deuteron emission in the output state, (p, d), a formalism was employed that allows, within the framework of the phenomenological description of pre-equilibrium reactions, the contribution of direct processes to be accounted for [180]. On the other hand, for the (p, pn) reaction channel, a hybrid approach based on the Ewing–Weisskopf model was used [181]. Analysis of Figure 62 shows that the contribution of the (p, d) channel must be considered over the entire energy range studied. As previously noted, for energies below 20 MeV, the observed underestimation of cross sections obtained using this theoretical formalism may result from either an incomplete consideration of the direct contribution from pickup processes or an inaccurate treatment of the permeability coefficients within the optical model. At the same time, it is noted in [182] that for the production of the radionuclide $^{99}$Mo, the yield function in the low-energy region can be described using data obtained from approximation by appropriate polynomials.

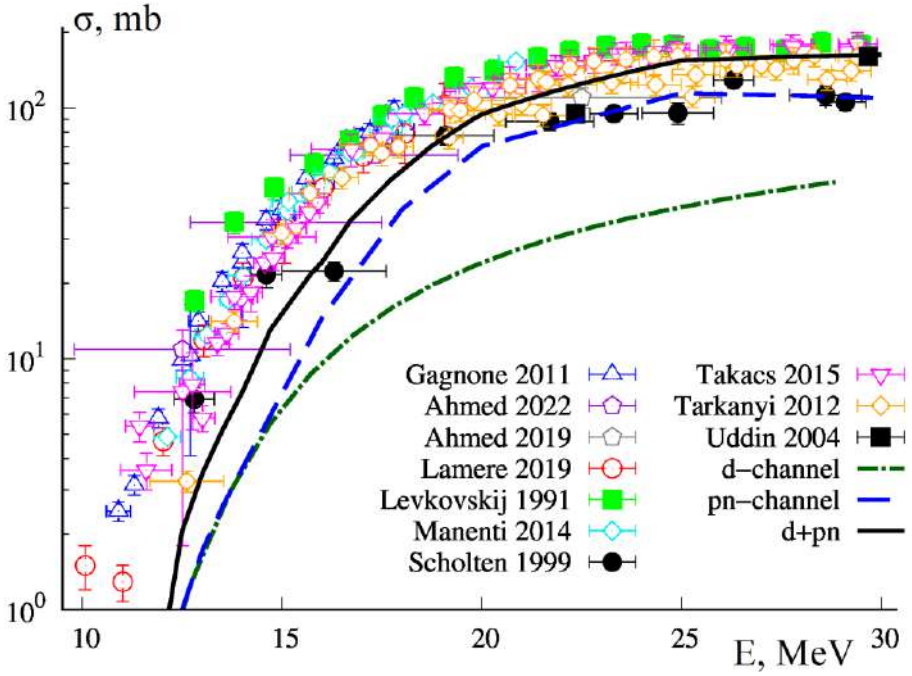


Figure 62 – Low-energy part of the excitation function of the reaction $^{100}$Mo(p, x)$^{99}$Mo. Experimental data are taken from [173]. The blue dashed curve is theoretical calculations (description in the text) for the channel: $^{100}$Mo(p, pn)$^{99}$Mo; the green dashed-dotted curve is theoretical calculations for the channel: $^{100}$Mo(p, d)$^{99}$Mo; the black curve is the sum of the channels (p, pn) and (p, d) [33].

Let us now consider the nuclear reaction: $^{100}$Mo(p,2n)$^{99m}$Tc, which directly produces the radionuclide $^{99m}$Tc. Figure 63 shows the excitation function of this reaction, where the black solid curve represents calculations performed in the Talys program with default parameters, and the blue dashed-dotted curve corresponds to calculations using the JLM potential. The use of this potential describes the behavior of the excitation function in the region of its decline, while the region of the maximum aligns with the lower boundary of the experimental data. Adjusting the parameters does not provide a significant advantage for describing the maximum of this excitation function. Therefore, it can be concluded that additional mechanisms of this reaction (such as the opening of other channels involving particle emission) and its complex dynamics in this energy range are not fully accounted for.

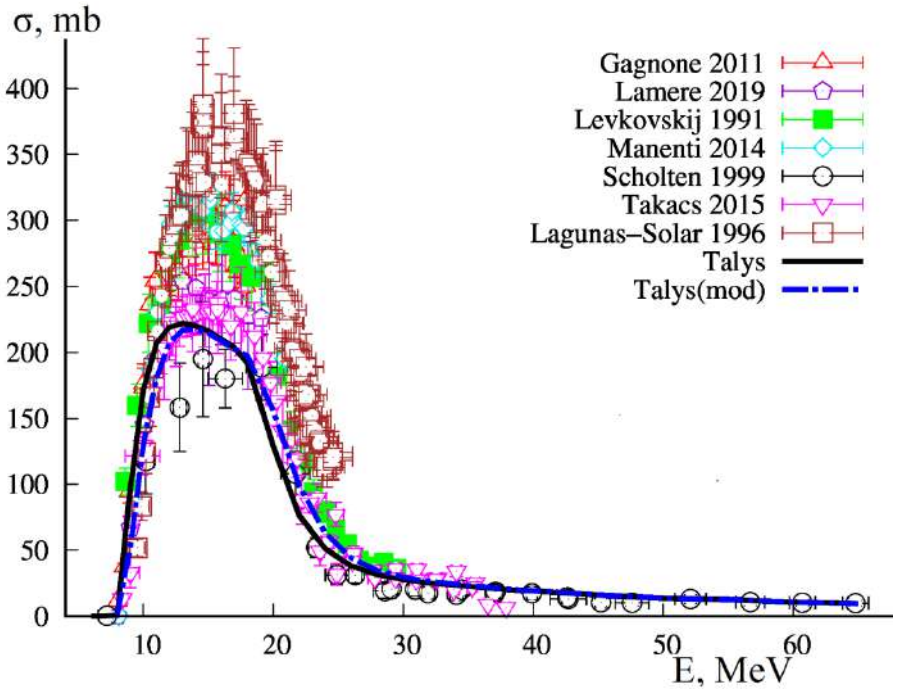


Figure 63 – Excitation function of the reaction $^{100}$Mo(p,2n)$^{99m}$Tc. The experimental data are taken from [173]. The black curve is theoretical calculations using the Talys program with default parameters; the blue dashed-dotted curve is theoretical calculations using the Talys program with modified parameters [33].

### 2.2.4.3 Nuclear reactions with formation of $^{161}$Tb radionuclide

Reactions involving nuclei of a heavier mass group also were investigated. Figure 64 presents the results of studies on the nuclear reaction of deuterons interacting with a

$^{160}$Gd target, leading to the formation of the $^{161}$Tb radionuclide in the output channel: $^{160}$Gd(d,x)$^{161}$Tb. The figure also includes theoretical model calculations performed using the Talys program with default parameters. It is evident that the neutron stripping channel (proton capture) dominates in the formation of the excitation function maximum. Figure 64 also displays results from calculations performed in Talys by adjusting the scaling factor responsible for the breakup reaction with proton emission: (d, p), as well as modifying the scaling factor for the proton stripping reaction: (d, n), along with similar calculations in the PRECO-2006 program. In this case, the maximum region of the excitation function was successfully described; however, questions remain regarding the right edge of the excitation function, as very few experimental data are currently available, and the cross sections at the corresponding energies exhibit significant discrepancies.

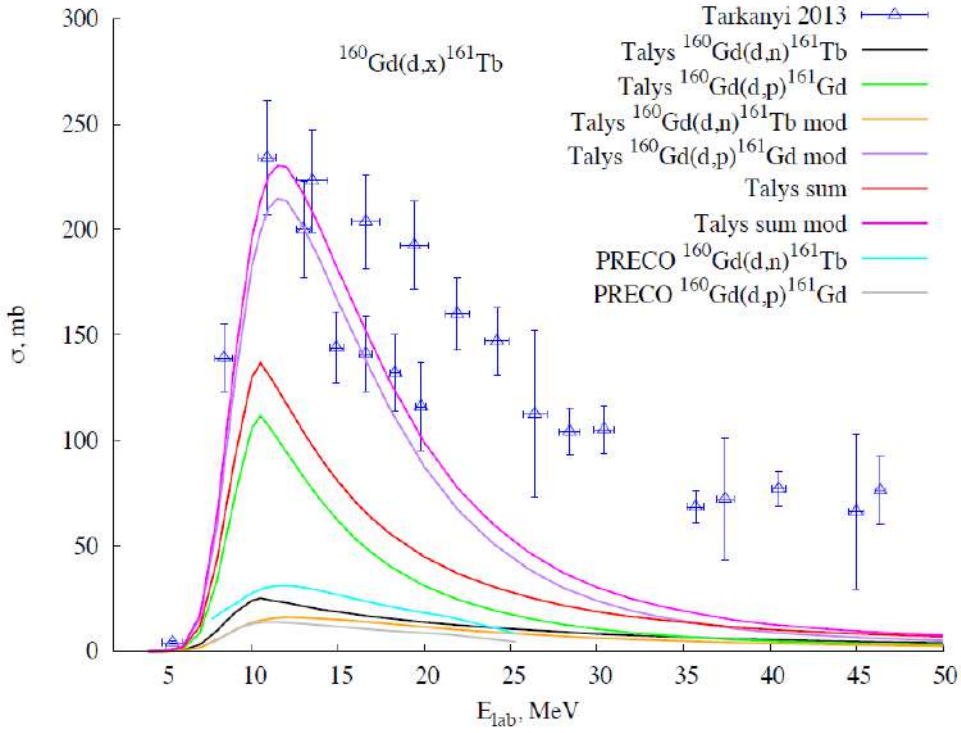


Figure 64 – Excitation function of the reaction $^{160}$Gd(d,x)$^{161}$Tb. The experimental data are taken from [173]. Black, green, red curves – theoretical calculations using the Talys program; orange, violet, purple curves – theoretical calculations using the Talys program with modified parameters (see more details in the text); turquoise and gray curves – theoretical calculations using the PRECO-2006 program taking into account direct processes.

Thus, the obtained results highlight the necessity of accounting for direct

processes [183] and can be applied to describe nuclear reactions leading to the formation of other radionuclides in the medium and heavy mass range, with incident deuteron energies up to 200 MeV [184]. It should be noted that assessing direct contributions is further complicated by the greater uncertainty in the deuteron-nucleus interaction potential compared to the nucleon-nucleus potential. However, due to the limited availability of experimental data, it is not possible to perform unambiguous model calculations in the energy range above 15 MeV. On the other hand, the relatively high maximum of the excitation function for the formation of $^{161}$Tb in the deuteron-induced reaction opens up prospects for its use in the industrial production of isotopes in medical and commercial low-energy cyclotrons. It is important to recognize that the presence of multiple open channels for this reaction can have a detrimental effect on the purity of the produced material, as it may contribute to the formation of radioactive impurity isotopes of other elements [33].

### 2.2.5 Experiments with irradiations of highly enriched targets containing tin isotopes: $^{117}$Sn and $^{119}$Sn to study the excitation functions of nuclear reactions: $^{117}$Sn(p,n)$^{117}$Sb and $^{119}$Sn(p,n)$^{119}$Sb

In this dissertation, experiments with using highly enriched $^{117}$Sn and $^{119}$Sn targets (85.5% enrichment) and a proton beam with energies of up to 14 MeV were carried out. The excitation functions of the reactions: $^{119}$Sn(p,n)$^{119}$Sb and $^{117}$Sn(p,n)$^{117}$Sb were investigated. These experiments were performed using proton beams from the MGC-20 cyclotron (V.G. Khlopin Radium Institute, Rosatom) with energies of up to 14 MeV. The motivation for studying these reactions stems from the limited availability of experimental data on their excitation functions in the EXFOR database [45], particularly in the region of the maximum.

The analysis of the presented excitation functions revealed that for the reaction $^{119}$Sn(p,n)$^{119}$Sb, the peak region and the energy regions on the declining slopes of the excitation function curve are not well studied. For the reaction: $^{117}$Sn(p,n)$^{117}$Sb, the

maximum of the excitation function was not identified at all. Preliminary analysis indicated that the maxima of the excitation functions occur in the proton energy range of 11 MeV to 13 MeV, which can be readily achieved using modern compact cyclotrons employed for the production of medical radionuclides (see Section 2.2.3). Consequently, a series of experiments was done to obtain the missing data on the cross sections of nuclear reactions with protons for medium-mass targets ($^{117}$Sn and $^{119}$Sn), where antimony radionuclides are produced in the output channels. These radionuclides are considered promising for their potential applications in medical technologies.

As previously noted, the excitation functions of the reactions: $^{119}$Sn(p,n)$^{119}$Sb and $^{117}$Sn(p,n)$^{117}$Sb were studied using targets highly enriched $^{119}$Sn and $^{117}$Sn isotopes, along with a proton beam with an initial energy of 14 MeV. In the experiment, the foil stacked method was utilized, where the cross section of the nuclear reaction producing the radionuclide was determined from the measured activity of the resulting radionuclide (see Section 2.2.2 for details). Stainless steel foils (60% Fe, 20% Cr, 20% Ni) with a thickness of 10 μm, which had proven effective in previous research stages, were used as monitors. The experimental setup and methodology are illustrated in Figure 65. To implement this, energy losses in all foils were modeled using the SRIM and GEANT4 programs [156, 157]. These programs were used to calculate the energy losses with high accuracy as the proton beam passed through each subsequent foil, taking into account the thicknesses, materials of the foils, and the initial energy of the proton beam. The experimental setup (see Figure 65) depicts the sequence of foils, their thicknesses, and the average energy of the proton beam after passing through each foil. The average proton energies were determined by considering the estimated errors in the calculations from each program, with corresponding weighting factors applied to each energy value. The calculations also accounted for energy losses at the aluminum input window of the target complex and in the helium volume used to cool the front part of the targets. Additionally, based on experimental experience gained from similar setups, aluminum foils with a thickness of 11 μm were included in the setup. These foils act as a buffer for recoil nuclei of the produced target radionuclide, which are emitted in the opposite direction. The recoil nuclei are absorbed by the aluminum foils, preventing them from

penetrating the corresponding target. This ensures the radionuclide production process is as "clean" as possible, allowing for the determination of its activity with minimal error [34]. Figure 66 shows the target holder with the complete set of target foils and monitor foils used in this experiment.

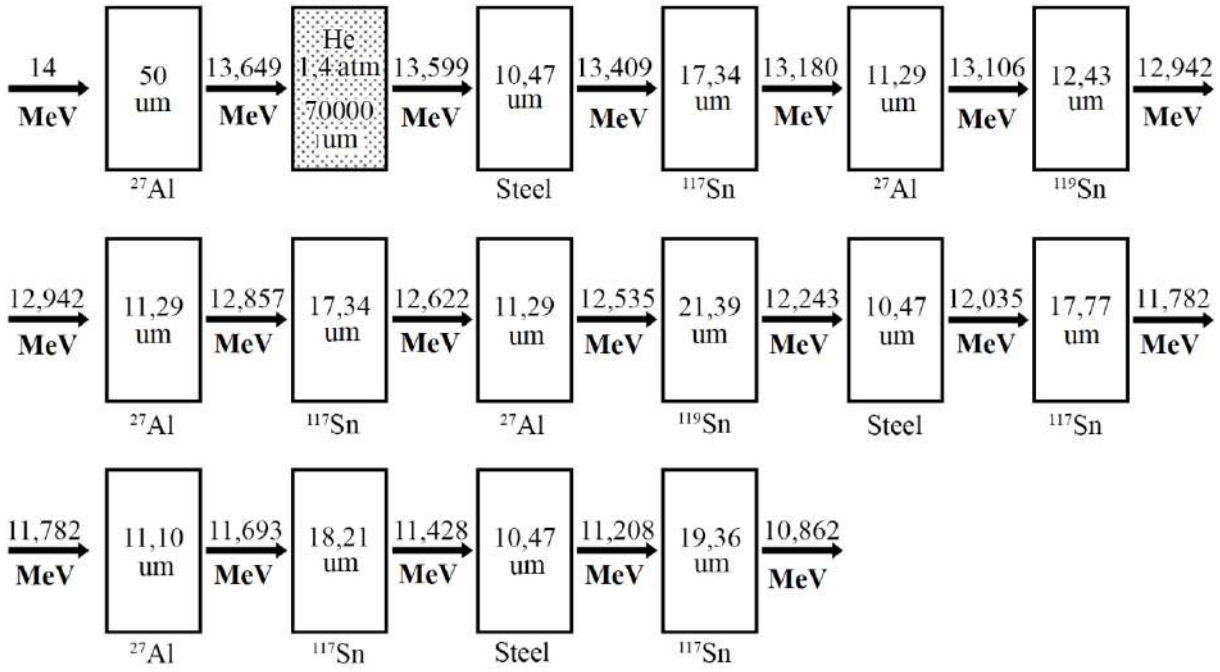


Figure 65 – Schematic diagram of the experiment for irradiating highly enriched foils containing tin isotopes ($^{119}$Sn and $^{117}$Sn) to study the excitation functions of the nuclear reactions: $^{119}$Sn(p,n)$^{119}$Sb and $^{117}$Sn(p,n)$^{117}$Sb [34].

Figure 66 – Target holder: a tantalum substrate (400 μm thick) into which target foils are inserted, as well as foils for monitoring beam parameters. The foils are clamped by a special aluminum ring.

Based on a detailed analysis of the monitor reactions, measured activities, and radionuclides produced in these foils, data on the beam current on the foils were obtained. This enabled the accurate determination of the cross sections of the studied nuclear reactions, taking into account the measured activity of antimony radionuclides in target foils made of highly enriched $^{117}$Sn and $^{119}$Sn isotopes. The activities of the antimony radionuclides produced in the target were measured by detecting gamma rays: a) for the $^{119}$Sb radionuclide (half-life 38.2 h), gamma rays with an energy of 23.9 keV were registered [185]; b) for the $^{117}$Sb radionuclide (half-life 2.8 h), gamma rays with an energy of 158.6 keV were registered [185].

The energy losses in the entire set of foils were also determined, when compared with the model calculations, resulted in an energy uncertainty of no more than 70 keV for each monitor foil and target foil. As a result, seven new cross-section values were obtained for the $^{119}$Sn(p,n)$^{119}$Sb reaction in the energy range of 7.5 to 13.1 MeV, with five points located in the region of the excitation function maximum (see Fig. 67).

Additionally, two new points in the energy range of 7.5–8 MeV align well with the general systematics of experimental data in the low-energy region (3 MeV to 9 MeV).

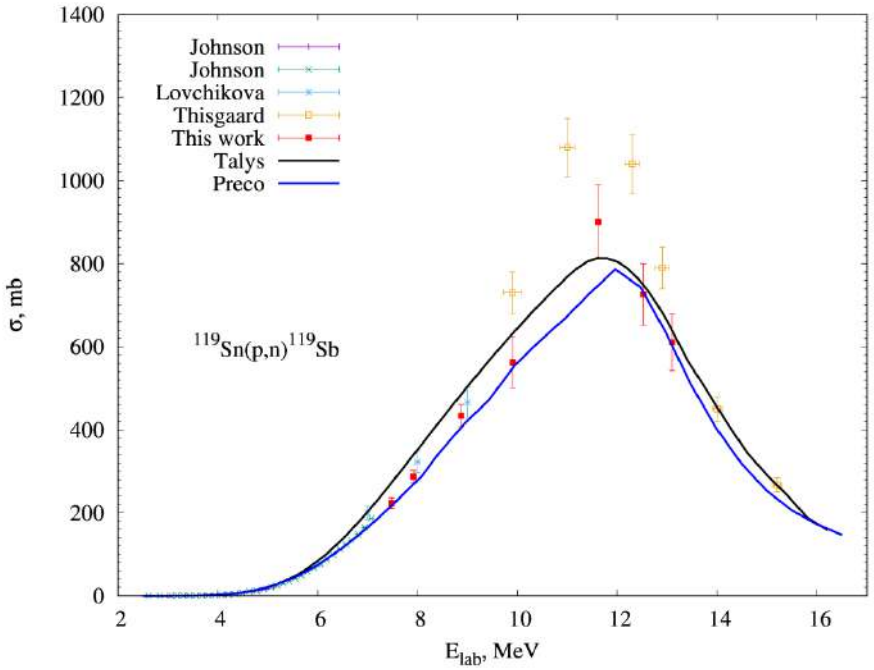


Figure 67 – Excitation function of the reaction $^{119}$Sn(p,n)$^{119}$Sb. Red squares represent experimental data obtained in this work; other points correspond to experimental data from other authors (EXFOR database [45]). The black curve shows theoretical calculations using the TALYS program, while the blue curve represents theoretical calculations using the PRECO-2006 program.

For the reaction $^{117}$Sn(p,n)$^{117}$Sb, five new data points were obtained for the first time in the region of the excitation function maximum, covering the energy range from 11.2 to 13.4 MeV (see Figure 68). It is noteworthy that experimental data for this reaction were previously unavailable in this energy region.

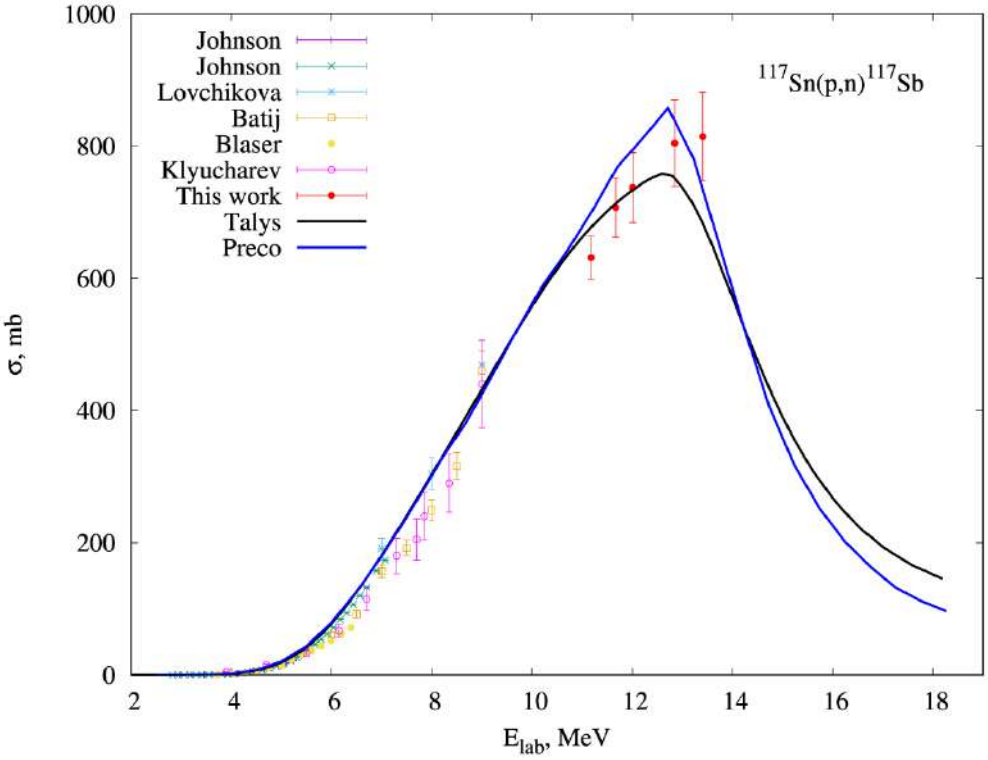


Figure 68 – Excitation function of the reaction $^{117}$Sn(p,n)$^{117}$Sb. Red circles represent experimental data obtained in this work; other points correspond to experimental data from other authors (EXFOR database [45]). The black curve shows theoretical calculations using the TALYS program, while the blue curve represents theoretical calculations using the PRECO-2006 program.

The initial analysis of the experimental data on the cross sections of these reactions raised the question of whether there are other reaction channels that produce antimony radionuclides ($^{117}$Sb and $^{119}$Sb) in the final state. Such channels include reactions with deuterons, for example: $^{117}$Sn(d,x)$^{117}$Sb. Since no experimental data exist for this reaction, a series of experiments were done at the MGC-20 cyclotron (NTC "Nuclear Physics" SPbPU) using a deuteron beam with an energy of 9 MeV to measure cross sections in the energy range of 6 MeV to 7.6 MeV. The measurement results are shown in Figure 69. It is clearly seen that the cross sections in the specified energy range are almost two times smaller than similar data for the reaction: 117Sn(p,n)117Sb (see Figure 68). This indicates limited prospects for the use of deuteron-induced reactions to produce the radionuclide $^{117}$Sb.

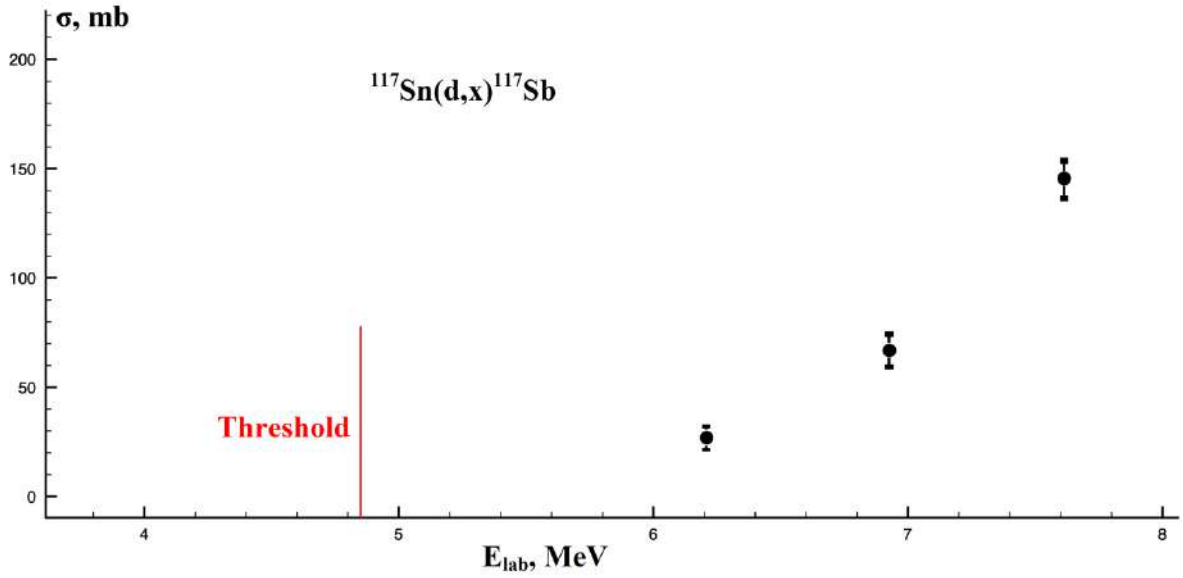


Figure 69 – Experimental values of the excitation function cross sections for the reaction: $^{117}$Sn(d,x)$^{117}$Sb. The threshold of this reaction is indicated by the red line.

Therefore, let us return to the consideration of (p,n) reactions and, based on previously developed algorithms for model calculations, perform preliminary modeling of the excitation functions for the two reactions under study. During these calculations, satisfactory agreement was observed between the calculated cross-section values and their experimental counterparts (see Figures 67–68, calculated dependencies obtained using the TALYS program and the PRECO-2006 program). However, to better describe the regions of the maxima, significantly more experimental cross-section values are required in these regions. Thus, based on the obtained excitation functions for the two nuclear reactions under study (see Figures 67–68), the basis has been laid for providing experiments aimed at a detailed investigation of the maxima of these functions.

### 2.2.6 Experiments on a detailed study of the excitation functions maxima of nuclear reactions: $^{117}$Sn(p,n)$^{117}$Sb and $^{119}$Sn(p,n)$^{119}$Sb. Systematics of the obtained data

At this stage of the experimental studies, a similar foil stack technique was used to investigate the left and right declines of the excitation function maximum for the

reactions $^{119}$Sn(p,n)$^{119}$Sb and $^{117}$Sn(p,n)$^{117}$Sb in detail. The experiments were done at the MGC-20 cyclotron (NTC "Nuclear Physics" SPbPU) using a proton beam with an energy of 15 MeV. In all cases, the activity of the produced antimony radionuclides was determined by detecting gamma rays, and the corresponding reaction cross sections were calculated for both new energy values and a number of values obtained during the previous experimental stage. As a result, across two stages of experimental studies, ten new data points were obtained for the first time in the region of the excitation function maximum for the reaction $^{119}$Sn(p,n)$^{119}$Sb, covering the energy range from 7.5 MeV to 13.1 MeV. Figure 70 shows the corresponding excitation function of this reaction, including the cross-section values obtained in this work (red squares) and experimental data from other authors (taken from the EXFOR database [45]). Within the measurement error, the results of this work are consistent with the currently available experimental data, and the left and right regions of the excitation function maximum reflect the general trend in its behavior. Figure 70 also presents the results of the corresponding modeling using the TALYS and PRECO-2006 programs, a detailed analysis of which will be provided in Section 2.2.6.

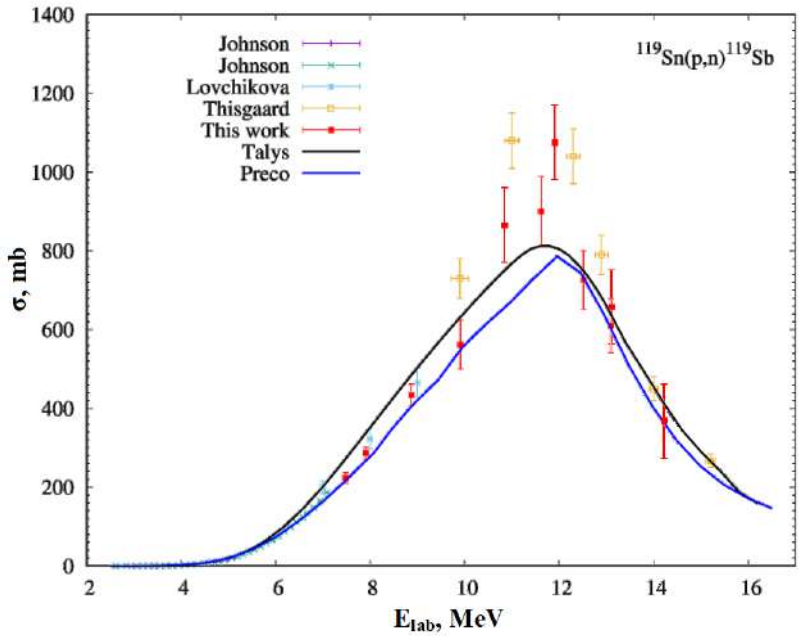


Figure 70 – Excitation function of the nuclear reaction $^{119}$Sn(p,n)$^{119}$Sb. Red squares represent experimental data obtained in this work; other points correspond to experimental data from other authors (EXFOR database [45]). The black curve shows theoretical calculations using the TALYS program, while the blue curve represents theoretical calculations using the PRECO-2006 program.

For the reaction $^{117}Sn(p,n)^{117}Sb$, 12 new data points were obtained in the region of the excitation function maximum, covering the energy range from 11 MeV to 14 MeV (see Figure 71, red points), during two experimental stages. Figure 71 also presents the results of the corresponding modeling using the TALYS and PRECO-2006 programs, with a detailed analysis provided in Section 2.2.6.

Since no experimental data were previously available for the reaction $^{117}Sn(p,n)^{117}Sb$ in this energy region, the results obtained in this work represent the only experimental data to date.

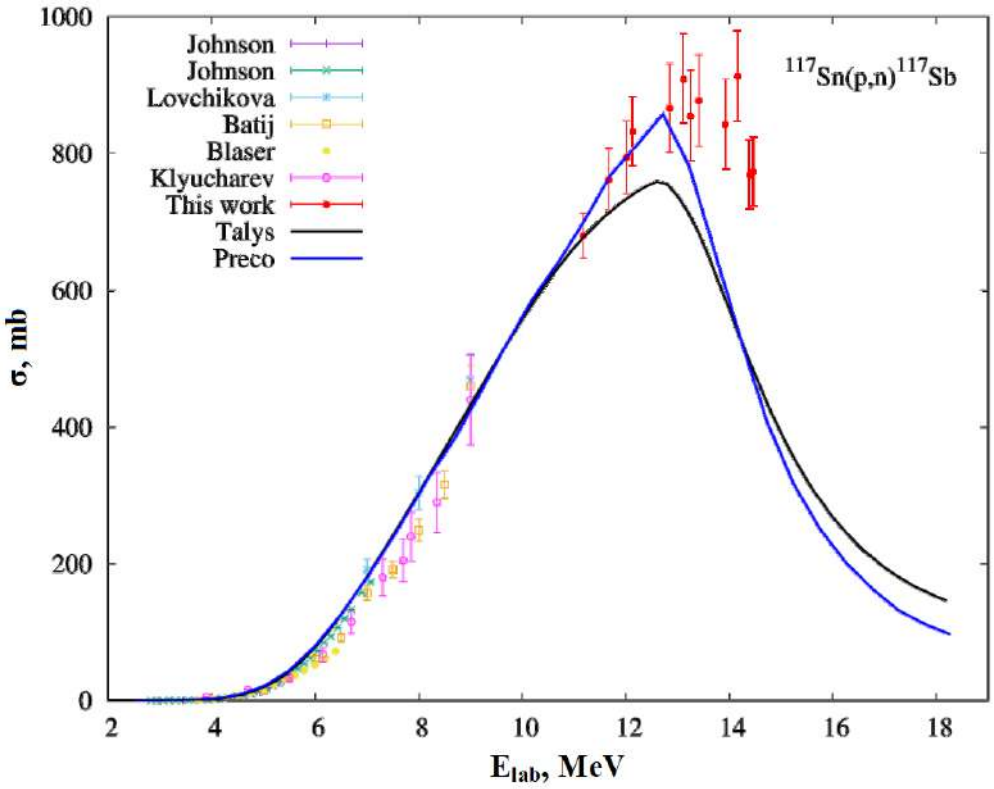


Figure 71 – Excitation function of the nuclear reaction $^{117}Sn(p,n)^{117}Sb$. Red circles represent experimental data obtained in this work; other points correspond to experimental data from other authors (EXFOR database [45]). The black curve shows theoretical calculations using the TALYS program, while the blue curve represents theoretical calculations using the PRECO-2006 program.

Thus, the results of the nuclear reactions: $^{117}Sn(p,n)^{117}Sb$ and $^{119}Sn(p,n)^{119}Sb$ excitation functions experimental studies have provided comprehensive data for further theoretical investigations into the processes and mechanisms underlying the formation of these medium-mass nuclear systems.

### 2.2.7 Selection of theoretical models for analyzing the excitation functions of nuclear reactions: $^{117}Sn(p,n)^{117}Sb$ and $^{119}Sn(p,n)^{119}Sb$. Analysis of these reactions using theoretical models

The excitation functions of nuclear reactions leading to the formation of antimony isotopes ($^{117}Sb$ and $^{119}Sb$) in the output channels, which are used in medical technologies, were studied. Within the framework of this work, nuclear-physical models were used in conjunction with a developed theoretical approach, enabling the description of the processes involved in the formation and decay of these nuclear systems into specific channels.

Modeling of the nuclear reactions $^{117}Sn(p,n)^{117}Sb$ and $^{119}Sn(p,n)^{119}Sb$ excitation functions along with the corresponding results, is shown in Figures 70 and 71. In the TALYS program, based on the combination of the incident nucleus and the target nucleus (using systematics and structural parameters of nuclei stored in the program database), "standard" parameters for the models are defined, and the cross sections of the most typical reactions are calculated. However, these "standard" parameters do not always show good agreement between theoretical calculations and experimental data. Therefore, it is necessary to adjust the model parameters to achieve the best possible agreement between theoretical and experimental results. Such parameter optimization was performed for the reaction $^{119}Sn(p,n)^{119}Sb$ (black curve in Figure 70). In the energy region preceding the peak of the excitation function, the cross section of the compound nucleus formation, which is determined by the interaction potential, plays a dominant role. This potential (taken from [186]) was adapted in this work to describe the reaction under study. Improved agreement between the theoretical calculations and the experimental data for the decay of the excitation function was achieved by adjusting the level density parameters (using the Back-Shifted Fermi Gas Model [187]) of the residual $^{119}Sb$ nucleus.

Upon analyzing the obtained distributions, several features inherent to the processes of such reactions were identified. For the excitation functions involving the

formation of Sb radionuclides in the output channels, better agreement with experimental data was achieved using the Koning-Delaroche (KD) potential [171] compared to the Becchetti-Greenlees (BG) potential (or rather its parameterization) [188]. The KD potential was used both to calculate the cross sections for the formation of the compound nucleus and to estimate the cross sections of the other reactions. Calculations using the BG potential systematically overestimated the cross sections compared to the experimental values, except for the $^{119}$Sn nucleus, where the experimental points in the maximum region lie relatively high. Additionally, the BG potential performs poorly in the energy region close to the reaction threshold. Consequently, in Figures 70 and 71, the excitation function in the PRECO program was modeled using the KD potential. It is also note, that the normalization constant for the density of single-particle states (K) in the PRECO program is set to K=15 by default. Its influence primarily extends to the energy region above the cross section maximum and is responsible for reducing the excitation function cross section. In the presented model calculations, the best agreement with the experimental data was achieved for K=18. The intensity of gamma decays competing with secondary particle emission was estimated by introducing the parameter Rg. In the presented calculations, this parameter was set to 0.005, based on the existing systematics for nuclei in the mass range A = 27 – 93. The simulation results demonstrated that this parameterization satisfactorily describes the behavior of the excitation function for the (p,n) reaction on the tin nucleus near A = 119 [34].

A general analysis of the performed model calculations of the two excitation functions shows that the PRECO and Talys programs give different results when describing the maximum region, both in determining the cross section and for the corresponding energy of protons bombarding the target. This can be explained by the absence or insufficient amount of experimental data in the maximum region and the use of a limited number of parameters in the models used for theoretical calculations. It is also note an interesting feature of the theoretical calculations in the region of low excitation energies (to the left of the maximum). By varying certain parameters, it is

possible to achieve the best agreement with experimental data using both PRECO and Talys programs.

The analysis of the $^{117}Sn(p,n)^{117}Sb$ reaction shows that a sufficiently good description within the PRECO formalism with the density parameter of single-particle states has been achieved for it: K=18 (see Figure 71). Also good agreement in the low energy region (up to 9 MeV) is achieved using the Talys program. However, the maximum region is rather sensitive to changes in the model parameters, and in this case one can need to change the level density parameter to obtain a satisfactory agreement with the experimental data.

For the $^{119}Sn(p,n)^{119}Sb$ reaction, initial theoretical analysis revealed uncertainties in the cross-section estimates in the region of the excitation function maximum when using different theoretical models. This uncertainty was primarily due to the lack of sufficient experimental data. To extend the energy range of the excitation function and supplement it with experimental data, measurements of the corresponding cross sections in the region of the excitation function maximum were carried out. Based on the obtained model calculations and incorporating the new experimental data, the parameters of the models were updated. Similar to the $^{117}Sn(p,n)^{117}Sb$ reaction, a good description of the $^{119}Sn(p,n)^{119}Sb$ reaction has been achieved within the framework of the PRECO formalism, using the single-particle state density parameter K = 18 and the BG potential (its parameterization) (see Figure 70 and the description above). Good agreement was also achieved using the Talys program with a similar potential and choice of the level density parameter. Analysis of the excitation function of this reaction demonstrates that the region of the maximum is highly sensitive to changes in the model parameters. However, in this work, it was possible to satisfactorily describe this part of the excitation function.

In conclusion, one can note that the calculations performed enabled the prediction and detailed study of various states of nuclear systems in the medium-mass region. The models used provided estimates of the probability of reaction product formation. Thus, the obtained results allowed for a comprehensive study of the excitation functions of the nuclear reactions: $^{117}Sn(p,n)^{117}Sb$ and $^{119}Sn(p,n)^{119}Sb$. The maxima of the excitation

functions for these reactions were determined, which provides a basis for further industrial production of antimony radionuclides. These radionuclides are promising for use in advanced medical technologies for the therapy and diagnosis of oncological diseases (see Section 2.2.8).

### 2.2.8 Excitation function analysis of (p,n) reactions with tin isotopes at mass numbers: 115, 116, 118, 120, 122, with formation of antimony radionuclides in exit channels

The excitation functions of nuclear reactions involving tin isotopes (in the input channel) with mass numbers: 115, 116, 118, 120, and 122, and with the formation of the corresponding antimony radionuclides in the output channels were modeled. Based on the available experimental data, the energy region up to the maximum (on the left side) of the excitation functions for the (p,n) reactions was investigated using similar model calculations (see Section 2.2.6).

For a comprehensive analysis of (p,n)(p,n) reactions on tin isotopes, resulting in the formation of antimony radionuclides in the output channels, and to evaluate the role of parameters associated with theoretical models, studies of the excitation functions of reactions: $^{115}$Sn(p,n)$^{115}$Sb, $^{116}$Sn(p,n)$^{116}$Sb, $^{118}$Sn(p,n)$^{118}$Sb, $^{120}$Sn(p,n)$^{120}$Sb, $^{122}$Sn(p,n)$^{122}$Sb, $^{124}$Sn(p,n)$^{124}$Sb were carried out. The experimental data were taken from the nuclear reactions database (EXFOR database [45]). As was obtained during the analysis of the reactions: $^{117}$Sn(p,n)$^{117}$Sb and $^{119}$Sn(p,n)$^{119}$Sb the parameters of model calculations have a significant influence in the energy region in the vicinity of the maximum of the excitation function. This is explained by the fact that, in this region, the cross section of the (p,n) reaction begins to be suppressed by the opening of competing channels. The probability of a particular channel being realized depends on the density of states in the residual nuclei. The most significant competing channel is (p,2n), and the maximum of the excitation function is formed approximately at the energy threshold for the opening of this channel. Thus, to determine the boundaries

within which the parameters of theoretical calculations should exist, experimental data are required for a broader energy range. Currently, the experimental data for the (p,n) reaction on tin isotopes mainly cover the energy range up to the maximum of the excitation function. In this case, the cross section of the reaction is determined by the probability of the formation of a compound nucleus, which is calculated using the optical potential for nuclei in the input channel. Therefore, the energy range up to the maximum of the excitation function allows for the verification of the applicability of the optical potential used in the analysis. In theoretical calculations using the Talys program, default parameters were adopted as the base parameters, and the Back-Shifted Fermi Gas Model [187] was used to describe the level density distribution.

#### 2.2.8.1 Analysis of the excitation function of reaction: $^{115}$Sn(p,n)$^{115}$Sb

The results of the excitation function for the reaction $^{115}$Sn(p,n)$^{115}$Sb studies, obtained using the modeling technique developed in this work (see Section 2.2.6), are presented in Figure 72 in comparison with the experimental data. Analysis of this distribution demonstrates that the modeling accurately describes the available experimental data when using the Konig-Delaroche (KD) potential [171].

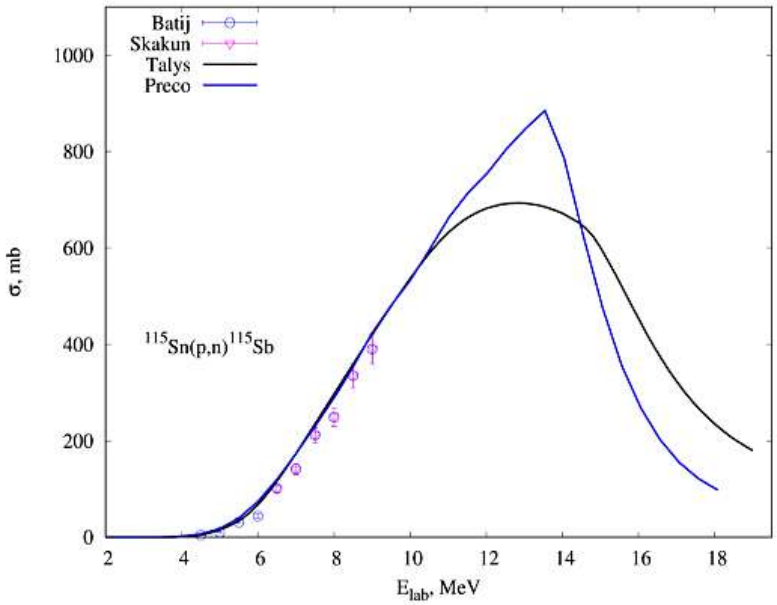


Figure 72 – Excitation function of the nuclear reaction: $^{115}$Sn(p,n)$^{115}$Sb. The experimental data (EXFOR database [45]) are shown, corresponding to the formation of the radionuclide $^{115}$Sb in the (p,n) reaction on targets enriched with the isotope $^{115}$Sn. The black curve represents theoretical calculations using the Talys program, while the blue curve represents theoretical calculations using the PRECO-2006 program.

In addition to the data on the reaction $^{115}$Sn(p,n)$^{115}$Sb, there are also experimental results for the formation of the radionuclide $^{115}$Sb in the (p,xn) reaction on natural tin ($^{nat}$Sn). For such reactions, the dominant channels are $^{114}$Sn(p,γ)$^{115}$Sb and $^{115}$Sn(p,n)$^{115}$Sb (see Figure 73). From the distribution, it follows that above the energy of 8 MeV and up to the threshold energy of 13.5 MeV for the beginning of the reaction $^{116}$Sn(p,2n)$^{115}$Sb, the cross section of the reaction on natural tin is determined mainly by the reaction $^{115}$Sn(p,n)$^{115}$Sb.

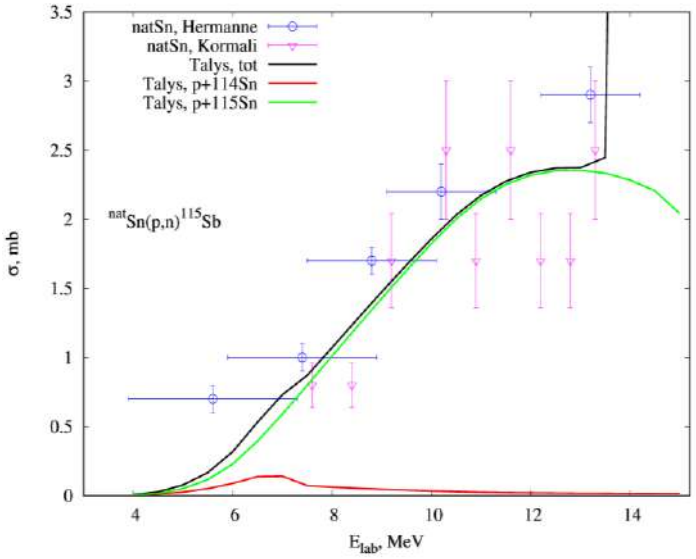


Figure 73 – Excitation function of the nuclear reaction $^{nat}Sn(p,xn)^{115}Sb$. The experimental data (EXFOR database [45]) are shown for the formation of the isotope $^{115}Sb$ in the (p,xn) reaction on natural tin. The red curve represents the theoretical calculation using the Talys program for the $^{114}Sn(p,\gamma)^{115}Sb$ reaction channel; the green curve represents the theoretical calculation using the Talys program for the $^{115}Sn(p,n)^{115}Sb$ reaction channel; and the black curve represents the theoretical calculation using the Talys program for the sum of these two reaction channels.

Figure 74 shows the excitation function for the reaction $^{115}Sn(p,n)^{115}Sb$, taking into account the experimental points obtained by renormalizing the data from the reaction $^{nat}Sn(p,xn)^{115}Sb$. A significant experimental error in the estimated data, caused by the low content of the $^{115}Sn$ isotope in the natural mixture (0.34%), does not allow for an unambiguous estimation of the cross section in the region of the expected maximum. In addition, the rightmost point in the figure corresponds to an energy of (13.2±1) MeV, the range of which covers the region above the threshold of the reaction $^{116}Sn(p,2n)^{115}Sb$. As a result, the cross section for this point may be overestimated. Despite this, it is possible to estimate the energy range for the maximum of the excitation function of this reaction, which lies between 12.8 and 13.5 MeV.

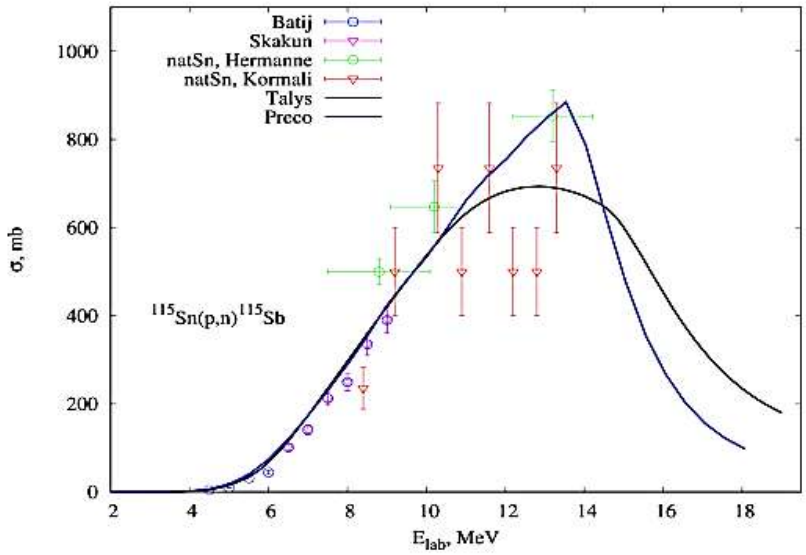


Figure 74 – Excitation function of the nuclear reaction $^{115}$Sn(p,n)$^{115}$Sb. The experimental data (EXFOR database [45]) are shown for the formation of the isotope $^{115}$Sb, taking into account the experimental points obtained by renormalizing the data from the reaction $^{nat}$Sn(p,xn)$^{115}$Sb. The black curve represents theoretical calculations using the Talys program, while the blue curve represents theoretical calculations using the PRECO-2006 program.

#### 2.2.8.2 Analysis of the excitation function of reaction: $^{116}$Sn(p,n)$^{116}$Sb

For the reaction $^{116}$Sn(p,n)$^{116}$Sb, the modelling was performed using two types of potentials: the Konig-Delaroche (KD) potential and the Bechetti-Greenlees (BG) potential [188]. The results are presented in Figure 75. Using the simulation performed, estimates were made for the excitation function maximum region. Nearly all calculations indicate that this region lies between 13.4 and 14.2 MeV.

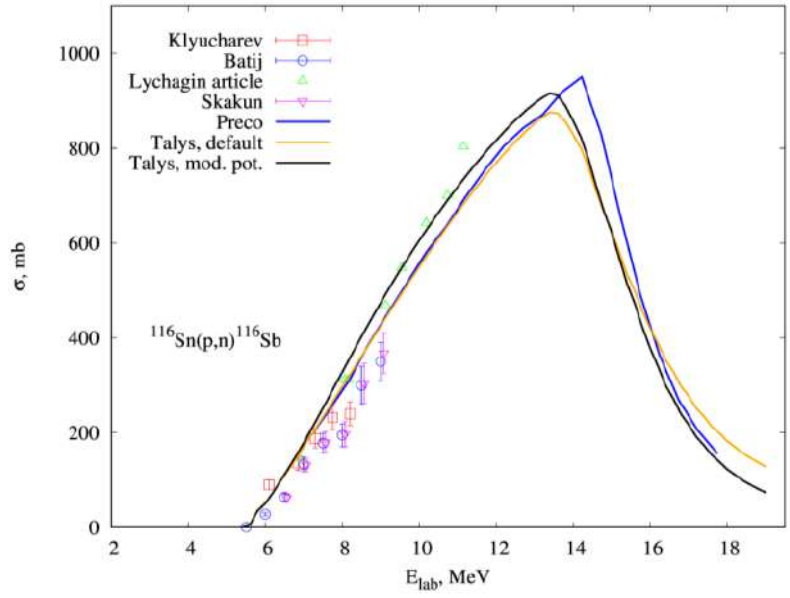


Figure 75 – Excitation function of the nuclear reaction $^{116}$Sn(p,n)$^{116}$Sb. Experimental data are taken from the EXFOR database [45]. The black curve represents theoretical calculations using the Talys program with modified parameters; the yellow curve represents theoretical calculations using the Talys program with default parameters; and the blue curve represents theoretical calculations using the PRECO-2006 program.

### 2.2.8.3 Analysis of the excitation function of reaction: $^{118}$Sn(p,n)$^{118}$Sb

The excitation function for the reaction $^{118}$Sn(p,n)$^{118}$Sb is shown in Figure 76. Model calculations using the Konig-Delaroche (KD) potential show good agreement with the experimental data. For the PRECO-2006 program, agreement with the experimental data is achieved with the single-particle state density parameter set to K=18.

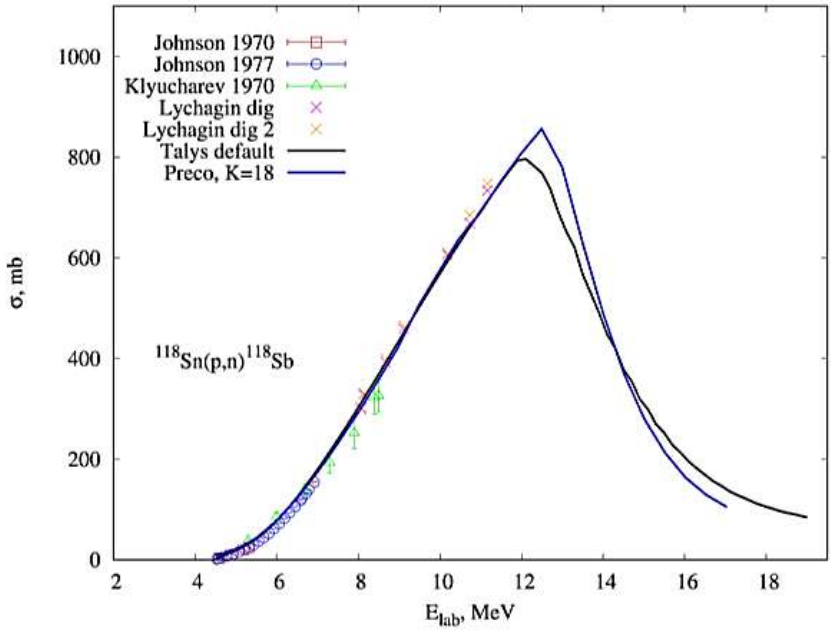


Figure 76 – Excitation function of the nuclear reaction $^{118}$Sn(p,n)$^{118}$Sb. Experimental data are taken from the EXFOR database [45]. The black curve represents theoretical calculations using the Talys program with default parameters; the blue curve represents theoretical calculations using the PRECO-2006 program with the single-particle state density parameter set to K = 18.

#### 2.2.8.4 Analysis of the excitation function of reaction: $^{120}$Sn(p,n)$^{120}$Sb

Figure 77 shows the excitation function for the reaction $^{120}$Sn(p,n)$^{120}$Sb. The spread of experimental data is attributed to the presence of a metastable state in the $^{120}$Sb nucleus. The formation cross section of this metastable state, at energy of approximately 9 MeV, is estimated experimentally to be ~5% of the total formation cross section of $^{120}$Sb in this reaction. In Figure 77, the experimental data labeled with the index (G) represent the formation cross section of $^{120}$Sb in the ground state.

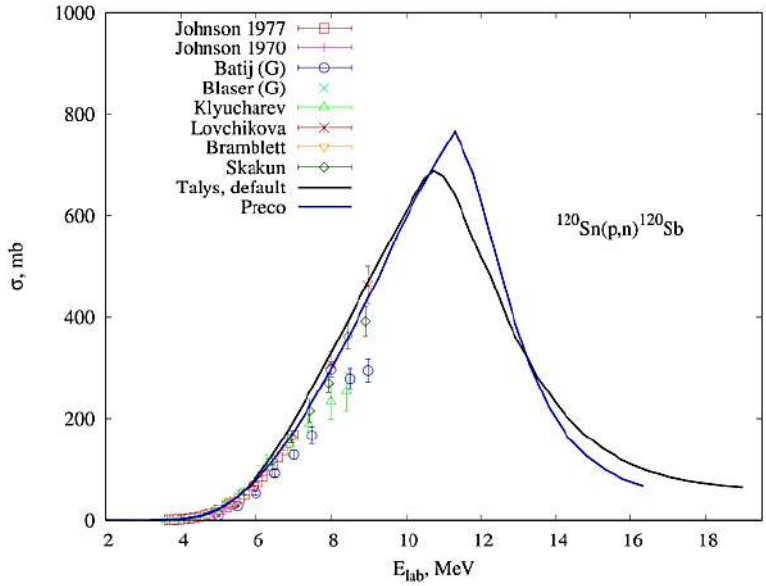


Figure 77 – Excitation function of the nuclear reaction $^{120}$Sn(p,n)$^{120}$Sb. Experimental data are taken from the EXFOR database [45]. The black curve represents theoretical calculations using the Talys program with default parameters; the blue curve represents theoretical calculations using the PRECO-2006 program.

### 2.2.8.5 Analysis of the excitation function of reaction: $^{122}$Sn(p,n)$^{122}$Sb

Figure 78 shows the excitation function for the reaction $^{122}$Sn(p,n)$^{122}$Sb. Also shown are the experimental data points for the cross section of $^{122}$Sb formation in the ground state (labeled with the index (G)). The model curves provide a good description of the experimental data for the cross sections of this reaction.

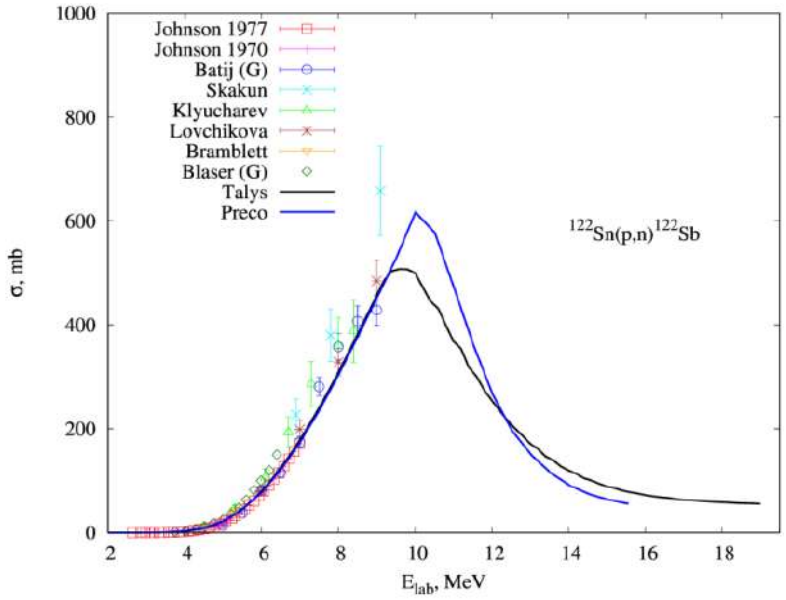


Figure 78 – Excitation function of the nuclear reaction $^{122}$Sn(p,n)$^{122}$Sb. Experimental data are taken from the EXFOR database [45]. The black curve represents theoretical calculations using the Talys program with default parameters; the blue curve represents theoretical calculations using the PRECO-2006 program.

### 2.2.8.6 Analysis of the excitation function of reaction: $^{124}$Sn(p,n)$^{124}$Sb

The excitation function for the reaction $^{124}$Sn(p,n)$^{124}$Sb was measured with the highest statistics. As a result, this reaction is well suited for testing the parameters of the models used. The results of calculating the excitation function for different parameter values are shown in Figure 79. In general, acceptable agreement with the experimental data was achieved. When using the default parameters embedded in the Talys program, the cross section is underestimated, and the maximum is shifted to the left relative to the experimental values. Parameters affecting the level densities can improve the description of this reaction. The parameter "colenhance" (as indicated in the figure) accounts for the influence of collective effects on the level density. This leads to a more accurate alignment of the excitation function maximum and its behavior on the decline with the experimental data. Modifying the level density of the residual $^{124}$Sb nucleus also helps optimize the modeling; Figure 79 shows two examples of parameterization, labeled as lev. dens (1) and lev. dens (2). In this case, to achieve a match between the calculated distributions and the experimental data, it is possible to renormalize the

permeability coefficient for gamma transitions (labeled as Talys gamma in the figure). This parameter determines the probability of the (n,γ) reaction, which is also related to the level density in the residual nucleus. Thus, while varying a number of parameters can yield similar results, it is not possible to draw definitive conclusions about the complete parameterization of the model used.

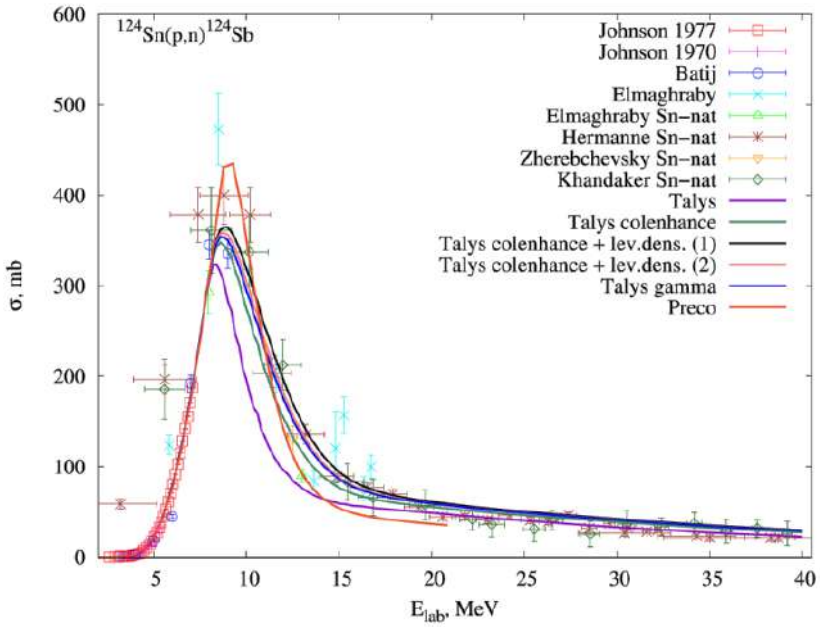


Figure 79 – Excitation function of the nuclear reaction $^{122}$Sn(p,n)$^{122}$Sb. Experimental data were taken from the EXFOR database [45]. Calculated curves were obtained using the Talys and PRECO-2006 programs (see details in the text).

### 2.2.8.7 Systematics of identified maxima of (p,n) reaction excitation functions on tin isotopes with mass numbers from A = 115 to A = 124

Taking into account all the model approximations performed to study the maxima of the excitation functions of nuclear reactions on tin isotopes (from A = 115 to A = 124), a systematic analysis of the positions of these maxima (peaks of the excitation functions) for (p,n) reactions was provided. The results of modeling using the Talys and PRECO-2006 programs are presented in Table 3, which lists the proton energies at the maxima of the excitation functions for (p,n) reactions on tin isotopes, resulting in the formation of antimony radionuclides in the output channels.

Table 3 – Proton energy at the maximum of excitation functions for (p,n) reactions occurring on tin isotopes.

| Target | $E_{peak}$, MeV (Talys) | $E_{peak}$, MeV (Preco) |
|---|---|---|
| $^{115}$Sn | 12.8 | 13.5 |
| $^{116}$Sn | 13.4 | 14.2 |
| $^{117}$Sn | 12.6 | 12.7 |
| $^{118}$Sn | 12.1 | 12.5 |
| $^{119}$Sn | 11.6 | 12.0 |
| $^{120}$Sn | 10.7 | 11.3 |
| $^{122}$Sn | 9.6 | 10.0 |
| $^{124}$Sn | 8.8 | 9.3 |

Note that the calculations performed using the PRECO-2006 theoretical formalism, give slightly overestimated values for the excitation function peak positions compared to the Talys calculations. However, the general trend shows that in both cases, the peak position shifts to lower energies as the mass number of the tin isotope used as a target increases. This can be explained by a decrease in the threshold energy of the competing (p,2n) reaction from $^{115}$Sn to $^{124}$Sn, which gradually begins to dominate over the main (p,n) channel. The thresholds of the (p,2n) reaction for the corresponding tin isotope targets have the following values: 14.5 MeV ($^{115}$Sn), 13.5 MeV ($^{116}$Sn ), 12.5 MeV ( $^{117}$Sn ), 12.0 MeV ( $^{118}$Sn ), 11.0 MeV ( $^{119}$Sn ), 10.6 MeV ($^{120}$Sn ), 9.3 MeV ($^{122}$Sn ), 7.9 MeV ($^{124}$Sn ). Figure 80 shows the distribution of the averaged values of the excitation function maxima with the corresponding weights (the error estimate taking into account the comparison with the available experimental data is no more than 5% and 7% for the corresponding Talys and PRECO-2000 calculations) depending on the thresholds (p, 2n) of the reactions for the corresponding tin isotopes. It is possible to analyze the dynamic features of the studied nuclear reactions and the influence of an additional neutron on the decay modes of the compound nuclear system formed as a result of such reactions. Note that $^{115}$Sn is an exception to this trend based on model estimates, the position of the excitation function maximum lies significantly below the threshold for the (p,2n) reaction.

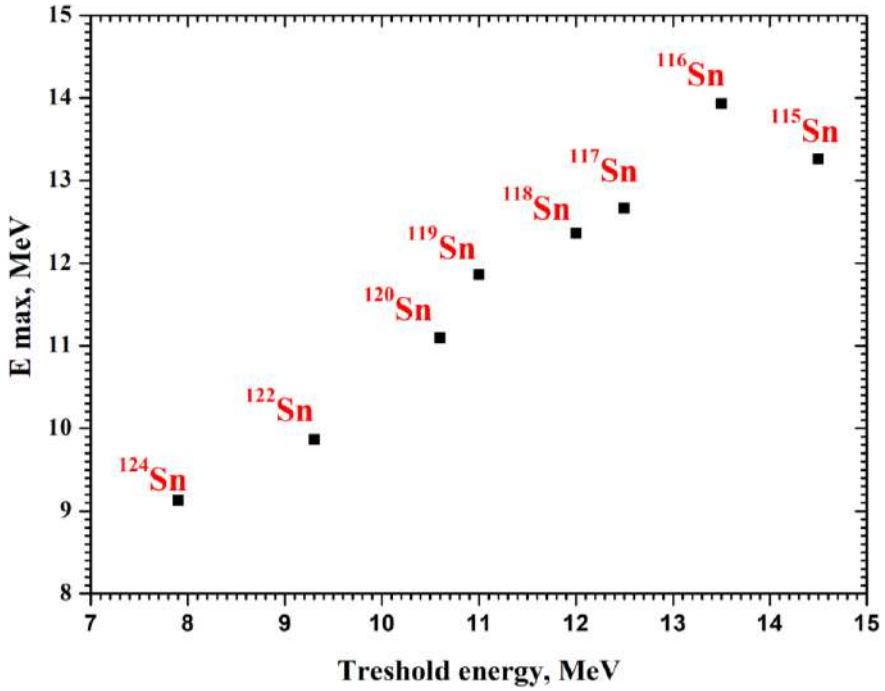


Figure 80 – Distribution of the average values of the excitation function maxima for (p, n) reactions with tin isotopes depending on the thresholds of (p, 2n) reactions for the same tin isotopes.

In conclusion, it should be noted that the use of the Konig-Delaroche (KD) potential and the corresponding adjustment of parameters affecting the level densities allows for a reasonably accurate description of the excitation function behavior for the (p,n) reactions leading to the formation of antimony isotopes in the output channels. This enables a detailed analysis of such reactions dynamics within the given mass range.

### 2.2.9 Thick target yield functions for the investigated (p,n) reactions with formation of radionuclides $^{117}$Sb and $^{119}$Sb in exit channels

For applied work with the aim of producing antimony radionuclides in proton accelerators, based on the obtained experimental data for the excitation functions of reactions: $^{117}$Sn(p, n)$^{117}$Sb and $^{119}$Sn(p, n)$^{119}$Sb (see Sections 2.2.4 and 2.2.5), the thick-target yield functions were obtained. The results are shown in Figures 81 and 82, respectively.

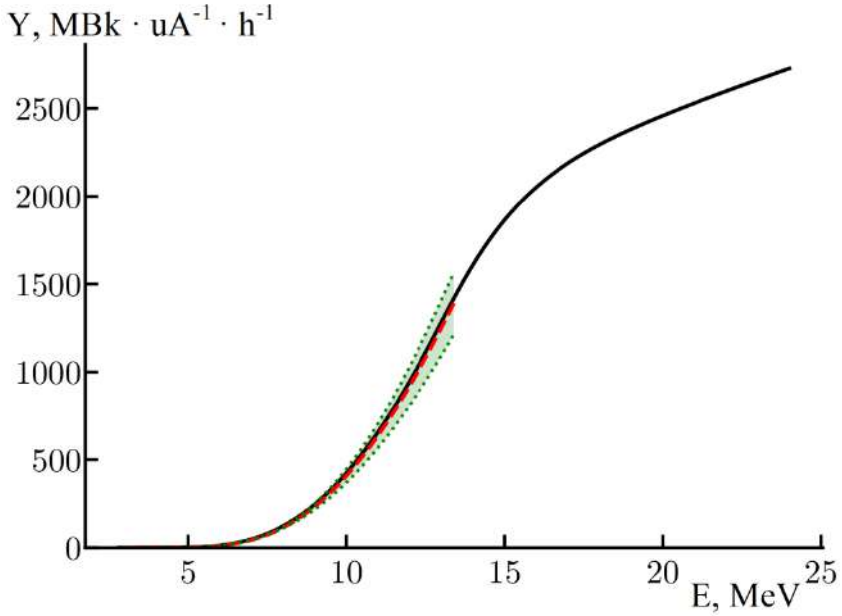


Figure 81 – Thick-target yield function for the reaction: $^{117}$Sn(p,n)$^{117}$Sb. The red dashed curve represents the yield calculated based on the approximation of the experimental excitation function obtained in this work; the black curve represents the theoretical calculation using the excitation function obtained from Talys with default parameters; and the green area indicates the uncertainty of the yield function due to errors and spread in the experimental data used for the approximation [33].

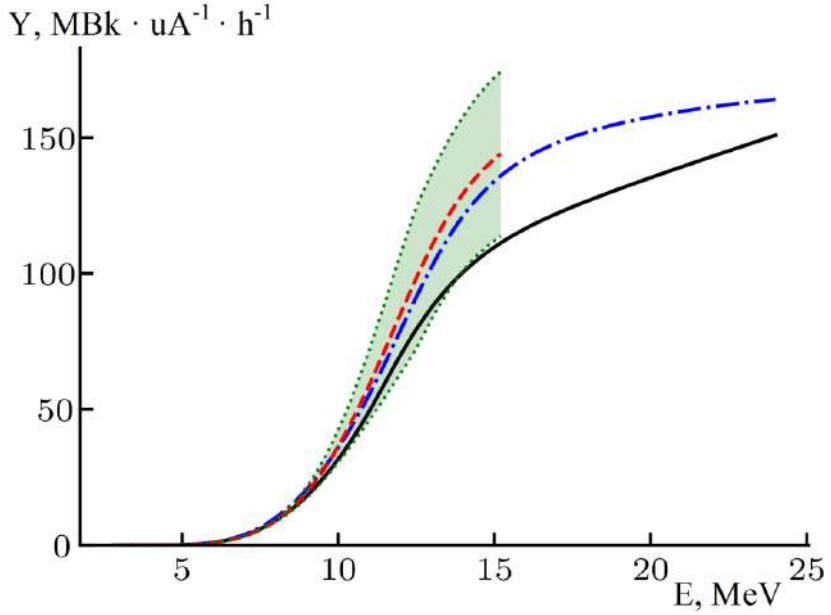


Figure 82 – Thick-target yield function for the reaction: $^{119}$Sn(p,n)$^{119}$Sb. The red dashed curve represents the yield calculated based on the approximation of the experimental excitation function obtained in this work; the black curve represents theoretical calculations using the excitation function obtained from Talys with default parameters; the blue dash-dotted curve represents theoretical calculations using the excitation function obtained from Talys with modified parameters; and the green area indicates the uncertainty of the yield function due to errors and spread in the experimental data used for the approximation [33].

The analysis of the presented distributions yields several important results: 1) it was found that, in the energy range from 5 to 12 MeV, the calculations are in good agreement with the experimental data for both reactions. For the reaction $^{117}Sn(p,n)^{117}Sb$, the theoretical data obtained completely match the experimental data within the specified energy range. 2) As an applied example, we can cite calculations showing that irradiating a tin target for 6 hours with a proton beam of relatively low current (10 μA) and an energy of 15 MeV can produce radionuclides $^{119}Sb$ and $^{117}Sb$ with activities of approximately 8 GBq and 120 GBq, respectively. This provides an excellent opportunity to apply the performed calculations to the production of $^{117}Sb$ radionuclides in reactions with protons at energies greater than 15 MeV, i.e., in energy ranges where experimental data are currently unavailable [33].

# CONCLUSION

In this dissertation, modern theoretical, experimental, and computational methods of nuclear physics research were applied to study nuclear reactions that play an important role in nucleosynthesis processes. For nuclear reactions leading to the formation of radionuclides in the medium-mass range, answers to a number of questions related to the excitation functions of such reactions were obtained. These findings have practical applications in nuclear physics technologies for producing radionuclides used in modern nuclear medicine for the diagnosis and therapy of oncological diseases.

Most of the problems addressed in this dissertation were solved for the first time. Using an experimental setup equipped with precision charge-sensitive preamplifiers and a multisensor system for monitoring beams of charged particles and heavy ions, the energy spectrum of alpha particle scattering on a highly enriched target, the neutron-rich nucleus $^{14}$C was measured with high resolution. This allowed for the precise identification of the elastic scattering peak and the separation of closely located excited states in the nuclear systems $^{14}$C and $^{12}$C. Furthermore, by utilizing modern techniques for focusing and guiding the accelerator beam (independent of the accelerator design) and on-line diagnostics, it became possible to effectively study the reactions of alpha particles with neutron-rich, alpha-cluster-unstable targets.

In the study of nuclear reactions: $^{14}C + {}^{12}C \rightarrow {}^{26}Mg^* \rightarrow {}^{22}Ne^* \rightarrow {}^{18}O$ high-spin, highly excited states were discovered in the $^{22}$Ne nucleus. In experimental studies of the characteristics of this nuclear reaction, a specialized method of processing detector signals based on pulse shape analysis was used. This method enabled the identification of energy bands corresponding to protons, deuterons, tritons, alpha particles, and light nuclei: $^{6,7}$Li, $^{9,10}$Be, $^{11}$B, $^{12,14}$C. Also, for the first time in such a reaction, exotic neutron-rich nuclei $^{6}$He were registered and the corresponding reaction channel: $^{14}C(^{12}C,^{6}He)^{20}Ne^*$ was discovered. A detailed analysis of the high-spin, highly excited states observed in the $^{22}$Ne nucleus was carried out, enabling their identification as rotational bands with a specific structure characteristic of nuclear molecules. The processes involving the formation of alpha clusters in neutron-rich nuclei were

analyzed, leading to the conclusion that such states are formed through a scenario similar to that in self-conjugate nuclei. Evidence for this is provided by the formation of high-spin rotational bands with a molecular structure. Thus, the addition of neutrons to the nuclear system enhances the stability of cluster states.

The nuclear reaction $^{12}C + ^{16}O$ was studied in detail. The use of a specialized complex potential enabled the description of the angular distribution of the reaction products across a wide energy range, including states that can be attributed to rotational bands (molecular configurations). A large number of resonances were predicted for a specific region of excitation energies in the compound nucleus. The developed theoretical analysis, applied to the angular distributions of the $^{12}C + ^{16}O$ reaction, allowed for the identification of so-called "false resonances" associated with the rotational band. Additionally, resonances in the optical potential were identified in this reaction, and it was demonstrated that their positions exhibit weak dependence on the type of potential used.

The processes of nuclear fusion, which play an important role in astrophysical phenomena (particularly fusion reactions at energies near the Coulomb barrier), were analyzed. Corresponding calculations of both the astrophysical S-factor and the reaction cross section were performed using potentials derived for describing nuclear reactions in the light mass range. A method for analyzing the astrophysical S-factor, based on the rectangular potential well formalism, was also proposed and developed. Using this model, it was demonstrated that the contribution to the reaction at short distances is dominated by the Coulomb potential, while the contribution of the nuclear interaction is small and nearly constant across the entire range considered. The proposed method, which employs the rectangular potential well model to determine the astrophysical S-factor of fusion reactions involving light spinless nuclei, enabled the comparison of process intensities in different interacting systems. As a result, it became possible not only to predict and determine fusion cross sections at low energies but also to gain a deeper understanding of the reaction mechanisms for light nuclei of astrophysical interest.

During theoretical studies of the excitation functions of (p,n) nuclear reactions for the mass range A>40, a new systematics was developed, and optimal modeling parameters were selected for all considered regions of the excitation function. This allowed for the confirmation of the mechanisms underlying the nuclear processes. As part of this work, 120 experimental excitation functions of nuclear reactions were analyzed across an energy range from several MeV to 60 MeV and a mass range from A = 40 to A = 60. A comparative analysis with cross-section calculations based on the developed systematics showed good agreement between the theoretical results and the experimental data. It was found that the largest deviations from the proposed systematics occur in the low-energy region, indicating potential errors in the experimental data. Additionally, in some cases, discrepancies with the systematics were observed for energies below the Coulomb barrier. For several nuclear reactions near their threshold energies, a systematic energy shift in the experimental data was identified. This highlights existing errors in experimental studies, as well as in the procedures used to analyze the experimental results.

The main outcome of these studies is that this approach can be used for the quantitative assessment of the formation processes of specific radionuclides in the output channels of reactions involving different targets. This is because the developed systematics provides a reliable description of the dependence of the (p,n) reaction cross section on the incident proton energy. At the same time, the observed deviations between theoretical calculations and experimental data for certain nuclear reactions, particularly in the region of the excitation function maximum, provide a strong argument for doing additional experiments in this direction.

To study nuclear reactions involving medium-mass isotopes and to address challenges related to radionuclide production, an experimental setup was developed and constructed. A key component of this setup was a new target complex. A system for monitoring target heating was created, and optimal parameters for the target cooling system were determined.

In this dissertation, nuclear reactions for the production of antimony radionuclides were investigated. These experimental studies were carried out in several

stages. In the first stage, reactions involving proton bombardment of targets with a natural composition of tin isotopes were studied. A modernized target complex, equipped with a system for real-time operational monitoring of target heating and cooling during irradiation, was utilized. During the studies, several monitor reactions optimal for determining the parameters of accelerated particle beams were identified. Theoretical investigations of the excitation functions for both the monitor reactions and the reactions leading to the formation of antimony radionuclides in the output channel were also performed. This provided a good opportunity to predict the maxima in the excitation function cross-sections for the subsequent practical application of the obtained results in the production of radionuclides used in medical technologies [41].

In this dissertation, data on the excitation functions of nuclear reactions leading to the formation of radionuclides in the medium-mass range were obtained. This is particularly significant because experimental studies of the excitation functions for a number of reactions producing radionuclides important for nuclear medicine either lack sufficient data (especially in the incident proton energy range of 10 to 20 MeV) or are entirely absent.

The dissertation focused on nuclear reactions involving proton bombardment of $^{117}$Sn and $^{119}$Sn targets, resulting in the formation of antimony radionuclides in the output channels. These radionuclides are promising for their potential applications in medical technologies.

Experiments were done using targets such as Cd and stainless steel foil with elevated chromium and nickel content to refine the methodology for experiments with highly enriched (over 85%) tin targets: $^{117}$Sn and $^{119}$Sn. As a result, corresponding experiments were carried out to study the excitation functions of the nuclear reactions: $^{117}$Sn(p,n)$^{117}$Sb and $^{119}$Sn(p,n)$^{119}$Sb [34].

A significant part of this dissertation was dedicated to the study of nuclear technologies and nuclear reactions for the production of radionuclides used in nuclear medicine. The results of experimental and theoretical investigations of the excitation functions of (p,xn) reactions in the energy range of 6–80 MeV were analyzed for nuclear systems in the medium-mass range, leading to the formation of radionuclides:

$^{44}$Sc, $^{99m}$Tc, $^{117,119}$Sb, $^{161}$Tb, promising for use in high-precision visualization of tumor formations, targeted radionuclide therapy, and combined cancer treatment methods such as theranostics. However, experimental studies of the excitation functions for a number of nuclear reactions producing these radionuclides lack sufficient data, particularly in the energy range of charged particles bombarding the target, which corresponds to the region of the excitation function maxima for the respective reactions. Therefore, in this dissertation, nuclear reactions involving protons and deuterons of the following types: (p, n), (p, 2n), (p, d), (p, pn), (p, d + pn), (d, n), (d, p) were studied. A comprehensive analysis using theoretical models to investigate the excitation functions of nuclear reaction: $^{44}$Ca(p, n)$^{44}$Sc, $^{45}$Sc(p, 2n)$^{44}$Ti, $^{100}$Mo(p, x)$^{99}$Mo, $^{100}$Mo(p, 2n)$^{99m}$Tc, $^{160}$Gd(d, x)$^{161}$Tb, $^{117}$Sn(p, n)$^{117}$Sb, $^{119}$Sn(p, n)$^{119}$Sb was done and a number of questions regarding the mechanisms of these reactions and the behavior of the excitation functions in the region of their maxima was solved and described. However, the calculations also raised several interesting questions concerning the dynamics of these reactions. As a result, the study of the excitation function in the region of the maximum ("One peak fighting is enough to fill the heart... [189]") must be continued, both through the development of new theoretical algorithms and the design of new experiments. The latter is of significant practical importance. This includes the results obtained in this dissertation for determining the thick targets yields in reactions producing $^{99m}$Tc, widely used in SPECT (as well as its generator form $^{99}$Mo/$^{99m}$Tc) and the radionuclides $^{117}$Sb and $^{119}$Sb, which are promising for theranostic applications. An assessment of the accumulated activity was performed, leading to the conclusion that the production of $^{99m}$Tc on proton accelerators in the energy range of 40–80 MeV, and antimony radionuclides on compact cyclotrons with energies up to 15 MeV, can meet the existing demands of medical institutions for the corresponding radiopharmaceuticals [33].

These findings provide strong justification for continuing research into nuclear reactions, both in the medium and heavier mass ranges. Such research is essential not only for fundamental science but also for the applied aspects of nuclear physics and medical technologies, ultimately contributing to the goal of Health for every citizens of of our Planet!

# ACKNOWLEDGEMENTS

During the work on this dissertation, the author received invaluable and comprehensive assistance, as well as support, from numerous colleagues and friends. The author considers it to express deepest gratitude to the following individuals and organizations:

to my co-authors and colleagues, Sergei Yuryevich Torilov and Nikolay Aleksandrovich Maltsev, for the significant scientific work accomplished together;

to my s close colleague, Grigory Aleksandrovich Feofilov, for meaningful discussions regarding this work and for his critical comments on the core issues described;

to my scientific mentors, Professors Wolfram von Oertzen, Konstantin Aleksandrovich Gridnev, and Leonid Vasilyevich Krasnov;

to my colleague, Igor Evgenievich Alekseev, for conducting comprehensive joint experimental research at a qualitatively new level;

to my many students from the Educational Laboratory of Nuclear Processes for their assistance in the work and the wish to conquer many scientific peaks;

to my colleagues from the Department of Nuclear Physics Research Methods and the Laboratory of Ultrahigh Energy Physics of St. Petersburg State University, as well as colleagues from the Kurchatov Institute National Research Center, and the B.P. Konstantinov Petersburg Nuclear Physics Institute, the Joint Institute for Nuclear Research, the A.F. Ioffe Physical-Technical Institute, and the V.G. Khlopin Radium Institute for fruitful cooperation and the solution of many common problems that arose during the creation of this work. The author also expresses special gratitude to the staff of the MGC-20 cyclotron of the V.G. Khlopin Radium Institute, the staff of the MGC-20 cyclotron of the Nuclear Physics Scientific Technical Centre of St. Petersburg Polytechnical University and to the staff of the Unique Scientific Setup "Cyclotron" of the A.F. Ioffe Institute and personally with great gratefully to M.F. Kudoyarov for the opportunity to provide experimental studies within the framework of this work;

to my colleagues from leading foreign universities and research centers: Helmholtz Centre for Materials and Energy – Hahn-Meitner-Institut Berlin, Texas A&M University, The University of Jyvaskyla, CERN, Nazarbayev University, L. N. Gumilyov Eurasian National University, for extensive discussions, criticism and assistance in my work;

to my friends from Russia and other countries for the moral and spiritual support provided throughout the entire period of work on my dissertation.

In conclusion, I would like to express my heartfelt gratitude to my Family for the unique atmosphere of harmony, understanding, and care that surrounded me throughout the entire process of creating this scientific work.

# LITERATURE

1. Rutherford E., Selected scientific works. The structure of the atom and artificial transformation of elements, M: Science, 1972, 964 p.

2. Sliv L. A., Frontiers of Nuclear Physics, Uspekhi Fizicheskikh Nauk, v.133, issue. 2, 1981, pp. 337-350.

3. Nuclear Science Advisory Committee (NSAC) [E-resource]: http://science.energy.gov/np/nsac/

4. Thompson I. J., Nunes F. M., Nuclear reactions for astrophysics, Cambridge University Press, 2009, ISBN 978-0-521-85635-5, 456 p.

5. [E-resource]: https://spbu.ru/news-events/novosti/fiziki-spbgu-smodelirovali-klyuchevoy-process-dlya-evolyucii-zvezd/

6. Fowler W.A., Caughlan G.R., Zimmerman B.A., Thermonuclear Reaction Rates, II, Annu. Rev. Astron. Astrophys., V. 13, 1975, P. 69.

7. Chamon L.C., Carlson B.V., Gasques L.R., Sao Paulo potential version 2 (SPP2) and Brazilian nuclear potential (BNP), Comput. Phys. Commun., vol. 267, 2021, p. 108061.

8. Hudan S., deSouza R.T., Umar A.S., Lin Z., Horowitz C.J., Enhanced dynamics in fusion of neutron-rich oxygen nuclei at above-barrier energies, Physical Review C, vol. 101, iss. 6, 2020, p. 061601.

9. Singh, V, Johnstone J. E., Giri R. et al, Impact of shell structure on the fusion of neutron-rich mid-mass nuclei, Physical Review C, vol. 104, iss. 4, 2021, p. L041601.

10. Wang B., Ren Z., Bai D., $^{16-18}O+^{16}O$ and $^{16,18}O+^{12,13}C$ fusion-evaporation reactions at near-Coulomb-barrier energies from statistical model calculations, Physical Review C, vol. 101, iss. 2, 2020, p. 024606.

11. Jiang C.L., Back B.B., Rehm K.E. et al., Heavy-ion fusion reactions at extreme sub-barrier energies, Eur. Physical Journal A, vol. 57, №235, 2021.

12. Durant V., Capel P., Schwenk A., Dispersion relations applied to double-folding potentials from chiral effective field theory, Physical Review C, vol. 102, iss. 1, 2020, p. 014622.

13. Dohet-Eraly J., Descouvemont P., Exchange effects in nucleus-nucleus reactions, Physical Review C, vol. 103, iss. 3, 2021, p. 034619.

14. Taniguchi Y., Kimura M., $^{12}C+^{16}O$ molecular resonances at deep sub-barrier energy, Phys. Lett. B, vol. 800, Art. No 135086, 2020.

15. Fang X., Tan W.P., Beard M., et al., Experimental measurement of $^{12}C+^{16}O$ fusion at stellar energies, Phys. Rev. C, vol. 96, Art. No 045804, 2017.

16. Jaeger, M., Kunz, R., Mayer, A. et al., $22Ne(\alpha,n)25Mg$: The Key Neutron Source in Massive Stars, Phys. Rev. Lett, vol. 87, iss. 20, 2001, p. 202501.

17. von Oertzen, W., Zherebchevsky V., Gebauer, B., et al., Fission decay of $N$=$Z$ nuclei at high angular momentum: $^{60}Zn$, Phys. Rev. C, vol. 78, iss. 4, 2008, p. 044615.

18. von Oertzen W., Gebauer, B., Efimov G., Zherebchevsky V., et al., Fission and ternary cluster decay of hyper-deformed $^{56}Ni$, Eur. Phys. J. A, vol. 36, 2008, p. 279.

19. Torilov S.Y., Gridnev K.A., Zherebchevsky V.I. et al., Cluster states in the neutron excess nucleus $^{22}Ne$, JETP Lett., vol. 94, iss. 1, 2011, p. 6.

20. Beck C, Papka P…., von Oertzen W, Zherebchevsky V, et al., Clusters in light nuclei, Acta Physica Polonica B, vol. 42, no. 3-4, 2011, p. 747.

21. Torilov S.Y., Brenner M…., Zherebchevsky V, et al., High-spin states in $^{22}Ne$ populated in the $^{14}C(^{12}C, \alpha)$reaction, Eur. Phys. J. A, vol. 47, iss.12, Art. No 158, 2011.

22. Torilov S.Y., Maltsev N.A., Goldberg V.Z…., Zherebchevsky V.I., et al., Quasimolecular states in a reaction with carbon isotopes, JETP Lett., vol. 102, iss. 2, 2015, p. 69.

23. Torilov S.Y., Maltsev N.A., Goldberg V.Z…..., Zherebchevsky V.I., et al., Decay of quasimolecular states in 26Mg, Bull. Russ. Acad. Sci. Phys. vol. 80, iss.8, 2016, p. 871.

24. Kumbartzki G. J., Benczer-Koller N., Burcher S….., Zherebchevsky V.I., et al., Transition from collectivity to single-particle degrees of freedom from magnetic moment measurements on $^{82}Sr_{44}$ and $^{90}Sr_{52}$, Phys. Rev. C, vol. 89, iss. 6, 2014, p. 064305.

25. Nurmukhanbetova A.K., Goldberg V.Z., Nauruzbayev D.K….., Zherebchevsky V.I., et al., Implementation of TTIK method and time of flight for resonance reaction

studies at heavy ion accelerator DC-60, Nucl. Instr. Meth. Phys. Res. A, vol. 847, 2017, p. 125.

26. Zherebchevsky V.I., Igolkin S.N., Krymov E.B. et al., Extra lightweight mechanical support structures with the integrated cooling system for a new generation of vertex detectors, Instruments and Experimental Techniques, vol. 57, 2014, p.356.

27. Zherebchevsky V.I., Altsybeev I.G., Feofilov G.A., et. al., Experimental investigation of new ultra-lightweight support and cooling structures for the new Inner Tracking System of the ALICE Detector, Journal of Instrumentation, vol. 13., № T08003, 2018.

28. Nesterov D.G., Zherebchevsky V.I., Feofilov G.A. et al., Cooling Systems for the Novel Pixel Detectors, Phys. Part. Nuclei, vol. 53, 2022, p. 582.

29. Rakhmatullina A., Zherebchevsky V., Maltsev N. et al., New Calorimetry Based on Silicon Pixel Detectors, Phys. Part. Nuclei, vol. 53, 2022, p. 342.

30. Mutterer M., Trzaska W. H., Tyurin G et al., Breakthrough in pulse-shape based particle identification with silicon detectors, 1999 Nuclear Science Symposium and Medical Imaging Conference (Cat. No. 99CH37019). Vol. 1. IEEE, 1999, p. 148.

31. Mutterer M., Trzaska W.H., Kopatch Yu.N, et al., Particle identification with time-of-flight and pulse-shape discrimination in neutron-transmutation-doped silicon detectors, Nucl. Instr. Meth. Phys. Res. A, vol. 608, iss. 2, 2009, p. 275.

32. Zherebchevsky V.I., Radionuclide or scalpel, Journal of St. Petersburg State University, № 6(3926), 2020, P. 29.

33. Zherebchevsky V.I., Alekseev I.E., Maltsev N.A. et al., Modern Technologies for Producing Radionuclides for Nuclear Medicine, Bull. Russ. Acad. Sci. Phys., vol. 87, iss. 8, 2023, p. 1207.

34. Zherebchevsky, V.I., Alekseev, I.E., Lazareva, T.V. et al. New Radionuclides for Personalized Medicine. Bull. Russ. Acad. Sci. Phys. vol. 85, iss. 10, 2021, p. 1128.

35. Gallego Manzano L., Abaline J.M., Acounis S., et al., XEMIS2: A liquid xenon detector for small animal medical imaging, Nuclear Instruments and Methods in Physics Research Section A, , vol. 912, 2018, p. 329-332.

36. Lang C., Habs D., Parodi K., Thirolfa P.G., Sub-millimeter nuclear medical

imaging with high sensitivity in positron emission tomography using $\beta^{+}\gamma$ coincidences, Journal of Instrumentation, vol. 9, P01008, 2014.

37. Rosar F., Bohnenberger H., Moon E.S., et al., Impact of prompt gamma emission of $^{44}$Sc on quantification in preclinical and clinical PET systems, Appl. Radiat. Isotopes, vol. 170, 2021, p. 109599.

38. Mueller C., Zhernosekov K., Koester U., et al., A unique matched quadruplet of terbium radioisotopes for PET and SPECT and for α- and β- radionuclide therapy: an in vivo proof-of-concept study with a new receptor-targeted folate derivative, J. Nucl. Med., vol. 53, no. 12, 2012, p. 1951.

39. Borgna F., Haller S., Rodriguez J.M.M., et al., Combination of terbium-161 with somatostatin receptor antagonists—a potential paradigm shift for the treatment of neuroendocrine neoplasms, Eur. J. Nucl. Med. Mol. Imaging, vol. 49, 2022, p. 1113.

40. Baum R.P., Singh A., Kulkarni H.R., et al., First-in-Humans Application of $^{161}$Tb: A Feasibility Study Using $^{161}$Tb-DOTATOC, J. Nucl. Med., 2021, vol. 62, no. 10, p. 1391.

41. Zherebchevsky V.I., Alekseev, I.E., Gridnev K.A. et al., The study of the nuclear reactions for the production of antimony isotopes, Bull. Russ. Acad. Sci. Phys. vol. 80, iss. 8, 2016, p. 888.

42. Gomez-Tejedor G.G., Fuss M.C., Radiation Damage in Biomolecular Systems, New York: Springer, ISBN: 978-94-007-2563-8, 2012.

43. International Atomic Energy Agency, Technical Reports Series No. 468, Austria, 2009.

44. Mayeen Uddin K., Kwangsoo K., Kyung-Sook K., et. al., Excitation functions of the proton-induced nuclear reactions on $^{nat}$Sn up to 40 MeV, Nuclear Instruments and Methods in Physics Research B, vol. 267, 2009, p. 23.

45. EXFOR: Experimental Nuclear Reaction Data. [E-resource]: https://www-nds.iaea.org/exfor/exfor.htm

46. Thisgaard H., Jensen M., Production of the Auger emitter $^{119}$Sb for targeted radionuclide therapy using a small PET-cyclotron, Applied Radiation and Isotopes, vol. 67, iss. 1, 2009, p. 34.

47. Thisgaard H., Jensen M., Elema D.R., Medium to large scale radioisotope production for targeted radiotherapy using a small PET cyclotron, Applied Radiation and Isotopes, vol. 69, iss. 1, 2011, p. 1.

48. D. Bromley, Nuclear Molecules, Uspehi Fizicheskih Nauk, v. 131, 1980, p. 695.

49. Fulton B.R.,Nuclear clusters and nuclear molecules, Z. Physik A - Hadrons and Nuclei, vol. 349, 1994, p. 227.

50. von Oertzen W., Dynamics of α-clusters in N = Z nuclei, Eur. Phys. J. A vol. 29, 2006, p. 133.

51. Zhang J., Rae W.D.M., Systematics of 2-dimensional α-cluster configurations in 4N nuclei from 12C to 44Ti, Nuclear Physics A, vol. 564, iss. 2, 1993, p. 252.

52. Zhang J., Rae W.D.M., Merchant A.C., Systematics of some 3-dimensional α-cluster configurations in 4N nuclei from $^{16}$O to $^{44}$Ti, Nuclear Physics A, vol. 575, iss. 1, 1994, p. 61.

53. Itagaki N., Aoyama S., Okabe S. Ikeda K., Cluster-shell competition in light nuclei, Phys. Rev. C, vol. 70, iss. 5, 2004, p. 054307.

54. Mueller G.P., Clark J.W., Ground state properties of alpha matter, Nuclear Physics A, vol.155, 1979, p. 561.

55. Baz A.I., On the effect of strong repulsion of composite particles (nuclei, atoms) at small distances, JETP Letters, vol. 14, 1971, p. 607.

56. Wheeler J. A., Molecular Viewpoints in Nuclear Structure, Phys. Rev. vol. 52, iss. 11, 1937, p. 1083.

57. Hafstad L. R., Teller E., Phys. Rev. vol. 54, iss. 9, 1938, p. 681.

58. Lombardo I., Dell Aquila D., Clusters in light nuclei: history and recent developments, La Rivista del Nuovo Cimento, vol. 46, iss. 9, 2023, p. 521.

59. Wei K., Ye Y., Yang, Zh., Clustering in nuclei: progress and perspectives, Nuclear Science and Techniques, vol. 35, iss. 12, 2024, p. 216.

60. Buck B., Friedrich H., Pilt A.A., Nuclear Physics A, vol. 290, iss. 1, 1977, p. 205.

61. Gridnev K.A., Torilov S. Yu., Kartavenko V.G., Greiner W., Model of bindin galpha-particles and structure of the light nuclei, Int. Journal Mod. Phys. E., vol.16, 2007, p.1059.

62. Liu Y., Ye Yl, Nuclear clustering in light neutron-rich nuclei, vol. 29, iss. 12, 2018, p. 184.

63. Schuck P., Funaki Y., Horiuchi H., Röpke G., Tohsaki A., Yamada T., Alpha-particle condensation in nuclei, Nuclear Physics A, vol. 738, 2004, p. 94.

64. von Oertzen W., Alpha-cluster Condensations in Nuclei and Experimental Approaches for their Studies, In: Beck, C. (eds) Clusters in Nuclei. Lecture Notes in Physics, vol 818. 2010, Springer, Berlin.

65. Demyanova, A., Starastsin V., Ogloblin A. Danilov A., et al, The spin-parities of the 13.35 MeV state and high-lying excited states around 20 MeV in C nucleus, Eur. Phys. J. A, vol. 57, 2021, p. 204.

66. Schuck P., Horiuchi H., Ropke G., Tohsaki A., Alpha-particle condensation in nuclei, C. R. Physique 4, 2003, p. 537.

67. V. I. Zherebchevsky, S. Yu. Torilov, K. A. Gridnev, et al., Elastic scattering of alpha particles on the neutron-rich nucleus 14C, Bulletin of St. Petersburg State University, Series 4, Issue 1, 2013.

68. Zherebchevsky V. I., Torilov S. Yu., Gridnev K. A., Determination of the sizes of nuclei, Textbook-method manual, ISBN 978-5-9651-0827-5, VVM Publishing House, St. Petersburg, 2013.

69. Zherebchevsky V. I., Zemlin E. O., Maltsev N. A., Multisensor system for charged particle and heavy ion beams monitoring, Patent for invention, № 2830097, 2024.

70. Buck B. Merchant A. C., Perez S. M., Parameter-free characterization of nuclear band spectra, Phys. Rev. C, vol. 76., N 5, 2007, p. 034326.

71. El-Azab F. M., Mahmoud Z. M. M., Hassan G. S., Analysis of Heavy Ions Elastic Scattering using the Double Folding Cluster Model, Nucl. Phys. A, vol. 691, N 3, 2001, p. 671.

72. Chamon L. C., Carlson B. V., Gasques L. R., et al., Toward a global description of the nucleus-nucleus interaction, Phys. Rev. C, vol. 66, N 3, 2002, p. 014610.

73. Chamon L. C, The Sao Paulo Potential, Nucl. Phys. A, vol. 787, 2007, p. 198.

74. Buck B., Dover C. B., Vary J. P., Simple Potential Model for Cluster States in

Light Nuclei, Phys. Rev. C, vol. 11, 1975, p. 1803.

75. Barioni A., Zamora J. C., Guimaraes V., et al., Elastic scattering and total reaction cross sections for the $^{8}$B, $^{7}$Be, and $^{6}$Li+$^{12}$C systems, Phys. Rev. C, vol. 84, 2011, p. 014603.

76. Artukh A.G., Avdeichikov V.V., Ero J., Gridnev G.F., Mikheev V.L., Volkov V.V., Wilczynski J., On some regularities in multinucleon transfer reactions with heavy ions, Nuclear Physics A, vol. 160, iss. 3, 1971, p. 511.

77. Volkov V. V., Deep inelastic transfer reactions – the new type of reactions between complex nuclei, Phys. Rep., vol. 44, 1978, p. 93.

78. V.V. Volkov, Nuclear reactions of deeply inelastic transmissions, M: Enegologizdat, 1982.

79. Zagrebaev V., Greiner W., Production of New Heavy Isotopes in Low-Energy Multinucleon Transfer Reactions, Phys. Rev. Lett., vol. 101, iss. 12, 2008, p. 122701.

80. Perez-Vidal R.M., Galtarossa F., Mijatovic T. et al., Nuclear structure advancements with multi-nucleon transfer reactions, Eur. Phys. J. A, vol. 59, 2023, p. 114.

81. Panagiotou A. D., Gove H. E., Harar, S., High-Spin States in $^{20}$Ne and Their Possible Classification into Rotational Bands, Phys. Rev. C, vol. 5, iss. 6, 1972, p. 1995.

82. Hill D., Wheeler J., Nuclear constitution and the interpretation of fission fhenomena, Phys. Rev., vol. 89. N 5. 1953, p. 1102.

83. Ragnarsson I., Aberg S., Sheline R.K., A New Formalism for High Spin States Applied to the sd-Shell Region, Phys. Scr., vol. 24, 1981, p. 215.

84. Tilley D.R., Cheves C.M., Kelley J.H., Raman S., Weller H.R., Energy levels of light nuclei A = 20, Nuclear Physics A, vol. 636, iss. 3, 1998, p. 249.

85. Kimura M., Molecular orbitals and α+ $^{18}$O molecular bands of $^{22}$Ne, Phys. Rev. C, vol. 75, iss. 3, 2007, p. 034312.

86. Keyes K. L., Papenberg A., Chapman R., et al., Spectroscopy of Ne, Na and Mg isotopes approaching the Island of Inversion, Journal of Physics G: Nuclear and Particle Physics, vol. 31, N 10, 2005, p. 1903.

87. Freeman R. M., Basrak Z., Haas F., Hachem A. et al., Resonant and nonresonant

behavior of the heavy-ion reaction $^{14}C+^{12}C$, Phys. Rev C, vol. 46, iss 2, 1992, p. 589.

88. Abbondanno U., Cindro N., Resonances in heavy-ion reactions: an overview of current models, Int. J. Mod. Phys. E, vol. 2, iss. 1, 1993, p. 1.

89. Curtis N., Caussyn D. D., Chandler C., et al., Phys Rev C, vol. 66, iss. 2, 2002, p. 024315.

90. Hindi M.M., Thomas J.H., Radford D.C., Parker P.D., Physics Letters B, vol. 99, iss. 1, 1981, p. 33.

91. Ledoux R. J., Ordonez C. E., Bechara, M. J., et al., Phys. Rev. C, vol. 30, iss. 3, 1984, p. 86.

92. Yildiz S., Freer M., Soic et al., α-decaying states $^{18}O$, $^{20}Ne$ and $^{22}Ne$ in $^{18}O$ beam induced reactions, Phys. Rev. C, vol. 73, iss. 3, 2006, p. 034601.

93. Rogachev G. V., Goldberg V. Z., Lonnroth T.,Trzaska W. H., Fayans S. A, et. al., Phys. Rev. C, vol. 64, iss. 5, 2001, p. 051302.

94. Allcock S. C., Rae W. D. M., Keeling P.R. et al., $10^+$ states in $^{20}Ne$, Phys. Lett, vol. 138,1988, p.201.

95. von Oertzen W., Dorsch T., Bohlen H.G. et al., Molecular and cluster structures in $^{18}O$, Eur. Phys. J. A, vol. 43, 2010, p. 17.

96. Kubono S., Nuclear clustering aspects in astrophysics, Z. Physik A – Hadrons and Nuclei, vol. 349, 1993, p. 237.

97. Kubono S, Binh, D. N, Hayakawa S, Hashimoto H et al., Role of clusters in nuclear astrophysics with Cluster Nucleosynthesis Diagram (CND), Journal of Physics: Conference Series, vol. 436, iss. 1, 2013.

98. Ikeda K., Takigawa N., Horiuchi H., The Systematic Structure-Change into the Molecule-like Structures in the Self-Conjugate 4n Nuclei, Progress of Theoretical Physics Supplement E, vol. E68, 1968, p. 464.

99. von Oertzen W., Kanada-Enyo Y., Kimuraet M, Covalent Binding with Neutrons on the Femto-scale, J. Phys.: Conf. Ser. vol. 863, 2017, p. 012066.

100. Bazin D., Ahn T., Ayyad Y., Beceiro-Novo S., Macchiavelli A.O., et al., Low energy nuclear physics with active targets and time projection chambers, Progress in Particle and Nuclear Physics, vol. 114, 2020, p. 103790.

101. Michel F., Albinski J., Belery P., et al., Optical model description of $\alpha$+$^{16}$O elastic scattering and alpha-cluster structure in $^{20}$Ne, Phys. Rev. C., vol. 28. 1983, p. 1904.

102. Buck B., Johnston J. C., Merchant A. C., Perez S. M., Unified treatment of scattering and cluster structure in α+closed shell nuclei: $^{20}$Ne and $^{44}$Ti, Phys. Rev. C., vol. 52, 1995, p. 1840.

103. Balaram D., et al., Exotic nuclear shape due to cluster formation at high angular momentum, Phys. Rev. C, vol. 102, 2020, p. 031301.

104. Courtin S., Goasduff A., Haas F., et al., Radiative capture in the 12C+16O system: structural versus statistical aspects of the decay, Acta Physica Polonica B, vol. 42, No 3–4, 2011.

105. Ohkubo S., Yamashita K., Parity-doublet $^{16}$O+$^{12}$C cluster bands in $^{28}$Si, Phys. Lett. B, vol. 578, 2004, p. 304.

106. Nicoli M.P., Haas F., Freeman R.M., et al., Detailed study and mean field interpretation of $^{16}$O+$^{12}$C elastic scattering at seven medium energies, Phys. Rev. C, vol. 61, 2000, p. 034609.

107. S. Yu. Torilov, N. A. Maltsev, V. I. Zherebchevsky et al., A study of resonance states in nuclear systems formed in reactions with heavy ions, Physics of Particles and Nuclei, Vol. 53, iss. 2, 2022, p. 403.

108. Programm FRESCO, [E-resource]: http://www.fresco.org.uk/

109. Vertse T., Pal K. F., Balogh Z., Gamow, a program for calculating the resonant state solution of the radial Schrodinger equation in an arbitrary optical potential, Comput. Phys. Commun., vol. 27, 1982, p. 309.

110. Buck B., Merchant A., Perez S., Cluster selection in binary nuclear models, Few-Body Systems vol. 29, iss. 1, 2000, p. 53.

111. Charles P., Auger F., Badawy I., Berthier B., et al., Resonant Behaviour of the $^{16}$O + $^{12}$C Elastic Scattering Cross Section, Phys. Lett. B, vol. 62, 1976, p. 289–292.

112. Branford D., Nagorcka B.N., Newton J.O., Further Evidence for Resonance Anomalies in the $^{16}$O+$^{12}$C System, J. Phys. G: Nucl. Phys., vol. 3, 1977, p. 1565.

113. Jachcinski C. M., Braun-Munzinger P., Berkowitz G. M., et al., $^{16}$O+$^{12}$C

Resonances within the Strong Absorption Region for Ecm ≥ 23 MeV, Phys. Rev. C, vol. 22, 1980, p. 101.

114. Malmin R.E., Siemssen R.H., Sink D.A., Singh P.P., Resonance in $^{12}C+^{16}O$ Scattering at $E_{cm} \approx 19.7$ MeV, Phys. Rev. Lett., vol. 28, 1972, p. 1590.

115. Froehlich H., Dueck P., Treu W., Voit H., Experimental Evidence for Dinuclear Structure of $^{16}O + ^{12}C$ Resonances in the Coulomb Barrier Region, Phys. Rev. C, vol. 27, 1983, p. 578.

116. Frawley A.D., Roy A., Fletcher N.R., Transparency to the $l = 9$ Partial Wave in the Region of the 14.7-MeV Resonance in $^{12}C+^{16}O$, Phys. Rev. Lett., vol. 44, 1980, p. 1377.

117. Soga F., Schimizu J., Kamitsubo H., Takahashi N., et al., Intermediate Structures in $^{12}C+^{16}O$ System through Alpha-Induced Reactions on $^{24}Mg$, Phys. Rev. C, vol. 18, 1978, p. 2457.

118. Eberhard K.A., Bohn H., Bernhardt K.G., Narrow $I^{\pi} = 10^{+}$ Resonance for $^{12}C+^{16}O$ in the Region of Strong Absorption, Phys. Rev. Lett., vol. 42, 1979, p. 432.

119. Hurd J. R., Fletcher N.R., Frawley A.D., Mateja J. F., Intermediate Structures and Their Dominant *l* Values in $^{16}O(^{12}C, ^{8}Be)^{20}Ne$ Reactions, $E_{cm} = 11.5$ to 18.6 MeV, Phys. Rev. C, vol. 22, 1980, p. 528.

120. James D. R., Fletcher R. N. Energies and J Values of Resonances in $^{16}O(^{12}C, ^{8}Be)^{20}Ne$ Reactions, Phys. Rev. C, vol. 20, 1979, p. 560.

121. Kato N., Anai K., Tachikawa T., et al., Spin Alignment in Resonant $^{12}C+^{16}O$ Inelastic Scattering, Phys. Lett. B, vol. 120, 1983, p. 314.

122. Froehlich H., Duck P., Galster W., et al., Oscillations in the Excitation Function for Complete Fusion of $^{16}O+^{12}C$ at Low Energies, Phys. Lett. B, vol. 64, 1976, p. 408.

123. Chapuran T., Balamuth D. P., Wells W. R., et al., Angular Momenta of Intermediate Width Structures in $^{12}C+^{16}O$, Phys. Rev. C, vol. 34, 1986, p. 2358.

124. Katori K., Furuno K., Ooi T., Enhancement of the Excitation Function for the $0^{+}$, 6.049 MeV State of $^{16}O$ in the Reaction $^{12}C(^{16}O, ^{12}C)^{16}O$, Phys. Rev. Lett., vol. 40, 1978, p. 1489.

125. S. Yu. Torilov, V. I. Zherebchevsky, N. A. Maltsev, Editor's Choice of the

Journal "Bulletin of the Russian Academy of Sciences. Physical Series", No. 8, Volume 87, 2023, [E-resource]: https://izv-fiz.ru/ru/redchoice/

126. Jiang C.L., Back B.B., Esbensen H., et al., Origin and Consequences of $^{12}C + ^{12}C$ Fusion Resonances at Deep Sub-barrier Energies, Phys. Rev. Lett., vol. 110, 2013, p. 072701.

127. Torilov S., Maltsev N., Zherebchevsky V., Studying Low-Energy Resonances in the $^{12}C + ^{16}O$ System, Bulletin of the Russian Academy of Sciences: Physics, vol. 85, iss. 5, 2021, p. 548.

128. Igo G., Optical-Model Analysis of Excitation Function Data and Theoretical Reaction Cross Sections for Alpha Particles, Phys. Rev., vol. 115, Art. No. 1665, 1959.

129. Christensen P.R., Switkowskiw Z.E., Dayras R.A., Sub-barrier fusion measurements for $^{12}C+^{16}O$, Nucl. Phys. A, vol. 280, 1977, p. 189.

130. Cujec B., Barnes C.A., Total reaction cross section for $^{12}C + ^{16}O$ below the Coulomb barrier, Nucl. Phys. A, vol. 266, 1976, p. 461.

131. deSouza R. T., Hudan S., Oberacker V. E., Umar A. S., Confronting measured near- and sub-barrier fusion cross sections for $^{20}O+^{12}C$ with a microscopic method, Phys. Rev. C: Nucl. Phys., vol. 88, 2013, p. 014602.

132. Patterson J.R., Nagorcka B.N., Symons G.D., Zuk W.M., Experimental investigation of $^{16}O + ^{12}C$ nuclear burning at stellar energies, Nucl. Phys. A, vol. 165, 1971, p. 545.

133. Hagino K., Rowley N., Kruppa A.T., A program for coupled-channel calculations with all order couplings for heavy-ion fusion reactions, Comput. Phys. Commun., vol. 123, 1999, p. 143.

134. Kocak G., Analysis of the fusion cross sections for $^{16,18,20}O + ^{12}C$ systems at low energies, Canad. J. Phys., vol. 97, 2019, p. 803.

135. Yakovlev D.G., Gasques L.R., Afanasjev A.V., et al., Fusion reactions in multicomponent dense matter, Phys. Rev. C: Nucl. Phys., vol. 74, 2006, p. 035803.

136. Ogura R., Hagino K., Bertulani C.A., Potential model for nuclear astrophysical fusion reactions with a square-well potential, Phys. Rev. C: Nucl. Phys., vol. 99, 2019, p. 065808.

137. S. Yu. Torilov, N. A. Maltsev, V. I. Zherebchevsky, Astrophysical S-Factor in the Model of a Square Potential Well, Bulletin of the Russian Academy of Sciences: Physics, vol. 87, iss. 8, 2023, p. 1217.

138. Michaud G., Fowler W.A., Thermonuclear-Reaction Rates at High Temperature, Phys. Rev. C, vol. 2, 1970, p. 2041.

139. Jiang C.L., A modified-Wong formula for heavy-ion fusion reactions, Eur. Phys. J. A, vol. 58, 2022, p. 72.

140. Kocak G., Karakoc M., Boztosun I., Balan-Tekin, A.B., Effects of $\alpha$-cluster potentials for the $^{16}$O +$^{16}$O fusion reaction and $S$ factor, Phys. Rev. C, vol. 81, 2010, p. 024615.

141. Michaud G., Scherk L., Vogt E., Nuclear Optical Model and Wave Properties: Barrier Penetration, Reflection, Absorption, and Resonance, Phys. Rev. C, vol. 1, 1970, p. 864.

142. Salvat F., Fernandez-Varea J.M., A Fortran subroutine package for the solution of the radial Schrodinger and Dirac wave equations, Comput. Phys. Commun., vol. 240, 2019, p. 165.

143. Gasques L.R., Brown E.F., Chieffi A., et al., Implications of low-energy fusion hindrance on stellar burning and nucleosynthesis, Phys. Rev. C, vol. 76, 2007, p. 035802.

144. Montagnoli G., Stefanini A.M., Jiang C.L., et al., Fusion of $^{12}$C+$^{24}$Mg far below the barrier: Evidence for the hindrance effect, Phys. Rev. C, vol. 101, 2020, p. 044608.

145. S. Yu. Torilov, N. A. Maltsev, R. B. Panin, V. I. Zherebchevsky, Investigating the Excitation Functions of the (p, n) Reaction for 40 < A < 239 Nuclei, Bulletin of the Russian Academy of Sciences: Physics, vol. 83, iss. 9, 2019, p. 1151.

146. Cyclotron Produced Radionuclides: Physical Characteristics and Production Methods, Vienna: IAEA, 2009.

147. Broeders C.H.M., Konobeyev A.Y., Systematics of (p, n) reaction cross-section, Radiochim. Acta, vol. 96, 2008, p. 387.

148. Elmaghraby E.K., Said S.A., Asfour F.I., Systematics of the (p, n) excitation functions belonged to several isotopes at energies < 60 MeV, Ann. Nucl. Energy, vol.

36, 2009, p. 1070.

149. Seidel K, Zeliger D, Reif R, Toneev VD, Pre-equilibrium decay in nuclear reactions, Physics of Elementary Particles and Atomic Nuclei, v.7, no.2, 1976, p. 499.

150. Gadioli E., Gadioli Erba E., Sona P.G., Intermediate-state decay rates in the exciton model, Nucl. Phys. A, vol. 217, 1973, p. 589.

151. Dostrovsky I., Frakenkel Z., Friedlander G., Monte Carlo Calculations of Nuclear Evaporation Processes. III. Applications to Low-Energy Reactions, Phys. Rev., vol. 116, 1959, p. 683.

152. Bardeen J., On the Density of Energy Levels of Heavy Nuclei, Phys. Rev., vol. 51, 1937, p. 799.

153. Murthy K.H.N., Gupta S.K., Chatterjee A., Transmission coefficients for light projectiles, Z Physik A, vol. 305, 1982, p. 73.

154. Report OECD Nuclear Energy Agency, The supply of medical radioisotopes: review of potential molybdenum-99/technetium-99m production technologies, 2010.

155. Cyclotron based production of technetium-99m, IAEA Radioisotopes and radiopharmaceuticals reports No. 2.

156. Energy Loss Calculation Program SRIM, [E-resource]: http://www.srim.org

157. Energy Loss Calculation Program GEANT 4, [E-resource]: https://geant4.web.cern.ch

158. Monitoring Reactions Database, [E-resource]: https://www-nds.iaea.org/medical/monitor_reactions.html

159. Nuclear Reaction Analysis Program TALYS, [E-resource]: https://nds.iaea.org/talys

160. Kalbach C., Proc. PRECO-2006, Durham, 2007, p. 182.

161. Chatterjee A., Murthy K.H.N., Gupta S.K. Optical reaction cross-sections for light projectiles. Pramana - J. Phys., vol. 16, 1981, p. 391.

162. Rosar F., Buchholz H.-G., Michels S., et al., Image quality analysis of $^{44}$Sc on two preclinical PET scanners: a comparison to $^{68}$Ga, EJNMMI Phys., vol. 7, 2020, p. 16.

163. Rosar F., Bohnenberger H., Moon E.S., et al., Impact of prompt gamma emission

of $^{44}$Sc on quantification in preclinical and clinical PET systems, Appl. Radiat. Isotopes, vol. 170, 2021, p. 109599.

164. Khawar A., Eppard E., Sinnes J.P., et al., Prediction of Normal Organ Absorbed Doses for [$^{177}$Lu]Lu-PSMA-617 Using [$^{44}$Sc]Sc-PSMA-617 Pharmacokinetics in Patients With Metastatic Castration Resistant Prostate Carcinoma, Clin. Nucl. Med., vol. 43, 2018, p. 486.

165. G.W. Severin, J.W. Engle, H.F. Valdovinos, T.E. Barnhart, R.J. Nickles, Cyclotron produced $^{44g}$Sc from natural calcium, Applied Radiation and Isotopes, vol. 70, iss. 8, 2012, p. 1526.

166. van der Meulen N.P., Hasler R., Talip Z., et al., Developments toward the Implementation of $^{44}$Sc Production at a Medical Cyclotron, Molecules, vol. 25, 2020, p. 4706.

167. Filosofov D.V., Loktionova N.S., Rösch F., A $^{44}$Ti/$^{44}$Sc radionuclide generator for potential application of $^{44}$Sc-based PET-radiopharmaceuticals, Radiochim. Acta, vol. 98, iss. 3, 2010, p. 149.

168. Guertin A., Nigron E., Sitarz M., et al., Proc. 15th Int. Conf. Nuclear Reaction Mechanisms, Varenna, CERN-Proceedings-2019-001, vol. 1, 2018, p. 355, [E-resource]: https://cds.cern.ch/record/2669285

169. Pupillo, G., Mou, L., Martini, P., et al., Proc. 15th Int. Conf. Nuclear Reaction Mechanisms, Varenna, CERN-Proceedings-2019-001, vol. 1, 2018, p. 341, [E-resource]: https://cds.cern.ch/record/2669285

170. Fontana, A., Calzaferri, S., Canton, L., et al., Proc. 15th Int. Conf. Nuclear Reaction Mechanisms, Varenna, CERN-Proceedings-2019-001, vol. 12018, p. 349, [E-resource]: https://cds.cern.ch/record/2669285

171. Koning A.J., Delaroche J.P., Local and global nucleon optical models from 1 keV to 200 MeV, Nucl. Phys. A, vol. 713, 2003, p. 231.

172. Kalbach C., Toward a global exciton model: the equilibrium component, J. Phys. G, vol. 25, 1999, p. 75.

173. Otuka N., Dupont E., Semkova V., et al., Towards a More complete and accurate experimental nuclear reaction data library: International collaboration between nuclear

reaction data centres (NRDC), Nucl. Data Sheets, vol. 120, 2014, p. 272.

174. de Waal T.J., Peisach M., Pretorius R., J., Activation cross sections for proton-induced reactions on calcium isotopes up to 5.6 MeV, Inorg. Nucl. Chem., vol. 33, 1971, p. 2783,

175. Krajewski S., Cydzik I., Abbas K., et al., Cyclotron production of $^{44}$Sc for clinical application, Radiochim. Acta, vol. 101, 2013, p. 333.

176. Carzaniga T.S., Auger M., Braccini S., et al., Measurement of $^{43}$Sc and $^{44}$Sc production cross-section with an 18 MeV medical PET cyclotron, Appl. Radiat. Isotopes, vol. 129, 2017, p. 96.

177. J.P. Jeukenne, A. Lejeune, C. Mahaux, Optical-model potential in finite nuclei from Reid's hard core interaction, Phys. Rev. C, vol. 16, 1977, p. 80.

178. Liang, H., Han, Y., and Shen, Q., Calculation and analysis of p + $^{40,42,43,44,46,48,nat}$Ca reaction cross sections at incident energies from threshold to 250 MeV, Nucl. Instrum. Methods Phys. Res., Sect. B, vol. 269, 2011, p. 597.

179. Database, Charged-particle cross section database for medical radioisotope production, [E-resource]: https://www-nds.iaea.org/medical

180. Kalbach C., Preequilibrium reactions with complex particle channels, Phys. Rev. C, vol. 71, 2005, p. 034606.

181. Blann M., A priori pre-equilibrium decay models, Nucl. Phys. A, vol. 213, 1973, p. 570.

182. Qaim, S.M., Sudar, S., Scholten, B., et al., Evaluation of excitation functions of $^{100}$Mo(p,d+pn)$^{99}$Mo and $^{100}$Mo(p,2n)$^{99m}$Tc reactions: Estimation of long-lived Tc-impurity and its implication on the specific activity of cyclotron-produced $^{99m}$Tc, Appl. Radiat. Isotopes, vol. 85, 2014, p. 101.

183. Tarkanyi, F., Hermanne, A., Takacs, S., et al., Cross-section measurement of some deuteron induced reactions on $^{160}$Gd for possible production of the therapeutic radionuclide $^{161}$Tb, J. Radioanal. Nucl. Chem., vol. 298, 2013, p. 1385.

184. Avrigeanu, M., Rochman, D., Koning, A.J., et al., Advanced breakup-nucleon enhancement of deuteron-induced reaction cross sections, Eur. Phys. J. A, vol. 58, 2022, p. 3.

185. Database, National Nuclear Data Center, [E-resource]: http://www.nndc.bnl.gov

186. Bangert R., Gonsior B., Roth M., Steinmetz B., Stroemich A., The (p, n) reaction between analog states in isotopes of Sn and Sb, Nucl.Phys. A, vol. 287, 1977, p. 280.

187. Dilg W., Schantl W., Vonach H., Uhl M., Level density parameters for the back-shifted fermi gas model in the mass range 40 < a < 250, Nucl. Phys. A, vol. 217, 1973, p. 269.

188. Becchetti F. D., Greenlees G. W., Nucleon-nucleus optical-model parameters, A > 40, E < 50 MeV, Phys. Rev., vol. 182, 1969, p. 1190.

189. Camus A., L'Homme révolté, M: Politizdat 1990, p. 415.

## AUTHOR'S PUBLICATIONS LIST INCLUDED IN THE DEFENSE

1. von Oertzen, W., Zherebchevsky V., Gebauer, B., et al., Fission decay of $N$=$Z$ nuclei at high angular momentum: 60Zn, Phys. Rev. C, vol. 78, iss. 4, 2008, p. 044615.
2. von Oertzen W., Gebauer, B., Efimov G., Zherebchevsky V., et al., Fission and ternary cluster decay of hyper-deformed 56Ni, Eur. Phys. J. A, vol. 36, 2008, p. 279.
3. Torilov S.Y., Gridnev K.A., Zherebchevsky V.I. et al., Cluster states in the neutron excess nucleus 22Ne, JETP Lett., vol. 94, iss. 1, 2011, p. 6.
4. Beck C, Papka P…., von Oertzen W, Zherebchevsky V, et al., Clusters in light nuclei, Acta Physica Polonica B, vol. 42, no. 3-4, 2011, p. 747.
5. Torilov S.Y., Brenner M…., Zherebchevsky V, et al., High-spin states in 22Ne populated in the 14C(12C, α)reaction, Eur. Phys. J. A, vol. 47, iss.12, Art. No 158, 2011.
6. Torilov S.Y., Maltsev N.A., Goldberg V.Z…., Zherebchevsky V.I., et al., Quasimolecular states in a reaction with carbon isotopes, JETP Lett., vol. 102, iss. 2, 2015, p. 69.

7. Torilov S.Y., Maltsev N.A., Goldberg V.Z…..., Zherebchevsky V.I., et al., Decay of quasimolecular states in 26Mg, Bull. Russ. Acad. Sci. Phys. vol. 80, iss.8, 2016, p. 871.
8. Kumbartzki G. J., Benczer-Koller N., Burcher S….., Zherebchevsky V.I., et al., Transition from collectivity to single-particle degrees of freedom from magnetic moment measurements on 82Sr44 and 90Sr52, Phys. Rev. C, vol. 89, iss. 6, 2014, p. 064305.
9. Nurmukhanbetova A.K., Goldberg V.Z., Nauruzbayev D.K….., Zherebchevsky V.I., et al., Implementation of TTIK method and time of flight for resonance reaction studies at heavy ion accelerator DC-60, Nucl. Instr. Meth. Phys. Res. A, vol. 847, 2017, p. 125.
10. Zherebchevsky V.I., Igolkin S.N., Krymov E.B. et al., Extra lightweight mechanical support structures with the integrated cooling system for a new generation of vertex detectors, Instruments and Experimental Techniques, vol. 57, 2014, p.356.
11. Zherebchevsky V.I., Altsybeev I.G., Feofilov G.A., et. al., Experimental investigation of new ultra-lightweight support and cooling structures for the new Inner Tracking System of the ALICE Detector, Journal of Instrumentation, vol. 13., № T08003, 2018.
12. Nesterov D.G., Zherebchevsky V.I., Feofilov G.A. et al., Cooling Systems for the Novel Pixel Detectors, Phys. Part. Nuclei, vol. 53, 2022, p. 582.
13. Rakhmatullina A., Zherebchevsky V., Maltsev N. et al., New Calorimetry Based on Silicon Pixel Detectors, Phys. Part. Nuclei, vol. 53, 2022, p. 342
14. Zherebchevsky V.I., Alekseev I.E., Maltsev N.A. et al., Modern Technologies for Producing Radionuclides for Nuclear Medicine, Bull. Russ. Acad. Sci. Phys., vol. 87, iss. 8, 2023, p. 1207.
15. Zherebchevsky, V.I., Alekseev, I.E., Lazareva, T.V. et al. New Radionuclides for Personalized Medicine. Bull. Russ. Acad. Sci. Phys. vol. 85, iss. 10, 2021, p. 1128.

16. Zherebchevsky V.I., Alekseev, I.E., Gridnev K.A. et al., The study of the nuclear reactions for the production of antimony isotopes, Bull. Russ. Acad. Sci. Phys. vol. 80, iss. 8, 2016, p. 888.
17. S. Yu. Torilov, N. A. Maltsev, V. I. Zherebchevsky et al., A study of resonance states in nuclear systems formed in reactions with heavy ions, Physics of Particles and Nuclei, Vol. 53, iss. 2, 2022, p. 403.
18. Torilov S., Maltsev N., Zherebchevsky V., Studying Low-Energy Resonances in the 12C + 16O System, Bulletin of the Russian Academy of Sciences: Physics, vol. 85, iss. 5, 2021, p. 548.
19. S. Yu. Torilov, N. A. Maltsev, V. I. Zherebchevsky, Astrophysical S-Factor in the Model of a Square Potential Well, Bulletin of the Russian Academy of Sciences: Physics, vol. 87, iss. 8, 2023, p. 1217
20. S. Yu. Torilov, N. A. Maltsev, R. B. Panin, V. I. Zherebchevsky, Investigating the Excitation Functions of the (p, n) Reaction for $40 < A < 239$ Nuclei, Bulletin of the Russian Academy of Sciences: Physics, vol. 83, iss. 9, 2019, p. 1151.